Seismic tomography of the La Réunion mantle plume



Maria Tsekhmistrenko

St Edmund Hall

University of Oxford

A thesis submitted for the degree of

Doctor of Philosophy

Michaelmas 2018

To Kasra,
because words are not enough.

Acknowledgements

At the end of every big, long, tedious project there might be only one persons' name on the front page of the written work, but there are always many others behind the scenes. Indeed there are not enough words in this language to express my gratitude to all the people that were important to me during my PhD but I hope these two pages mirror at least a fraction of it.

I want to thank Karin first and foremost. Meeting you during a field trip in the Alps had a whiff of destiny to it. Despite me being a geology student at the time you let me join the RHUM-RUM cruise. You let me work on the OBS dataset despite the fact that I'm not a seismologist by training. I had to learn a lot starting this PhD and without your endless patience and support it would not have been possible do this work. Thank you.

At this point, I also want to thank Bernd Lammerer, who organised the field trip during the *Fragile Earth* conference in Munich where I met Karin for the first time.

When I started my PhD in the seismology group we were a very small group: Karin, Tarje, Kuangdai, Afsaneh and me. My thanks goes to the original "SeismOx" group.

With time more amazing, wonderful and interesting students and PostDocs joined our group. I want to thank Paula, my personal hero when it comes to planning. I don't know how you do it but never stop doing it! To Marta, I'm amazed how you can almost always laugh and stay positive, even if everything else sucks. To Ben Schwarz (who unfortunately only stayed for a short while with us) you were always exited about research, this inspired me to do the same. I want to thank Harriet, who gave the saying "calm waters are deep" a new meaning to me. If I ever need a lawyer, you are the first person I will call.

Over the last two years our small SeismOx group expanded dramatically and I want to thank Alex, Eoghan, Ben F., Claudia, Laura, Tom and Andy for being great colleagues. It's been a blast.

During my time in Oxford I was fully funded by the NERC DTP and Teddy Hall. Many thanks for supporting my studies, travels, conferences and workshops throughout the years. A big thanks to the exquisite canteen of Teddy Hall which provided me with food when I did not have a kitchen of my own. I want also to thank Victoria and Claudia

who kept the DTP running despite all difficulties. You two were always helpful and had an open ear to us students.

I was able to travel to various conferences and meetings during my PhD , where I met some incredible people. I can not mention all of them, but here are the ones that inspired and affected me the most: Mitch, Henning, Shanti, Andreas, Carmen, Eric, Mat and Guilhem. Thank you all for the great time and inspiration!

I want to thank my previous office mates Dave and Will, you were my first friends in the department and you made me so crazy that I had to leave you.

At this point a special thanks to my office mates in 30.13 a.k.a. *The Marine Lab*: Dirk, Brook & Brook, Rebecca, Marta, Harriet and Tony. This office is crazy and I love every single bit of it! I have been laughing, crying, gardening, discussing, being silly, drinking and celebrating in this office; watching rugby, football, TED talks and the *Great British Bake-off*. Eventually I was also working. Surprisingly, I actually finished this thesis (somehow). Thank you all for this memorable time.

I also want to thank Patrick and Doro. Whenever you two visited the Marine Lab it always made my day. We need more Doros in this world.

I want to thank my mother, Natalie. You never liked me moving further away from Munich, nevertheless you supported me whenever you could, even if you couldn't. Thank you.

Inevitably "the best for last": You were first a fellow student on the *Marion Dufresne*, you became my friend, my partner, my colleague, my financé and soon you will be my husband. You were there for the good, the bad and the ugly times and you never wavered. Thank you, Kasra.

Abstract

This study aims to generate a multifrequency tomography model of the mantle beneath the Réunion hotspot, where a whole mantle conduit may be present.

From 2011 to 2016, the RHUM-RUM project (Réunion Hotspot Upper Mantle – Réunions Unterer Mantel) instrumented a 2000 km × 2000 km area of the Indian Ocean seafloor, islands and Madagascar with broadband seismometers and hydrophones. The central component was a 13-month deployment of 57 German and French Ocean Bottom Seismometers (OBS) deployed at 2300-5600 m depth. This was supplemented by deployments of 37 stations on Réunion, Mauritius, Rodrigues, the southern Seychelles, the Iles Eparses and southern Madagascar. More than 200 teleseismic events during the 13-month long deployment were recorded and additional 400 events before and after the main OBS deployment were recorded by permanent stations.

Here, I present the data yield, processing methods and P wave images based on over 55,000 multifrequency cross-correlations measurements in passbands between 30 and 2.7 seconds dominant periods. Ideally, all frequency bands that efficiently transmit body-waves would be used but this meets practical limits in the noise characteristics of ocean-bottom recordings. The multifrequency traveltime observations are embedded into a global ray theoretical inversion. This new high-resolution tomographic model, which illuminates the mantle column beneath La Réunion and surrounding areas, is discussed and compared to existing global models.

The model reveals a massive upwelling rooted in the African LLVP. Branches tilting up- and outward from a central cusp at around 900 km above the CMB (∼2000 km depth), and connect to the hotspot locations of La Réunion, Afar, Kerguelen, and possibly Crozet. These mantle connections support evidence of long-standing observations of geochemical similarities across Indian Ocean hotspots.

Extended Abstract

La Réunion is proposed to be a prominent candidate for a hotspot fed by a deep mantle plume (Courtillot et al., 2003). Surface observations, such as connections to a volcanic chain and flood basalt, active volcanism and high helium isotope ratios support this hypothesis. Like most oceanic hotspots, the Réunion mantle plume has not been well-resolved by seismic tomography due to the sparsity of seismic instrumentation in its vicinity (Montelli et al., 2004, 2006; French and Romanowicz, 2015).

RHUM-RUM (Réunion Hotspot Upper Mantle - Réunions Unterer Mantel) instrumented a 2000 × 2000 km^2 area of the western Indian Ocean. The central component was a 13-month deployment (09.2012-11.2013) of 57 German (DEPAS) and French (INSU) ocean bottom seismometers (OBS) in 2300-5600 m deep water (Barruol and Sigloch, 2013). This was supplemented by 2-3 years deployments of 37 island stations on Réunion, Mauritius, Rodrigues, Seychelles, the Iles Eparses and southern Madagascar. As La Réunion is near Africa, onshore stations deployed in a large area around the island have been used as well. Two partner projects SELASOMA (Tilmann et al., 2012) and MACOMO (Wysession et al., 2011) contributed another 30+ land-based stations on Madagascar and the Seychelles. This ocean island experiment has been one of the largest to instrument an oceanic basin around an active hotspot. The large deployment vastly improved the seismological illumination of a previously sparsely instrumented oceanic region. More than 200 teleseismic events during the 13-month long OBS deployment yielded multifrequency traveltime measurements, supplemented by another 400 events recorded by the land stations before and after the OBS deployment.

The scientific goal of RHUM-RUM is to image the mantle beneath La Réunion by applying a state-of-the-art multifrequency seismic tomography method (Sigloch et al., 2008; Hosseini, 2016) to this unique seismic dataset. I measured 55,657 cross-correlation traveltimes of teleseismic P-wave in eight overlapping frequency bands between 30 to 2.7 seconds dominant period. The multifrequency method has the benefit that measurements in noisy passbands can be selectively rejected, which increases the yield of usable OBS data in high microseismic noise conditions (Hosseini and Sigloch, 2015; Sigloch and Nolet, 2006). Measurements from the RHUM-RUM network and other regional experiments are complemented by high-quality analyst-picked, teleseismic P arrivals from the ISC-EHB Bulletin (Engdahl et al., 1998; Weston et al., 2018) to enhance

the data coverage in the upper and mid-mantle. I constrain the lower third of the mantle with the dataset of 189,439 cross-correlation traveltime measurements of core-diffracted P-waveforms in five frequency bands between 30-7.5 seconds from Hosseini and Sigloch (2015). Synthetic seismograms were computed by the numerical wave propagation tool AxiSEM using a spectral element method (Nissen-Meyer et al., 2014). The ISC-EHB and the P-diffracted dataset form our global dataset. The RHUM-RUM dataset is embedded into this inversion to increase the resolution beneath the western Indian Ocean. These datasets provide sufficient data for a multi-scale whole-mantle tomographic inversion below the western Indian Ocean; a poorly sampled and studied region in existing tomography models. After correcting for topography, crustal structure, and global ellipticity and calculating finite-frequency sensitivity kernels, I jointly invert the three datasets for P-wave velocity anomalies in the mantle.

Here, I present a high-resolution body-wave tomography of the whole mantle with a focus on the La Réunion hotspot in the western Indian Ocean. The new P-wave model images a whole-mantle plume beneath La Réunion ascending from the African Large Low Velocity Province (LLVP). Consistent with previous studies, "fat" plumes are observed in the lower mantle; however, the plume is more complex in the mid- and upper-mantle. Rather than being near-vertical, the upwelling shows a strong tilt in the lower mantle consistent with other seismic observations (Nyblade and Robinson, 1994; Ritsema et al., 1999; Ni et al., 2002) and geodynamic predictions (Steinberger and Antretter, 2006). The tilted conduit narrows into thinner branches closer to the surface.

A preliminary regional S-wave tomography model is also based on 145,546 S measurement from S40RTS (Ritsema et al., 2011), 133,925 picked S arrivals from ISC/ISC-EHB (Engdahl et al., 1998; Weston et al., 2018) catalogue and 45,056 multifrequency waveform measurements from the RHUM-RUM experiment. There is a high correlation between the P- and S-models throughout the mantle; however, additional low-velocity features are imaged in the S-model.

The South African topographic high can be explained by the LLVP cusp beneath the continent as imaged in our P- and S- models. The imaged plume cluster with several arms branching out from a "common source" in the mid-mantle can explain the surface geochemistry observation of the DUPAL anomaly (Dupre and Allegre, 1983).

Contents

List of Figures **x**

List of Abbreviations **xiii**

1 Introduction **1**

1.1 Studying Earth's Interior . . . 3
1.2 Seismic tomography . . . 3
1.2.1 A very brief history of seismic tomography . . . 5
1.3 Mantle plumes . . . 8
1.4 Objective of this study . . . 12
1.5 Thesis Outline . . . 13

2 RHUM-RUM experiment **15**

2.1 Motivation . . . 15
2.2 Tectonic setting around La-Réunion . . . 17
2.3 Experiment . . . 19
2.4 Performance . . . 21
2.4.1 Earthquakes . . . 21
2.4.2 Data . . . 22
2.4.3 Data coverage . . . 24

3 Inversion framework **27**

3.1 Ingredients for seismic tomography . . . 27
3.2 Rays vs. multifrequency measurements . . . 31
3.3 Parametrisation and sensitivity kernels . . . 33
3.4 Linear inversion . . . 35
3.5 Selection of preferred models . . . 39
3.6 Resolution tests . . . 40

4 Multifrequency seismic tomography of the mantle beneath La Réunion 42
4.1 The RHUM-RUM project . . . 44
4.2 Data . . . 45
4.3 Inversion framework . . . 51
4.4 Results . . . 57
4.5 Plumes and LLVPs in other models . . . 65
4.6 Conclusion . . . 66

5 La Réunion hotspot: a plume among a plume cluster? 69
5.1 A new regional tomography model for the western Indian Ocean . . . 70
5.2 Results & observation of a plume cluster . . . 70
5.3 Comparison with other models . . . 74
5.4 Discussion . . . 76

6 S-wave tomography beneath La Réunion: preliminary results 79
6.1 Data . . . 80
6.2 Tomography models . . . 83
6.3 $\frac{\delta V_s}{\delta V_p}$ ratio . . . 85
6.4 Discussion and outlook . . . 87

7 Discussion, Conclusion & Outlook 89
7.1 Discussion . . . 90
7.1.1 Surface observations . . . 90
7.1.2 How did the mantle evolve? . . . 93
7.1.3 Unanswered questions . . . 97
7.2 Conclusion . . . 98
7.3 Outlook . . . 99
7.3.1 Hydrophone data in seismic tomography . . . 99
7.3.2 Future of deep Earth exploration . . . 103

Appendices

A Inversion results 106

B Resolution tests 122

C Model comparison 147

D Station performance, station quality and earthquake distribution 151

References 161

List of Figures

1.1 Deep Earth 2
1.2 Timeline of seismic tomography and plume research 4
1.3 High and low-velocity vote maps 6
1.4 Perception of mantle plumes through time 9

2.1 Plate reconstruction from 150 - 0 Ma 18
2.2 Legacy overview map of RHUM-RUM ship route 20
2.3 Anatomy of an OBS 21
2.4 Earthquake distribution 2011-2016 22
2.5 Comparison between vertical and hydrophone components 23
2.6 Ray coverage for ISC, P-diff and RHUM-RUM data 25
2.7 Comparison of kernel densities 26

3.1 Tomographic methods on regional and global scales 28
3.2 Frequency content of for tomographic models 28
3.3 Picking phases vs. cross-correlation 31
3.4 Matched filters 32
3.5 Gabor filters 33
3.6 Example of an inversion mesh 34
3.7 Example sensitivity kernels 35
3.8 Illustration of linear system of equations I 36
3.9 Illustration of linear system of equations II 38
3.10 Illustration of L-curve 39
3.11 Schematics of resolution test 41

4.1 Overview map of the RHUM-RUM experiment 43
4.2 Multifrequency tomography workflow 45
4.3 Source inversion workflow 46
4.4 Example STF of a shallow earthquake 47
4.5 Comparison between real and synthetic data 49
4.6 Example multifrequency measurements 50

4.7 Traveltime corrections . . . 53
4.8 Model parametrisation . . . 55
4.9 L-curves for different *damping/smoothing* ratios . . . 57
4.10 Tomographic images along the L-curves . . . 58
4.11 Inversions with different datasets . . . 59
4.12 Cross-section through the "preferred" model in 2-D and 3-D . . . 62
4.13 Resolution test . . . 64
4.14 Comparison with other models . . . 67

5.1 Cross-section through P-model . . . 71
5.2 3-D slices through RR-Ox19 . . . 72
5.3 Comparison with other models . . . 75

6.1 Histogram of goodness of fit for S measurements . . . 80
6.2 Histogram for multifrequency S measurements . . . 81
6.3 Average traveltimes for S and P measurements . . . 81
6.4 Inversions with different S-wave datasets . . . 84
6.5 Tomographic models and $\frac{\delta V_s}{\delta V_p}$ ratio maps . . . 86

7.1 DUPAL anomaly . . . 91
7.2 Evolution of mantle plumes . . . 95
7.3 Schematics of a hydrophone . . . 100
7.4 Hydrophone data for an earthquake in Banda Sea . . . 101
7.5 Cross-correlation of hydrophone data . . . 102

A.1 L-curve for ISC-EHB (P phase) . . . 108
A.2 L-curve for ISC-EHB with Pdiff . . . 109
A.3 L-curve for RHUM-RUM+ dataset . . . 110
A.4 L-curve for RR-Ox19 with $\frac{damping}{smoothing} = 0.3$ . . . 111
A.5 L-curve for RR-Ox19 with $\frac{damping}{smoothing} = 0.5$ . . . 112
A.6 L-curve for RR-Ox19 with $\frac{damping}{smoothing} = 0.7$ . . . 113
A.7 L-curve for RR-Ox19 with $\frac{damping}{smoothing} = 0.9$ . . . 114
A.8 L-curve for RR-Ox19 with $\frac{damping}{smoothing} = 1.2$ . . . 115
A.9 L-curve for RR-Ox19 without traveltime corrections . . . 116
A.10 L-curve for ISC (S phase) . . . 117
A.11 L-curve for S40RTS dataset (S phase) . . . 118
A.12 L-curve for S40RTS dataset and ISC-EHB . . . 119
A.13 L-curve for RHUM-RUM+ (S phase) . . . 120
A.14 L-curve for RR-Ox-S19 . . . 121

B.1 Big chequerboards without noise . . . 124
B.2 Big chequerboards with noise . . . 125
B.3 Small chequerboards without noise . . . 126
B.4 Small chequerboards with noise . . . 127
B.5 Whole mantle columns without noise . . . 128
B.6 Whole mantle columns with noise . . . 129
B.7 Upper mantle columns without noise . . . 130
B.8 Upper mantle columns with noise . . . 131
B.9 Lower mantle columns without noise . . . 132
B.10 Lower mantle columns with noise . . . 133
B.11 Alternating amplitudes in mantle columns without noise . . . 134
B.12 Alternating amplitudes in mantle columns with noise . . . 135
B.13 Geodynamic columns without noise . . . 136
B.14 Geodynamic columns with noise . . . 137
B.15 Thin whole mantle columns beneath station locations without noise . . . 138
B.16 Thin upper mantle columns beneath station locations with noise . . . 139
B.17 Input equal output without noise . . . 140
B.18 Input equal output minus sphere without noise . . . 141
B.19 Input equal output minus sphere with noise . . . 142
B.20 Input equal output minus upper 400 km without noise . . . 143
B.21 Input equal output minus high velocities without noise . . . 144
B.22 Input equal surface model without noise . . . 145
B.23 Input equal surface model with noise . . . 146

C.1 Model comparison for La Réunion . . . 148
C.2 Model comparison for Afar . . . 149
C.3 Model comparison for Kerguelen . . . 150

D.1 RHUM-RUM station performance . . . 152
D.2 RHUM-RUM station and earthquake distribution . . . 153
D.3 Histogram of RHUM-RUM+ dataset . . . 154
D.4 Earthquake distribution . . . 155
D.5 Signal to noise ratio . . . 156
D.6 Pie chart of network contributions to RHUM-RUM+ dataset . . . 157
D.7 Number of measurements and average dT plotted on station locations . . . 158
D.8 Example Dispersion I . . . 159
D.9 Example Dispersion II . . . 160

List of Abbreviations

1-D, 2-D, 3-D One-, two- or three-dimension.

AxiSEM . . . A spectral-element method (SEM) code for 3D (an-)elastic, anisotropic and acoustic wave propagation in axisymmetric domains.

CIR . . . . . Central Indian Ridge.

DEPAS . . . . Deutscher Geräte-Pool für Amphibische Seismologie.

DSC . . . . . Deep Sound Channel or SOFAR.

EGELADOS . Exploring the GEodynamics of subducting Lithosphere using an Amphibian Deployment Of Seismographs.

GCMT . . . . Global Centroid Moment Tensor Catalog.

IASP91 . . . . 1-D background model used for inversion (Kennett and Engdahl, 1991).

INSU . . . . . Institut National des Sciences de l'Univers.

ISC . . . . . International Seismological Centre.

ISC-EHB . . . ISC Bulletin with relocated events using the EHB (Engdahl - van der Hilst - Buland) algorithm.

JASON . . . . LLVP beneath the Pacific Ocean.

LIP . . . . . Large igneous province.

LLVP . . . . . Large Low Velocity Province.

LLSVP . . . . Large Low *Shear* Velocity Province.

Ma . . . . . Million years.

MERMAIDS . Mobile Earthquake Recording in Marine Areas by Independent Divers.

MOHO . . . . Mohorovicic boundary - boundary between lithosphere and asthenosphere.

MOR . . . . . Mid Ocean Ridge.

OBS . . . . . Ocean Bottom Seismometer.

P . . . . . Preliminary seismic phase.

PP . . . . . Preliminary seismic phase with one bounce point at the surface.

P-diff . . . . . Preliminary seismic phase diffracted at the Earth core.

PGZ . . . . . Plume generation zone.

PREM . . . . Preliminary Reference Earth Model (Dziewonski and Anderson, 1981).

RHUM-RUM Réunion Hotspot Upper Mantle - Réunions Unterer Mantel.

RHUM-RUM+ RHUM-RUM dataset, including partner projects other temporal and permanent stations in western Indian Ocean.

RR-Ox19 . . . Our "preferred" tomography model presented in this thesis (RHUM-RUM Oxford 2019).

S . . . . . Secondary seismic phase.

SNR . . . . . Signal to noise ratio.

SOFAR . . . . Sound Fixing and Ranging channel or DSC.

STA/LTA . . . Short time average divided by long time average.

STF . . . . . Source Time Function.

SubMachine . A collection of web-based tools for exploring seismic tomography models (Hosseini et al., 2018).

SWIR . . . . . South West Indian Ridge.

TUZO . . . . . LLVP beneath Africa.

Daß ich erkenne, was die Welt
Im Innersten zusammenhält [...]

That I know what holds the world
Together at its core [...]

— Johann Wolfgang von Goethe
Faust: Der Tragödie Erster Teil - Nacht.

1 Introduction

Contents

1.1 Studying Earth's Interior 3
1.2 Seismic tomography 3
1.2.1 A very brief history of seismic tomography 5
1.3 Mantle plumes 8
1.4 Objective of this study 12
1.5 Thesis Outline 13

This thesis starts with a fundamental question: "Why is it important to study Earth's interior?". Seismic tomography as one of the most useful tools for imaging Earth's deep interior will be reviewed in Section 1.2. I give a very brief summary on the history of seismic tomography, which can be further reviewed in Romanowicz (1991, 2003); Nolet (2008); Shearer (2009). For a more detailed account on the early history of seismometry, see Dewey and Byerly (1969). Section 1.3 discusses past and recent advances in mantle plume research. The motivation behind this study and the specific aspects of the work will be described briefly in Section 1.4. Finally, Section 1.5 outlines the contents of the following chapters.

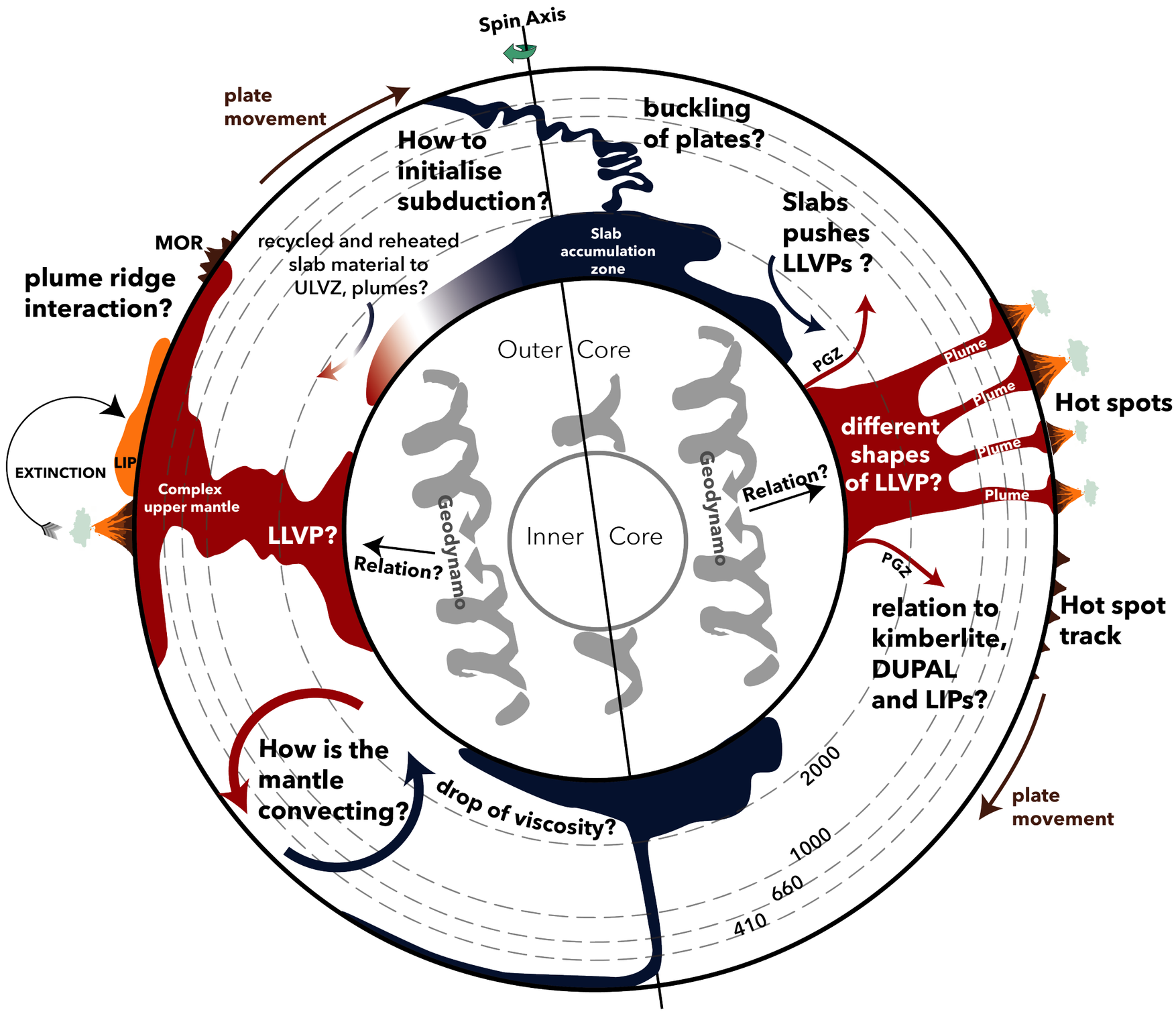

Figure 1.1: Schematic of our current understanding of Earth's internal structure and its complex processes.

1.1 Studying Earth's Interior

In 1912, Alfred Wegener hypothesised that continents are not stationary, and that they are slowly drifting relative to each other (Wegener, 1920). However, his theory was rejected by many at the time. Four decades later and after validation of seafloor spreading (Wilson, 1963; Heirtzler, 1968), plate tectonics, a theory built on the concept of Wegener's continental drift, was widely accepted. Plate tectonic theory was a paradigm shift and a scientific revolution. Since then, Earth scientists have understood that plate movements are the result of complex convection processes inside Earth as depicted in Figure 1.1.

There are still fundamental questions about Earth's interior remained unanswered, for example, *What is the composition of Earth? What is the heat budget of Earth? How much water is in the mantle? How does the mantle convect? What is the fate of subducted material? What do mantle plumes look like? What drives the continents and plates to move in the first place?*

Seismic tomography has been an important tool to image the Earth's internal structure. Its resulting models have been extensively interpreted, and have been used as inputs for other branches of Earth sciences to better understand the dynamic processes in our planet. Research into Earth's mantle will ultimately help us to answer these questions.

1.2 Seismic tomography

Direct observations of Earth's interior are very limited. The deepest borehole on Earth is located in Russia and is ∼12 km deep. Ocean drills penetrate into the oceanic crust as deep as 2 km. Assuming that with a major effort, we would be able to directly sample Earth's properties down to 12 km depth globally, only 0.2% of Earth's radius would be covered. However, drilling programs have the possibility to analyse the materials down to the grain. Seismic tomography, on the other hand, can be used to obtain knowledge about the physical properties of the whole Earth on the basis of inferences drawn from observations, and it is one of the most effective tools that we have at this moment to learn about Earth's deep interior.

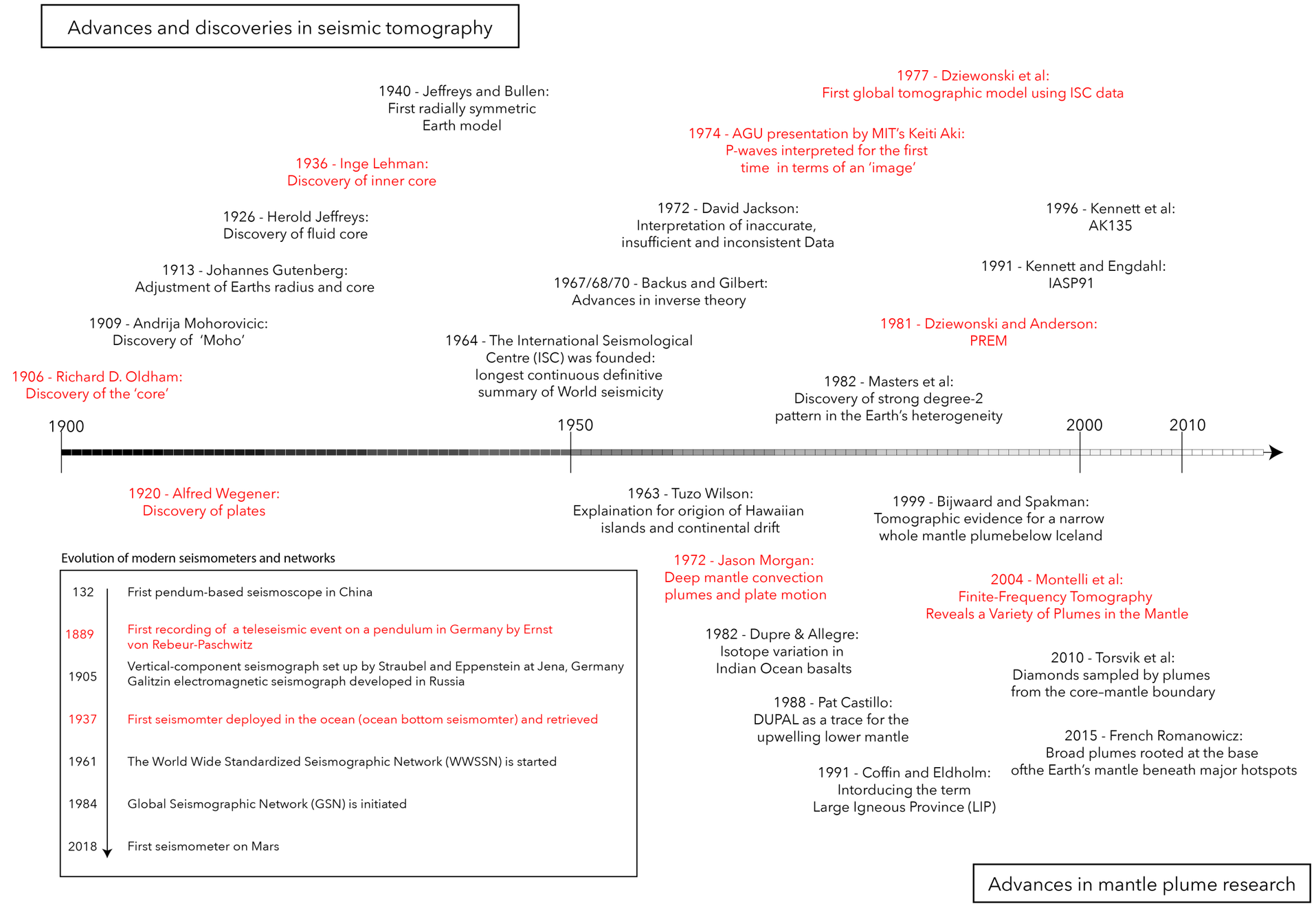

Figure 1.2: A timeline of selected publications on advances and discoveries in seismic tomography, mantle plume research and progress in seismography.

1.2.1 A very brief history of seismic tomography

Although the first pendulum-based seismograph was designed in 132 A.D. (Dewey and Byerly, 1969), modern seismology had its birth around 1889 when the first teleseismic event was recorded on a pendulum seismograph in Germany (Ewing and Ewing, 1961; Dewey and Byerly, 1969). The increased instrumentation which followed showed that earthquakes are not randomly distributed, but their connection to plates was only understood after the plate tectonic revolution in the 1960s.

With the advanced instrumentation developed at the beginning of the 20th Century, a cascade of new findings followed. Oldham (1906) discovered the central "core", roughly halfway between the Earth's surface and its centre. Mohorovicic introduced a new discontinuity between crust and mantle in 1909, the "Moho". In 1914, Gutenberg calculated the size of the Earth's fluid outer core and 22 years later, in 1936, Lehmann estimated the Earth's solid inner core.

In the 20's and 30's of the 20th century, seismographs were soon understood to be a preferable tool for locating oil reservoirs, and active source seismic quickly evolved. Active source tomography can usually image structures down to 60 km, whereas passive source tomography can sample the whole Earth.

In 1940, traveltime tables for seismic phases were published and with that it was possible to establish Earth's average radial velocity and density structures.

In 1960, the great Chile earthquake occurred and for the first time Earth's free oscillation could be observed on modern seismometers. A new branch of seismology formed, normal modes seismology. Normal modes can give an alternative way to constrain large scale structures and density inside Earth. Further, in the 60's, the discovery of spreading along mid ocean ridges (MOR) and subduction at trenches lead finally to an acceptance and understanding of plate tectonics.

By 1970, Earth's average velocity structure is well established (including the transition zones at the 410 km and 660 km), the next goal was to understand the lateral differences, which lead to the development of seismic tomography techniques.

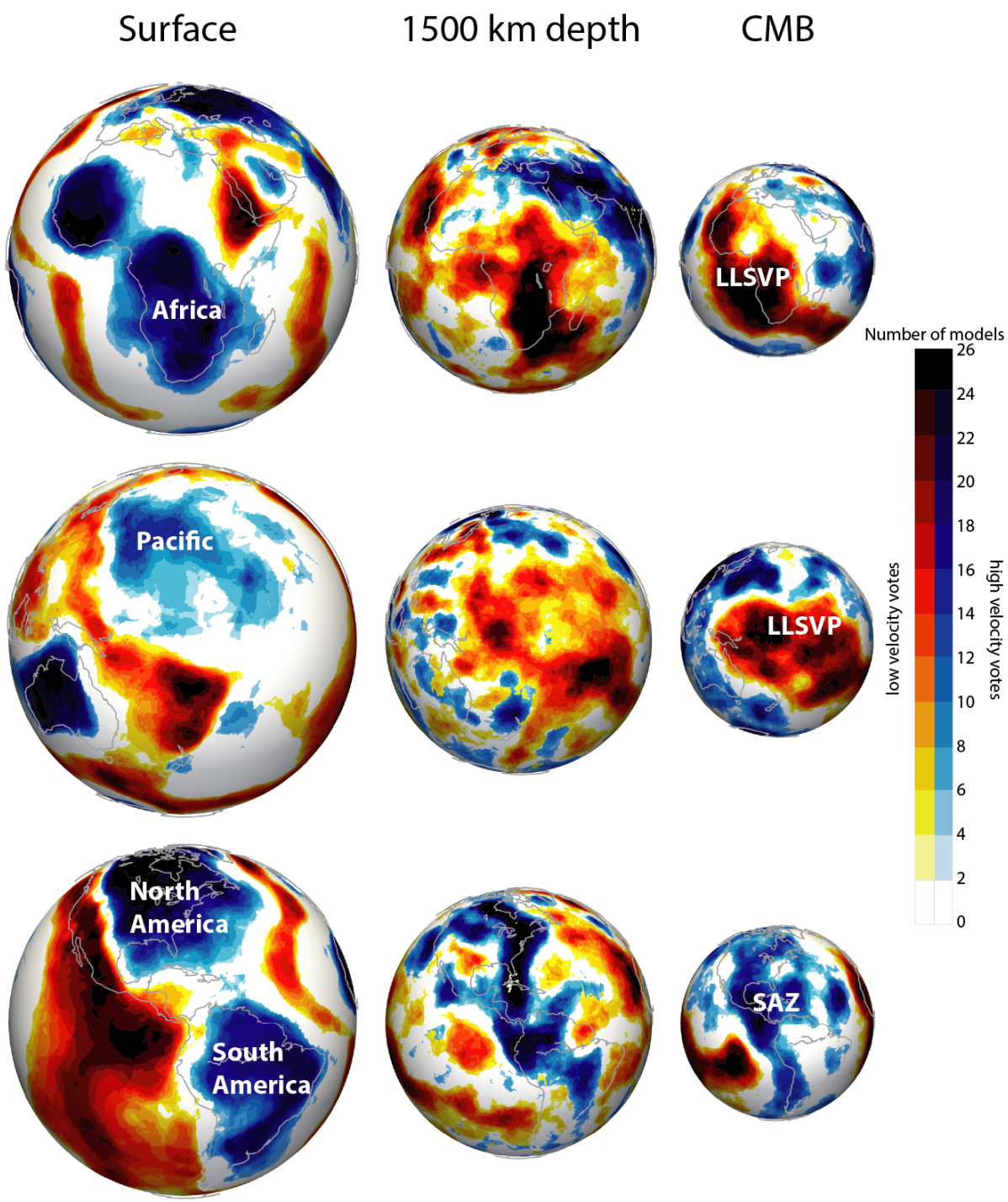

Figure 1.3: Combined high- and low-velocity vote maps zooming on Africa, Pacific Ocean and America at different depths. This vote map is based on 26 body-wave models from SubMachine (Hosseini et al., 2018) and is visualised with ParaView. Blue and red colours show high and low-velocity votes, respectively. Consistent structures in almost all models are the mid ocean ridges (MOR, North and South Atlantic), cratons (Africa, North and South America), slab (Farallon, Tethyan), SAZ (beneath Asia and North America) and LLSVPs (TUZO and JASON).

In the 1970's, Backus and Gilbert (Backus and Gilbert, 1967, 1970) advanced inverse theory and provided formulations to deal with geophysical inverse problems. In 1974 at the AGU (American Geophysical Union) conference, Keith Aki presented the first "image" produced by using arrival times of P-waves. In 1977, Dziewonski et al. (1977) followed with the first global 3-D seismic tomography model of Earth's interior using 700,000 P wave traveltime residuals from ISC (International Seismological Centre), which collected arrival time data since 1964. In 1981, PREM (Preliminary Reference Earth Model: Dziewonski and Anderson, 1981) a 1-D velocity model of Earth, was introduced which is still widely used today.

In the last 40 years, a substantial number of global and regional tomography models have been generated. Masters et al. (1982) used free oscillation data to determine the degree 2 pattern of Earth, and Dziewonski and Anderson (1981) presented the first global 3-D model of long-wavelength P-wave velocity variations. van der Hilst et al. (1997) and Grand et al. (1997), by using P and S-wave tomography (respectively) imaged slabs under the Northwest Pacific which were entering into the lower mantle. Bijwaard and Spakman (1999) produced for the first time a tomographic evidence for an Iceland whole mantle plume (whereas Wolfe et al. (1997) only presented the upper 400 km).

Despite the different datasets and techniques used to generate tomographic models, they started to converge not only on long wavelengths (thousands of kilometres) but also on intermediate length scales (hundreds of kilometres). Amplitudes and small length scales (100 km) are still in disagreement in various locations, but the differences are on a decline. The biggest difference comes from the data that goes into the model (see Chapter 3 for more discussion).

As an example, Figure 1.3 shows the consistency between 26 global tomography models on the mid-ocean ridges (MOR, North and South Atlantic), cratons (Africa, North and South America), slabs (Farallon, Tethyan), D" (beneath Asia and North America) and LLSVPs (Large Low Shear Velocity Provinces TUZO and JASON, named after *Tuzo* Wilson and *Jason* W. Morgan). The first panel in Figure 1.3 explores the mantle structure beneath Africa. At the surface, the cratons are visible in all the models.

In the mid-mantle, the top of the LLSVP has been imaged by almost all the underlying models. Finally, at the CMB, an overwhelming agreement between all the models on the outlines of the African LLSVP is apparent with its characteristic *gap* beneath Nigeria.

In the Pacific Ocean of Figure 1.3 (middle row), the cold Pacific plate is clearly imaged by at least half of the underlying models. This area is relatively remote and not all body-wave models have the coverage to image this feature with confidence. In the mid-mantle, the JASON LLSVP starts to emerge in most models; more patchy areas of agreement are observed compared to TUZO at both mid-mantle and the CMB.

In Figure 1.3 (bottom row), fast anomalies with high votes (dark blue) exist beneath North and South America at shallow depths. The MOR in the South Pacific has scattered votes compared to the well-defined votes in the Atlantic MOR. In the mid-mantle, remnants of the so-called Farallon slab with its characteristic kink shape appear, and at the CMB, a slab accumulation zone (SAZ) with high-votes is visible.

Although the vote maps of Figure 1.3 suggest a very good agreement between existing tomography models on various long- and intermediate-scale features, there is still a long way to go to achieve agreement on all wavelengths.

1.3 Mantle plumes

Fifty years ago, Jason Morgan proposed the existence of whole mantle plumes (Morgan, 1971). They are described as thermally thin, buoyant conduits rising vertically from the core mantle boundary to the surface of Earth with a preceding plume head, producing volcanic hotspots (e.g., Hawaii, Tristan da Cunha and Iceland) and large igneous provinces (LIP, e.g. Deccan Traps, Ontong Java, Kerguelen Plateau) when reaching the surface (Figure 1.4; Morgan, 1972). This discharge can take several millions of years which may create layered LIPs (Sheth, 2007). In the last two decades, the structures and shape of these low-velocity features have been under debate. This was partly due to the fact that most hotspots are located in remote areas beneath ocean islands with sparse instrumentation, and consequently, are poorly illuminated in tomography models.

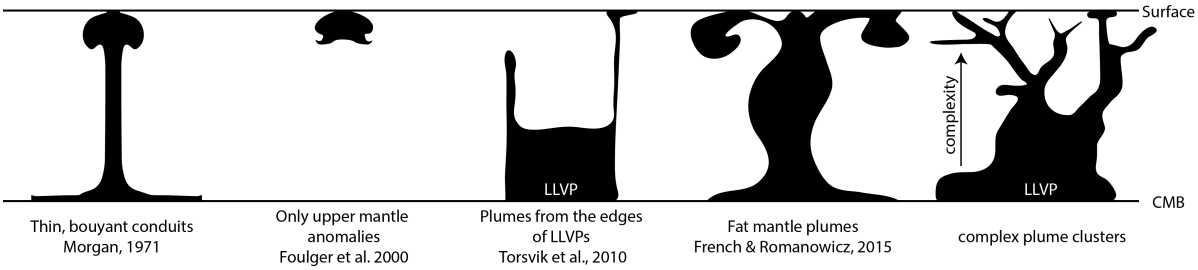

Figure 1.4: Schematic diagram (not to scale) showing four concepts of how mantle plumes were perceived at different times. From left to right: the classic thin conduit (Morgan, 1971, 1972); no plume hypothesis (Foulger et al., 2000); plumes from the border of the LLSVP (Torsvik et al., 2010) and fat plumes (French and Romanowicz, 2015). In this study, I propose a new type of mantle plumes in between broad and plumes rising from the border of LLSVP (right).

Mantle plumes are stationary over a long period of time (∼120 Ma, e.g., Richards et al., 1989; Sleep, 1990), and they are associated with volcanic chains (e.g., Morgan, 1971, 1972; Courtillot et al., 2003). This theory could explain the surface observations (e.g. volcanic chain, continuous volcanic activity and swell) of several oceanic islands, for example, Hawaii, Iceland and Tristan da Cunha. Thermal plumes, thin conduits with large heads, from analogue and numerical models (Richards et al., 1989; Olson and Singer, 1985; Olson and Nam, 1986) agreed with the proposed concept by Morgan (1971, 1972).

The first images of mantle plumes showed only upper mantle (400 km) low-velocity anomalies (VanDecar et al., 1995; Wolfe et al., 1997) but Bijwaard and Spakman (1999) imaged a whole mantle plume beneath Iceland. In their model, the Iceland plume, a faint (-0.5%) low-velocity anomaly, extends down to the CMB with its characteristic shape that scientists still observe in state-of-the-art tomography models, e.g., Hosseini et al. (2019). However, in the 2000s, Foulger et al. (2000) hypothesised that there is no deep mantle plume in this region (Figure 1.4). They suggested that whole mantle conduits are merely the result of a smearing effect which occurs during the inversion process. The disagreement between the two models (Bijwaard and Spakman (1999) vs. Foulger et al. (2000)) could be due to the different datasets used in the inversions: Bijwaard and Spakman (1999) incorporated 5 million global ray bundles from Engdahl et al. (1998), whereas Foulger et al. (2000) used a local dataset of 3,200 compressional and 1,300 shear wave arrival

times. Indeed, whole mantle plumes are difficult to image; they are supposedly thin structures located in remote areas beneath ocean islands with little to no data coverage.

For the first time, Montelli et al. (2004) presented a catalogue of globally distributed mantle plumes imaged by finite-frequency tomography. Their study provided firm tomographic evidence for the existence of deep-rooted mantle plumes. A few plumes showed low-velocity conduits throughout the whole mantle while others showed anomalies reaching only to mid-mantle; others even had gaps in the mid-mantle. This publication caused a new line of controversial discussions. It came at a time when mantle plume theory (Morgan, 1971) was itself under discussion (Anderson, 2005) and was fuelled by the fact that the advantage of banana-doughnut kernels (Dahlen et al., 2000) was debated.

The distribution of seismic instruments on Earth's surface is heterogeneous. The bulk of seismic stations are on land, and most earthquakes are located in narrow belts along plate boundaries. Structures in body-wave tomography beneath continents using traveltimes are better resolved than underneath the oceans (Simmons et al., 2012), and this heterogeneity in data coverage leads to biases in tomographic images (e.g., Maguire et al., 2018). Only in 1937, the first seismometer was deployed in the ocean in an attempt to create seismic refraction profiles (Ewing and Vine, 1938). Since the 60's, refraction and reflection surveys exploring Earth's oceanic crust have dominated geophysical research in marine environments. These instruments usually record only short-periods (1 Hz), they are deployed for a short time (days to weeks), and they can only capture Earth's crustal structure.

In 1993, a passive experiment was designed to investigate Lau basin, West of Tonga Trench using an ocean floor array (Zhao et al., 1995, 1997). Data from twenty-five OBSes were used to create a high-resolution three-dimensional (3-D) regional model down to 700 km depth. Passive seismic experiments continued to provide data for other regional tomographic images. In 2008, Wolfe et al. (2009) published a tomography model as part of the PLUME Hawaii experiment. The model showed a broad mantle plume throughout the upper and mid-mantle.

In the 1980s, two enormous low-velocity structures at the CMB were imaged and associated with the hotspot locations on Earth's surface (Dziewonski and Anderson, 1984). They are called "Large Low Shear Velocity Provinces" (LLSVP). Each of these structures has a surface area of $\approx 2 \times 10^7 km^2$ of the CMB, and they are found nearly on opposite sides of the globe beneath the Pacific ocean and Africa (Figure 1.3). Their connection to surface observations (e.g., kimberlite, hotspot and LIPs location) became apparent early on (e.g., Castillo, 1988; Burke et al., 2008; Garnero and McNamara, 2008; Torsvik et al., 2010), and Torsvik et al. (2010) promoted the connection between LLSVPs and the surface observations. Paleogeographic reconstructions of the surface tectonic plates for the last 300 Ma places hotspots and other surface manifestations of mantle plumes at the borders of the LLSVPs (Torsvik et al., 2008b) (Figure 1.4), the so called plume generation zone (PGZ). However, this hypothesis could not be confirmed tomographically as no vertical whole-mantle conduits emerging from the PGZ have been imaged so far in global and regional tomographic studies. Only near vertical whole-mantle low-velocity structures have been imaged (Nelson and Grand, 2018; Nolet et al., 2016) close to LLSVPs but with no direct connection to the surface.

One important question is whether LLSVPs are thermal (e.g., Olson and Nam, 1986; Richards et al., 1989; Davaille et al., 2002; Farnetani and Richards, 1995) or thermochemical (e.g., Hofmann and White, 1982; Davaille et al., 2005; Farnetani and Samuel, 2005; Steinberger and Torsvik, 2012) in origin. Most observations, for example, existence of a sharp edge of the African LLSVP in almost all tomographic models (see Figure C.1; Ni et al., 2002; Tan and Gurnis, 2005), low-velocity piles at the CMB (Bull et al., 2009; Nakagawa et al., 2009), broad and complex low-velocity structures in the mantle (French and Romanowicz, 2015; Farnetani and Samuel, 2005; Davaille et al., 2005; Tan and Gurnis, 2007), point towards a thermochemical regime.

Nevertheless, if LLSVPs have remained stationary over ∼300 Ma or more, this will have some implications on global mantle convection and hence plate tectonics. Mantle convection is viewed as a "top-down process" driven by tectonic plates at the surface and subducted slabs. If, on the other hand, LLSVPs have been stable for ∼300 Ma, this

may suggest that mantle convection is controlled by "bottom-up processes" where hot material originating from the deep mantle controls the movement of plates at the surface.

At the time of writing this thesis, fundamental questions about the nature and origin of LLSVPs, their connection to hotspots and mantle plumes, their longevity, mobility, composition and role in mantle convection remain largely unanswered.

1.4 Objective of this study

Generally speaking, global tomography models do not have sufficient resolution below remote areas, such as ocean islands. New instrumentation and high-resolution regional-scale tomographies are crucial to image the structural complexities in such regions. Although many plume studies have been published since the 2000's (Bijwaard and Spakman, 1999; Ritsema et al., 1999; Montelli et al., 2004; Hansen et al., 2012; French and Romanowicz, 2015; Nelson and Grand, 2018), plumes still stay elusive and their structures cannot be traced confidently through all depths (e.g., Foulger et al., 2000; Montelli et al., 2004; Schlömer et al., 2017a). When exploring various global tomography models (e.g., Hosseini et al., 2019), all (S and P wave models equally) show a degree two pattern (Becker and Boschi, 2002) at the CMB (LLVP: Garnero et al., 2016) beneath Africa and the Pacific Ocean. Torsvik et al. (2006) suggested that plumes may rise from the border of the LLVPs, but such a connection could not be shown in tomographic models. Also, no entirely vertical conduit rising from the CMB has been confidently imaged in existing tomography models. The challenge in illuminating low-velocity structures like mantle plumes and their presumably connection to LLVP comes primarily from a poor data-coverage beneath oceans and wavefront healing effects (e.g., Nolet et al., 2007; Maguire et al., 2018).

One major question in Earth sciences is how the mantle and core have evolved over time. It was hypothesised that intraplate hotspots underlain by deep mantle plumes (Morgan, 1972) might have a considerable contribution to Earth's global heat budget depending on their size and number (e.g., Davies, 1988; Sleep, 1990; Davies, 1992;

van Keken, 1997; Keken and Ballentine, 1999; Samuel and Farnetani, 2003). Passive seismology could explore the existence and significance of plumes by imaging plume conduits or lack thereof. The main challenge is that most hotspots are located in the oceans where there are little to no seismic instruments.

La Réunion is considered to be a prominent candidate for a deep sourced mantle plume (Courtillot et al., 2003) due to the presence of an age-progressive volcanic chain at the surface, a large igneous plateau, a high $^{3}He/^{4}He$ ratio, a swell and the volcanic flux, and low-velocity anomalies rising vertically beneath the hotspot in global tomography models (e.g., Montelli et al., 2004; French and Romanowicz, 2015).

This study aims to generate a high-resolution body-wave tomography model as part of a global inversion of the mantle beneath the western Indian Ocean. The scientific goal is to estimate whether a Réunion mantle plume exists. The focus is primarily on the volcanic hotspot of La Réunion with the data collected from the RHUM-RUM experiment in order to answer questions at the forefront of Earth science research, for example, is there a connection between the African LLVP and volcanism in the western Indian Ocean? What are the morphological characteristics of the mantle plume beneath La Réunion? Is there a hotspot-ridge interaction? Can we image the plume head?

1.5 Thesis Outline

Chapter 2 describes the RHUM-RUM project, its objectives, motivation, experimental set up and data performance.

Chapter 3 provides a short overview on the theory of seismic tomography. Methodologies for data processing and inversion are mostly based on already published work of Dahlen et al. (2000); Montelli et al. (2004); Sigloch and Nolet (2006); Tian et al. (2007b); Nolet (2008) and Hosseini and Sigloch (2015).

Chapter 4 discusses details of the inversion framework and the “preferred” tomography model. Here, I explain the generation of source time functions (STF), retrieving and filtering waveform data and cross-correlation of real and synthetic seismograms to extract multifrequency measurements. I will also discuss the tomographic results.

Chapter 5 explores mantle structures as imaged by the model in a wide-area in the western Indian Ocean. A possible "common source" for various mantle plumes in this region and the imaged plume cluster will be discussed.

Chapter 6 shows preliminary results of a S tomography model beneath La Réunion and compares it to the P model.

Finally, in Chapter 7, I discuss the results in the light of surface observations and geodynamic models and give a brief outline of possible future projects.

The Appendix contains various inversions (including detailed L-curves), resolution tests, and model comparisons.

"Data! Data! Data!" he cried impatiently. "I can't make bricks without clay."

— Arthur C. Doyle
The Adventure of the Copper Beeches

2
RHUM-RUM experiment

Contents

2.1 Motivation 15
2.2 Tectonic setting around La-Réunion 17
2.3 Experiment 19
2.4 Performance 21
2.4.1 Earthquakes 21
2.4.2 Data 22
2.4.3 Data coverage 24

This chapter introduces the RHUM-RUM project, its motivation, the tectonic setting of the western Indian Ocean and the experimental set up. Data performance will be discussed, which is partially based on a published paper in Advances in Geosciences in 2016 (Stähler et al., 2016a).

2.1 Motivation

The existence of mantle plumes remains hotly debated, even forty years after they were postulated by Morgan (1972). Imaging a whole mantle plume with seismic tomography would help constrain to Earth's global heat budget. Not all plumes are located beneath oceans (e.g. Afar and Yellowstone), but because to their nature they are mostly found in

remote areas, this makes them difficult to investigate, due to limited instrumentation and data coverage. In the last 20 years, large-scale and long-term instrumentation of the seafloor has been more feasible, but still only a small number of experiments has been conducted to investigate the deep structure under ocean islands:

PLUME Polynesia (Polynesian Lithosphere and Upper Mantle Experiment) was one of the first large-scale passive experiments to investigate a mantle plume. The instrumentation with 10 OBS between 2001 and 2006 and permanent island stations spanned an area of 2000 × 2000 km^2 (Barruol, 2002; Suetsugu et al., 2005, 2009). Tomographic results from Suetsugu et al. (2009) showed that the structure beneath the Pacific hotspots resembles a "birthday cake", with the main mass reaching to 1000 km depth and thin conduits sticking out like candles and connecting to the surface.

PLUME Hawaii (Plume-Lithosphere Undersea Melt Experiment) consisted of two year-long deployments of 36 OBS and 10 portable seismometers on the Hawaiian Islands. The experiment was conducted between 2005 and 2007 and spanned an area of 1100 × 1300 km^2 (Wolfe et al., 2009). The results showed a low-velocity structure stretching down to 1200 km depth, with a high-velocity halo around the main conduit, which was introduced through a regularisation problem.

Tristan & ISOLDE was conducted as part of the DFG Schwerpunktprogramm SAMPLE project in 2012 until 2013. 24 OBS were deployed around Tristan da Cunha, one of the most remote prospective hotspot islands on Earth. The aperture of the experiment spanned only several hundred kilometres. Schlömer et al. (2017b) imaged a conduit with a radius of 10 km from the surface down to a depth of 250 km, but no further.

These experiments were performed for prominent candidates of deep sourced mantle plumes beneath ocean islands, but could not settle the debate definitely as two of the experiments did not have enough resolution deeper than upper or mid-mantle. Generally,

few designated OBS experiments were performed to investigate mantle plumes despite their importance as a major driving force for mantle convection.

La Réunion Island in the western Indian Ocean is among the most active volcanoes in the world and also a very strong candidate for a hotspot underlain by a deep, mantle plume (Courtillot et al., 2003). Indication for a deep sourced mantle plume comes from it having a hotspot track, ongoing volcanic activity, a high $^{3}He/^{4}He$ ratio, a swell around the hotspot and an associated flood basalt (Courtillot et al., 2003). Tomography models of La Réunion were published by Montelli et al. (2004) and French and Romanowicz (2015). Both showed that directly under La Réunion low-velocities do not reach further than 1000 km which could have been caused by the sparse instrumentation of the Indian Ocean. Nolet et al. (2006) showed a thickening beneath the mantle transition zone, but otherwise, no vertical continuation into the deep mantle.

The German-French project RHUM-RUM (Réunion Hotspot and Upper Mantle – Réunions Unterer Mantel) was set up to increase the data coverage in the area (Barruol and Sigloch, 2013). OBS and stations on Mauritius, Rodriguez, Seychelles, Madagascar and La Réunion were deployed in order to image the whole mantle structure and to confirm or reject the presence of a deep, continuous plume. This experiment might be able to explain the plumbing and feeding mechanism of the hotspot volcanism, estimate ascending material and heat fluxes, document interaction with the overlying African plate and with neighbouring mid-ocean ridges.

2.2 Tectonic setting around La-Réunion

In order to understand the deep mantle beneath La Réunion, an understanding of the tectonic evolution is crucial. The Indo-Atlantic Ocean went through several active phases of spreading, volcanic eruptions and ridge extinctions in a short period of time.

Around 150 Ma, Madagascar separated from Africa creating the Somali Basin. The accompanying ridge went extinct after a short time at 120 Ma (Figure 2.1). The Mozambique Ridge formed between South Africa and Antarctica at 140 Ma, followed

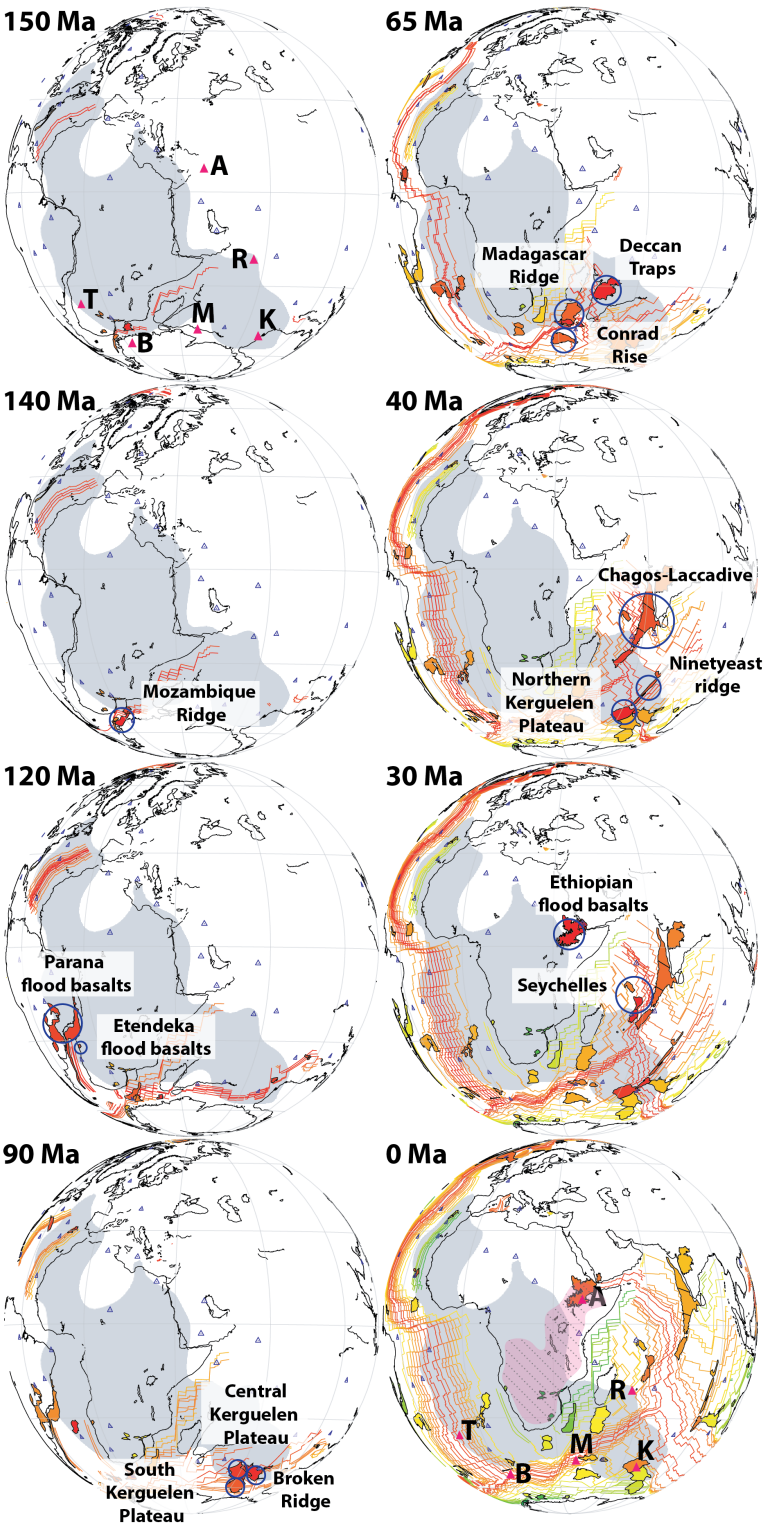

Figure 2.1: Plate reconstruction from 150 Ma to present. At different stages, the onset of LIPs are marked. At 0 Ma the hatched -grey area in South and East Africa marks the location of the anomalous African topographic high. Grey shaded area marks the LLVP at the CMB (Torsvik et al., 2006). **A** - Afar, **T** - Tristan da Cunha, **B** - Bouvet, **M** - Marion, **K** - Kerguelen, **R** - La Réunion. Refer to text for more discussion. Figure was generated with GPlates (Whittaker et al., 2013; Müller et al., 2016) and LIP dataset from Whittaker et al. (2015).

by the onset of spreading between India and Antarctica at 120 Ma with an extinction at 115 Ma. The LIPs around Kerguelen created the South Kerguelen Plateau, Central Kerguelen Plateau and the Broken Ridge between 120 and 90 Ma. The Conrad Rise was formed by the Marion hotspot around 88 Ma together with the Madagascar Ridge.

Finally, 65 million years ago, the La Réunion mantle plume surfaced and created the Deccan Traps which are located in western India at present day. The Seychelles were part of the Deccan Traps before they were separated by the spreading of the Carlsberg Ridge. A 5500 km long hotspot track connects India with Réunion. The track was interrupted when the Réunion plume jumped from the Indian plate to the Somalian plate (60 - 40 Ma). The interaction between mantle plumes and ridges can create an asthenospheric flow in the upper mantle from plume to the ridge (Whittaker et al., 2015), where the plume is "captured". At 30 Ma, Afar erupted the Ethiopian flood basalts which was the latest big eruption event in the Indo-Atlantic area.

An anomalous topographic high of the South and East African continent in addition to the traces of eruption and spreading are observed. Doucouré and de Wit (2003) pointed out the bimodal topography of south and east Africa. The likely cause of the African topographic anomaly is hot upwelling at different times (periodically from 200 to 5 Ma), which could be constrained from stratigraphic and sedimentary records (Doucouré and de Wit, 2003)(Figure 2.1). Though, the question remains if there is a deep mantle dynamic process creating Africa's topography high (Lithgow-Bertelloni and Silver, 1998; Gurnis et al., 2000), or is it a result of localised asthenospheric upwelling (King and Ritsema, 2000)?

2.3 Experiment

In 2012, RHUM-RUM deployed 57 broadband ocean bottom seismometers over an area of 2000 $\times$ 2000 km^2 with the *R/V Marion Dufresne*. This ocean-bottom component is supplemented by 20 existing and 10 new land stations on La Réunion Island as well as 27 temporary RHUM-RUM stations on Mauritius, Rodrigues, the southern Seychelles,

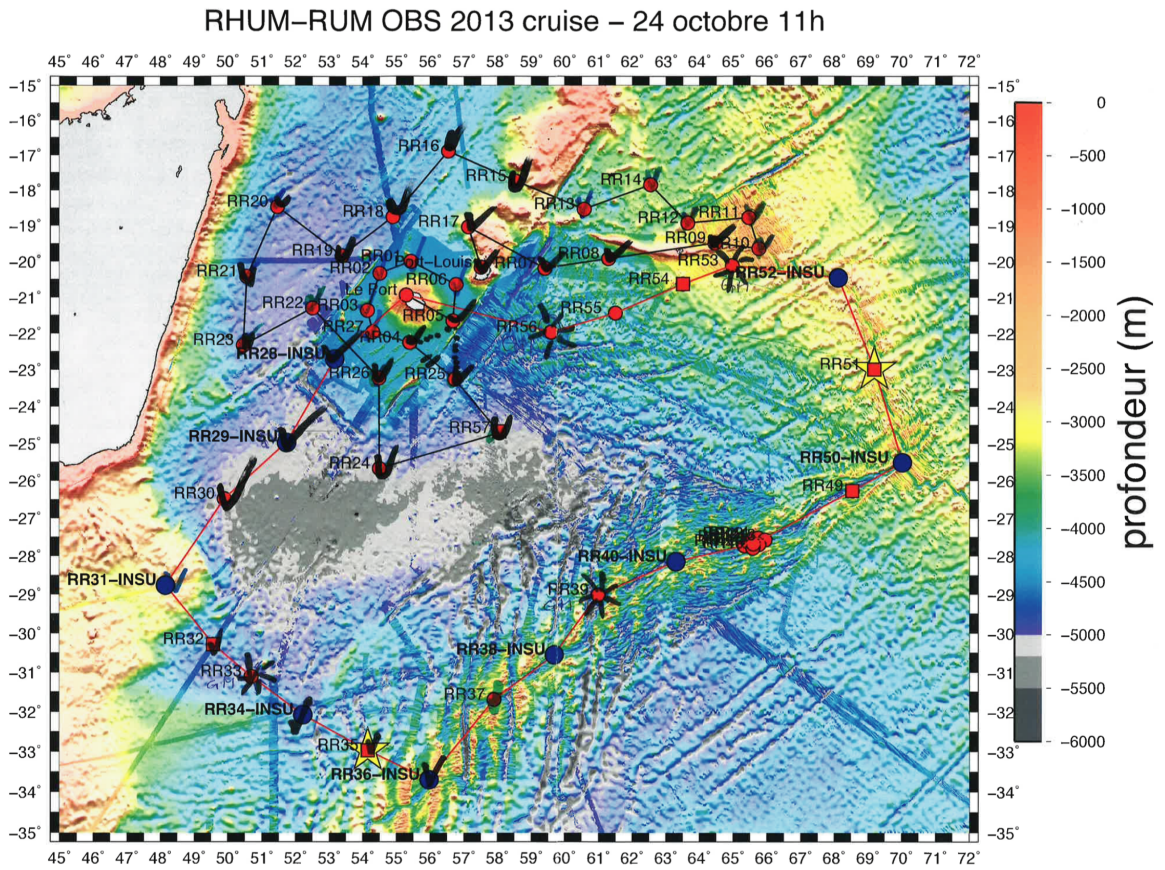

Figure 2.2: This bathymetry map was used during the recovery cruise with a total route length of roughly 11,472 km collecting 57 OBS (48 German and 9 French instruments). The duration for 2 Legs (1st leg blue and 2nd leg red lines on the map) was estimated 791 hours with an assumed ship velocity of 11 knots (20.4 km/h). Black tick marks represent successfully recovered OBS at the time.

Madagascar, and the Iles Eparses in the Mozambique Channel (Figure 2.2). Existing land instrumentation on Africa and Madagascar extends the effective array aperture to several thousand kilometres. In total, around 120 broadband seismometers have been operating in the western Indian Ocean instrument. Once the OBS is secured on the deck, it is synchronised with a GPS signal to correct for clock errors. Unfortunately, most of the DEPAS OBS in the RHUM-RUM experiment ran out of battery power before the scheduled recovery; hence, the recorders could not safely shut down and most of them lost the synchronisation. Fortunately, Hable et al. (2018) could estimate the linear clock drifts of 52 OBS in the RHUM-RUM experiment by using multiple-

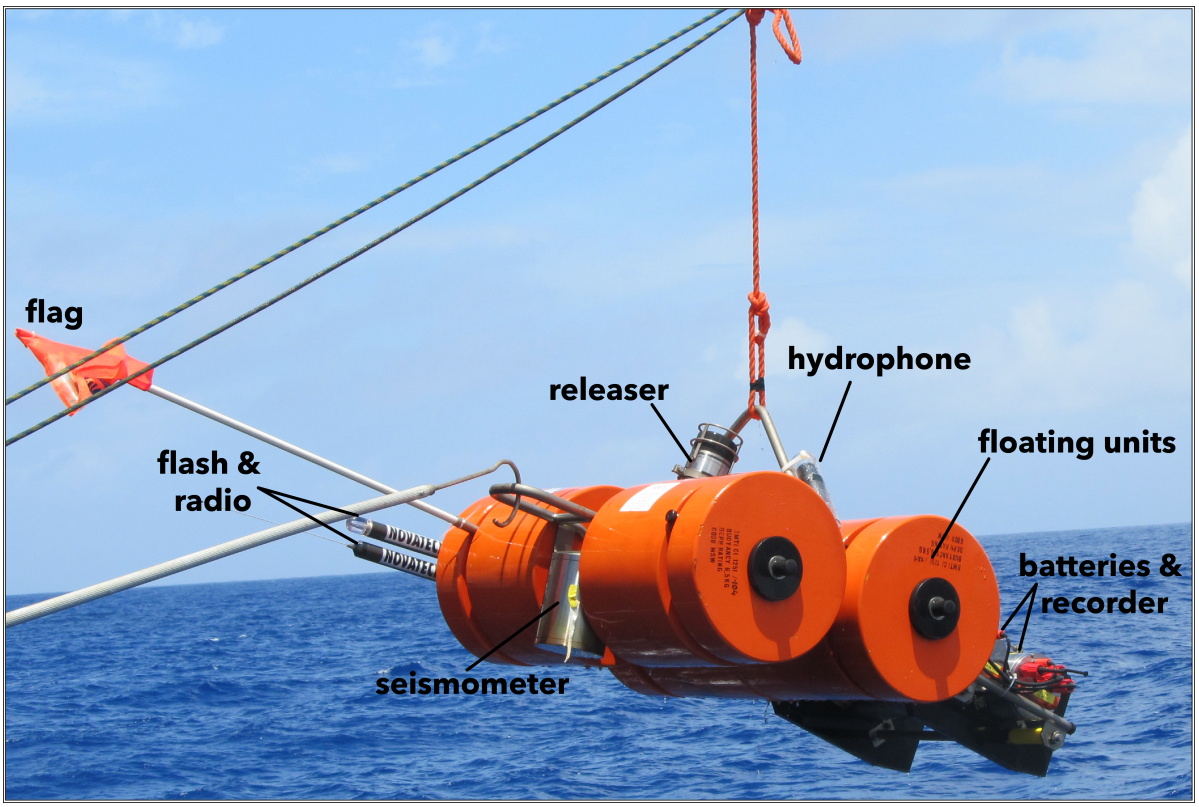

Figure 2.3: The OBS consists of floating units (orange cylinders) responsible for bringing the instrument back to the surface. The releaser is the most important part of every OBS system as it detaches the main body from the heavy anchor (not in picture) which keeps the OBS at the ocean bottom for the duration of the experiment.

component noise cross-correlation.

2.4 Performance

2.4.1 Earthquakes

All earthquakes in teleseismic distance (32-85 degrees) with moment magnitude higher than 5.5 that occurred in 2012-2013 were selected. obspyDMT (Hosseini and Sigloch, 2017) was used to select and retrieve earthquake information and seismic data, obspyDMT is a convenient tool for the mass download of seismic data. The program finds earthquakes according to given search parameters, and it automatically downloads waveforms and sets up a database. Figure 2.4 shows 177 events in teleseismic distance to the RHUM-RUM stations and 57 local events (between 25, September 2012 and 05, December 2013).

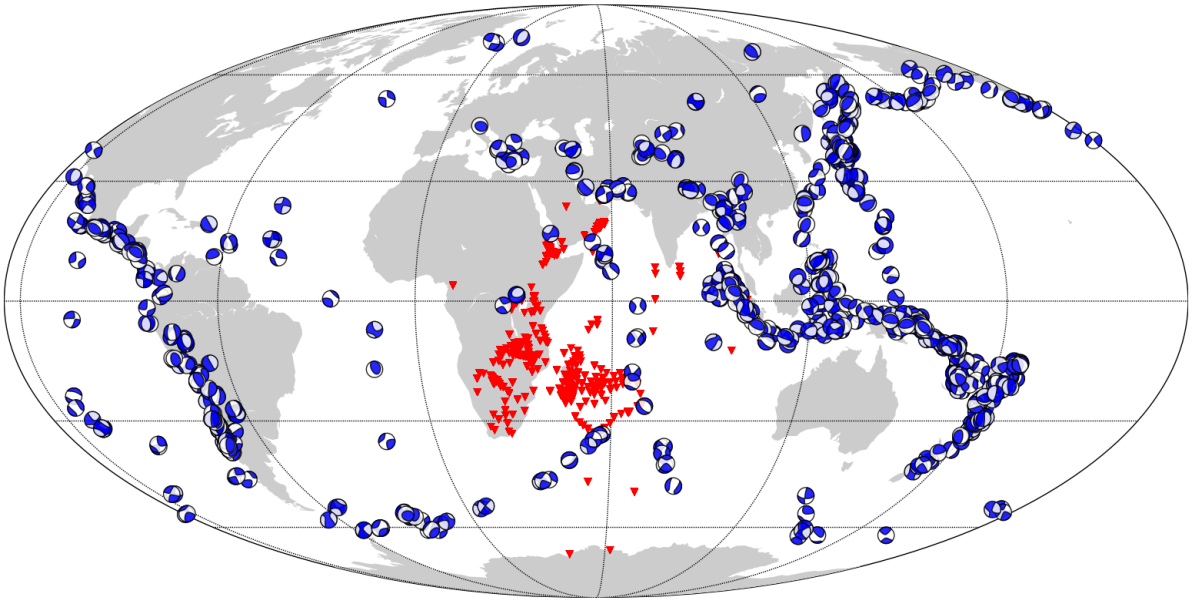

Figure 2.4: Distribution of stations (red triangles) and earthquakes (blue beachballs) between 01. January 2011 and 31. December 2016.

Overall 635 events between 2011 and 2016 in teleseismic distance are available for the whole extent of the deployment of RHUM-RUM stations, permanent (is)land stations and other partner projects (see also Appendix D Figure D.2). This dataset will be referred to as RHUM-RUM+ as other stations (from permanent and temporal experiments) which did not belong to the original project were also included in the dataset.

2.4.2 Data

Stähler et al. (2016a) published a preliminary report on the quality of OBS data. The analysis revealed that out of 19,751 total deployment days (∼12 months × 31 days × 53 instruments), 18,735 days (94%) yielded usable hydrophone, and 15,941 days (80%) were usable on seismometer recordings. They reported that at periods >10 s, German DEPAS instruments were afflicted by a higher self-noise than the French INSU OBS. The reason for this difference lies in the design of the OBS. The French seismometers are detached from the main body whereas the seismometer in the German design is integrated into the frame (Figure 2.3). Hence, any movement of the main body of the

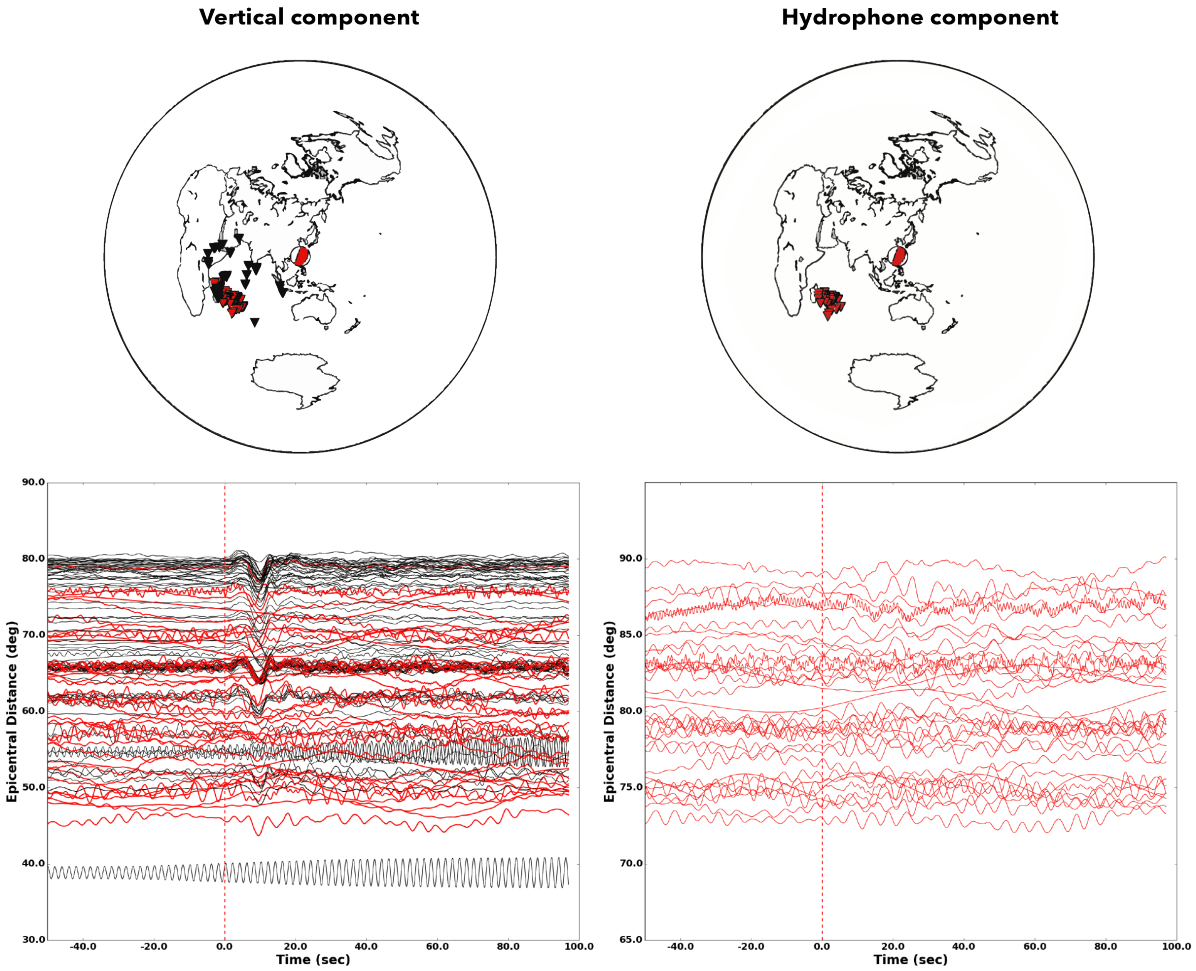

Figure 2.5: Comparison between broadband vertical (left) and hydrophone (right) components. Record section of a magnitude 6.3 Mw event in Taiwan (2013/07/01 05:43:03 UTC, at 23.8°N, 121.06°E, 17.0 km depth). Red waveforms and red triangles belong to the YV network (RHUM-RUM). All other stations are black. The red waveforms are noisier compared to the black ones, but the P-wave (close to the dashed red vertical line) are clearly visible on all seismograms. The hydrophone data (right panel) does not show a coherent signal and significant reverberations exist in the waveforms.

OBS (due to currents, buoy, flag and etc.) can be seen as self-noise on the recordings. Hydrophone recordings were more reliable than 3-component seismometers for both instrument types (DEPAS and INSU). However, hydrophones were significantly affected by reverberations in the water-column (see Chapter 7, Section 7.3.1 for more discussion).

Figure 2.5 shows record sections of an event in Taiwan (2013/07/01 05:43:03 UTC, at 23.8°N, 121.06°E, 17.0 km depth, $M_W = 6.3$) for both vertical and hydrophone components. Despite the YV network (RHUM-RUM) shows more noise compared to land stations (red waveform in Figure 2.5), the onset of the P-wave is clearly visible in almost all epicentral distances. However, the hydrophone waveforms show significant reverberations for the same event. In general, the hydrophone components recorded more reliably, but the signals are complicated by reverberations.

2.4.3 Data coverage

Figure 2.6 shows how different datasets incorporated in the tomographic inversion contribute to the data coverage. The ISC dataset has a good coverage throughout the mantle, where the upper 600 km and lower 500 km show a sparse coverage. P-diffracted has a good coverage in the lower-third of the mantle as expected, the upper mantle and surface are barely covered. Finally, the RHUM-RUM data shows sampling between 600-2500 km around La Réunion and Northern Indian Ocean.

We used ray theory (hypothetically infinite frequency) to compute the sensitivity kernels of onset times selected from ISC-EHB/EHB bulletins. Rays are numerically integrated on the inversion grid. On the other hand, for each cross-correlation traveltime observation in the dataset, we computed 3-D sensitivity kernels using the method of Dahlen et al. (2000). This method can efficiently estimate sensitivity kernels using the paraxial approximation in conjunction with ray theory and the Born approximation. Dahlen kernels are frequency-dependent, and depend on the type of filters (e.g., Gabor filters) and the selected time window (Chapter 3 - Figure 3.7). Figure 2.7 compares the data coverage of ISC to ISC combined with multifrequency measurements using projected sensitivity kernels on our inversion gird (more details in Chapter 4). The ISC

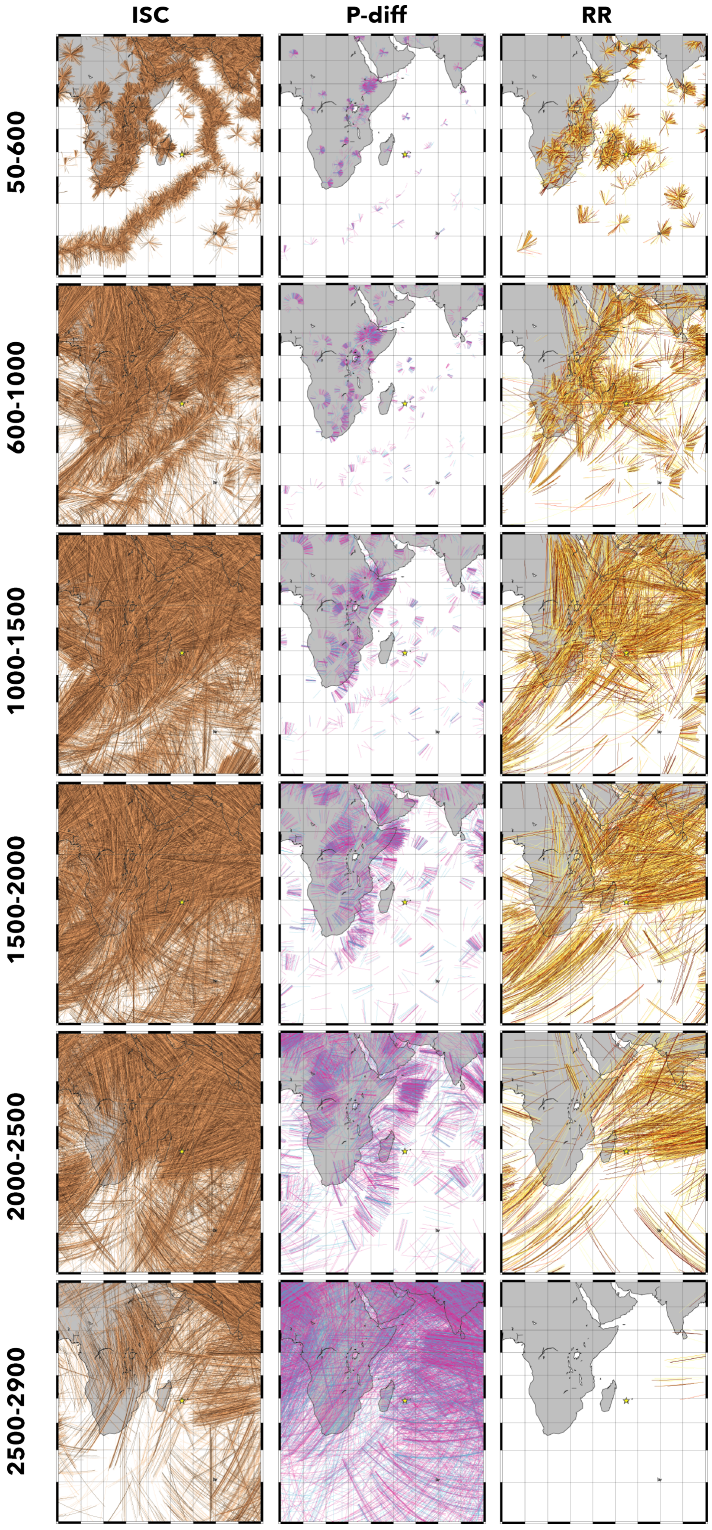

Figure 2.6: Ray coverage for ISC (left), Pdiff (middle) and RHUM-RUM (right) at different depths. Raypaths are calculated for source-receiver pairs in our dataset and projected over a defined depth range on a map.

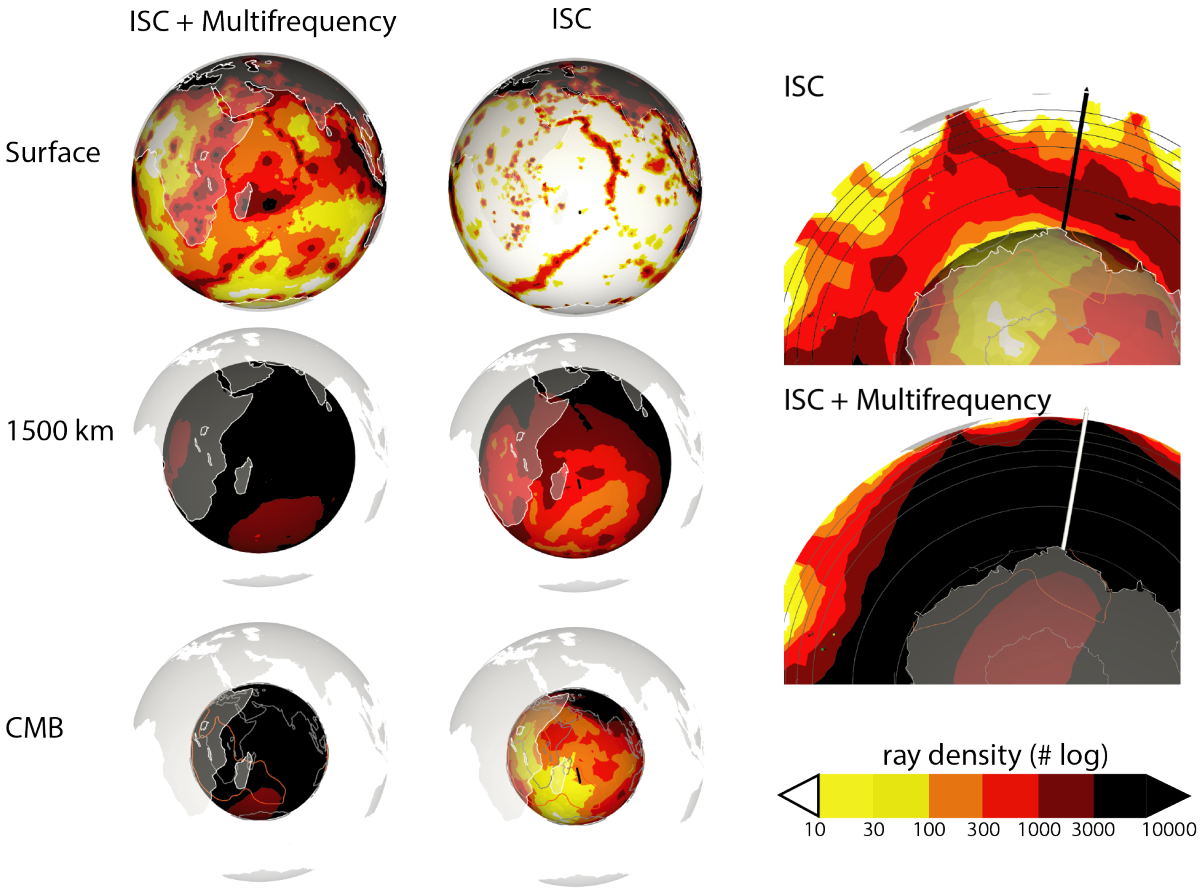

Figure 2.7: Multifrequency cross-correlation kernels and rays from our dataset are projected on the inversion grid, and their amplitudes are shown at different depth slices and cross-sections. The colour represents the kernel density on a logarithmic scale where dark colours show high density. ISC alone has a good coverage in the mid-mantle beneath the Central Indian Ocean. Adding multifrequency Dahlen kernels (ISC + multifrequency) increases the density significantly at all depths.

cross-section in Figure 2.7 shows that most rays come from the East which might cause smearing effects. Adding multifrequency data increases the data coverage significantly. Nevertheless, ray coverage and sensitivity kernels in Figure 2.6 and 2.7 alone do not accurately mirror the resolving power of the data. This will be assessed by resolution tests in the next chapters (see Chapter 4, Section 4.4 and Appendix B).

Alles Gescheite ist schon gedacht worden.
Man muss nur versuchen, es noch einmal zu denken.

All intelligent thoughts have already been thought;
what is necessary is only to try to think them again.

— Johann Wolfgang von Goethe, 1829

3 Inversion framework

Contents

3.1 Ingredients for seismic tomography 27
3.2 Rays vs. multifrequency measurements 31
3.3 Parametrisation and sensitivity kernels 33
3.4 Linear inversion 35
3.5 Selection of preferred models 39
3.6 Resolution tests 40

This chapter gives a brief overview of the theory of teleseismic body-wave tomography. My methodologies for data processing and inversion are based on already published and established work of Dahlen et al. (2000); Montelli et al. (2004); Sigloch and Nolet (2006); Tian et al. (2007b); Nolet (2008) and Hosseini and Sigloch (2015).

3.1 Ingredients for seismic tomography

Various seismological observations can be used to generate seismic tomographic models. This includes onset times, cross-correlation traveltimes, phase velocities, normal mode frequencies, waveforms, time-frequency misfits, instantaneous phase measurements or amplitudes. They can be used to invert for P or S velocity variations, seismic anisotropy,

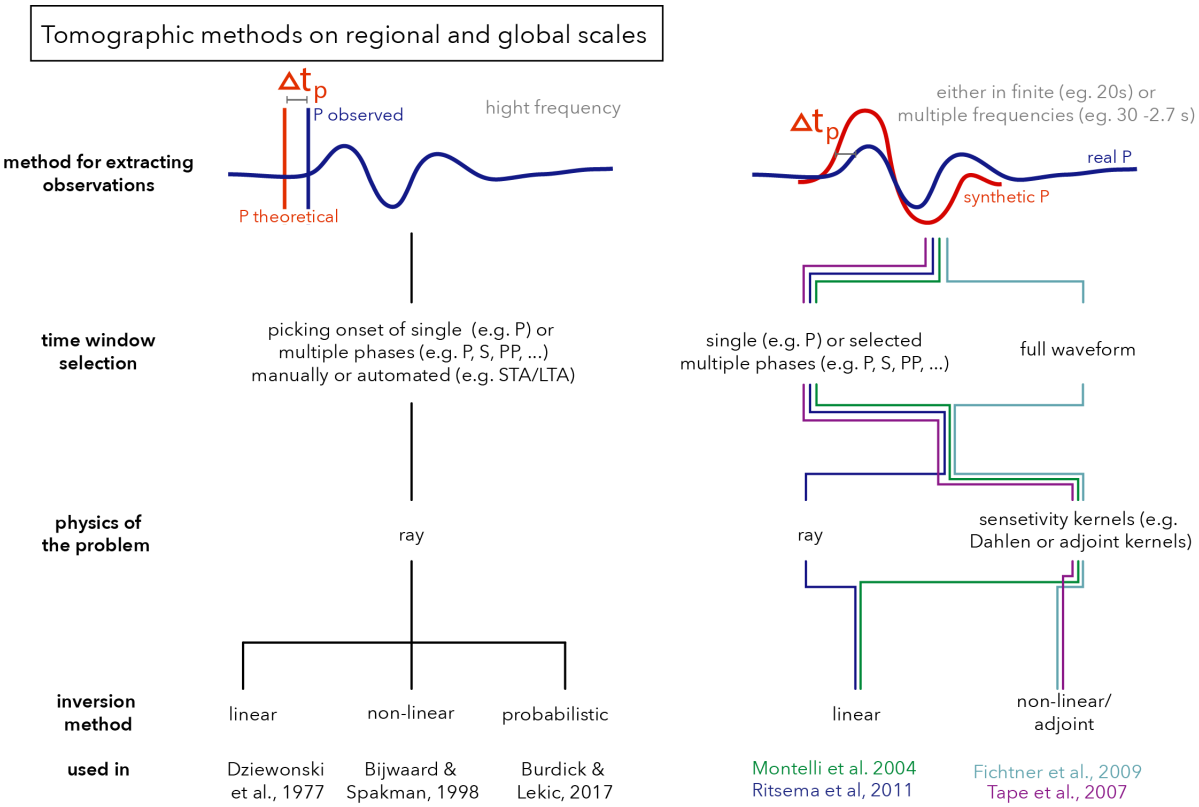

Figure 3.1: Different methods used in existing global and regional body-wave tomography models with example publications. Two main groups for traveltime measurements: **left** for phase picking and **right** for waveform cross-correlation. In the next steps, the "physics of the problem" and the inversion method are listed. References from left to right: Dziewonski et al. (1977); Bijwaard et al. (1998); Burdick et al. (2017); Montelli et al. (2004); Ritsema et al. (2011); Fichtner et al. (2009); Tape et al. (2007).

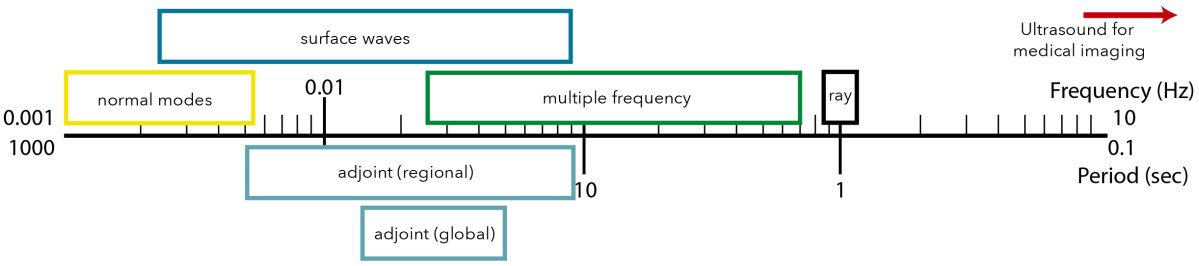

Figure 3.2: Overview of frequency content for some tomographic methods. Global adjoint method (e.g., Fichtner et al., 2009; Zhu et al., 2012; Fichtner and Leeuwen, 2015) uses lower frequencies compared to linear inversions, like multiple frequency (e.g., Montelli et al., 2004; Sigloch et al., 2008; Hosseini et al., 2019) and ray (e.g., since Dziewonski et al., 1977) . Despite the fact regional adjoint method spans a wide range similar to surface wave models (e.g., Ritsema et al., 2011; Schaeffer and Lebedev, 2013; Auer et al., 2014), they cannot incorporate a huge amount of data. Normal modes use long periods > 200 sec (e.g., Woodhouse and Deuss, 2007; Zaroli et al., 2015).

visco-elastic dissipation or density. Moreover, different modelling techniques (e.g., ray-theory, finite-frequency or adjoint) can be employed. Figure 3.1 summarizes observations, model parameters and modelling techniques used in existing global and regional body-wave tomography models.

Among all the variations in seismic tomography methods, our inversion framework is built upon multiple-frequency, waveform-based measurements formulated in an explicit linear form as:

$$Gm = d \tag{3.1}$$

Entries of vector d are observations; each row of matrix G links the target model parameters in vector m to one measurement in data vector d.

Data. Data plays a major role in any inverse problem. The first global tomographic models (e.g., Dziewonski et al., 1977) was based on hand picked arrival times (onset times) of seismic phases, e.g., from the ISC Bulletin. Phase picking is a labour-intensive task, particularly for large seismological datasets. Moreover, the uncertainties associated with each measurement cannot be easily quantified. The development of 3-D forward modelling methods, it is now possible to directly compare the observed seismograms with synthetic waveforms (Montelli et al., 2004; Sigloch and Nolet, 2006; Hosseini and Sigloch, 2015; Hosseini, 2016). In this study, we measure finite-frequency traveltimes of P and S teleseismic waves by cross-correlating observed waveforms with synthetic seismograms across a broad frequency range. The main advantages of this method are: **(1)** it can be applied automatically to large seismological datasets. **(2)** traveltimes and amplitudes of seismic phases can be measured in different frequency bands (Figure 3.2, also refer to Section 3.2) which can potentially increase the data yield from one single source-receiver pair. **(3)** uncertainties can be estimated for each observation according to the goodness of fit measured by the cross-correlation factor, for example.

Physics. Each row of matrix G in Equation 3.1 corresponds to a sensitivity kernel which links one measurement in vector d to all model parameters in vector m. For our multifrequency measurements, we compute 3-D finite-frequency sensitivity kernels which estimate the frequency-dependent interaction between waves and structural heterogeneities (Figure /reffig:tomographicmethods right). For analyst-picked arrival times from ISC-EHB/EHB (Engdahl et al., 1998; Weston et al., 2018), we use ray theory (hypothetically infinite frequency; Figure 3.2) to efficiently compute the sensitivity kernels of onset times (Figure /reffig:tomographicmethods left).

Solving for m. The goal of inverse theory is to obtain knowledge about the physical world on the basis of inferences drawn from observations (Menke, 2018). One way of formulating the inverse problem is as an optimisation problem, that is, to minimize a misfit between observation and model parameters. Generally, the existing deterministic inverse methods can be categorised into two groups:

1. **Linear.** In this case, the misfit is minimised in one step or iteratively. For example, in this work, we minimize L_2 norm $||prediction - observation||_2^2$ with LSQR (Paige and Saunders, 1982; Nolet, 1985). This is a conjugate-gradient solver that uses a recursive scheme to monotonically reduce the residual vector. The main advantages of linear methods are computational efficiency and their applicability to very large seismological datasets (e.g., Montelli et al., 2004; Ritsema et al., 2011; Schaeffer and Lebedev, 2013; Hosseini, 2016) (see Figure 3.1).

2. **Adjoint.** The misfit gradient is re-computed at each iteration. The adjoint inversions can better handle the non-linearity of waveform data in models with strong parameter gradients. Compared to linear inversions, the adjoint method is computationally expensive, and therefore, in practice, it has been applied only to low frequency waveforms (Fig. 3.2) and a limited number of sources.

Understanding Earth from a snapshot. The imaged structures in seismic tomography are blurry snapshots of convection in Earth's mantle (Grand et al., 1997). How can a snapshot give information about past and the future evolution of Earth?

Like Sherlock Holmes and his "science of deduction", a researcher needs to use a "top-down" logic. *In solving a problem of this sort, the grand thing is to be able to reason backwards. [...] Most people, if you describe a train of events to them, will tell you what the result would be. They can put those events together in their minds, and argue from them that something will come to pass. There are few people, however, who, if you told them a result, would be able to evolve from their own inner consciousness what the steps were which led up to that result. This power is what I mean when I talk of reasoning backwards, or analytically* (Doyle, 1887).

When presented with a "crime scene", the scientist has to pick up the presented clues left behind and try to understand their connections and relevance. The tomographic snapshot combined with geochemistry, geodynamics and tectonics provide a framework to infer the Earth's evolution.

3.2 Rays vs. multifrequency measurements

Phase arrivals are determined visually and compared to predicted arrival times based on a 1-D background model, e.g., PREM (Dziewonski and Anderson, 1981) or IASP91 (Kennett and Engdahl, 1991).

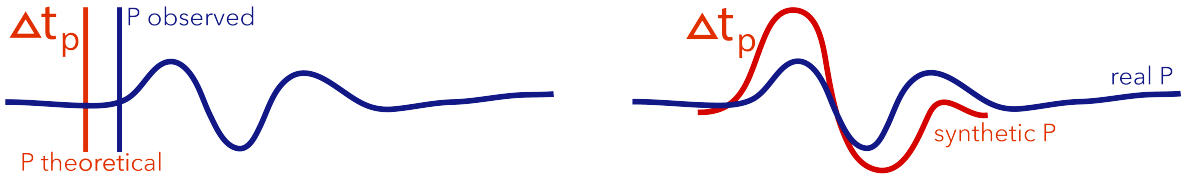

Figure 3.3: Illustration of phase picking for ray theoretical inversion approach (left) and cross-correlation of real with synthetic waveform data (right) for multiple frequency inversion. Red colours indicate either a predicted arrival time or a synthetic waveform, while blue represents real data. For an example with real data refer to Figure 4.6.

In this study, a cross-correlation technique is used instead (Fig. 3.3). The advantage of cross-correlating synthetic with recorded waveforms is that it can be automated and

the cross-correlation produces a goodness of fit for each measurement, which is later used as a weighting factor. Predicted waveforms or matched filters are synthesised from fully numerical Green's functions convolved with source time functions (STF). The Green's function is the response of an Earth model (in this study we use IASP91, see Chapter 4) to a Dirac delta pulse and a STF is a function of the moment release of an earthquake in time (see also Section 4.2). Here, we use AxiSEM (Nissen-Meyer et al., 2014; van Driel et al., 2015) to compute synthetic waveforms. My methodology of inverting for a STF was introduced by Sigloch and Nolet (2006) in order to get an new estimate for source depth to improve the spacing of direct and depth phases (e.g., P, pP and sP) in synthetic waveforms (matched filter). Using this method, I determined the STF of approximately 177 teleseismic and 56 local events, recorded by RHUM-RUM dataset.

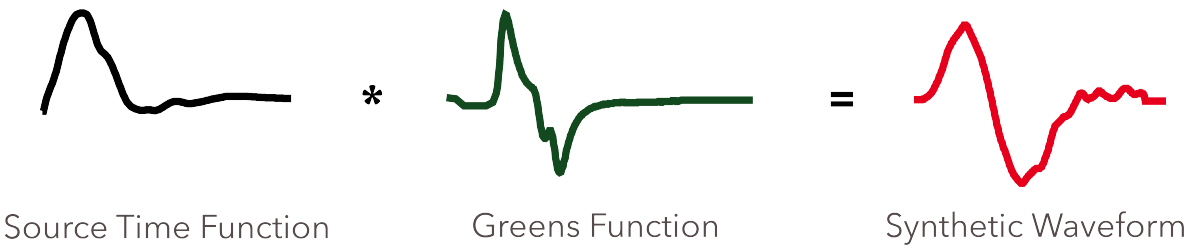

Figure 3.4: Convolution (star) between a Green's function (green) and a STF (black) results in a matched filter or synthetic waveform (red).

In our multifrequency measurement technique, the broadband and synthetic data are both filtered through the same bandpass filters, and measurements are done for each frequency band. In this study, I use Gabor filters, Gaussian filters in the log-frequency domain and good spectral concentration characteristics, with dominant periods between 30 and 2.7 seconds, whereas the central frequencies are spaced by $\sqrt{2}$. Eight overlapping passbands are the result within an usable frequency range (Figure 3.5). I do not go below 2.7 seconds because the number of successful fits becomes very small (Sigloch, 2008; Hosseini and Sigloch, 2015; Hosseini, 2016).

The time difference that maximizes the cross-correlation function between real and synthetic waveforms at each filter is defined as traveltime measurement. This procedure was applied to all source and receiver pairs in our dataset (e.g. Figure 4.6). Only

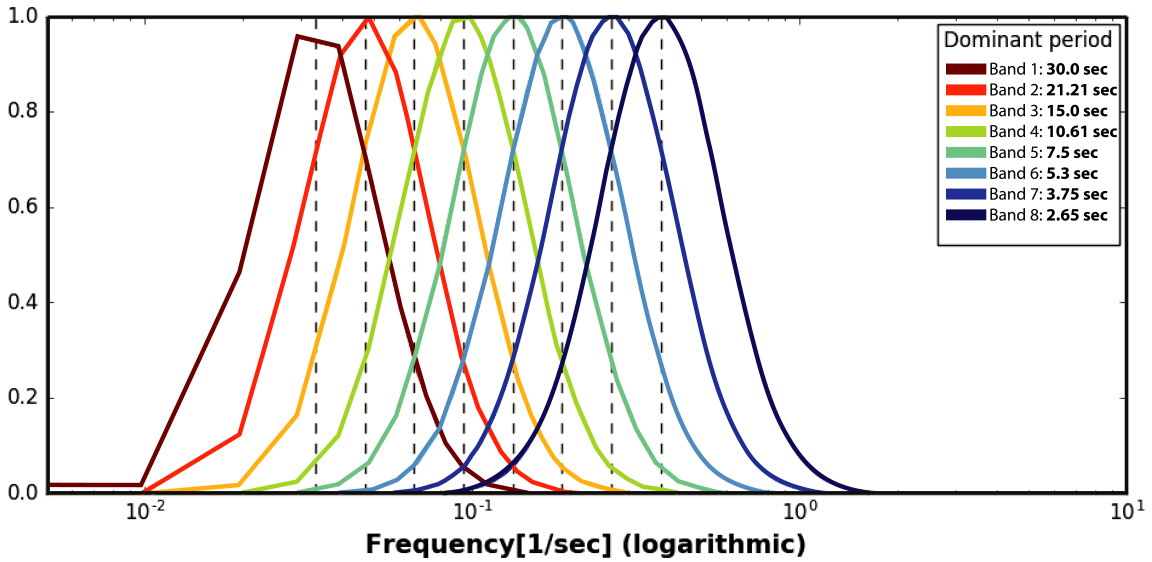

Figure 3.5: Gabor filter for passbands between 30 to 2.7 s dominant period on logarithmic scale in frequency domain.

measurements with a high cross-correlation coefficient were selected and added to the data vector $d_i (i = 1, ..., N)$, where N is the number of measurements. An uncertainty is assigned to each measurement according to the goodness of fit (or cross-correlation factor; see also Chapter 4, Section 4.3).

3.3 Parametrisation and sensitivity kernels

Parametrisation. I use a tetrahedral mesh to locally parametrise the continuous Earth model $m(r)$. This can be written as:

$$m(r) = \sum_{j=1}^{M} m_j h_j(r) \tag{3.2}$$

where h_j is a set of basis functions, in this case the basis functions form tetrahedrons. $m_j (j = 1, ..., M)$ is the discretised Earth model and the unknown vector in the inversion, and M is the total number of unknowns (for example in this study M has 56709 unknowns).

Meshing is performed with *DistMesh* (Persson and Strang, 2004) and *Quickhull* (Barber et al., 1996) to generate non-overlapping tetrahedrons based on Delaunay criterion.

The Delaunay criterion is a triangulation for a given set of points in a plane so that no point is inside the circumcircle of a triangle. This criterion allows the generation of pseudo-regular meshes. *DistMesh* generates tetrahedral meshes in such a way that their edge-lengths can be locally adjusted. To always enclose the Earth's surface, the radius is set to $r + 50$ km (r=6371 km).

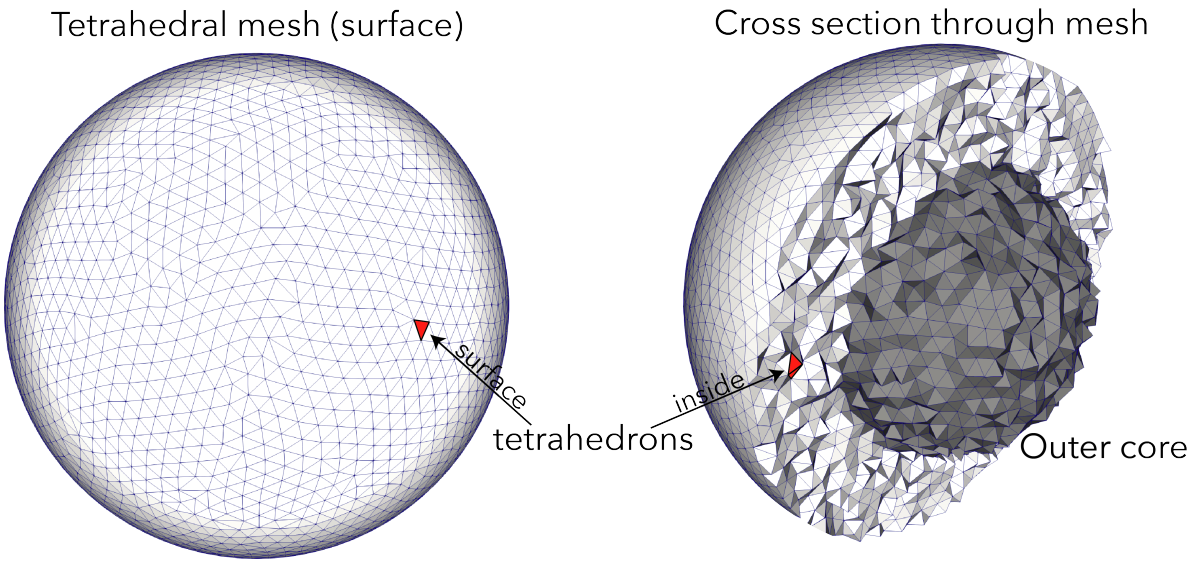

Figure 3.6: Regular tetrahedral mesh with 400 km edge-length everywhere ($M = 17632$). Two tetrahedrons are marked in red on the surface and inside the sphere.

DistMesh can accommodate an irregular mesh with different sampling densities in a straightforward manner. One advantage of tetrahedral grids is that the resolution of the mesh can be easily adjusted. For example, the mesh can be rendered more dense where stations are close (e.g., in arrays). In areas of sparse data coverage, tetrahedrons with larger edge-lengths can be generated. An example tetrahedral grid is shown in Figure 3.6.

Sensitivity Kernels. Sensitivity kernels are parts of a wavefield (depending on the phase, e.g. P, PP, etc.) that sense the Earth structure. A kernel K^T links a velocity anomaly $\delta ln(V_p)$ to the traveltime measurement δT:

$$\delta T = \int K^T(r)\delta ln(V_p)d^3r \tag{3.3}$$

The integral is over the whole volume of Earth. However, in practice, only a small part of Earth's volume has non-zero values (see Figure 3.8 for schematic example). These kernels are computed for a given seismic phase, source mechanism and a specific frequency content. There are two types of sensitivity kernels in our study, frequency dependent and ray-based kernels. For the calculation of 3-D frequency-dependent kernels, I used a method based on Dahlen et al. (2000) where kernels are calculated efficiently based on the paraxial approximation and Born theory (hence they are estimates of the sensitivity). Figure 3.7 shows examples of kernels computed for different Gabor filters used in this study. At lower frequencies kernels are broader. By increasing the frequency content, kernels are thinner for a given seismic phase (here P arrival). As a ray is assumed to have an infinite frequency content (with respect to the wavelength of the structure being imaged), the sensitivity kernel is approximated as a line.

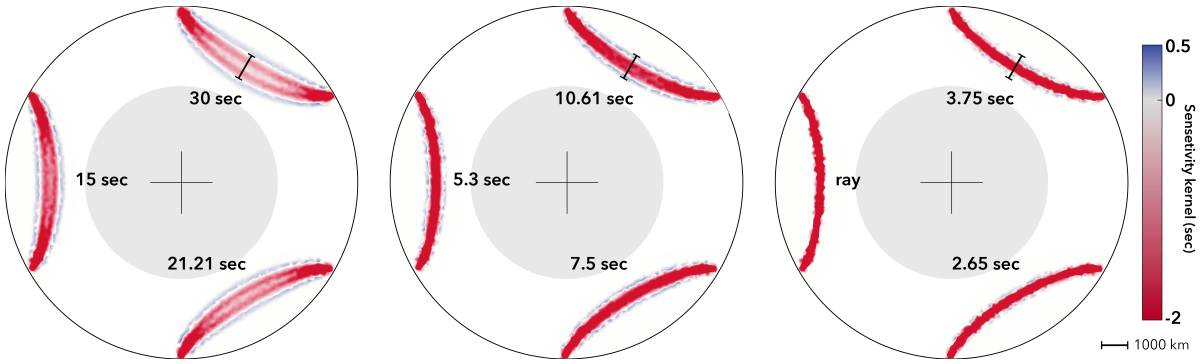

Figure 3.7: Eight example sensitivity kernels for direct P arrivals computed for Gabor filters with centre periods from 30 to 2.65 s and one example of a ray. All kernels are multiplied by Earth's volume and are projected on a regular tetrahedral grid (100 km edge-length), calculated for 60° epicentral distance and 50 km depth for the source. A ray projected on this grid resembles a sensitivity kernel of the highest frequency.

3.4 Linear inversion

Traveltime measurements d_i are linearly linked by kernels K to the Earth model $m(r)$:

$$d_i = \int_V K_i^T(r) m(r) d^3r \tag{3.4}$$

inserting Equation 3.2 leads to (discretised model parameters):

$$d_i = \sum_{j=1}^{M} m_j \int_V K_i^T(r) h_j(r) d^3r \tag{3.5}$$

The kernel matrix G_{ij} is defined as:

$$G_{ij} = \int_V K_i^T(r) h_j(r) d^3r \tag{3.6}$$

which results in:

$$d_i = \sum_{j=1}^{M} G_{ij} m_j \tag{3.7}$$

In matrix form, equation 3.7 can be written as:

$$\mathbf{Gm} = \mathbf{d} \tag{3.8}$$

Each row of matrix **G** contains one 3-D sensitivity kernel numerically integrated onto the inversion grid. Figure 3.8 shows this for an example with five model parameters and with an uneven distribution of kernel coverage. Some of the model parameters (m_4 and m_5 in this example) have not been sampled at all. To obtain one unique solution, we regularize the problem. This can be done by adding new rows to matrix **G** and vector **d**.

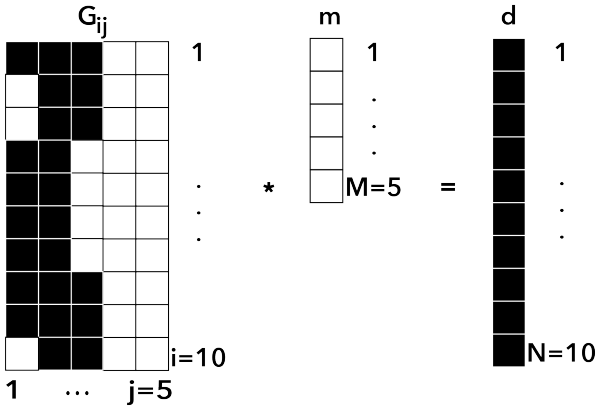

Figure 3.8: Schematic of the linear system of equations according to Equation 3.8. G_{ij} is the kernel matrix where the black squares represent kernel coverage, white squares are not covered by the kernels (zeros). Here, a typical inversion problem is represented, with more data d_i (black squares) than unknowns in m, but an uneven distribution of kernels makes the problem ill-posed and it does not have an unique solution.

Regularisation imposes extra conditions on the solution in order to convert an ill-posed problem to a well-posed one. To regularise the example inversion of Figure 3.8, we use both norm damping and smoothing. For norm damping, the first step is to add "artificial" data to vector **d** and corresponding rows to matrix **G**. This biases the model towards zero (damping) by adding M (number of model parameters) equations of the form $\epsilon_n m_i = 0$, with ϵ_n a tunable parameter to control the strength of norm damping:

$$\begin{pmatrix} G \\ \epsilon_n I \end{pmatrix} m = \begin{pmatrix} d \\ 0 \end{pmatrix} \tag{3.9}$$

Higher damping values will push m_j towards zero, hence the final model will be close to the a priori background model. In this case the effect of noise during the inversion decreases. Damping alone is unsatisfactory if the data coverage is unequally distributed. In such cases, some parts of the model might be damped more than others, this might lead to artefacts. This is usually the case on Earth for global inversions where station coverage and earthquake distribution are strongly biased towards continents and seismically active regions. A Bayesian method was introduced to deal with the neglected bias in the data, in order to reduce the number of unwanted structures or details (Nolet, 2008). This approach leads to the following equation:

$$\begin{pmatrix} C_d^{-1/2} G \\ \epsilon_n I \\ \epsilon_s c_m^{-1/2} \end{pmatrix} m = \begin{pmatrix} C_d^{-1/2} d \\ 0 \\ 0 \end{pmatrix} \tag{3.10}$$

C_d is a diagonal data covariance matrix (i.e., uncorrelated errors) with assigned a priori uncertainties σ_i^2 (standard deviation squared) as entries. Standard errors are chosen to each measurement according to its cross-correlation values, ranging from 0.3 s for high-quality measurements to 1 s for low cross-correlation factors. The smoothing operator $c_m^{-1/2}$ smooths the model for correlated model parameters when applied to m. ϵ_s is the smoothing factor that can be used to tweak the intensity of the smoothing operator.

Entries of m in equation 3.10 are the three-dimensional solutions for isotropic compressional P-wave velocity structure $\delta ln(V_p)$ with additional unknowns to account for hypocentral parameters (origin time, longitude, latitude and depth). Figure 3.9

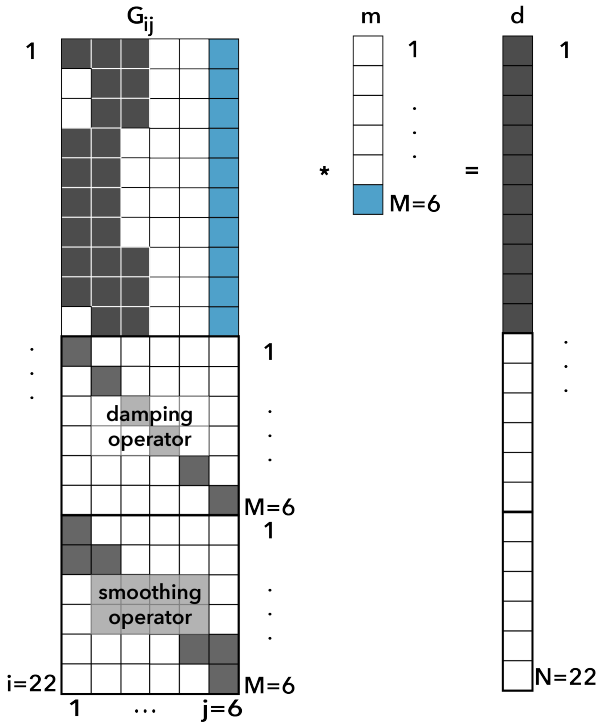

Figure 3.9: Schematic of the linear system of equations according to Equation 3.10. Since the problem is ill-conditioned, damping and smoothing operators are added to the system of equations and additional unknowns are added to account for hypocentral parameters (light blue squares). Due to the damping and smoothing operators added to the system of equations, the result will contain less unwarranted structure.

schematically shows the system of equations to solve $Gm = d_r$ with appended rows for regularisation and common corrections.

The system of equations cannot be solved explicitly, and instead, we minimize the L_2 norm given by:

$$||Gm - d_r||_2^2 \tag{3.11}$$

Equation 3.11 is solved with a LSQR algorithm, which is a conjugate–gradient type method for solving large linear and sparse problems (Paige and Saunders, 1982; Nolet, 1985). As a first step, an inversion with very low regularisation parameters (the model fits all the data, even the noise) is performed to identify outliers. The measurements that deviated more than 3σ from the general distribution are labelled as outliers and

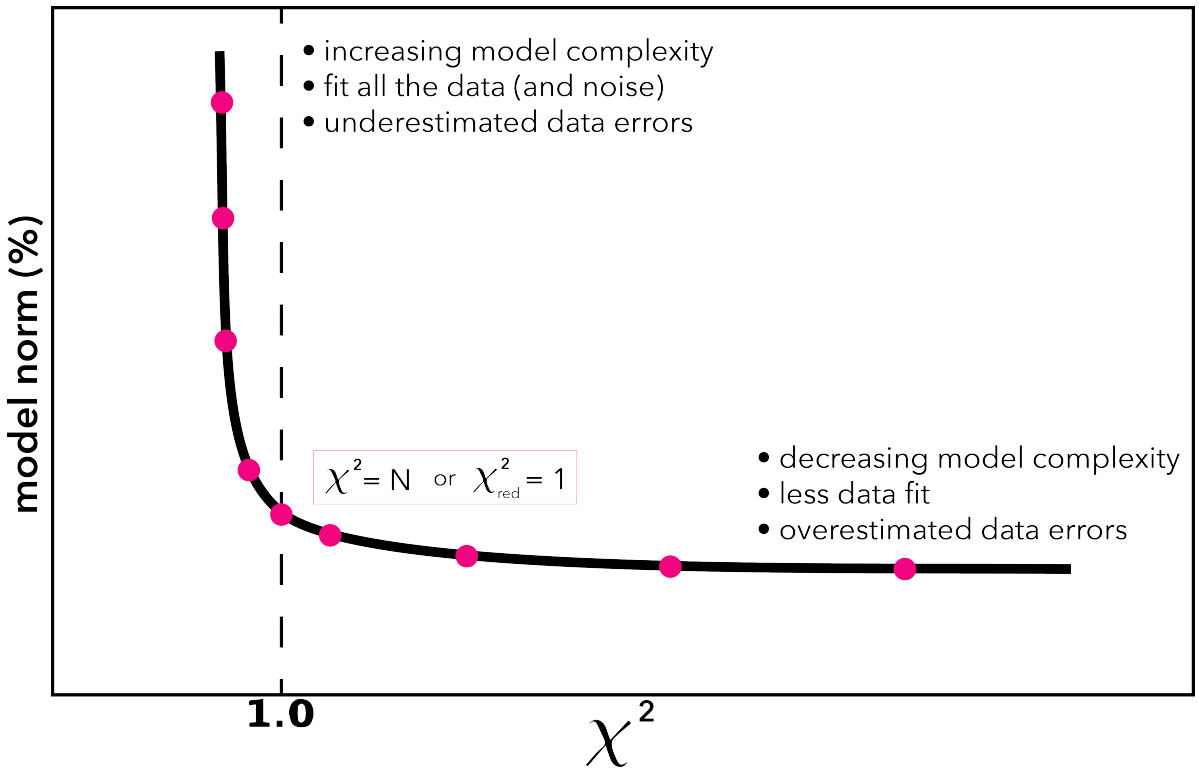

Figure 3.10: Illustration of L-curve, with χ^2 (data fit) on the x-axis and the model norm $||m||^2$ (model complexity) on the y-axis. By changing the regularisation parameters (pink dots), the best trade-off between model complexity and model norm, $\chi^2_{red} = 1$ can be found. Data is poorly exploited at the horizontal arm and dominated by noise at the vertical arm. The choice of the preferred model is subjective and usually chosen to be close to the bending of the L-curve due to the limited knowledge of data uncertainties.

removed from the subsequent inversions. In the next step, inversions with variable regularisation parameters are performed.

3.5 Selection of preferred models

By changing the regularisation parameters (ϵ_n for damping and ϵ_s for smoothing) in eq. 3.10, the trade-off between residual data misfit in terms of reduced chi-squared χ^2_{red} and the L_2 model norm $||m||^2_2$, as a measure of model complexity can be analysed, where χ^2_{red} is given by:

$$\begin{aligned}\chi^2_{red} &= \frac{1}{N}\sum_{i=1}^{N}\left(\frac{d_i^{obs}-d_i^{pred}}{\sigma_i}\right)^2 \\ &= \frac{1}{N}\sum_{i=1}^{N}\left(\frac{d_i^{obs}-\sum_{j=1}^{M}\left(G_{ij}m_j^{est}\right)}{\sigma_i}\right)^2\end{aligned} \tag{3.12}$$

Figure 3.10 shows a schematic of a L-curve, or trade-off. The location of the bend of the L-curve can be shifted by increasing the uncertainties σ (shift to the left - correct for overestimated data errors) or decreasing them (shift to the right - correct for underestimated data errors).

Usually a "preferred" model is selected from the bending of L-curve as it is the best compromise between minimizing both χ^2_{red} and $||m||_2^2$. However, there is an inherent subjectivity to the choice of models close to the bending of the L-curve due to the limited knowledge of data uncertainties.

3.6 Resolution tests

Resolution tests are done by constructing a synthetic input model m_{inp} (e.g., checkerboard test) and multiplying it with the matrix $\mathbf{G}$. This results in a new data vector d_{syn}:

$$Gm_{inp} + e = d_{syn} \tag{3.13}$$

To make the resolution tests more realistic, a noise vector e is added to Gm_{inp}, though it is difficult to assign noise with realistic properties to all data points (different noise models are discussed in Chapter 4). Figure 3.11 shows this procedure for the example in Figure 3.8. Solutions of the resolution test are obtained through the same inversion procedure and parameter settings as in the observed data. In the next step, the outputs are compared to the synthetic input model.

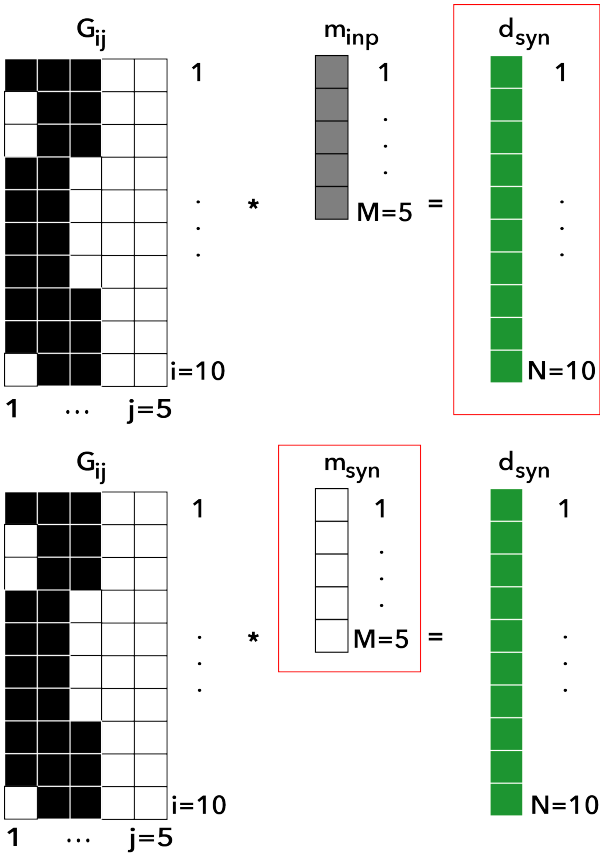

Figure 3.11: Upper panel shows input model m_{inp} (grey squares) multiplied with existing kernel matrix G_{ij}, which results in d_{syn} (green squares). In the second step, a normal inversion is preformed with the aim of retrieving values of m_{syn} as similar to m_{inp} as possible. For simplicity, damping and smoothing operators are not shown here. In practice, the same inversion procedure and parameter setting (including regularisation parameters) as in the observed data is used.

Frequently, I have been asked if an experiment I have planned is pure or applied research; to me, it is more important to know if the experiment will yield new and probably enduring knowledge about nature.

—William Shockley

4

Multifrequency seismic tomography of the mantle beneath La Réunion

Contents

4.1 The RHUM-RUM project 44
4.2 Data 45
4.3 Inversion framework 51
4.4 Results 57
4.5 Plumes and LLVPs in other models 65
4.6 Conclusion 66

This chapter discusses the inversion framework and the tomography models of the mantle beneath La Réunion. I start with the inversion of source information (depth, moment tensor and source-time function), data retrieval and pre-processing. Next, I will describe our multifrequency measurement technique in which traveltimes anomalies in different frequency bands are extracted by cross-correlation of numerical waveforms and observed data. Finally, the resulting tomography results will be shown and discussed, and their quality will be assessed via resolution tests.

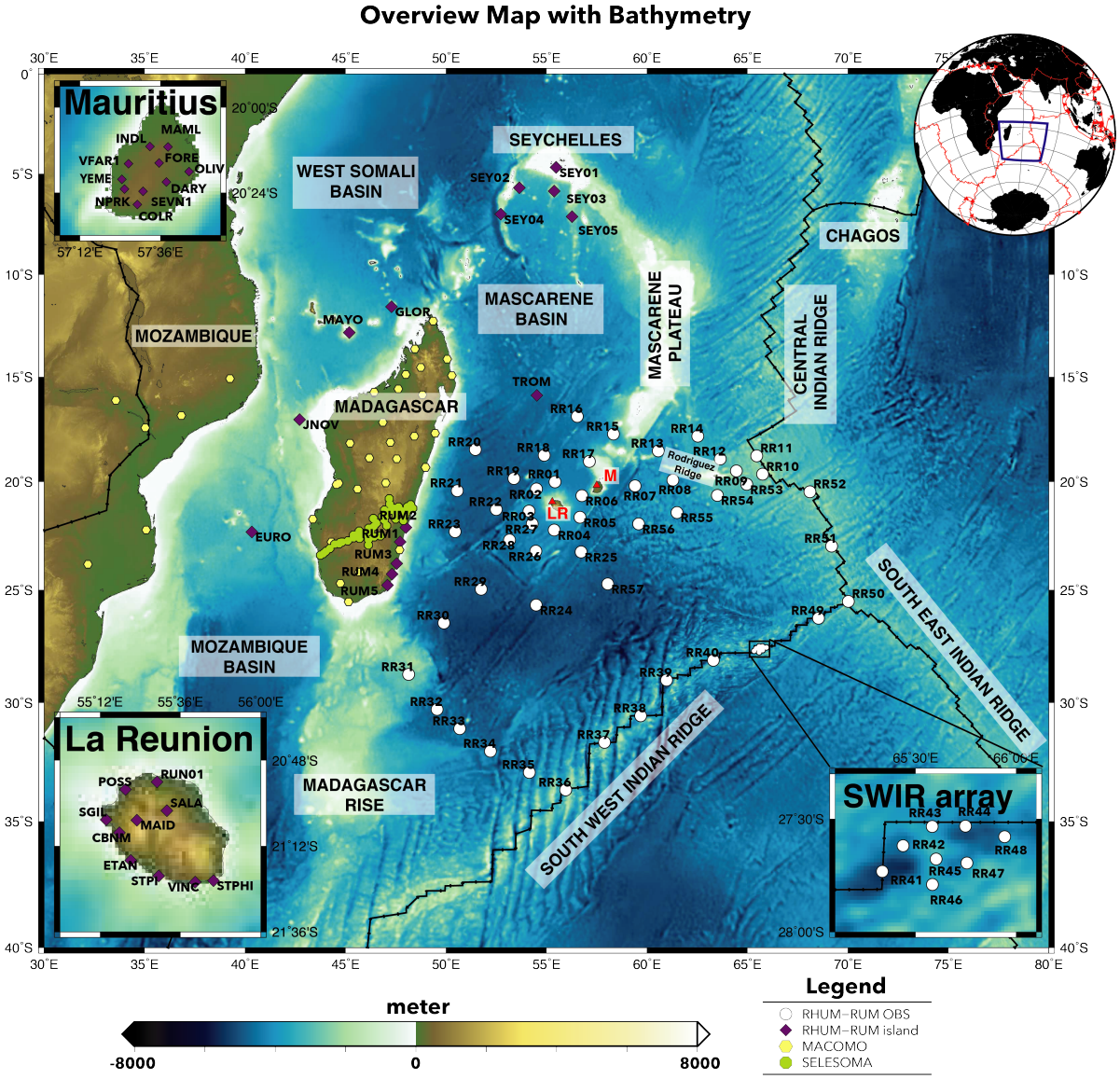

Figure 4.1: White dots show the location of OBS stations of the RHUM-RUM project. Violet diamonds represent the location of island stations (on La Réunion, Mauritius and Seychelles). Yellow and green symbols correspond to the MACOMO and SELASOMA projects, respectively. All in all, the area of the experiment spanned 2000 km × 2000 km.

4.1 The RHUM-RUM project

Here, I present a new high-resolution whole-mantle tomographic model of the western Indian Ocean using ocean bottom seismometer (OBS) data from the RHUM-RUM experiment. La Réunion, like Hawaii, Tristan da Cunha and Iceland is a prominent candidate for a deep sourced mantle plume (after Courtillot et al., 2003). Evidence for this include tomographically imaged slow anomalies beneath the island in the upper and mid-mantle, surface observations including ongoing volcanic eruptions, seamount chains, linked large igneous province (LIP, Deccan Traps) as well as an anomalous noble-gas composition (Courtillot et al., 2003).

The RHUM-RUM project was initiated by Karin Sigloch and Guilhem Barruol (German-French collaboration) in 2012 (Barruol and Sigloch, 2013). The scientific goal of the RHUM-RUM project is to seek evidence for the presence or absence of a mantle plume beneath the western Indian Ocean using a novel dataset and a teleseismic body-wave imaging technique (Sigloch et al., 2008; Tian et al., 2009; Hosseini, 2016; Hosseini et al., 2019).

The RHUM-RUM experiment instrumented a 2000 km × 2000 km area of western Indian Ocean floor (Figure 4.1) and islands as well as Madagascar with broadband seismometers. The central component was a 13-month long deployment of 57 German and French Ocean Bottom Seismometers (OBS). This was supplemented by a 3 year deployment of 37 seismic stations on Réunion, Mauritius, Rodrigues, the southern Seychelles, the Iles Eparses and southern Madagascar. Partner projects such as MACOMO (Wysession et al., 2011), SELASOMA (Tilmann et al., 2012) contributed another 30+ stations on Madagascar. I used a multiple-frequency measurement technique (Sigloch et al., 2008; Tian et al., 2009; Hosseini and Sigloch, 2015; Hosseini et al., 2019) to extract cross-correlation traveltimes in passbands between 30 and 2.7 s dominant period. The dataset, measurement technique and inversion framework are discussed further in the next Section.

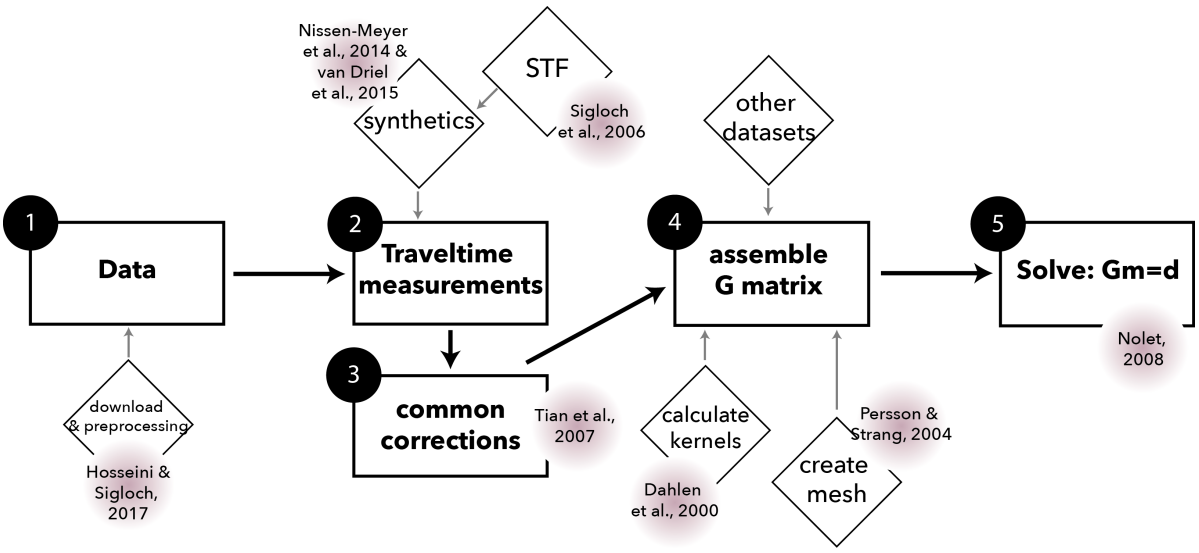

Figure 4.2: Main steps of the inversion framework. **(1)** Data retrieval and pre-processing with obspyDMT (Hosseini and Sigloch, 2017). **(2)** Traveltime measurements include bandpass filtering of seismic waveforms and cross-correlation between synthetic and real data for selected time-windows. **(3)** Common Corrections include crustal, ellipticity and elevation corrections (after Tian et al., 2007b). **(4)** In order to assemble the matrix G, or sensitivity matrix, first the tetrahedral mesh is generated (after Persson and Strang, 2004) and then the sensitivity kernels (after Dahlen et al., 2000) for each source receiver pair is calculated and projected on the inversion grid. Other datasets (e.g. picked arrival times) are included and also projected on the mesh. **(5)** The inversion solves a liner system of equations by minimizing the L_2 norm $||Gm - d||_2^2$ with LSQR(after Nolet, 2008). Since the problem is ill-posed and non-unique, smoothing and damping parameters are added.

4.2 Data

Broadband data

Raw broadband seismograms from the RHUM-RUM experiment are stored on RESIF seismic data portal (http://seismology.resif.fr/) together with response files in StationXML format. GPS and clock corrections (Hable et al., 2018) are already applied to the data, while orientation of horizontal components need to be corrected in a separate step by using the correction files (Scholz et al., 2016). Data retrieval and pre-processing was done using obspyDMT (Hosseini and Sigloch, 2017) (Figure 4.2). *obspyDMT* automatically applies instrument correction to ground displacement, bandpass-filtering between 0.01 and 3.5 Hz, local archiving, and updating of the dataset when new waveforms became available on the data centres. A preliminary performance analysis of the recorded

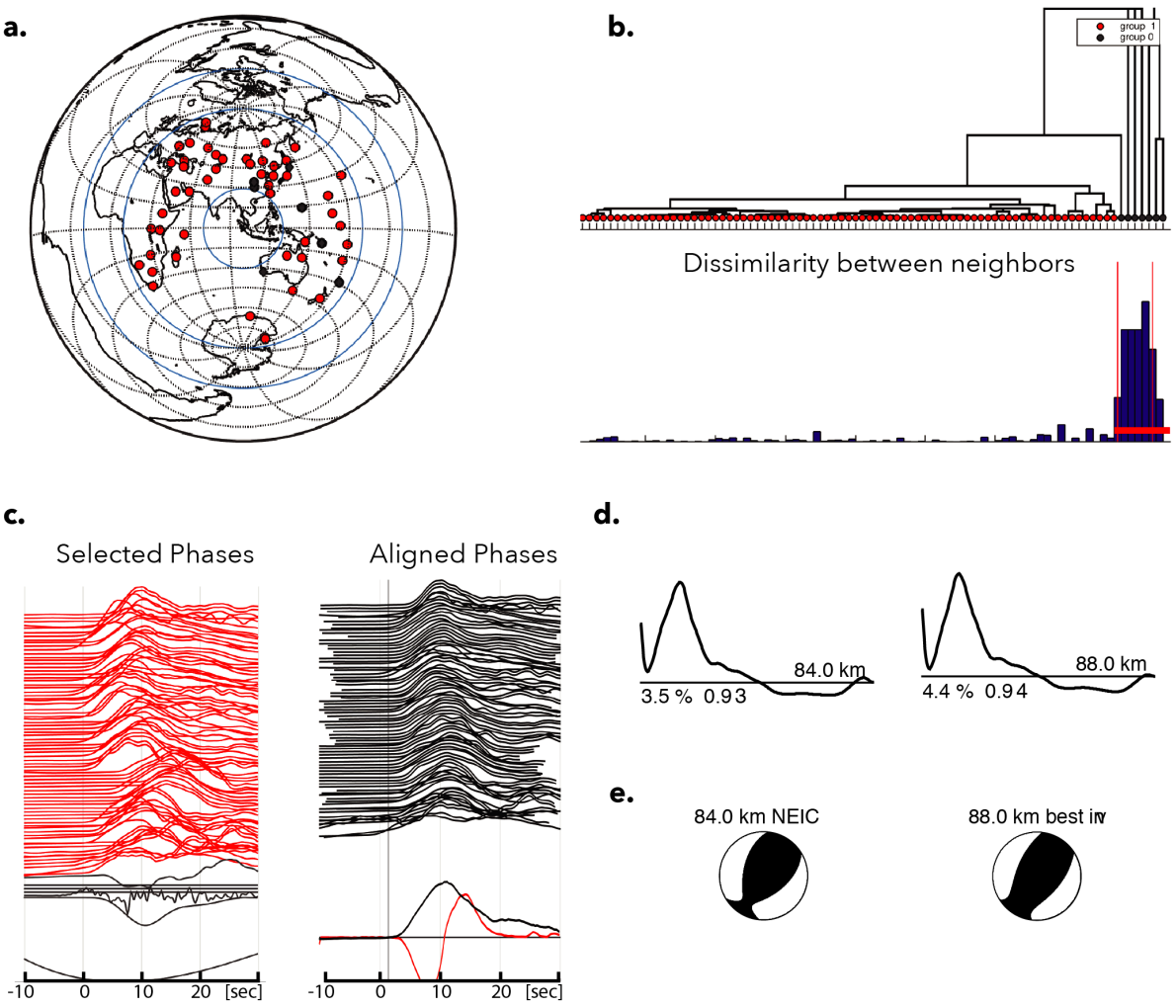

Figure 4.3: The workflow for seismic source inversion applied to a magnitude 6.6 Mw earthquake in Indonesia (2012/10/12). **(a)** Distribution of stations used in the source inversion; a good azimuthal coverage is required to determine "unbiased" (or "least biased") source information. Stations with high signal-to-noise ratios are represented by red circles and rejected ones by grey diamonds. **(b)** The dendrogram makes the selection of similar waveforms more convenient as waveforms are grouped based on similarity, and dissimilar waveforms show up as high (blue) columns. **(c)** The selected waveforms in (b) are shown in red (left panel). These waveforms are aligned in the right panel and their "arrival" times are selected manually (vertical solid line). **(d)** The aligned waveforms in step (c) are used in the inversion and two example deconvolved source time functions at 84.0 km and 88.0 km depths are plotted. The user should select the most physical source time function (simple shape and non-negativity of the inverted STFs). **(e)** Two beachballs show the focal mechanism of the event as reported by NEIC compared to the inverted moment tensor using this workflow. Note that NEIC reported 84 km for the depth of this event.

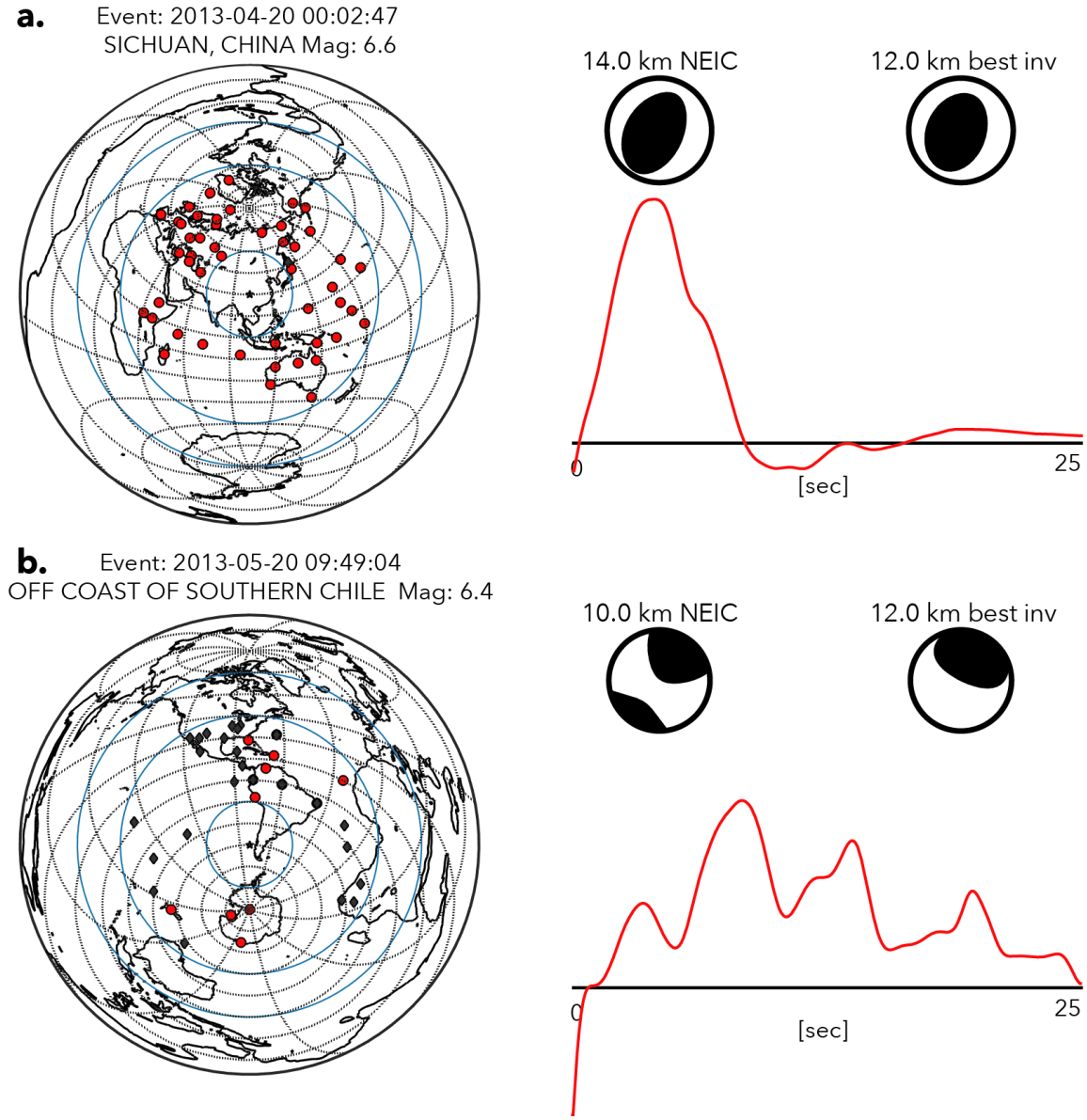

Figure 4.4: Example of two shallow events. **(a)** Earthquake on the 2013/04/20 in Sichuan, China with a magnitude of 6.6 and NEIC Depth of 14.0 km and the updated depth of 12.0 km. **(b)** Earthquake on the 2013/05/20 off the coast of Southern Chile with a magnitude of 6.4 and a NEIC depth of 10.0 km. Depending on the magnitude, duration of the earthquake and station distribution the shape of the STF can become boarder, narrower or more complicated.

waveforms of OBS stations was done by Stähler et al. (2016a). They reported high noise in most OBS. The comparison between INSU and DEPAS instruments showed a lower self-noise for the French OBS. While hydrophones recorded reliably, they were afflicted by high reverberations. All in all, OBS data showed a higher noise level compared to island or land stations, as expected.

Earthquakes and Source Time Functions

During the period of the RHUM-RUM deployment (25.09.2012-05.12.2013), 177 global earthquakes with magnitude >6mb and 57 local earthquakes in the Indian Ocean with a magnitude between 3 and 6 were recorded. I selected 635 earthquakes from the NEIC (National Earthquake Information Center) catalogue that occurred between 2011 and 2016 with magnitudes higher than 6mb. These events are all within a teleseismic distance (32°-85°) from the RHUM-RUM stations, and their observed seismograms were used in the P-wave multifrequency measurements (see Section 4.3).

In this study, source time functions for all 635 events were determined from teleseismic P waves (only global seismic stations - no RHUM-RUM stations) using the method of Sigloch and Nolet (2006) and were subsequently used to calculate predicted seismograms at all distance ranges (see Section 4.3). As an important side benefit, our source-inversion algorithm yields significantly more confident depth estimates than routine catalogue determinations, which afflicted by large uncertainties (e.g., Figure 4.3 and 4.4; Hosseini, 2016). The depth parameter is of great importance, because it improves the spacing of pulses (e.g., P, pP and sP), which is a non-linear effect, in synthetic waveforms (or matched filter), even for waveform tomography at relatively lower frequencies, where source time functions are somewhat less critical Hosseini (2016). The STF broadens and modulates the pulses when convolved with the Green's function (e.g. Figure 3.4). On the downside, STF determination is currently the bottleneck of our processing chain because it requires the most human supervision.

Our workflow for seismic source inversion is depicted in Figure 4.3 (and is placed in the context of the wider multifrequency tomography workflow in Figure 4.2). As

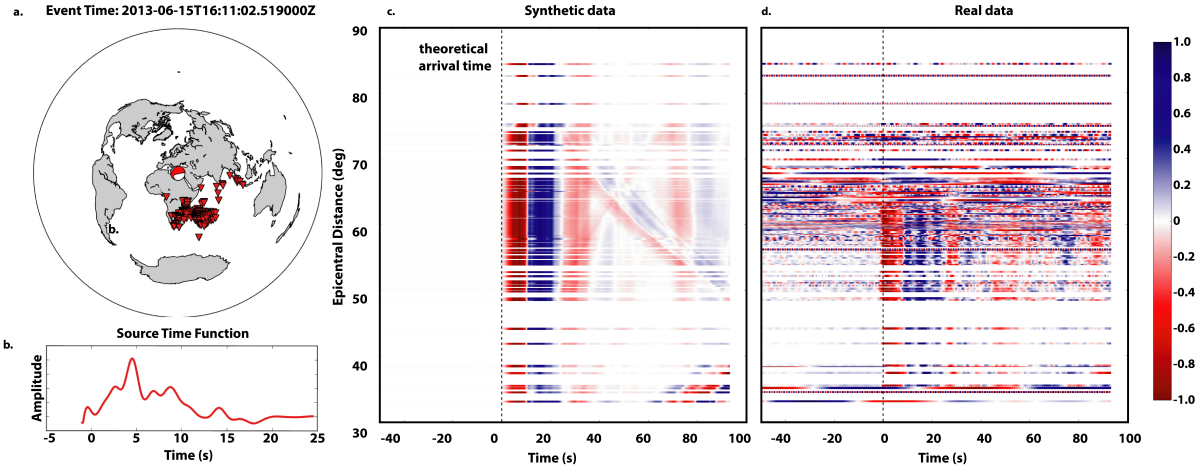

Figure 4.5: Modelled versus observed broadband seismograms of teleseismic P waves. Each line shows the vertical component of the seismogram with a normalised RMS amplitude, from 50 before to 100 seconds after P arrival; positive samples are blue, negative samples are red. **(a)** Station locations for an event in Crete, Greece (2013-06-15T16:11:02.519000Z; Mw 6.3). **(b)** Estimated source time function of the event. **(c)** Synthetic waveforms sorted by epicentral distance and aligned on their theoretical P arrival times. **(d)** Observed real data, notice how signal-to-noise ratio decreases by epicentral distance.

shown in Figure 3.4 the convolution of a Green's function with an estimated source time function results in a synthetic waveform. Hence, any uncertainty in the STF propagates through the cross-correlation measurements (Section 4.3) into the tomography inversion. Stähler and Sigloch (2014) have investigated this issue for P waves, estimating not just uncertainties in the STF but also how they propagate into traveltime delays, including correlations of errors. In a nutshell, these uncertainties are noticeable but can be estimated, and they can be used to properly fill the measurement covariance matrix for tomography. However, as the codes for fully probabilistic seismic source inversion are still under-development, we decided to use a diagonal measurement covariance matrix (i.e., uncorrelated measurement errors) for our inversions. We intend to adapt the workflow to incorporate these uncertainties into the covariance matrix.

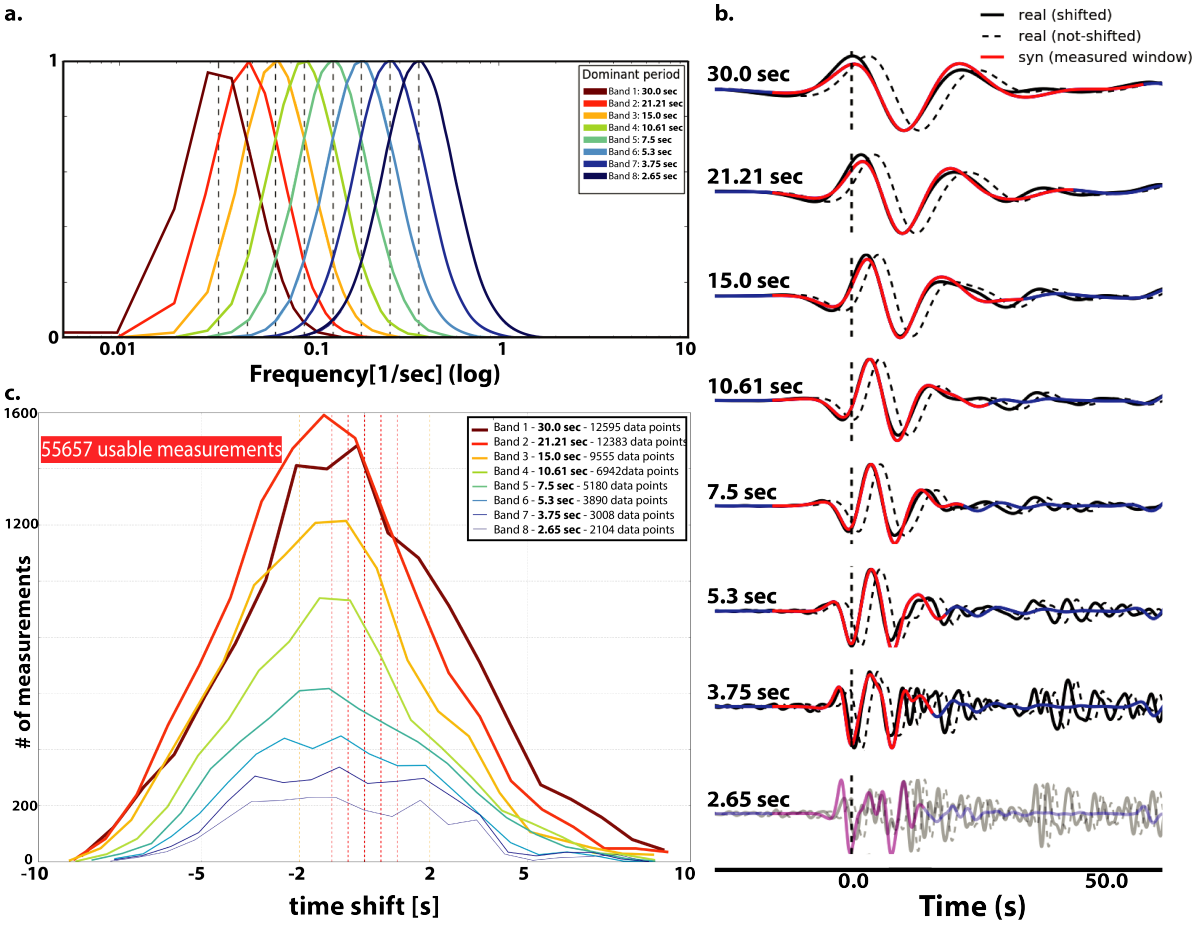

Figure 4.6: Multifrequency measurements. **(a)** Eight Gabor filters in frequency domain with dominant periods 30.0, 21.21, 15.0, 10.61, 7.5, 5.3, 3.75 and 2.65 seconds. The dominant period is calculated by subsequently dividing the lowest frequency band by $\sqrt{2}$. Warm colours demonstrate low frequencies and cold colours high frequencies. The width of the Gaussian filter is the same for all bands. **(b)** Example for multifrequency measurement for one station. Notice the increasing frequency content in the waveforms towards the bottom. Dashed line shows the real waveform, the blue-red line is the synthetic waveform where red indicates the cross-correlation time window. The solid black line shows the real corrected for the measured traveltime residual. The greyed-out waveform at the bottom is a not successful measurement (here $cc < 70\%$). **(c)** Histogram of high-quality measurements (including permanent stations) between 2011 and 2016 (without Pdiff or ISC-EHB/EHB). Low frequency bands have a higher number of successful measurements compared to the higher bands.

4.3 Inversion framework

Multifrequency measurements

Predicted broadband seismograms for one earthquake are computed by convolving the STF (Section 4.2) with the broadband Green's functions calculated up to 1 Hz by the fully numerical wave propagation tool AxiSEM (Nissen-Meyer et al., 2014). The waveforms are calculated for the spherically symmetric velocity model IASP91 (Kennett and Engdahl, 1991) using density and attenuation values from PREM (Dziewonski and Anderson, 1981). Figure 4.5 compares broadband synthetic seismograms and broadband observed data for a magnitude 6.3 Mw event in Greece. Each line in panels (c) and (d) of Figure 4.5 shows a seismogram (vertical component) of normalised RMS amplitude around the predicted teleseismic P arrival time (vertical dashed line).

Figure 4.6(b) shows eight filtered observed waveforms (dashed black line) compared with the corresponding filtered synthetic waveforms (solid red line). Our filter bank with eight Gabor filters is shown in Figure 4.6(a). Traveltime residuals in different frequency bands are extracted by cross-correlating the real and synthetic waveforms. This method was applied to a large dataset of teleseismic P waves, and histograms of multifrequency traveltime anomalies are shown in Figure 4.6(c). As the frequency increases, it becomes more and more difficult to successfully fit real and synthetic seismograms (e.g., waveforms filtered with centre periods of 3.75 and 2.65 s in Figure 4.6(b) and (c)). I do not analyse shorter than 2.7 s dominant period. When the signal is dominated by shallow reverberations, uncertainty in source time function and attenuation.

In a planet with lateral velocity variations, traveltime shifts of teleseismic P waves become dispersive, provided their wave lengths are of the same length scale as the mantle heterogeneity they interact with Nolet and Dahlen (2000). Figure D.9 demonstrates in an example dispersive behaviour throughout all frequency bands for 4 stations (two OBS and two land) for an event in Sichuan, China (Figure D.8). For a given wave path, the frequency dispersion between the low and high frequency bands can be up to one second.

55,657 multifrequency P measurements are used in the inversion. The mean time shift is ∼-0.5 s (correspond to faster velocities) for almost all frequency bands. A priori uncertainty factor was assigned to each measurement according to the cross-correlation factor in each band, as follows:

cc [%]	$sigma[s]$
< 60	10
60-70	2.0
70-80	1.5
80-85	1.0
85-90	0.6
90-95	0.4
> 95	0.3

The P traveltime observations are our main data source for the upper and mid-mantle. To cover the lowermost mantle, global diffracted P measurements were used form Hosseini (2016). Most Pdiff measurements cover the northern hemisphere, but a substantial number passes through the southern hemisphere and African LLVP at the CMB.

Analyst-picked arrival times from the ISC-EHB/EHB

To increase the data coverage, a global dataset of 2,342,621 traveltime picks from 8,000 events was selected from the ISC-EHB/EHB (Engdahl et al., 1998; Weston et al., 2018) database and was added to the inversion, with an assigned uncertainty of 1 second for all picks. The ISC-EHB/EHB bulletin contains data for approximately 140,000 events with millions of measurements for different seismic phases. To reduce this, I selected P arrival times with epicentral distances 30°-90°. Measurements with an arrival time reading precision >0.1 s were excluded.

Traveltime corrections

Synthetic seismograms are calculated on the spherically symmetric Earth model of IASP91 in which neither effects of the crust nor ellipticity and topography are incorporated; only a layer with constant thickness and velocity is considered as a crust. To account

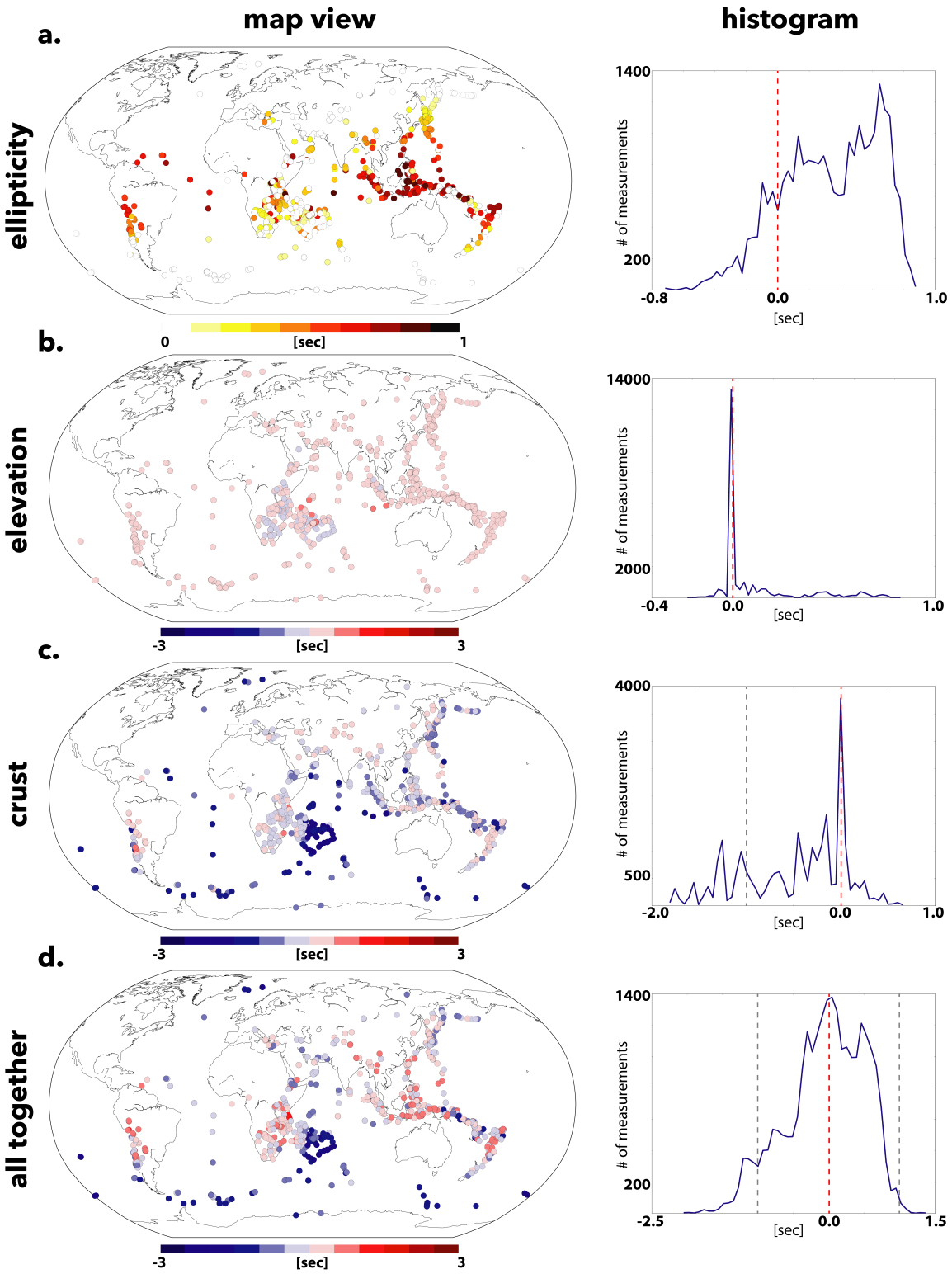

Figure 4.7: Traveltime corrections for the RHUM-RUM dataset, including temporal and permanent land stations on Africa. Circles represent stations and sources. **a.** Ellipticity corrections; **b.** elevation correction; **c.** crustal correction and **d.** sum of all corrections. Crustal corrections in the oceans have the highest values. Ellipticity corrections are highest towards the equator. The right column shows the corresponding histograms, red dashed line is located at 0 seconds and grey dashed line at ± 1.

for the known deviations from spherically symmetric earth models and to bring the predicted time closer to that of a 3-D Earth, corrections should be applied to the computed traveltimes (Nolet, 2008):

$$dt = (T_{obs} - T_{pred}) - \delta T_{cor} \tag{4.1}$$

where $(T_{obs} - T_{pred})$ is the measured traveltime anomaly and δT_{cor} is the correction term.

I use the 2°× 2° crustal model CRUST2.0 (Bassin et al., 2000) to correct for 3-D crustal structure. To account for the ellipticity effects, the Earth is approximated by an ellipsoid. Crust, topography and ellipticity corrections were applied to all the traveltime observations using the method described in Tian et al. (2007a). In case of crustal corrections this can be formulated as:

$$\delta T_{crust} = -t_{BG} + t_{3D} \tag{4.2}$$

t_{BG} is calculated according to the incident angle and the length of the ray in the crustal layer of IASP91, and t_{3D} is computed on the CRUST2.0. As shown in Figure 4.7, some corrections can reach up to a few seconds, especially in oceanic areas.

The crust has a frequency depended contribution to the traveltime delays. The frequency dependence of dt due to wave propagation in the crust is not modelled, because we apply ray-theoretical crustal corrections (Tian et al., 2007a). The expected error is small for the short wave periods (T < 30 s) used here (Ritsema et al., 2009).

Model parametrisation

The unknown global velocity structure in the mantle is parametrised by non-overlapping tetrahedrons generated by the DistMesh tool (Persson and Strang, 2004) and based on Delaunay criteria using QHULL tool (Barber et al., 1996) (Figure 4.8). In this inversion, the mesh was rendered denser in places where station coverage offered increased resolution; otherwise, node spacing increases continuously from 60 km up to 400 km at the lowermost mantle. In total, I have 56,709 unknowns (vertices or tetrahedrons).

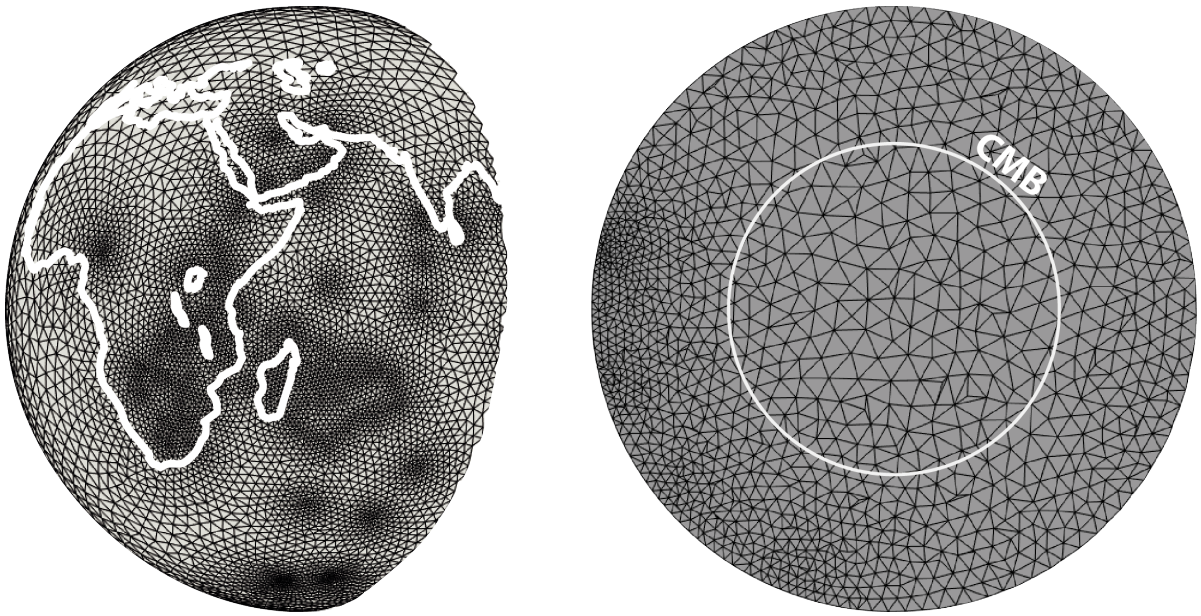

Figure 4.8: Global tetrahedral grid used for inversion. Left: view on Africa and La Réunion. Resolution of the inversion grid has increased (∼60 km edge-length) where stations were deployed. The node spacing continuously increases away from the stations. Right: At the CMB, tetrahedrons have an edge-length of around 400 km.

Sensitivity kernels

Sensitivity kernels are those parts of the wavefield that sense Earth's structure, and their 3-D geometry depends on the epicentral distance, selected time-window and the frequency content of the propagated wavefield.

To calculate cross-correlation traveltime kernels, I used the method of Dahlen et al. (2000) to compute efficiently a large number of frequency-dependent sensitivity kernels using paraxial approximation in conjunction with ray theory and the Born approximation. Each sensitivity kernel is projected on the tetrahedral inversion grid of Figure 4.8. The sensitivity kernels account for the sensitivity of a given seismic phase with a specific frequency content into the mantle. As I have two sets of traveltime observations (multifrequency measurements and analyst picked arrival times), two groups of sensitivity kernels are also calculated: frequency-dependent and ray-based kernels.

Inversion

The traveltime observations $d_i (1 \leq i \leq N)$ are linearly linked to the discretised Earth model $m_j (1 \leq j \leq M)$ in the following explicit form:

$$Gm = d \tag{4.3}$$

where each row of matrix G links all the model parameters m to one measurement in the data vector d. Elements of m in Equation 4.3 are the three-dimensional isotropic compressional P-wave velocity anomalies $\delta ln(V_p)$ with additional unknowns to account for origin time and hypocentre corrections (longitude, latitude and depth). *A priori* uncertainties were assigned to each component of the model vector as follows: 2% for $\delta ln(V_p)$, 20 km for latitude, longitude, 5 km for the depth of hypocentre corrections and 2.0 s for event origin time corrections.

A combination of norm damping and Laplacian smoothing operators was used to regularise the ill posed and non-unique inverse problem of equation 4.3. By changing the weighting of regularisation parameters, the trade-off between residual data misfit $||Gm - d||^2$ in terms of χ^2_{red} (absolute χ^2 divided by the number of data N) can be written as:

$$\chi^2_{red} = \frac{1}{N} \sum_{i=1}^{N} \left(\frac{d_i^{obs} - d_i^{pred}}{\sigma_i} \right)^2 \tag{4.4}$$

and the model norm $||m||^2$ can be analysed. In this equation, d^{obs} is the observed traveltime, d^{pred} is the predicted traveltime and σ is the a priori uncertainty assigned to the measurement (see table in Section 4.3). Figure 4.9 shows five examples of such trade-offs (L-curves) for the model. Each L-shape curve in this figure is derived by assuming a constant $\frac{damping}{smoothing}$ ratio but with different amplitudes of smoothing and damping parameters. In other words, each point of the L-curve is based on damping and smoothing parameters. Theoretically, $\chi^2_{red} = 1$ (dashed vertical line in Figure 4.9) is the optimal case assuming all σ_i (data uncertainties) are perfectly known. Unfortunately, the absolute values of data uncertainties are not known in practice, and usually, models close

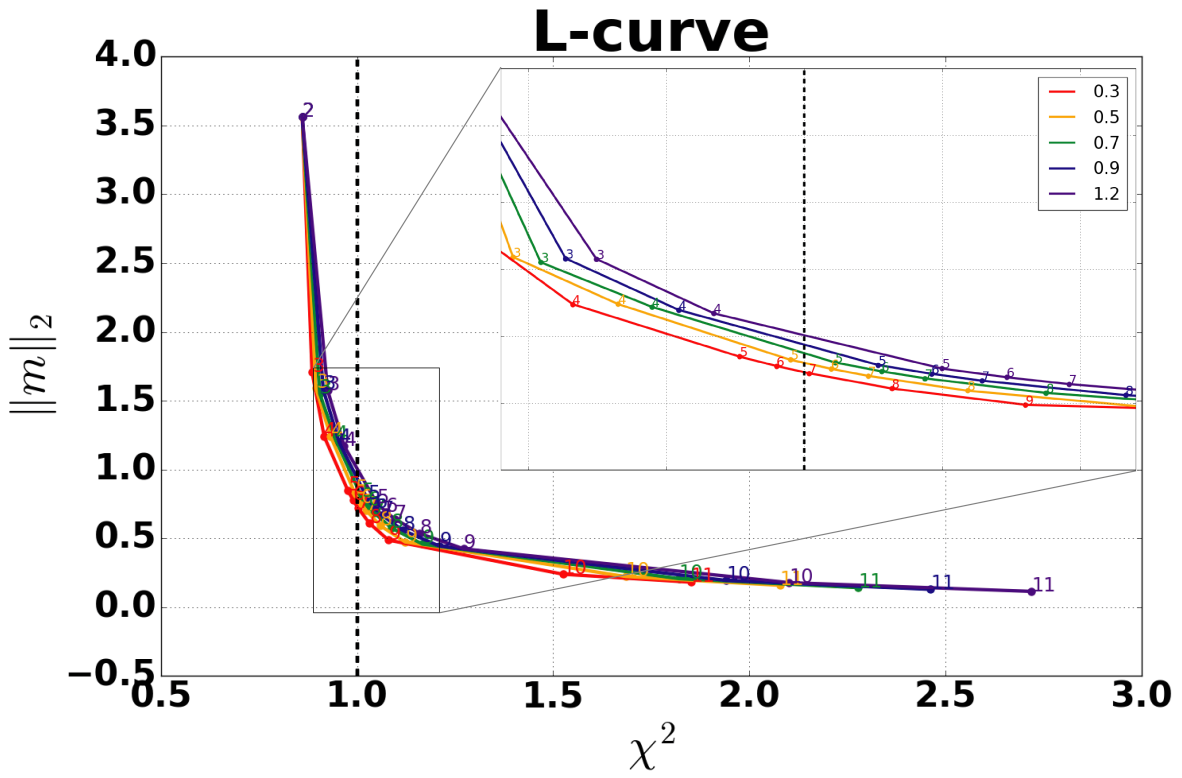

Figure 4.9: Trade-off between model norm $||m||_2^2$ and residual data misfit χ^2_{red}. The resulting L-curves are obtained by a constant $\frac{damping}{smoothing}$ ratio of 0.3, 0.5, 0.7, 0.9 and 1.2 but with different amplitudes for damping and smoothing parameters. The compromise between $||m||_2^2$ and χ^2_{red} is chosen to be the corner of the L-curves ($\chi^2_{0.3}$=0.977, $\chi^2_{0.5}$=0.990, $\chi^2_{0.7}$=1.002, $\chi^2_{0.9}$=1.032, $\chi^2_{1.2}$=1.080). Models far from the kink are either dominated by noise ("vertical" part of the curve with high $||m||_2^2$ values) or the data is poorly exploited in them ("horizontal" part with high χ^2_{red} and low $||m||_2^2$ values). The preferred model is number 7 along the L-curve with $damping/smoothing = 0.7$.

to the bending of the L-curve as the best compromise between data misfit $||Gm - d||^2$ and model norm $||m||^2$ are selected as "preferred" models.

4.4 Results

Selection of a set of "preferred" models

Figure 4.10 shows the imaged structures beneath La Réunion and South Africa along three selected L-curves of Figure 4.9. The constant ratio between damping and smoothing parameters is stated in the titles. Model complexity increases (models start to fit the noise)

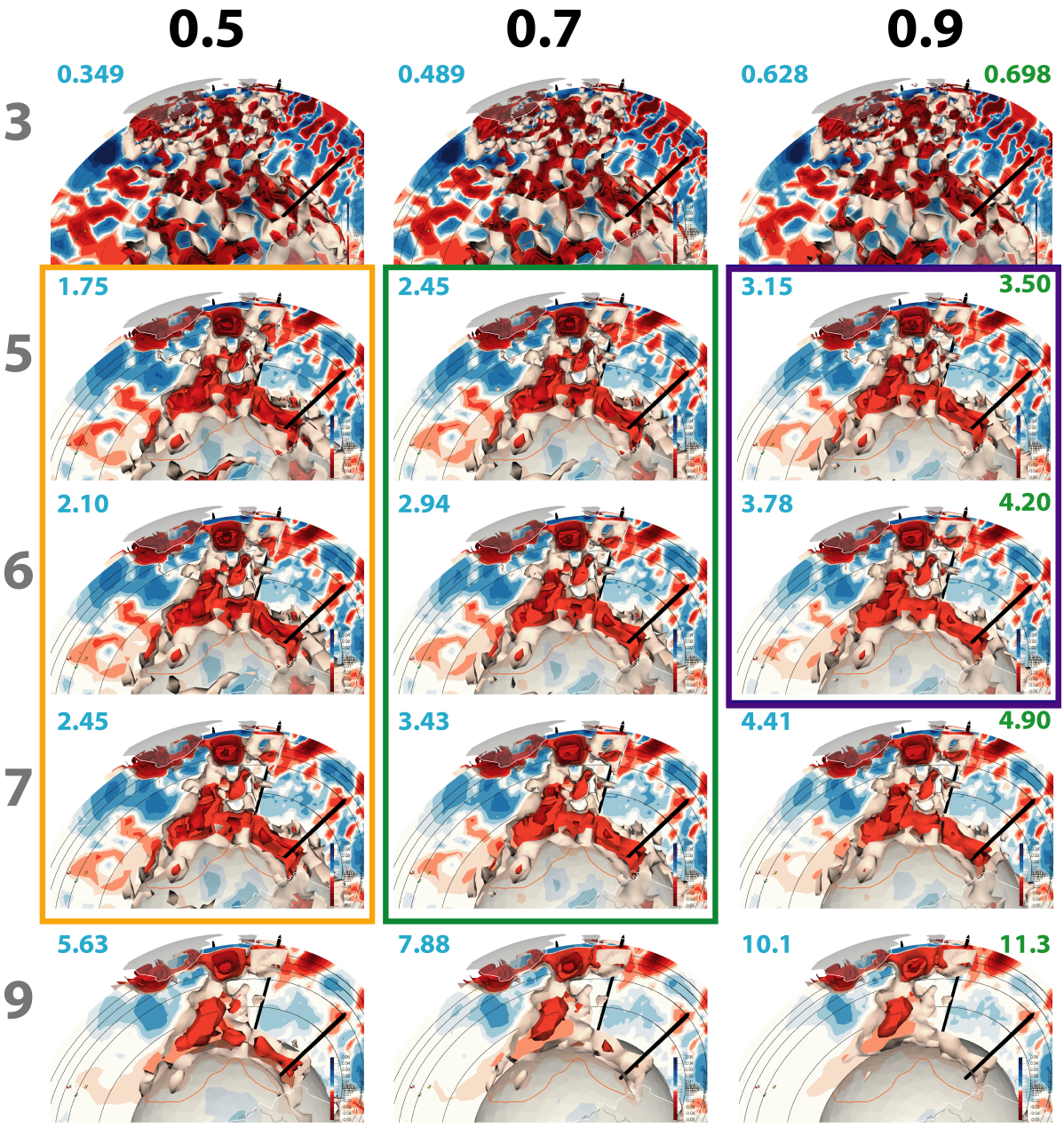

Figure 4.10: Solutions for $\frac{damping}{smoothing}$ = 0.5, 0.7 and 0.9 around the bend of the L-curves in Figure 4.9. Blue numbers are damping parameters, green numbers (valid for each row) are smoothing values, black numbers at top show the $\frac{damping}{smoothing}$ ratio. Grey numbers on the left correspond to the points along the L-curve of Figure 4.9. Coloured boxes correspond to the colours of curves in Figure 4.9. A detailed set of inversion solutions can be found in Appendix A. Seismically low-velocities are represented as red colours and fast velocities as blue colours. The view is from South (Antarctica) to North (South Africa). The black vertical columns in the cross-section mark the location of La Réunion and Kerguelen. Structures on the vertical arm of the L-curves (row 3) are incoherent with very high amplitudes, while on the horizontal arm (row 9), features are smooth and have low amplitudes. Models in the middle part (row 5, 6 and 7) show mostly similar structures.

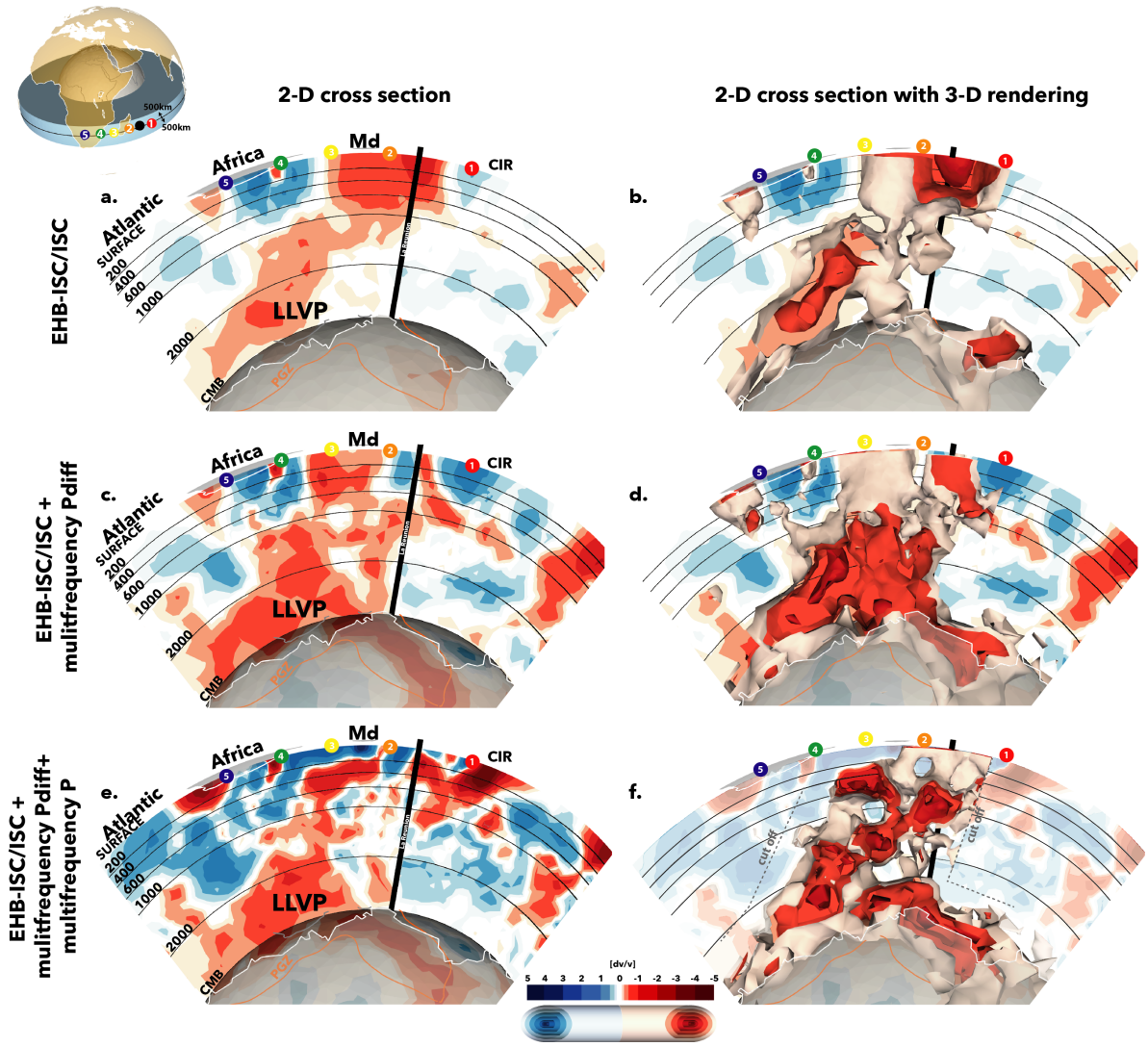

Figure 4.11: Tomography with different datasets. **(a)** An inversion with only ISC-EHB/EHB data ($\frac{damping}{smoothing} = 0.3$ and $\chi^2 = 1.1$; see Appendix A for the complete L-curve). The LLVP at the CMB is vaguely visible. In the mid-mantle, only a thin connection between lower and upper mantle is imaged. The upper mantle is dominated by one huge low-velocity structure which stretches from the Mozambique channel to CIR. This inversion resembles an over-regularised version of our preferred model in Figure 4.10 (see also Appendix A). **(b)** A joint inversion of ISC-EHB/EHB and Pdiff data ($\frac{damping}{smoothing} = 0.3$ and $\chi^2 = 0.991$). The LLVP is clearly visible at the CMB. In the mid-mantle, the low-velocities are broad and velocity amplitudes are higher compared to (a). The low-velocity structures in the upper mantle are broad and smooth. **(c)** A joint inversion of ISC-EHB/EHB and multifrequency P and Pdiff measurements. The shape of the LLVP is very similar to (b), but the mid and upper mantle are significantly different from the previous two inversions (refer to text for more discussion). Generally, the LLVP at the CMB and the sharp edge West of the LLVP are common features in all inversions. The main differences between the models show up in mid and upper mantle. **Md** - Madagascar; **CIR** - Central Indian Ridge; **LLVP** - Large low-velocity Province; **CMG** - Core Mantle Boundary.

for low χ^2 (top figures) while for high χ^2, models are much simpler and smoother (bottom figures - damped towards the background model). All models show anomalies in the lower and mid-mantle with a connection towards La Réunion and Central Indian Ridge (CIR).

The rows marked by 5, 6 and 7 in Figure 4.10 correspond to model solutions around the bend of the L-curves in Figure 4.9. I chose the model in row 7, middle column, as the preferred model. The decision was based on two criteria: first, the model has a $\chi^2 = 1.03$ which suggests that the observed data are explained by the model parameters (given the assigned a priori data uncertainties). Second, more regularised models show the same structural complexities but with lower amplitudes.

Tomography with different datasets

The RHUM-RUM data significantly enhanced the data coverage in the western Indian Ocean. Figure 4.11 shows the effects of different datasets on the resulting tomography models. In panel (a) of Figure 4.11, only ISC-EHB/EHB data is inverted which yields a smooth model. In this model, the African LLVP is visible, and it rises obliquely from the CMB to 1000 km depth (Figure 4.11a left). In the 3-D view, the LLVP is patchy, and the connection to the surface is through a thin structure at around 1200 km depth. The surface anomaly appears as a large low-velocity structure beneath La Réunion.

When adding Pdiff to the ISC-EHB/EHB dataset (Figure 4.11b), the picture changes significantly. The extent of the LLVP is now clearly visible. From 2000 km depth upwards, the structure shows broad features with little complexity in the upper mantle.

By adding multifrequency P measurements (Figure 4.11c), detailed structures throughout the mantle show up, which might be explained by the frequency dependence of the traveltimes. There are two main reasons which explain the frequency dependence of traveltimes: Firstly, quantitatively, our preferred models have reduced the residual ($||d-Gm||_2^2$) in all frequency bands. Secondly, qualitatively, by comparing the tomography model generated by the lowest frequency measurements (30 sec) with our preferred models, it is clear that high-frequency measurements have introduced smaller scale features (for both low and high velocities) throughout the mantle.

In the next section, I will investigate these structures in the preferred model – hereinafter RR-Ox19. Occasionally, I will refer to all model solutions along the L-curve as a measure of reliability of structural features.

Complex low-velocity structures beneath La Réunion

Figure 4.12a shows a cross-section through RR-Ox19 beneath La Réunion and Africa. A prominent feature is the low-velocity structure at the CMB marked as LLVP which extends up to around 2000 km depth. Close to the CMB, the LLVP stretches ∼7000 km laterally from South Africa to South Central Indian Ocean (Figure 4.12b), and it is characterised by an average velocity reduction of 1 - 2% compared to the background model (IASP91). On long wavelengths, outlines of the imaged LLVP are in agreement with the PGZ (Burke et al., 2008; Torsvik et al., 2010). The LLVP and its complexities show up in all tomographic inversions with changing $\frac{damping}{smoothing}$ ratios. The inclusion of Pdiff waves made it possible image the LLVP beneath Africa (see Figure 4.11b).

At mid-mantle the LLVP is located beneath South-East Africa (Figure 4.12a). At 2000 km depth, the model shows a low-velocity structure that branches out from the LLVP (Figure 4.10b). The resolution in the mid-mantle is very good due to the inclusion of the RHUM-RUM dataset. Additionally, the usage of ISC-EHB/EHB data constrains the surroundings of the region of interest.

To the west of the LLVP at mid-mantle a sharp edge shows up. This edge is relatively stable through model solutions using various regularisation parameters. The eastern flank shows more smaller-scale features in comparison. Interestingly, next to the sharp edge, which is also observed in other tomographic models (see Appendix C) a high-velocity structure appears.

A thin vertical low-velocity conduit emerges west of the sharp edge of the LLVP from the CMB and is stable throughout different regularisations. The data coverage in the upper mantle beneath South Atlantic is sparse, hence it is not quite clear if this feature is really only a mid-mantle plume, or part of the Tristan da Cunha mantle plume.

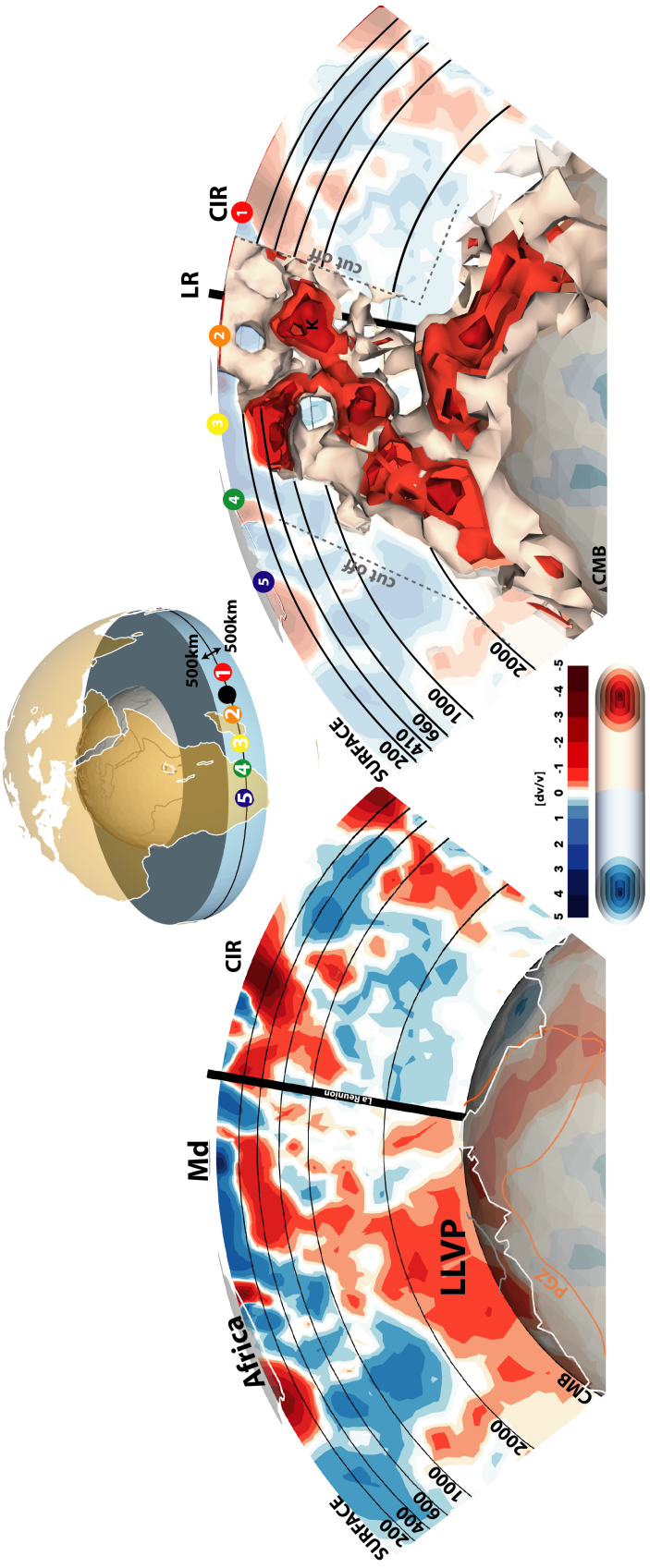

Figure 4.12: Cross-section through La Réunion and South Africa as imaged by RR-Ox19. The view is from South (Antarctica) to North. The black column marks the location of La Réunion Island. For orientation refer to the little globe in the middle. Seismically low-velocities are coloured red and fast velocities are in blue colours. Orange line at the CMB outlines the PGZ (after Torsvik et al., 2006). On the right, low-velocities are 3-D rendered (isosurfaces enclose seismically slow structures of dV_p/V_p =-0.25, -0.5, -1, -2, and -3%) in a 1000 km wide cut around the cross-section and 500 km above the CMB. For visibility, all other features are shaded and cut out. Black arrow follows the continuous low-velocities from 2000 km to La Réunion.

In the 3-D visualisation of Figure 4.12b, small-scale structures with 200-300 km radius are visible in the mid-mantle (1000-1200 km depth). One branch extends from the mid-mantle out- and upward towards the La Réunion island (marked with black arrow in Figure 4.12b). The branch shows continuous low-velocities from the LLVP to the upper mantle.

In Figure 4.12b, the thick and tilted conduit extends to ∼800 km depth. Here, a low-velocity accumulation is formed from which a thin conduit (200 km radius) branches out almost vertically to La Réunion. Resolution in the upper mantle (<400 km) is

Although the multifrequency measurements extensively sampled the mid-mantle, the resolution in the upper mantle is only good close to the stations. Therefore, the deep V-shaped connection between La Réunion and CIR may be due to the smearing of small-scale low-velocities in the upper mantle.

The overall structure of this complex whole-mantle plume is different than previously envisioned (Morgan, 1972) or imaged (Montelli et al., 2004). The shape of the La Réunion plume resembles a tree, with thick roots (LLVP), a thick stem (plume tail) with its branches reaching up and outward towards the tree crown (plume head). No vertical whole-mantle low-velocity structure is imaged directly beneath La Réunion.

Resolution analysis

For resolution tests, synthetic data vectors are constructed based on synthetic, user-defined input models and an error term (with realistic statistical properties). Solutions are then obtained through the same inversion procedure and parameter settings as for the observed data (see Chapter 3). The comparison between input and output models gives an insight into the general sensitivity of the tomography models at different depths.

I performed various resolution tests with two different noise levels (see Appendix B): **(1)** no noise and **(2)** noise using the estimated a priori uncertainties of each measurement as standard-deviation of the Gaussian noise (medium noise).

Figure 4.13 shows the inputs and outputs of a Gaussian chequerboard test (left) and a column test (right) with no and medium noise levels. The column test of Figure 4.13

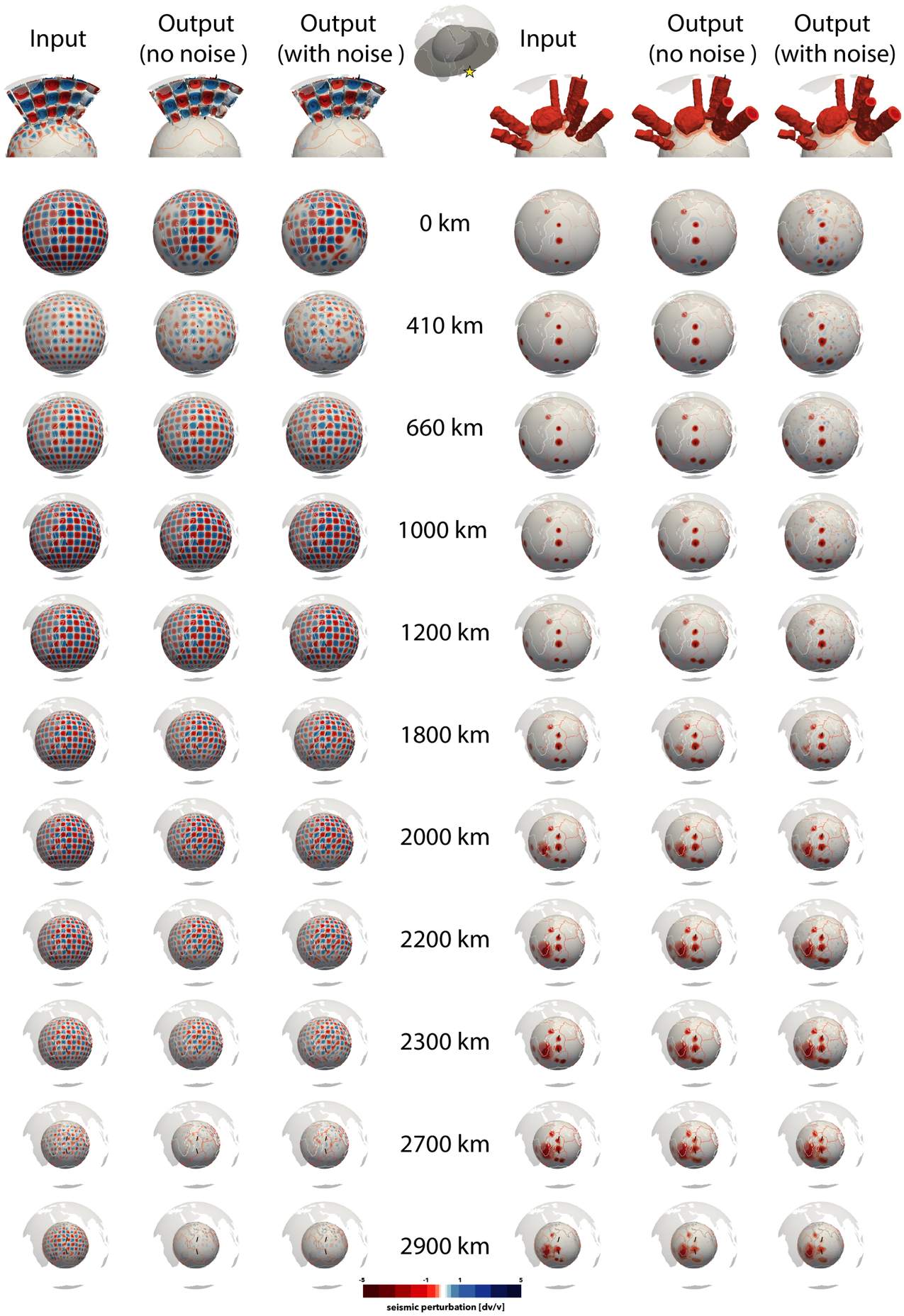

Figure 4.13: Resolution test. 2-D sections at 0, 410, 660, 1000, 1200, 1800, 2000, 2200, 2300, 2700 and 2900 km depths through input (left column) and output patterns for RR-Ox19 without and with noise. In each block of the chequerboard pattern and vertical columns, the centre has the highest velocity perturbation, and velocity profiles are extended laterally with a 3-D Gaussian function. In the top row, a 3-D visualisations of input/outputs are shown. Refer to Appendix B for more resolution tests.

shows that the preferred model has a good resolution at the CMB due to the inclusion of P-diffracted measurements. If the anomalies are smaller than the tetrahedral mesh (400 km edge-length at the CMB), these features cannot be resolved as shown in Figure 4.13 at 2700 and 2900 km depth. In the mid-mantle, the model shows high-resolution for various sizes of the input model (resolvable features down to 100 km radius) which is to be expected due to the data coverage from RHUM-RUM. Large scale features are stable in the Lithosphere (e.g. MOR), but smaller anomalies are only resolved close to stations (down to 50 km in diameter).

The column test analysis shows good resolution beneath the Indian Ocean and Afar. However, some lateral smearing appears below Kerguelen. Half plumes in the lower and upper mantle show consistent results (see Appendix B, pages 130 to 133). In the South Atlantic the model is not well resolved, as most anomalies smear with low amplitudes or vanish completely, e.g., Tristan da Cunha and St. Helena. This is, on the other hand, suggests that the applied regularisation can effectively suppress the effects of noise in the data.

In general, the model is well resolved in the mid-mantle beneath Africa, Madagascar and La Réunion. Smaller features than the inversion grid (∼400 km edge-length) cannot be resolved at the CMB, and the surface resolution strongly depends on the station location. Continuous structures (e.g., columns) are easier to resolve than alternating anomalies, for example chequerboard test and columns with alternating anomalies (see Appendix B).

4.5 Plumes and LLVPs in other models

Due to the lack of seismic instrumentation, the Indian Ocean had been sparsely sampled, and earlier tomographic studies did not have sufficient data to resolve detailed structural features in this region. Nevertheless, almost all recent global P and S tomography models are able to confirm the existence of a low-velocity province beneath Africa (Appendix C). I selected four global tomography models for comparison (2 P- and 2 S-wave). The models were downloaded from SubMachine (Hosseini et al., 2018) and were visualised

with ParaView. VM-26 in Figure 4.14 is a vote map generated out of 26 published tomography models which are specified in the figure caption.

PRI-P05 (Montelli et al., 2006) captures the LLVP and low-velocities around the MOR and La Réunion. The LLVP, consistent with RR-Ox19, concentrates into a cusp in the mid-mantle. The low-velocity connection between the upper and lower mantle is almost horizontal. Montelli et al. (2004) concluded that no vertical connection to the CMB was imaged in their model which is in agreement with this study. Their conclusion was based on the mantle structures in the close proximity of the hotspot location.

The GyPSuM (Simmons et al., 2010) model shows a larger LLVP than PRI-P05. The cone shaped structure of the LLVP is visible, but no connection to the upper mantle exists in this 3-D cross-section. The model images a shallow low-velocity anomaly in the upper mantle connecting La Réunion and the Central Indian Ridge.

Both S40RTS (Ritsema et al., 2011) and SEMUCB-WM1 (French and Romanowicz, 2014) show broad features in the lower mantle. S40RTS images a continues and tilted branch reaching the La Réunion island, but this connection is broader and more smooth than in this study. SEMUCB-WM1, on the other hand, shows no clear connection between the broad LLVP and the surface, although it extends up to 600 km depth.

The LLVP in the vote map appears in all models (26 underlying tomography models in VM-26). It rises to 1000 km depth in a broad column with a sharp edge on the western side of the LLVP. The LLVP becomes narrower towards La Réunion. However, a continuous connection does not appear in all the underlying models (see Appendix C for more model comparisons).

4.6 Conclusion

I present a high-resolution, regional tomography model in the western Indian Ocean. The model, RR-Ox19, is generated by fitting multifrequency cross-correlation traveltimes from teleseismic P and Pdiff waves as well as a large set of picked arrival times. A broad, whole mantle plume is imaged that connects the African LLVP at the CMB to the

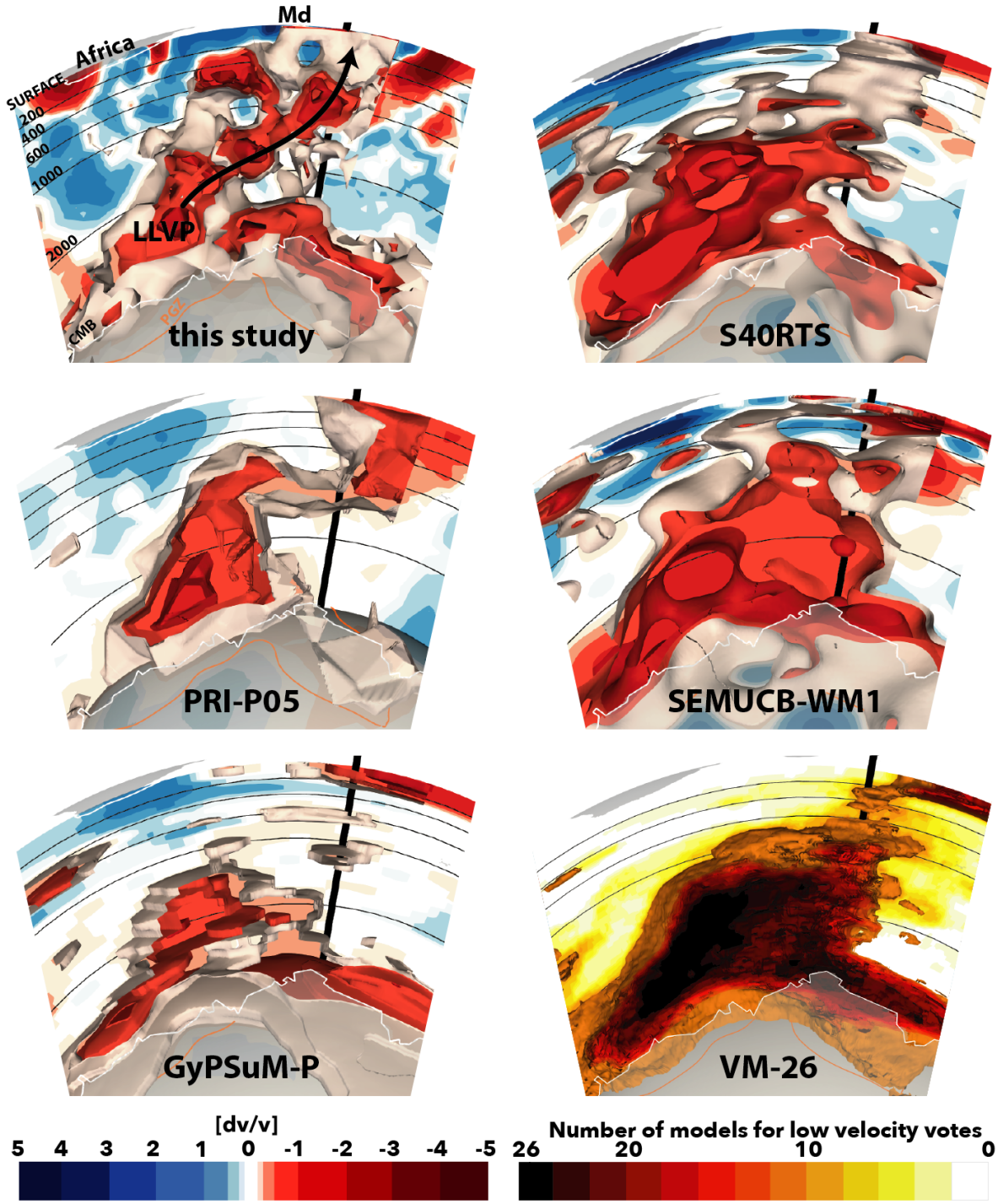

Figure 4.14: Visual comparison of RR-Ox19 (top-left) in 3-D cross-section (refer to Figure 4.12 for more details) with PRI-P05 (Montelli et al., 2006), S40RTS (Ritsema et al., 2011), SEMUCB-WM1 (French and Romanowicz, 2014) and GyPSum-P Simmons et al. (2010). Bottom right panel shows a vote map VM26 generated for 26 tomography models: GAP-P4, GyPSuM-P, GyPSuM-S, HMSL-P06, HMSL-S06, LLNL_G3Dv3, MIT2016, MITP08, PRI-P05, PRI-S05, s10mean, S20RTS, S40RTS, S362ANI+M, savani, SAW642ANb, SEMUCB-WM1, SEMum, SGLOBE-rani, SP12RTS-P,SP12RTS-S, SPani-P, SPani-S, TX2011, TX2015 and UU-P07. See SubMachine (Hosseini et al., 2018) for more information on the tomography models and Shephard et al. (2017) on vote maps. On long wavelengths, geometries of the imaged structures are similar but differ significantly between the models on smaller scales. The LLVP is visible in all models, but the connection between LLVP and La Réunion island is less defined except in S40RTS and PRI-P05 which are visually the closest to RR-Ox19 (refer to Appendix C for more model comparison).

surface. The imaged structures are more complex than previously envisioned. RR-Ox19 shows a tilted low-velocity branch from beneath South Africa towards several hotspots in the Indian Ocean. The model is consistent with previous studies in terms of "fat" (diameter 500–800 km) plumes in the lower-mantle but reveals sharper outlines for these complex features. It also images structures in the transition zone and upper mantle beneath the Réunion hotspot and surroundings in great details.

An experiment is a question which science poses to Nature, and a measurement is the recording of Nature's answer.

—Max Planck

5

La Réunion hotspot: a plume among a plume cluster?

Contents

5.1 A new regional tomography model for the western Indian Ocean 70
5.2 Results & observation of a plume cluster 70
5.3 Comparison with other models 74
5.4 Discussion 76

In this chapter, I further examine the complex mantle structure beneath the western Indian Ocean seen in the regional high-resolution P-wave tomography model, presented in Chapter 4. The model reveals a low-velocity structure which I interpreted as an upwelling rooted in the African LLVP in the lowermost mantle. At around 800 km above the CMB, several branches are tilting up- and outward from a central cusp which, in a tree-like arrangement, connecting to the hotspot locations of La Réunion, Afar, Comoros, Kerguelen and possibly Crozet and Bouvet. I discuss these mantle connections, which mirror long-standing geochemical observations across Indian Ocean hotspots and compare this result to existing global tomographic models.

5.1 A new regional tomography model for the western Indian Ocean

State-of-the-art tomographies image broad velocity anomalies in the lower mantle with complex upper mantle structures (Ritsema et al., 1999; Montelli et al., 2004; Hansen et al., 2012; French and Romanowicz, 2015). This suggests either current seismic tomography techniques cannot image small-scale features in the lower mantle or that the concept of thin plume-tails is too simplistic to explain the structures in different tomographic models.

Since mantle plumes are mostly located beneath oceans, where seismic instrumentation is extremely limited (Simmons et al., 2012), regional seismic tomography models using only island stations cannot image the structure through the whole mantle (e.g., Wolfe et al., 1997; Maguire et al., 2018). Plume experiments like PLUME Polynesia, PLUME Hawaii and ISOLDE (Tristan da Cunha experiment as part of the SAMPLE project) were able to increase data coverage in the upper mantle but not in the lower-third of the mantle (Barruol, 2002; Wolfe et al., 2009; Suetsugu et al., 2009; Schlömer et al., 2017b). By increasing the network aperture, like in the RHUM-RUM experiment, mantle plumes areas can be detected to test Morgan's hypothesis.

5.2 Results & observation of a plume cluster

Figure 5.1 shows 3D rendered low-velocities beneath the western Indian Ocean, where the LLVP stretches ∼7000 km laterally (from South West Africa to South Central Indian Ocean) and rises 900 km above the CMB. It is characterised by an average velocity reduction of 1 - 2% relative to the background model (IASP91) and is in good agreement with other global P and S tomography models (e.g., S40RTS, PRI-P05; see Chapter 4). The inclusion of P-diffracted measurements improved the resolution of the lower-third of the mantle and shows that P and S models can detect the huge low-velocity anomalous structures at the CMB equally well (Garnero et al., 2016).

In Figure 5.1, the LLVP narrows upward beneath South-East Africa at ∼2000 km depth, and a branch of slow material extends out- and upward towards Réunion. The

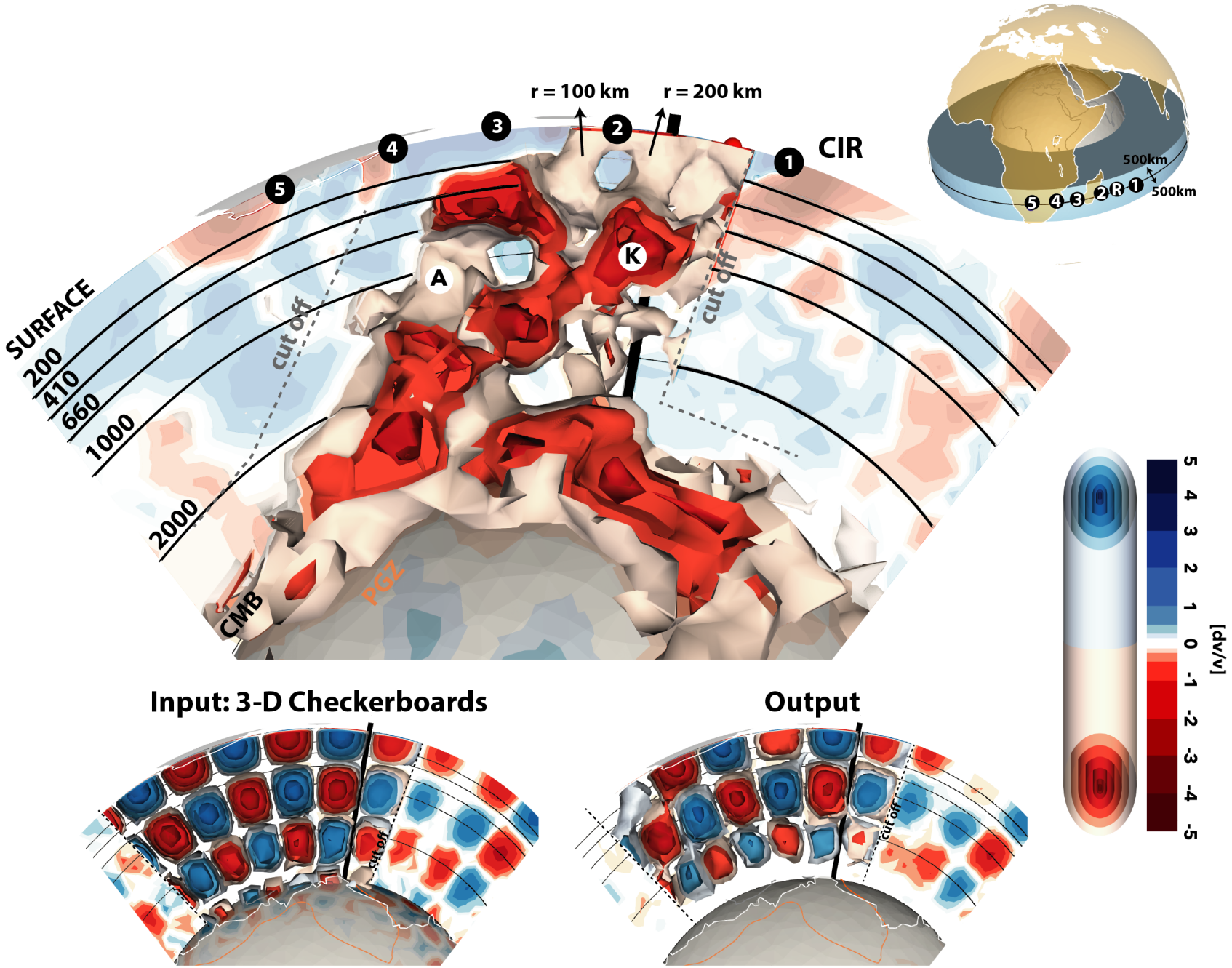

Figure 5.1: Tomographic cross-section and chequerboard resolution test (right); for details of the 3-D visualisation refer to Figure 4.12. **A** - Afar and **K** - Kerguelen in the left panel show the locations where their branches split off. In the chequerboard resolution test, noiseless synthetic traveltimes were created and inverted using the same inversion scheme as for the observed data (see Appendix B for other resolution tests).

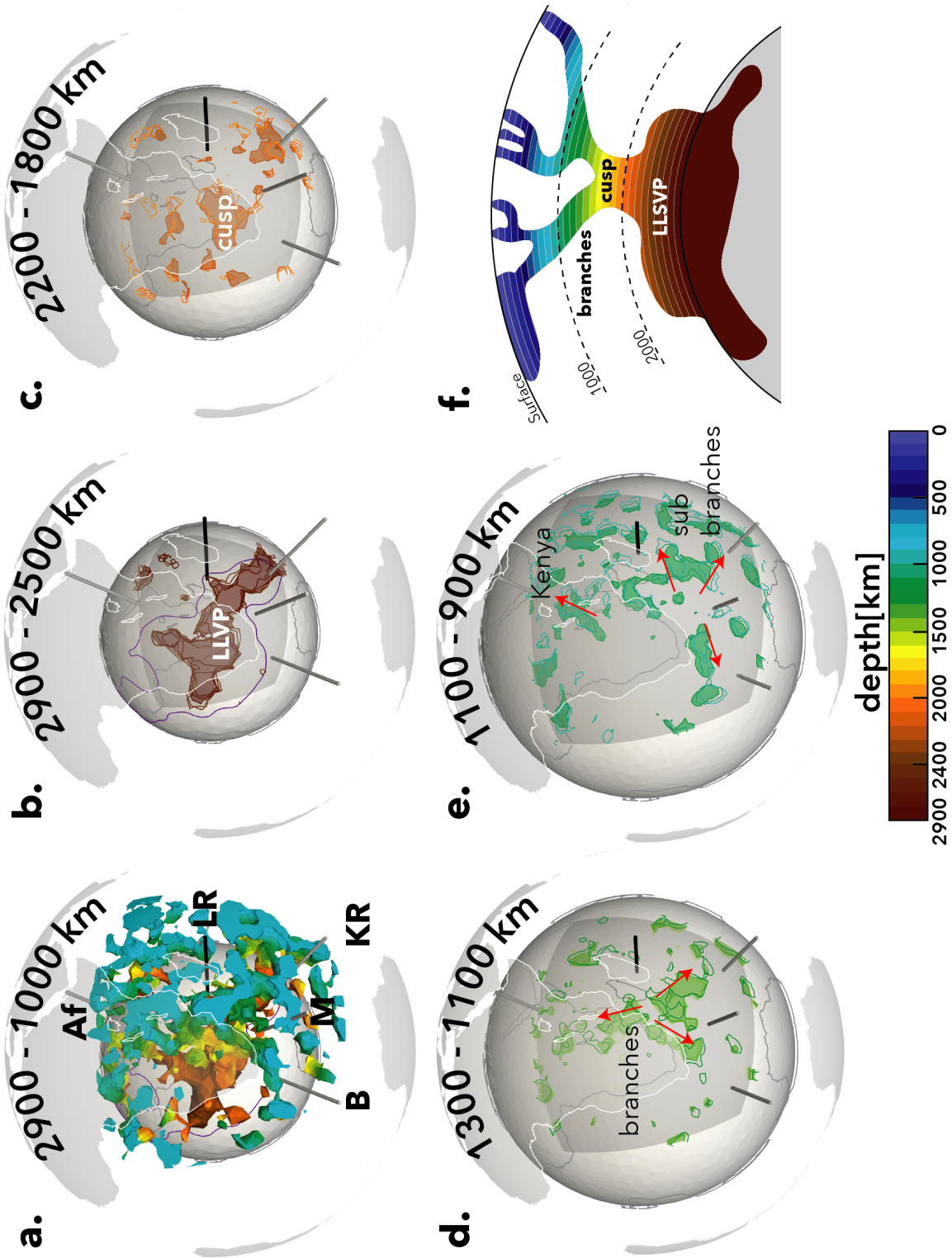

Figure 5.2: 3-D depth slices through the tomographic model. Low-velocities with $dVp/Vp < -0.3\%$ are rendered, creating 3-D isosurfaces. The colouring is according to depth (not amplitude). Dark grey area at each depth slice represents the borders of 3-D rendered structures and extends from lower left corner with lat/lon: -55°/-20° to upper right corner with lat/lon: -12°/50°. **a.** Whole mantle structure as seen from a satellite view with hotspot locations marked with black columns: **Af** - Afar, **LR** - La Réunion, **KR** - Kerguelen, **M** - Marion and **B** - Bouvet. **b.** Depth slices through the volume projected into the corresponding depth range. Extent of the LLVP is in agreement with PGZ (violet outline) at the CMB. **c.** The LLVP narrows towards mid-mantle to form a cusp. **d.** Branches start to spread out- and upward from the cusp (red arrows show direction of out- and upward spreading). **e.** Thicker branches of the LLVP extend towards directions of Afar, La Réunion, Kerguelen, possibly Bouvet and thinner branches connect vertically to hotspot locations. **f.** Schematic cartoon of the imaged mantle structure.

branch is 400 km in diameter and 0.5 - 1.5 % slower with respect to the background model. From 2000 to 600 km depth, the branch has the same thickness but at shallower depths, it starts thinning. The structures in the mid-mantle depths (2000 - 600 km) are well resolved (see Figure B.1 to B.23 for resolution tests).

At shallower depths (<600 km), low-velocity anomalies become thinner compared to the mid-mantle branches. This transition in thickness happens between 1000 and 600 km depth, where low-velocity material seems to pond. From this depth, semi-vertically thinner branches emerge which extend to the surface. Their radii are between 100 km (East of Madagascar) and 200 km (SW beneath La Réunion) (Figure 5.1). The connection to CIR shows up as a V-shape structure, however this feature could result from downward smearing where no station coverage is present. Overall, the model images small vertical branches that spread in the upper third of the mantle (see Figure 5.1 right).

By contouring the low-velocity structures ($\delta ln(V_p) < -0.3\%$) and colouring the structures for depth, Figure 5.2 illustrates the complex 3-D geometry and connectivity of the various plumes in the whole mantle range. Figure 5.2b demonstrates the extend of the LLVP and its agreement with the PGZ at the CMB (Torsvik et al., 2006). The LLVP gathers at mid-mantle depths (Figure 5.2c) to form a cusp from which branches spread out- and upward (Figure 5.2d). La Réunion seems to share one branch with Kerguelen (Figure 5.2e). At 1000 - 600 km depth, the branch is spreading out and separates into two sub-branches. One sub-branch extends northward into the upper mantle, while the other sub-branch extends South towards Kerguelen. At shallower depths (<600 km), branches narrow and vertically connect to the hotspot locations (Figure 5.2f) or in the case of Afar, the branch spreads along the East African rift down to a depth of 600 km.

Exploring the wider area of the western Indian Ocean in the 3-D rendering images, it becomes apparent that La Réunion may be considered as a plume among a wider plume cluster. The Afar plume displays tilting from the LLVP towards North, which was already observed in previous studies (Ritsema et al., 1999; Hansen et al., 2012). Other visible branches radiate south-westward towards the Bouvet hotspot (Figure 5.2e)

and northward beneath the Mozambique Channel. However, these connections are less well-constrained due to limited resolution and station coverage in these areas.

Figure 5.2 also demonstrates the vertical evolution of the imaged low-velocity structures in the mantle beneath the western Indian Ocean. The LLVP can be viewed as the roots and trunk of a tree (Figure 5.2b). The cusp is located in the mid-mantle depths (Figure 5.2c) from where the branches start spreading out (Figure 5.2d and e). The crown in the upper mantle, where we observe a relatively high number of small-scale low-velocities, connects the thicker branches of the mid-mantle vertically to the surface. The RHUM-RUM tomographic model extends the common view of "one plume per hotspot" (e.g., Montelli et al., 2004) to a plume cluster feeding several hotspots, at least in the western Indian Ocean.

5.3 Comparison with other models

In the previous section, I showed that low-velocity deep mantle structures do not form necessarily simple vertical conduits. Simple 2-D cross-sections and depth slices usually found in publications cannot fully capture all the structural details. This can lead to misinterpretation as these excerpts do not take into account all the relevant 3-D complexities. Here, I base the comparisons and interpretations on the 3-D rendered images of Figure 5.3.

Montelli et al. (2004) argued that the Réunion plume does not have a vertical connection between the crust and the CMB. Analysing their model in the same way as in Figure 5.2 shows that similar structures are imaged as in RR-Ox19. Figure 5.3 (second row) shows an extensive LLVP at the CMB imaged in PRI-P05 (Montelli et al., 2004) which narrows upwards. At 1300-1100 km depth, branches (less defined than in RR-Ox19) are spreading towards the north and south. The 3-D rendered model in the first row (RR-Ox19) shows another branch splitting of towards south of Madagascar at roughly 1300 km depth, which further connect upwards to La Réunion (marked with red circle).

Using the same visualisation for two other models S40RTS Ritsema et al. (2011) and SEMUCB-WM1 French and Romanowicz (2014) reveals similar results. S40RTS has a

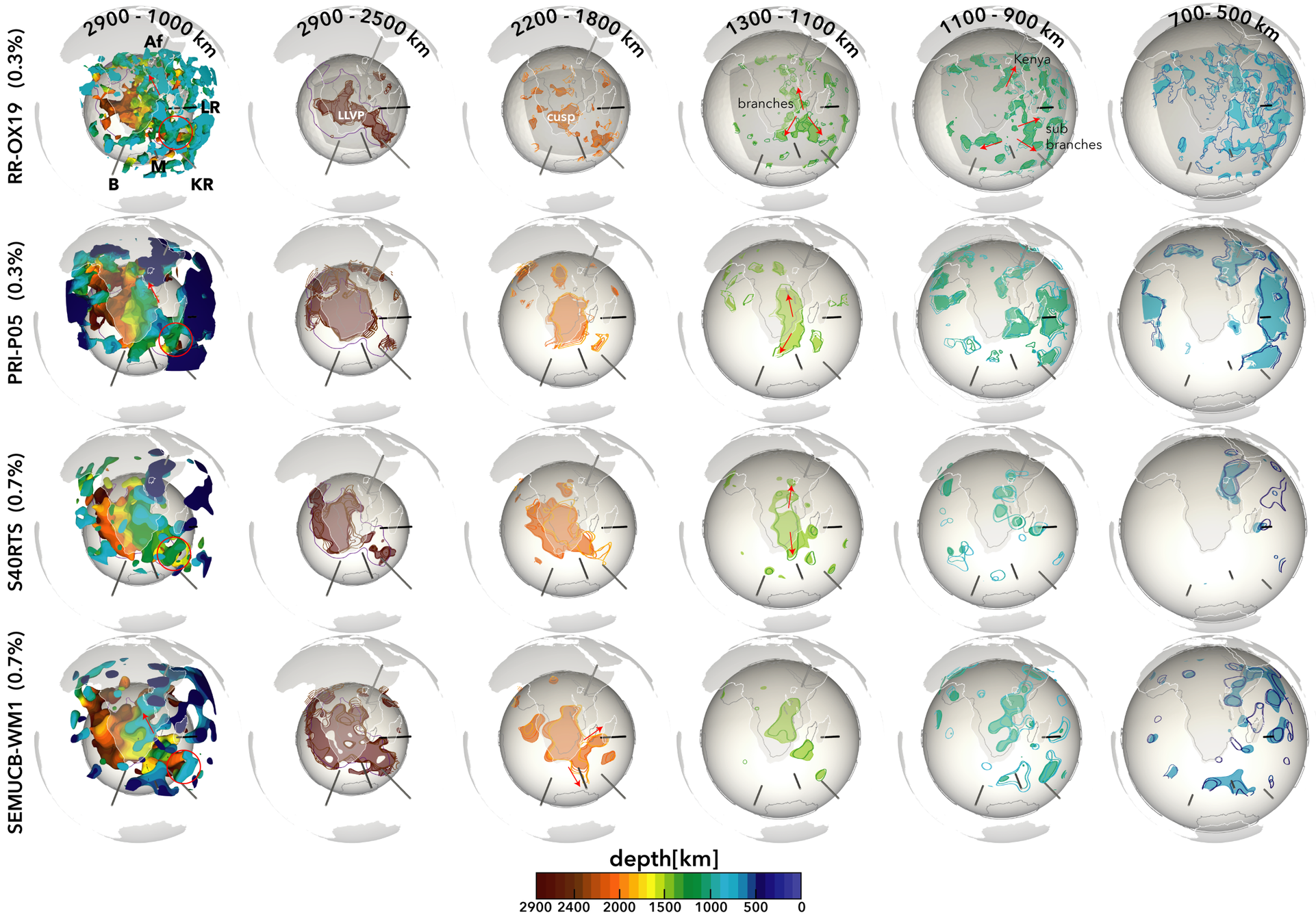

Figure 5.3: The model (RR-Ox19) compared to three global tomographic models sliced in the same way as in Figure 5.2. **PRI-P05** from Montelli et al. (2004) was rendered for $dVp/Vp < -0.3\%$. **S40RTS** from Ritsema et al. (2011) rendered for $dVs/Vs < -0.7\%$. **SEMUCB-WM1** from French and Romanowicz (2014) rendered for $dVs/Vs < -0.7\%$. The 3-D images are more informative for the upper mantle since some structures might not be present at the exact same depth slices in all models.

broad LLVP at the CMB which rises broadly to 2200-1800 km depth. This structure is wider compared to RR-Ox19 and PRI-P05, because S-waves are more sensitive to low-velocity structures. At 1300-1100 km, broad branches spread to the north and south, similar to PRI-P05. The low-velocity structure at ∼800 km is located in the same area as in our model and PRI-P05 (Figure 5.3, first column - red circles). SEMUCB-WM1 shows a ponding structure beneath South Madagascar, but this model is broader compared to the other three models. Interestingly, all models show a low-velocity emerging beneath the Mozambique channel.

In general and on long wavelengths, similar features are visible throughout the selected models. The first-order observation is that the structures in all presented models in Figure 5.3 are not simple conduits, solidifying the idea of a more complex, possibly tree shaped structure.

5.4 Discussion

Our model does not reveal a simple vertical plume that rises from the LLVP to the hotspot location. The La Réunion plume forms a cluster with other plumes (e.g., Afar and Kerguelen) in the mid-mantle; the tilted and thick conduits connect to the hotspots at the surface, which still overlie the edges of the LLVP. Compared to other mantle plumes, Afar is a well-studied and illuminated low-velocity feature as it is located directly beneath NE Africa. Tomographic models already displayed a tilted branch and a smeared low-velocity structure beneath the East African rise connecting to the LLVP (Figure 5.2d and Appendix C). Kerguelen is not as well illuminated, due to its remote location and sparse data coverage, and it shows increased structural complexity compared to the other plumes in the cluster (see Appendix C).

Another prominent feature of the model is the sharp edge to the west of the LLVP at mid-mantle depths. This edge is relatively stable throughout model solutions and is also observed in other tomographic models (see Appendix C). This feature should be well-resolved in our model according to the resolution tests (see Appendix B) and it is

located directly beneath the African continent where we have a good coverage. Two questions arise from this observation: Is this high-velocity feature causing the sharp edge and why is it imaged in that part of the mantle?

All tomographic models capture the sharp edge of the LLVP (see Appendix C), regardless if the models can image the high-velocity structure or not. The existence of a sharp velocity gradient might explain this agreement between models. Since Africa was relatively stable over a long period of time in space (Torsvik and Cocks, 2013) with no obvious subduction zones around, it seems unlikely that the high-velocity is a remnant of a slab in the mid-mantle above the LLVP, but not too far-fetched (e.g., Simmons et al., 2015). Another possibility is that the observed high-velocity anomaly is a "failed" plume, if the mantle plume consists of chemically heavier material, after cooling off, it will become denser than the ambient material and eventually sink back (Kumagai et al., 2008). In the future, a forward modelling analysis similar to Ni et al. (2002) could be conducted using high and low velocities next to each other to simulate these structures and evaluate their robustness with seismic waveforms.

Another important question at hand is whether the imaged plume cluster has persisted through time or is it capturing just a moment in the plume evolution? Three main surface observations in the western Indian Ocean provide clues to how the mantle may have evolved with time.

First, a new branch (of the plume cluster) seems to have formed from the cusp every ∼30 m.y. This interpretation is based on the regular occurrence of oceanic islands in the western Indian Ocean: Kerguelen erupted roughly 120 m.y ago (recently dated at 119–109 Ma by Coffin et al. (2002)), Marion 90 m.y ago (probably a sub-branch of Kerguelen, e.g., Steinberger and Torsvik, 2012), La Réunion at 65 m.y (Courtillot et al., 1986; Duncan and Pyle, 1988) and Afar at 30 m.y ago (Hofmann et al., 1997). This plume family likely broke up Gondwana (134-31 Ma, e.g., Torsvik and Cocks, 2013).

Second, a link between Indian Ocean hotspots has long been suggested by geochemical observations of common and regionally distinct isotopic characteristics (Pb-Sr-Nd) (Dupre and Allegre, 1983) for ocean island basalts, the so-called DUPAL anomaly. The Indian

Ocean DUPAL anomaly and OIB record (from Kerguelen, Marion, Bouvet and Tristan da Cunha) are associated with the LLVP (Castillo, 1988) and the plume cluster. The imaged, tree-like structure suggests a joint source region (cusp) for low-velocity material which surface in hotspots across the tree's "crown" (together forming the DUPAL anomaly).

Third, the cusp region may have caused South Africa's steeply-rising high plateau (roughly 1 km above the sea level), a major topographic anomaly which can be explained by long wavelength lower mantle anomalies (Colli et al., 2016). The high topography of southern Africa is supported by an anomalous low-density structure in the lower half of the lower mantle (Lithgow-Bertelloni and Silver, 1998; Gurnis et al., 2000). The area also experienced episodic uplift and subsidence throughout time (Doucouré and de Wit, 2003), which could be explained by a vertical movement of the cusp (e.g Kumagai et al., 2008).

The Indian Ocean plume family forms a cluster with a common connection point at 2000 km depth under South Africa, which is much more localised than previously envisioned (Figure 5.2c). Tomography provides a blurry snapshot of mantle convection; and it is ambiguous whether the upward-tilting branch maps out the trajectory of upwelling rock masses or whether its shape is dynamically stable over time. In the latter case, the Indian Ocean plumes would clearly not rise from the edges of LLVPs but rather from a central cusp and propagate in a tilted ascent. These structures should be stable over an extended time to be able to explain all surface observations and the tomographic model. However, the stability of tilted branches is contradictory to numerical studies (Steinberger and O'Connell, 1998), which suggest that such structures could survive not longer than 100 Ma. In both cases, the LLVP should be (relatively) stable spatially since magmatic episodes started as early as 180 Ma (Torsvik and Cocks, 2013).

The only question of interest is
"Is the model illuminating and useful?".

—George Box, 1979

6

S-wave tomography beneath La Réunion: preliminary results

Contents

6.1 Data **80**
6.2 Tomography models **83**
6.3 $\frac{\delta V_s}{\delta V_p}$ **ratio** **85**
6.4 Discussion and outlook **87**

In this chapter, I present a preliminary regional S-wave tomography model embedded into a global tomographic inversion for the mantle structure beneath La Réunion. The model is made using three different datasets: 45,056 multifrequency waveform measurements from the RHUM-RUM experiment, supplemented by 145,546 S measurements from S40RTS and 133,925 picked S-phases from ISC-EHB/EHB catalog.

Similar to the P-model, the new S-model reveals a whole-mantle low-velocity upwelling rooted in the African LLVP. There is a high correlation between the P- and S-models throughout the mantle; however, additional low-velocity features are imaged in the S-model. I will compare these structures with the P-model. Moreover, $\frac{\delta V_s}{\delta V_p}$ ratios will be visualised and discussed between two S-models (different regularisations) and one P-model (presented in Chapter 4 and 5).

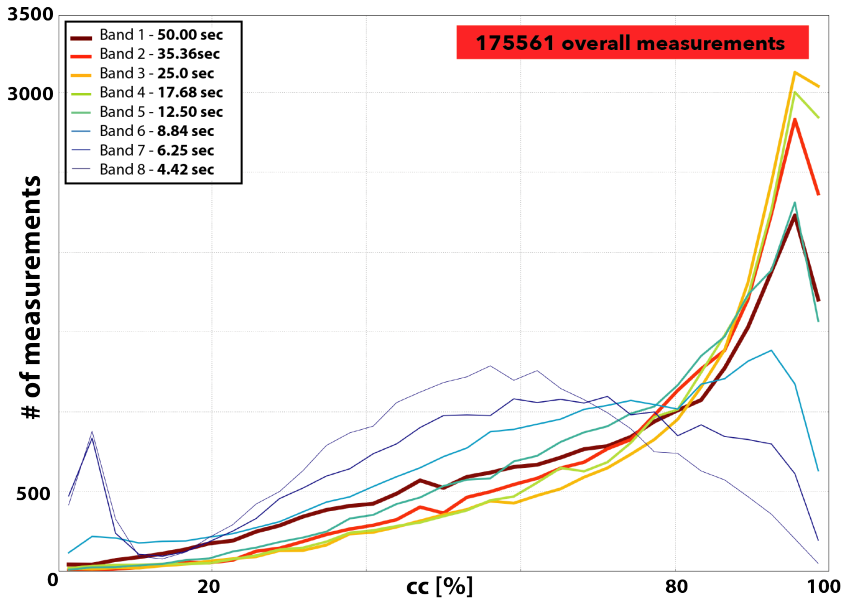

Figure 6.1: Histogram of goodness of fit for S measurements in the RHUM-RUM+ dataset. Coloured lines distinguish eight frequency passbands, labelled by their dominant periods. Similar to Figure D.3 in Appendix D, higher frequency bands show a peak at ∼50%. Band 3 (25.0 s dominant period) has the highest count of measurements with a cross correlation factor of >80%.

6.1 Data

Compared to multifrequency P-measurements (Chapter 4), one additional meta-data is required for the SH (horizontally polarised shear wave) measurements: horizontal orientation of seismic sensors. Although this is generally given for onshore seismic stations, no reliable, affordable system to measure the orientation of horizontal components at the seafloor exists. Scholz et al. (2016) developed two independent methods to estimate the absolute horizontal misorientation of seismic sensors. They measured the particle motion of P-waves and used a principal component analysis to determine the directions of the polarisations in multiple frequency passbands. In the case of Rayleigh waves, they determined the degree of elliptical polarisation in the vertical plane in the time and frequency domain. The two methods had a difference between 3.1°and 3.7°which is within the methods uncertainties. They could apply both methods to 44 OBSes of the RHUM-RUM experiment. Here, I rotate the horizontal components to their

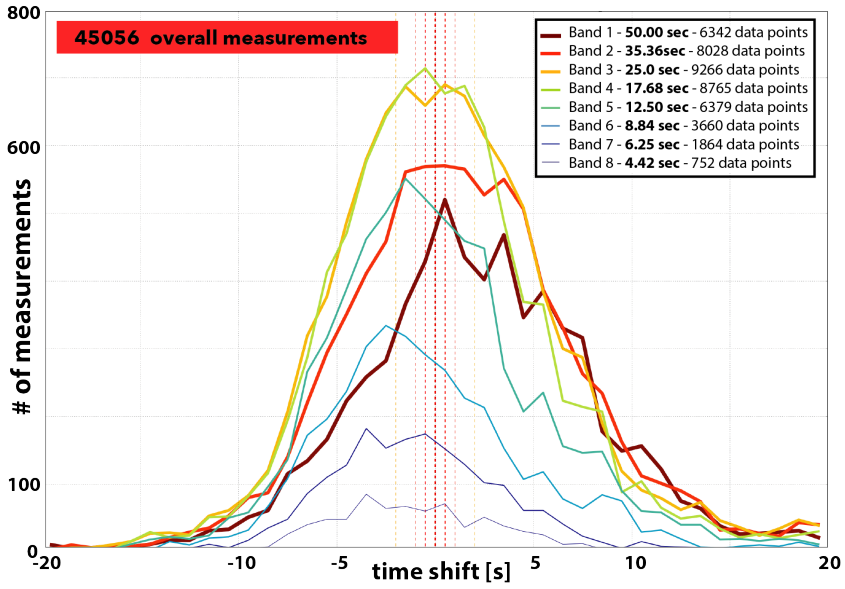

Figure 6.2: Histogram of multifrequency S traveltime measurements with $cc \geq 90\%$ before traveltime corrections (crust, topography and ellipticity corrections). A wide spread between -10 and 10 seconds is visible in all bands (compared to the histogram of P measurements in Figure 4.6 where the spread lies between -5 and 5 seconds). Band 3 (25.0 sec) and 4 (17.68 sec) have the highest number of successful measurements.

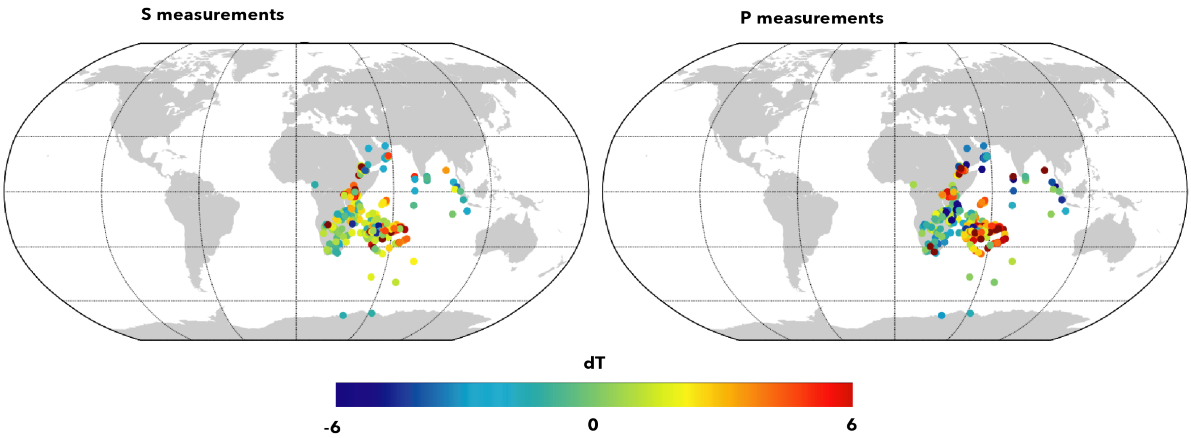

Figure 6.3: Average traveltimes for S (left) and P (right) measurements calculated at each receiver location and for all measurements regardless of the frequency and epicentral distance. The average P measurements show higher amplitudes compared to average S-wave anomalies, which can be explained by the averaging of measurements (see text for more discussion).

absolute horizontal orientation following Scholz et al. (2016). In the next step, using the geometry of each source-receiver pair, the North-South (N-S) oriented components are rotated to Radial-Transverse (R-T) components.

The main steps of the procedure for multiple-frequency SH traveltime measurement can be summarised as follows: **(1)** For each event, source parameters (moment tensor and depth) as well as a broadband source time function (STF) are deconvolved from the data using the method of Sigloch and Nolet (2006) (see Chapter 3 and 4). Teleseismic P-waves with good azimuthal coverage are used in this step. **(2)** Predicted broadband seismograms of two horizontal components (N-S) per station are computed by convolving the STF with the broadband Green's functions calculated by the fully numerical wave propagation tool AxiSEM (Nissen-Meyer et al., 2014; van Driel et al., 2015), up to 1 Hz, through the spherically symmetric velocity model IASP91 (Kennett and Engdahl, 1991) with density and attenuation parameters taken from PREM (Dziewonski and Anderson, 1981). **(3)** Both observed and predicted seismograms are rotated to R-T components using the given or estimated orientation of horizontal components and the event azimuth. **(4)** Broadband observed and predicted seismograms are passed through the same filter bank of bandpass filters. I use Gabor filters in eight overlapping frequency bands, with dominant periods ranging between 50.0 and 4.42 s (Figure 6.1 and 6.2). Gabor filters are Gaussian functions in the log-frequency domain of constant fractional bandwidth and good spectral concentration characteristics (Sigloch and Nolet, 2006). I do not go below 4.42 s dominant period because the number of successful fits becomes very small as shown in Figure 6.1 and 6.2. **(5)** The cross-correlation function between observed and predicted waveforms is then computed in each passband. The time shift that maximizes this function is defined to be the finite-frequency SH traveltime anomaly.

Figure 6.1 shows the cross-correlation yield for all measurements. The high-frequency measurements (filters with 12.5-4.42 s dominant period) show a characteristic peak at around 50%, possibly due to the effects of noise (Hosseini and Sigloch, 2015). Figure 6.2 compares the number of high-quality measurements (cross-correlation factor $\geq 90\%$) in eight bands. The overall time shift lies between -10 and 10 seconds which shows a much

broader spread compared to the P-measurements of Figure 4.6 in Chapter 4. The highest frequency band with 4.42 s dominant period has only 752 successful measurements; Band 3 with 25.0 s dominant period, the most-successful bandpass filter, has only 9,266 high-quality measurements (8% of the total number of source-receiver pairs in that band) of the total number of measurements. Here, I chose a higher threshold for the cross-correlation factor of successful S-measurements compared to teleseismic P-measurements (90% for S, 80% for P). This significantly helped to avoid cycle-skipping in global S-measurements. Figure 6.3 compares average traveltime measurements of S (left panel) and P (right panel) calculated at each receiver location and for all measurements regardless of the frequency. S-wave average traveltime patterns in Figure 6.3 resemble P-wave average traveltime patterns, although the amplitudes differs. Unexpectedly, average P measurements show higher amplitudes than S measurements. This could be due to the averaging of various frequency bands and epicentral distances. Normally, we expect stronger S anomalies from the lower mantle.

To enhance the coverage, two datasets were added to our multifrequency SH measurements: 145,546 S measurements from S40RTS (Ritsema et al., 2011) and 133,925 picked S-phases from ISC-EHB/EHB (Engdahl et al., 1998; Weston et al., 2018).

For all datasets, the resulting "raw" traveltime measurements were corrected for the effects of ellipticity, crust and surface topography using the 2°×2° global crustal model CRUST2.0 (Bassin et al., 2000) as described in Chapter 4.

6.2 Tomography models

I generate four global S models using different datasets: **(1)** only ISC-EHB/EHB picked arrival times (≈134K measurements using the same criteria as in Chapter 4); **(2)** $\sim 146K$ S measurements used in S40RTS model; **(3)** Multifrequency S measurements using RHUM-RUM data ($\sim 45K$); **(4)** Joint inversion of all three datasets with $\approx 325K$ measurements in total. Figure 6.4 compares the preliminary results of the four tomography models beneath the La Reunion hotspot (refer to Appendix A for detailed L-curve analysis).

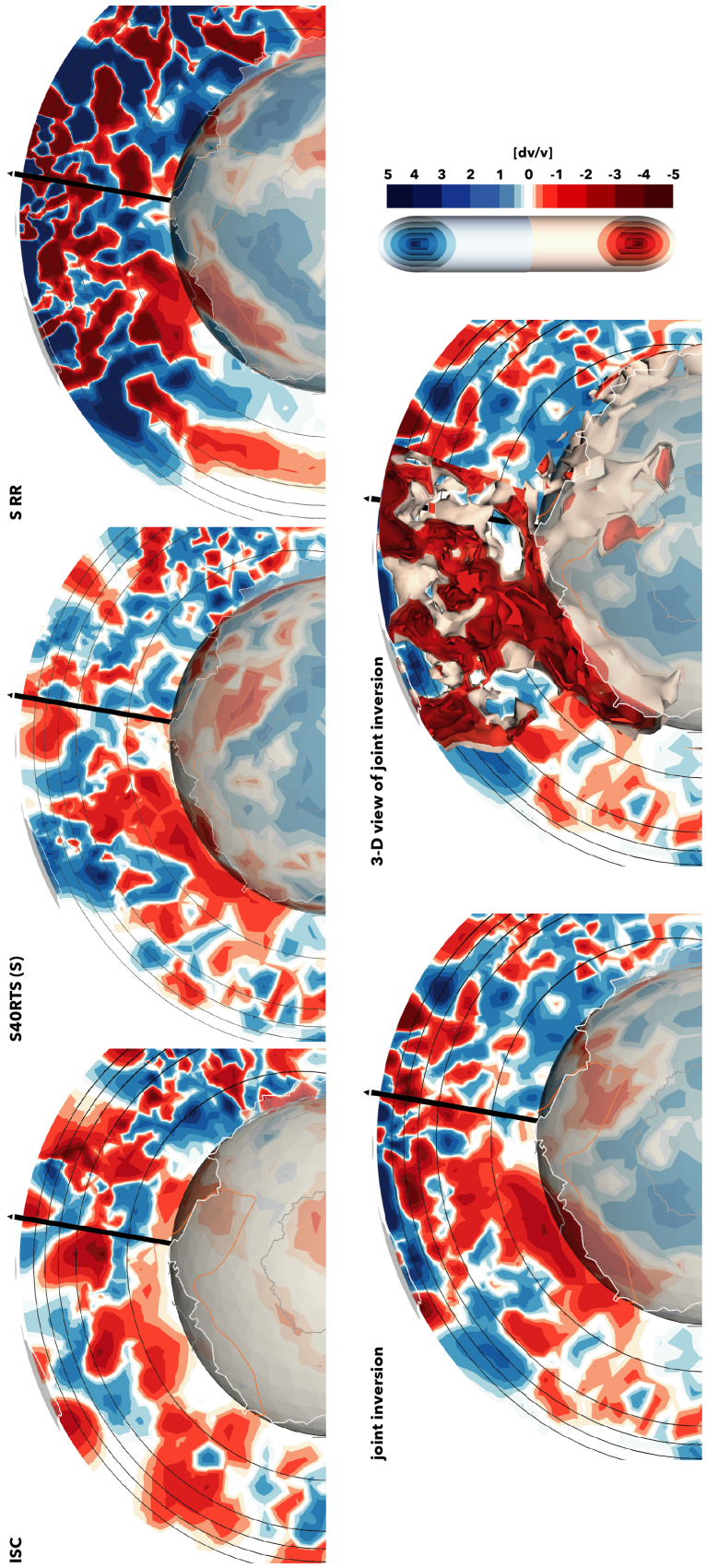

Figure 6.4: Inversions with different S-wave datasets. **ISC:** only ISC-EHB/EHB picked arrival times (∼134K measurements). **S40RTS:** $\sim 146K$ S measurements used in S40RTS model. **S RR:** multifrequency S measurements using RHUM-RUM+ data ($\sim 45K$). **RR-Ox-S19:** joint inversion of all three datasets with $\sim 325K$ measurements. When inverting the different datasets together each traveltime measurement is weighted with an a priori uncertainty (see Chapter 4). See text for discussion.

In the ISC-EHB/EHB inversion of Figure 6.4, the imaged structures show little correlation with the ISC-EHB/EHB P model (see Figure 4.11 of Chapter 4). The inversion using S40RTS measurements clearly images the LLVP beneath Africa that extends to the mid- and upper-mantle but shows no connection to the La Réunion island. The LLVP is cone-shaped with a sharp edge beneath Africa. The imaged features using only multifrequency S measurements are similar to the P-inversion of Chapter 4 and Chapter 5 (also see Appendix A for detailed L-curve), but with much higher amplitudes in the whole mantle.

The joint inversion of the three datasets images the LLVP at the CMB which rises and narrows towards the mid-mantle (cone-shaped). At that point, several low-velocity structures branch out as shown in the 3-D velocity rendering of Figure 6.4. One branch extends from the mid-mantle to the surface beneath Madagascar. A horizontally elongated arm connects these structures with velocity anomalies beneath the La Reunion island. Interestingly, various structures imaged in our P-model appear in the S model as well (Figure 6.5 for better comparison). This includes the tree-shape plume cluster, the cusp in the mid-mantle and the characteristic broad branches in the lower-third of the mantle and thin branches in the upper mantle (refer to Figure 5.1 in Chapter 5).

6.3 $\frac{\delta V_s}{\delta V_p}$ ratio

I have generated two regional P and S tomography models beneath La Réunion. In this section, I use these two models for the analysis of $\frac{\delta V_s}{\delta V_p}$ ratios as shown in Figure 6.5. As the two models are generated on one inversion grid, the $\frac{\delta V_s}{\delta V_p}$ ratios are computed by directly dividing δlnV_s and δlnV_p values point-by-point. In the left column of Figure 6.5 the actual velocity structures of the P model and two S models using two different regularisation parameters are plotted. In the right column, the $\frac{\delta V_s}{\delta V_p}$ ratio and the outlines of one underlying tomography model (as indicated in the title of each panel are plotted). From this figure, it is clear that P- and S- models image similar structures (but with different amplitudes) in the lowermost and mid-mantle ($\frac{\delta V_s}{\delta V_p} \geq 1$).

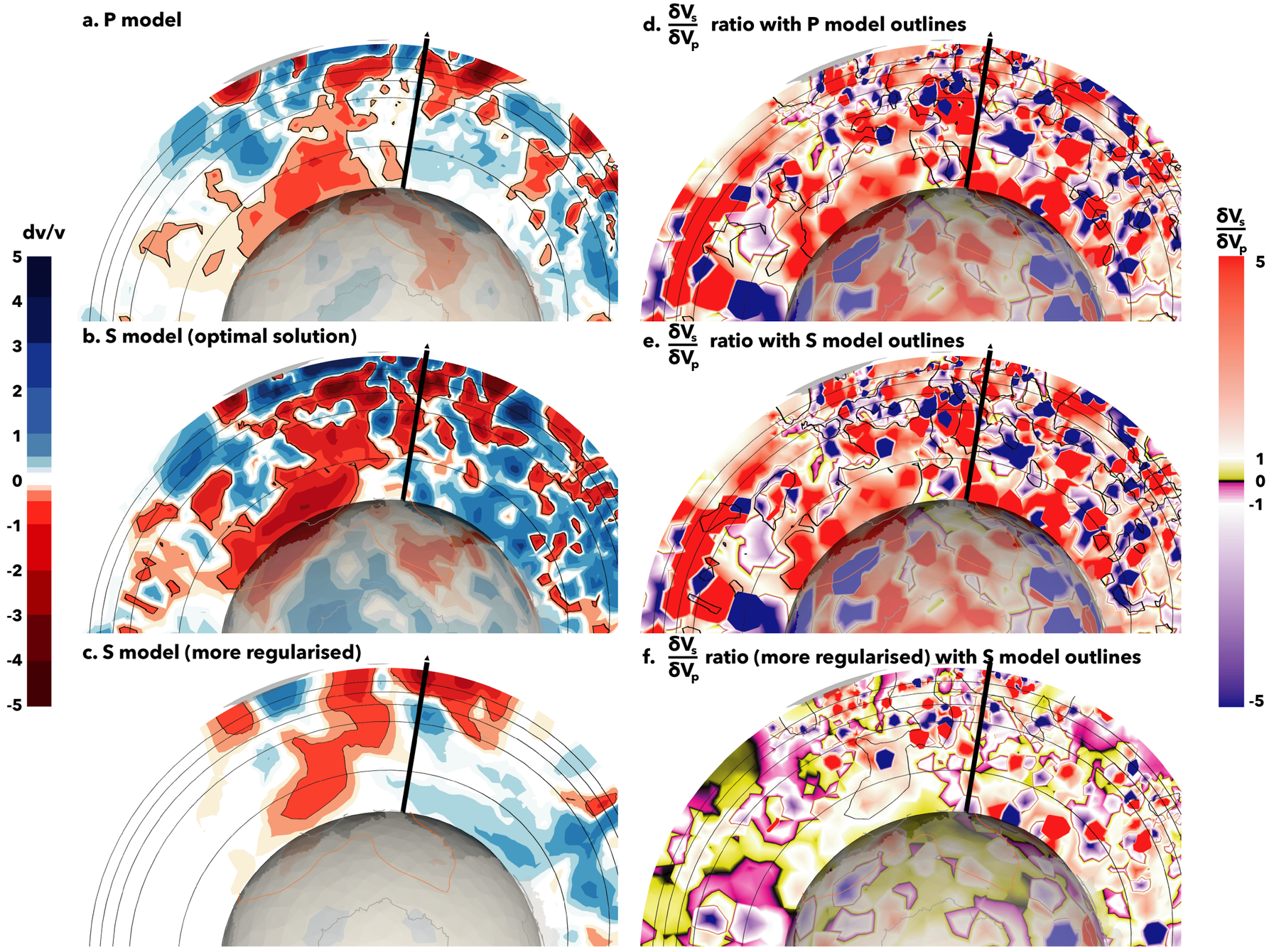

Figure 6.5: Tomography models and $\frac{\delta V_s}{\delta V_p}$ ratio maps beneath the western Indian Ocean. **a.** Cross section through P model (Chapter 4 and 5) and the outline of $dv/v = -0.25\%$ in black. **b.** Cross-section through the S model (optimal solution) with the outline of $dv/v = -0.5\%$ in black. **c.** Cross-section through a more regularised S model (see Appendix for details). **d.** Cross-section through $\frac{\delta V_s}{\delta V_p}$ model generated by the S model of (b.) and the P model of (a.), black outline from P model. The colour bar was designed to distinguish between $v_s > v_p$ case (red and blue colours) and $v_p > v_s$ case (violet and yellow colours). **e.** Same $\frac{\delta V_s}{\delta V_p}$ model as in (d.) but with S model outlines from (b.) **f.** $\frac{\delta V_s}{\delta V_p}$ model generated by the more regularised S model of (c.) and the P model of (a.). The patterns of P- and S-model are similar at the CMB and mid-mantle, hence the the ratio is mostly positive in these areas.

The ratio between shear (δV_s) and compressional velocities (δV_p) can be an indication for chemical heterogeneity in the D" (e.g., Moulik and Ekström, 2016), though Murakami et al. (2004) suggest that high ratios may indicate a phase change to pPv (post-perovskite). This ratio can also be used to indicate phase or iron spin transitions between 1,500 and 2,000 km depth (corresponding to the depth of cusp as discussed in Chapter 4 and 5; (e.g., Wu and Wentzcovitch, 2014). The ratios seen in Figure 6.5 show almost no negative $\frac{\delta V_s}{\delta V_p}$ ratio in the mantle beneath La Réunion. The small-scale negative ratios ($\frac{\delta V_s}{\delta V_p} < 0$) could be due to the differences in resolution. The lowermost mantle shows ratios of $\frac{\delta V_s}{\delta V_p} > 2$. Previous studies have argued that a $\frac{\delta V_s}{\delta V_p} > 2.7$ may indicate chemical heterogeneities as purely thermal effects (with no temperature-dependent phase changes) produce a $\frac{\delta V_s}{\delta V_p}$ ratio of up to ∼2.5 (Masters et al., 2000; Karato and Karki, 2001; Mora et al., 2011; Moulik and Ekström, 2016; Koelemeijer et al., 2018). However, as already mentioned, this may also indicate a phase change to post-perovskite (Murakami et al., 2004; Koelemeijer et al., 2018; Tesoniero et al., 2016).

The last row shows $\frac{\delta V_s}{\delta V_p}$ ratio for an over-regularised tomographic S model but with the same P model as in the first and second row of Figure 6.5. As expected, the overall ratio decreases (more yellow and violet colours). Analysing $\frac{\delta V_s}{\delta V_p}$ from tomographic models, even with similar datasets, can be misleading if regularisation is not handled carefully (Tesoniero et al., 2016). For example, in case of over-regularised S models but with one P model, very low $\frac{\delta V_s}{\delta V_p}$ ratios will be obtained, giving false information about the type of heterogeneities in the mantle.

Based on this comparison, key factors in successful comparisons of P- and S-models are: **(1)** comparable data coverage and inversion parameters (e.g. regularisation). **(2)** similar and unbiased P- and S-models in the region of interest, consistent with recent work by Tesoniero et al. (2016); Koelemeijer et al. (2016, 2018).

6.4 Discussion and outlook

Four S tomography models were presented and compared systematically. The model generated by the S40RTS dataset produces structures in agreement with our P model

(e.g. Chapter 4 and 5). The ISC-EHB/EHB inversion shows better results only at high χ^2 values corresponding to more regularised models. This may indicate that the assigned data uncertainties for the picked arrival times were underestimated. The same issue occurs for the inversion with RHUM-RUM+ dataset. High amplitude and small-scale structures dominate the model. The joint inversion images structures similar to the P-model; however, additional low-velocity features are imaged in the S-model.

In order to improve the preliminary S tomography model, I plan to:

- revisit the assigned uncertainties to RHUM-RUM+ and ISC-EHB/EHB datasets.
- include more seismic phases (e.g. SS, Sdiff). This should increase the data coverage and consequently enhance the resolution deeper down in the mantle below this region.
- compute waveform kernels (Stähler et al., 2016b) to correctly project the sensitivities of various seismic phases (e.g., SS, Sdiff) on the inversion gird.
- experiment with the filters and time-windows to avoid cycle skipping in S measurements. Tian et al. (2009) used relatively broad Gabor filters with five centre periods (40, 20, 10, 5 and 2.5 seconds). Here, I chose Gabor filters similar to our P-measurements (Chapter 4).

The preliminary results are informative but demand more work. Implementing these improvements will enable us to reanalyse the ratios again and to interpret their spatial variation.

Progress in science comes when
experiments contradict theory.

— Richard P. Feynman

7

Discussion, Conclusion & Outlook

Contents

7.1 Discussion 90
7.1.1 Surface observations 90
7.1.2 How did the mantle evolve? 93
7.1.3 Unanswered questions 97
7.2 Conclusion 98
7.3 Outlook 99
7.3.1 Hydrophone data in seismic tomography 99
7.3.2 Future of deep Earth exploration 103

In the first part of this chapter, I discuss the seismic tomography model RR-Ox19 and how it relates to geochemistry observations and geodynamic models. I suggest various scenarios for Earth's dynamic mantle in the western Indian ocean from the perspective of this tomographic model. After a brief conclusion in Section 7.2, the last section discusses possible future projects, particularly, for ocean seismological experiments and data analysis.

7.1 Discussion

In this study, I presented a new regional tomographic model and a hypothesis for the shape of the imaged structures: *a plume cluster*. Tilted and broad conduits rise through the mid-mantle beneath the Indo-Atlantic Ocean. In fact, part of this plume cluster beneath Afar was previously imaged (Ritsema et al., 1999; Hansen et al., 2012). Interestingly and as discussed in the next section, geochemistry observations, dynamic topography and age progression of hotspots in the western Indian Ocean are in agreement with the proposed tree-shape structure in this study.

7.1.1 Surface observations

The mantle structure beneath Afar, compared to most other hotspots, is well-illuminated as it is located directly beneath the African continent. Various studies have imaged broad tilted low-velocity anomalies in this region (Ritsema et al., 1999; Hansen et al., 2012) (see Appendix C). The model RR-Ox19, by using a multifrequency inversion technique applied to the largest available dataset in the western Indian ocean, extends the view to related mantle plumes in the region.

The resulting model clearly images the African LLVP, and low-velocity branches from a common point in the mid-mantle (cusp area beneath South Africa), e.g., Afar, Kerguelen, La Réunion and possibly Bouvet. Marion seems to emerge as a sub-branch from Kerguelen's main branch consistent with Steinberger and Antretter (2006). This "common-source" hypothesis or connectivity of the plumes in the western Indian Ocean can be also traced at the surface through three main observations: the DUPAL anomaly, dynamic topography and age progression of the hotspots.

DUPAL. Dupre and Allegre (1983) suggested a link between Indian Ocean hotspots through compositions of common and regionally distinct isotopic characteristics (Pb-Sr-Nd) of ocean island basalts, the so-called DUPAL anomaly (Figure 7.1). The main result, interpreting the isotopic peculiarity of the Indian Ocean islands, showed that Pb, Nd, Sr and He isotopes from different Indian Ocean islands are interpreted by the mixing

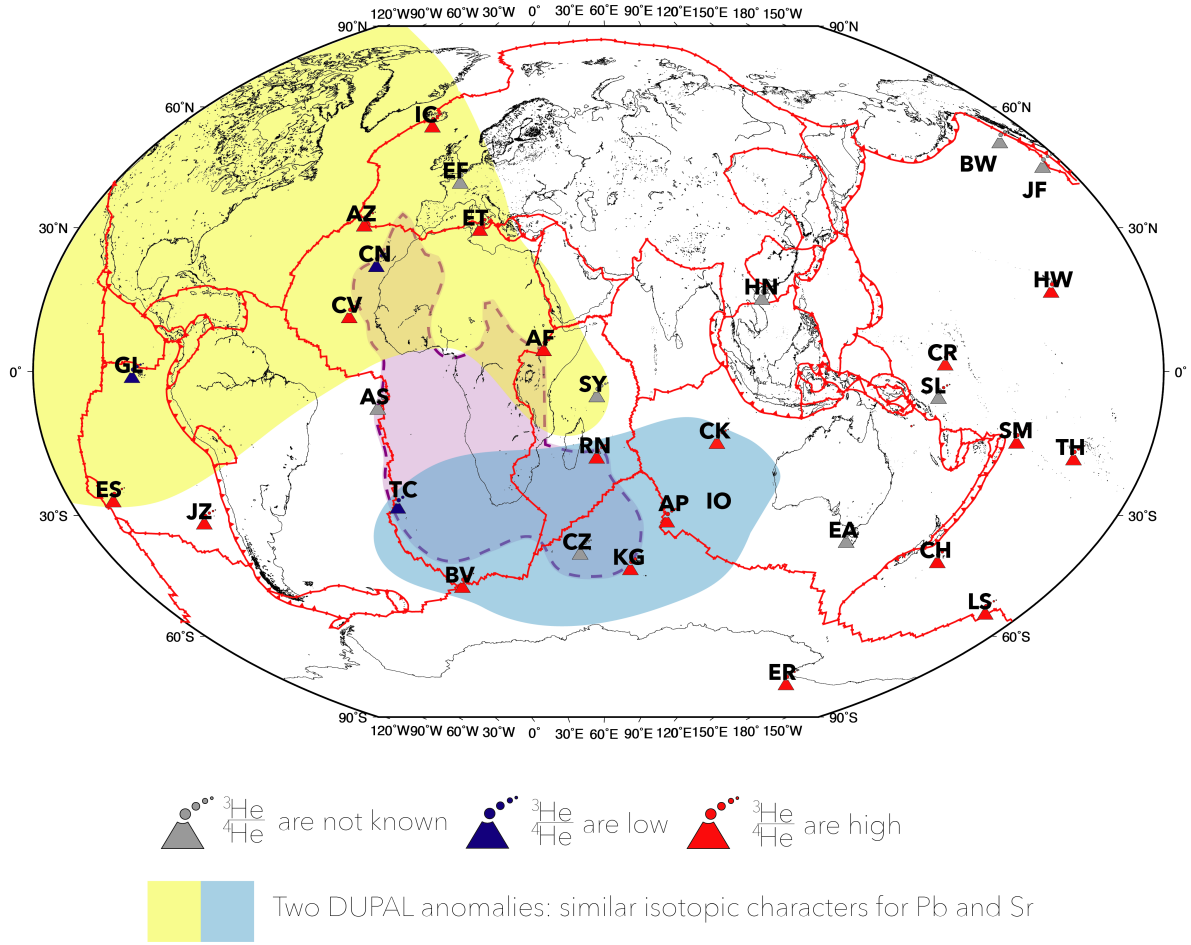

Figure 7.1: DUPAL anomalies are in yellow (Pacific and North Atlantic Ocean) and blue (South Atlantic and Indian Ocean), the violet area shows the location of the LLVP at the CMB, and the dashed line is the PGZ (Torsvik et al., 2006). Hotspot locations and $^3He/^4He$ ratio are after Farley and Neroda (1998), if no ratio available, a grey symbol was used. The blue DUPAL anomaly overlaps with the southern part of the African LLVP. Afar belongs to the yellow DUPAL anomaly, but the contamination with continental crust might have altered the isotope results.

of lower mantle material with subducted sediments and mixing between the oceanic islands source and the ridges. Our tree-shape structure provides an explanation for this geochemical observations on the surface. Both the P and S models image a joint source region (cusp) for upwelling rock that surfaces in hotspots along the tree's crown.

Age progression. One important observation is the periodicity for the onset of large eruptions in the western Indian Ocean with an interval period of ∼30 m.y.; Kerguelen

erupted for the first time roughly 120 m.y ago creating the Kerguelen plateau (Coffin et al., 2002; Gibbons et al., 2013), Marion 90 m.y ago, La Réunion at 65 m.y and Afar at 30 m.y ago (Coffin et al., 2002; Courtillot et al., 2003; Montelli et al., 2004). Although this is not a direct evidence for the connectivity of the mantle plumes, it implies a possible link between them. In analogue experiments by Anne Davaille (not published) plumes would trigger another plume in its proximity in regular intervals (personal correspondence).

Dynamic topography. The margins of the South Africa plateau are steep (1 km above sea level). Nyblade and Robinson (1994) interpreted the entire region from the south Atlantic mid-ocean ridge to the East African Plateau as the African Superswell, where also the topography developed through time. Gurnis et al. (2000) showed that the elevated topography of southern Africa is 300±600 m, with an average uplift rate of 5±30 m/Myr. Doucouré and de Wit (2003) analysis showed out Africas bimodality, through reconstructing the Mesozoic topography of Africa by removing the topographic effect of features (from Cretaceous age or younger). This bimodal topography exists since the early Mesozoic (251-145 Ma). Though Burke (1996) argued that the timing of the topography being rather 30 Ma years old.

In short, two explanations have been proposed for the origin of this major topography anomaly: either long wavelength lower mantle anomalies (2500 km depth) (Hager et al., 1985; Gurnis et al., 2000; Colli et al., 2016) or plate reorganisation (Moore et al., 2009). Fishwick and Bastow (2011) stressed the importance of a mantle flow field in order to explain the super-swell topography. Further analysis showed that southern Africa is currently in a downwelling mode and the lower mantle beneath East Africa is upwelling, whereas the process seems to be spatially and temporally out of phase (Doucouré and de Wit, 2003).

This observation fits geodynamic predictions (Kumagai et al., 2008) where thermo-chemical piles undergo several cycles of heating and upwelling, cooling and downwelling. Based on our tomography models, the African topographic anomaly can be caused by the “common source” imaged in the mid-mantle below this region. A momentarily

downwelling might suggest that the cusp is retreating (or collapsing) and negatively buoyant while still showing up as a low-velocity anomaly in the mid-mantle.

7.1.2 How did the mantle evolve?

How can the imaged low-velocity structures in the mantle and the surface observations be explained in terms of Earth dynamics and evolution? How has the African LLVP formed, and how are the plumes related to it (if there is any relation at all)?

Throughout the years, various explanations for the origin and composition of this roughly 200 km thick transition zone were proposed, including a phase boundary (e.g., Bullen, 1949), a thermal boundary (e.g., Stacey and Loper, 1983) or a slab graveyard (e.g., Hofmann and White, 1982), to name the top three.

Schubert et al. (2004) argued that so called "Superplume regions" are too large to be explained by a single instability of the D" layer. The D" has a thickness of 200 km and this limits the dimensions of the size of a mantle plume, even if the boundary layer is compositionally dense and hot.

Murakami et al. (2004) inferred from in situ x-ray diffraction measurements that the D" should be a phase transition from bridgmanite to post-perovskite. Later, Koelemeijer et al. (2017) identified anomalous splitting of Stoneley modes, which are explained when the density of the LLVPs are lower than the surrounding mantle (by the presence of post-perovskite).

Davies and Gurnis (1986) argued from a 2-D numerical simulations that "dregs" (segregated from subducted lithosphere and compositionally dense material) will form a discontinuous distribution with a maximum thickness of 230 km (possibly dense piles) under upwellings.

In general, tomography provides a low-resolution image of the current convection process inside Earth's mantle (Grand et al., 1997). In case of our regional tomography, it is ambiguous to speculate how this structure formed and if it stayed unchanged over a long period of time. The tilted branches and the mid-mantle cusp in our model can have different origins, as shown in Figure 7.2.

Figure 7.2(A), demonstrates how two thin mantle plumes originate from the edges of a LLVP (e.g., Schubert et al., 2004; Torsvik et al., 2006; Steinberger and Torsvik, 2012; Dannberg and Gassmöller, 2018). In this case the LLVP could be a thermochemical pile, whereas the rising conduits could be of thermal nature (e.g. Steinberger and Torsvik, 2012). Due to entrainment or mantle flow (e.g., Schubert et al., 2004; Steinberger and O'Connell, 1998) the vertical conduits start to bend toward each other, while their surface location stays fixed (e.g. through "plume capture" at ridges, Whittaker et al., 2015). Eventually, the vertical conduits are connected above the LLVP and form tilted structures.

Another possible mechanism for the formation of tilted low-velocity structures is through doming. A LLVP dome would push upward and generate "superswells" at the surface (Davaille et al., 2005). When the dome reaches a phase transition, it acts as a source for several smaller mantle plumes in the upper-mantle. Secondary plumes might be generated from the top of the dome (e.g., Davaille et al., 2005). These thinner plumes might be influenced by upper mantle dynamics and plate tectonics (Figure 7.2(B)).

The third possibility is illustrated in Figure 7.2(C). The Afar, Réunion and Kerguelen branches vertically overlie the LLVP (Figure 5.2), this 3-D structure is captured by the 2-D cartoon of Figure 5.2. If the branches are generated by vertically rising blobs then the branch tilt predicts a temporal progression through the mantle. The first blob is detached from the margin of the LLVP, and vertically rises throughout the mantle (e.g., Olson and Singer, 1985), while depleting the LLVP at the border. This process continues from the margin of the LLVP towards its centre.

The previously mentioned age progression might support this third possibility. The Afar flood basalts erupted 30 Ma, whereas less advanced rifting is happening now towards the south (Ring, 2014) and no rifting is observed where the tilting Afar branch has not reached the surface (south of Mozambique). In the tomographic model, the Kerguelen branch seems to be connected to Marion and La Réunion, hence the same train of thought can be also applied here. Flood basalts in Kerguelen occurred 120 Ma and the next blob appeared beneath Marion 90 Ma and then beneath La Réunion

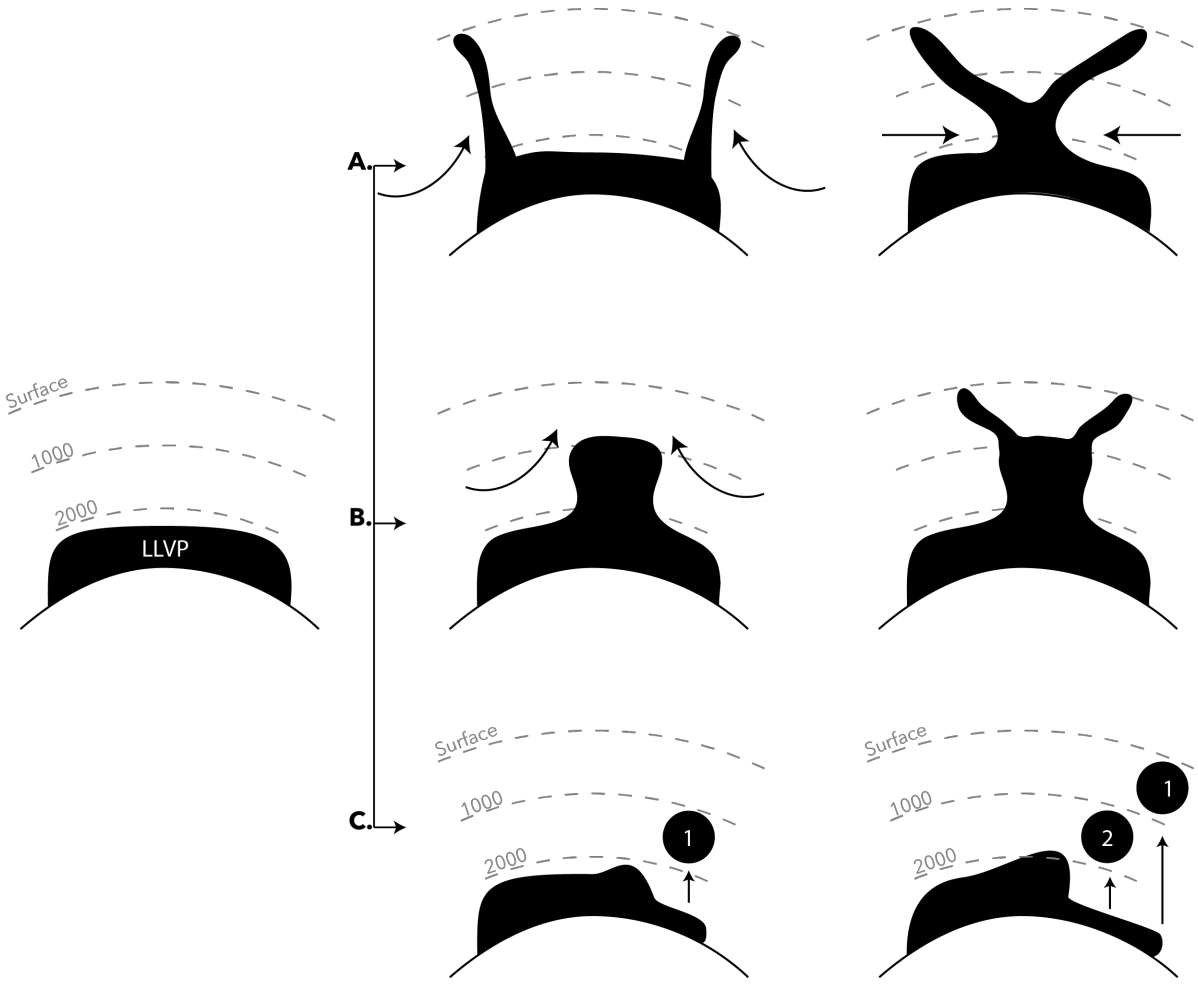

Figure 7.2: Cartoon shows three possible explanations for the evolution of the imaged plume cluster (see text for more discussion). All cases start initially with a LLVP. **A.** The conduits initially rise from the border of the LLVP (e.g., Schubert et al., 2004; Torsvik et al., 2006; Steinberger and Torsvik, 2012; Dannberg and Gassmöller, 2018). With time, mantle dynamic (mantle flow or entrainment) causes the conduits to sweep inward and connect at mid-mantle from where branches are tilting up- and outward. The branches at the surface stay mostly in place. **B.** Doming of the LLVP (e.g., Davaille et al., 2005), where secondary conduits evolve from the top of the dome towards the surface. Tilting of the smaller branches might develop because of the upper mantle flow (Steinberger and Antretter, 2006). **C.** The border of the LLVP becomes unstable and releases in a temporal progression "blobs" (e.g., Olson and Singer, 1985), marked in Figure by *1* and *2*. The LLVP retreats and regularly releases blobs into the mantle. In a tomographic model, this will show up as a continuous branch.

around 65 Ma. The question is if our cusp area is going to reach the surface eventually and break apart South Africa?

Fourel et al. (2017) demonstrated how the borders of internally heated thermochemical

piles become unstable, hence they are being prone to trigger the ascent of buoyant material. Based on these laboratory experiments, it seems possible that a blob, or plume head, rises from the margin of the LLVP, and vertically ascends throughout the mantle (e.g., Olson and Singer, 1985). In a tomographic model, this chain of blobs might be imaged as a continuous tilted low-velocity branch. Indeed, Figure 5.1 hints two blobby structures between 2000 and 1000 km depth (beneath South Africa) and another one at location marked with "K". These two structures look more like blobs than a tilted conduit with a constant thickness throughout the mantle.

Figure 7.2 demonstrates only three different possibilities how the observed low-velocity structures might have formed. All of them can explain the surface observations of the kimberlite distribution (Torsvik et al., 2010), the DUPAL anomaly Dupre and Allegre (1983), the anomalous African topographic high and even the periodic large eruptions in the western Indian Ocean. However, their composition is still difficult to predict, but the clear visibility of the low-velocity structures, and large diameters (700-800 km under Réunion) point towards a chemically dense upwelling (Davaille, 1999; Kumagai et al., 2008; Griffiths and James, 1989) because purely thermal plumes should be thin and retain their stems to the CMB. Ballmer et al. (2016) concluded that based on the observations the sharp edge of the African LLVP (e.g., Ni et al., 2002), the anti-correlation between shear-wave and bulk-sound velocity (e.g., Masters et al., 2000) and the decorrelation of shear-wave velocity with density anomalies (e.g., Moulik and Ekström, 2016) it is unlikely that a purely thermal anomaly originates from the LLVP.

Jellinek and Manga (2003) summarised that the existence and longevity of hotspots and mantle plumes in the Earth are a consequence of interactions among plate tectonics, core cooling, and the D". Regardless of the origin, dynamics and composition of LLVPs and plumes, their clear visibility in many models in recent years, relative fixed position and longevity are undisputed.

7.1.3 Unanswered questions

As discussed in the previous sections, RR-Ox19 spreads new light on the mantle structures beneath the western Indian Ocean and reconciles surface observations (e.g. DUPAL, African topography) while other questions still remain to be answered:

The stability of the LLVPs. The cusp of the LLVP is assumed to be stable over an extended period of time (at least ∼120 Ma) (e.g., Torsvik et al., 2014). If this is the case then new branches might have been generated in regular intervals (see **Age progression.**). But can these massive low-velocity piles be stable for more than 300 Ma (Torsvik et al., 2008a)? What is its implication for global mantle dynamics? Do we encounter a "top-down" process, where mantle dynamics are influenced by plates, or rather a "bottom-up" process, where plumes control mantle dynamics. Finally, how do slabs interact with these low-velocity piles (e.g. Dannberg and Gassmöller, 2018)?

Break-up of Gondwana and Africa. If plumes are spawned in regular intervals beneath Africa, can the location of the LLVP and its branches explain the break-up of Gondwana (e.g. Brown and Girdler, 1980)? Do the mantle plumes surrounding African hold the African plate, which is a slow plate in comparison, in place?

The shape of LLVPs. Suetsugu et al. (2009) and Obayashi et al. (2016) proposed that the Pacific LLVP and its plumes an arranged in a superplume (dome) structure with secondary plumes on top of it. In this hypothesis the branches emerge (semi)vertically from the LLVP. Where does this difference between the Pacific and African LLVP come from?

The sharp edge of the LLVP. Almost all tomographic models agree on a sharp edge west of the African LLVP (see Appendix C) and half of these models show on a high-velocity anomaly on top of this sharp edge. What are the implications of this edge and the high-velocity structure?

Plume-ridge interaction. The African LLVP is located beneath a *continent* surrounded by *slow*-spreading ridges, while the Pacific LLVP is located beneath an *ocean* fenced by *fast*-spreading ridges. Whittaker et al. (2015) argued that slow migrating ridges stabilize mantle plumes. What is the reach of the hotspot-ridge interaction, can it go as far as mid-mantle and influence the tilt of the branches for, say, 1,500 km (similar to Figure 7.2)?

Geochemistry and geodynamics. What is the circulation of materials inside the LLVP and can it be different from the circulation inside the branches? Can these two modes of circulation cause the lateral movements of conduits in the mantle?

Answering these questions is crucial for understanding the dynamic of LLVPs and the mantle itself. The next step is to design geodynamic models based on tectonics, plate motion, geochemistry and tomography to reconstruct possible scenarios shown in Figure 7.2.

7.2 Conclusion

From 2011 to 2016, the RHUM-RUM project instrumented a 2000 × 2000 km^2 area of the seafloor and islands surrounding the hotspot with broadband seismometers. I obtained >50,000 high-quality multifrequency P-wave traveltime measurements by cross-correlation of observed data with synthetic seismograms in different frequency bands. These measurements were then used in a traveltime tomography inversion to generate a P-wave model in the western Indian Ocean.

The new P-wave model shows a lowermost mantle source for the plume beneath La Réunion originating from the African LLVP. Consistent with previous studies, broad low-velocities are observed in the lower mantle; however, the model reveals more details and considerable complexity in the mid and upper mantle beneath the Réunion hotspot.

The imaged structures provide explanations for various, independent surface observations. The South African topographic high can be reconciled by the presence of a buoyant LLVP cusp beneath the continent. The “common source” imaged in

the mid-mantle for most hotspots in this region can explain the surface geochemistry observation of DUPAL anomaly.

As mantle plumes were generated in regular intervals of ∼30 Ma, the LLVP and cusp region should have been stable for at least ∼120 Ma. Our model cannot provide an explanation for whether the plume cluster evolved gradually into this shape by time or stayed in this shape since its formation.

7.3 Outlook

7.3.1 Hydrophone data in seismic tomography

In the RHUM-RUM experiment, the hydrophone instruments on the OBS recorded more reliable than the multicomponent seismometers, but they were highly affected by reverberations (see Chapter 2 for discussion). Nevertheless, hydrophones provide additional data that can potentially be used in tomographic inversions.

One of the reasons behind the reliability of hydrophones in extreme environments, such as seafloor, is its simple design. The hydrophone is based on a piezoelectric transducer that generates electricity when subjected to a pressure change (Figure 7.3).

Hydrophone data has not been used extensively in passive seismic tomography. The EGELADOS (Exploring the GEodynamics of subducting Lithosphere using an Amphibian Deployment Of Seismographs) project deployed several OBSes in the Mediterranean Sea. Unfortunately, due to defective levelling, the multicomponent seismometers did not produce usable data. Unreliable instrument response from the hydrophones made the pressure data equally unusable for seismic tomography. In another study, Montuori et al. (2007) used hydrophone data by picking first arrivals (on both hydrophone and seismogram) around the southern Tyrrhenian subduction zone in Italy. Nolet (2016) picked data from MERMAIDS (Mobile Earthquake Recording in Marine Areas by Independent Divers) around the Galapagos islands.

Here, for the first time, I plan to use the waveforms recorded by hydrophones in a multifrequency tomographic inversion. In order to automatically cross-correlate the



Figure 7.3: The different oil in a hydrophone are separated from each other with a differential pressure gauge. If displacement is applied to the rubber, the pressure in the left oil chamber is changing and the pressure change is measured.

observed hydrophone data with synthetic seismograms, the velocity waveforms computed by forward modelling tools, such as AxiSEM (Nissen-Meyer et al., 2014), need to be converted to pressure data, or reversely, pressure data recorded on hydrophones can be converted to velocity. I chose the latter. In theory, the signals (pressure and velocity) are proportional as both are a derivative of the vertical displacement (Nolet, 2016):

$$P = \kappa \frac{\partial u_z}{\partial z}$$

where P is pressure, $\frac{\partial u_z}{\partial z}$ is the derivative of the vertical displacement, and κ (incompressibility) is a constant set to $2.08 \frac{N}{m^2}$ for water. By using the chain rule, velocity can be written as:

$$v_z = \frac{\partial u_z}{\partial t} = \frac{\partial u_z}{\partial z}\frac{\partial z}{\partial t} = c\frac{\partial u_z}{\partial z}$$

with $c = 5800 \frac{m}{s}$ for sound velocity in water. Pressure waveforms can then be directly computed from velocity waveforms, as follows:

$$v_z = \frac{c}{\kappa} P \tag{7.1}$$

Implementing this in the multifrequency measurement scheme is straightforward. First, velocity synthetic waveforms are computed using *Instaseis* (van Driel et al., 2015). Second, the pressure waveforms recorded on hydrophones are converted to velocity signals using eq. 7.1 and then directly compared with synthetic velocity waveforms. Some

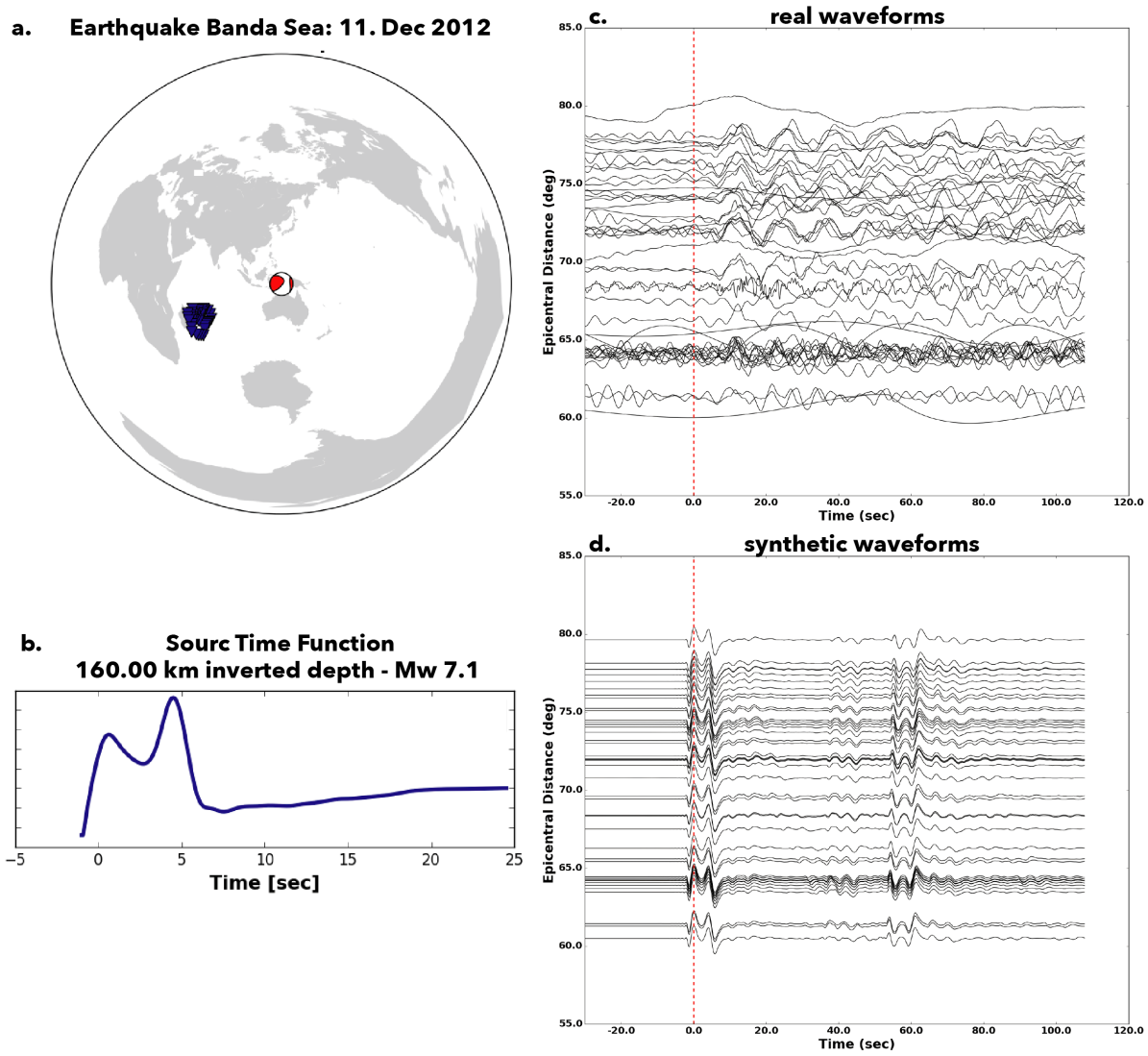

Figure 7.4: Real and synthetic waveforms for an earthquake in Banda Sea, Indonesia. The inverted source time function is shown in panel **(b)**. Only RHUM-RUM stations are used here. **(c)** Real hydrophone recordings, sorted for epicentral distance with normalised amplitudes. Hydrophone data shows a strong 20 sec periodic signal after the first arrival (marked by vertical dashed line in red). **(d)** Synthetic velocity seismograms calculated using Instaseis (van Driel et al., 2015) for the same stations as in panel (c).

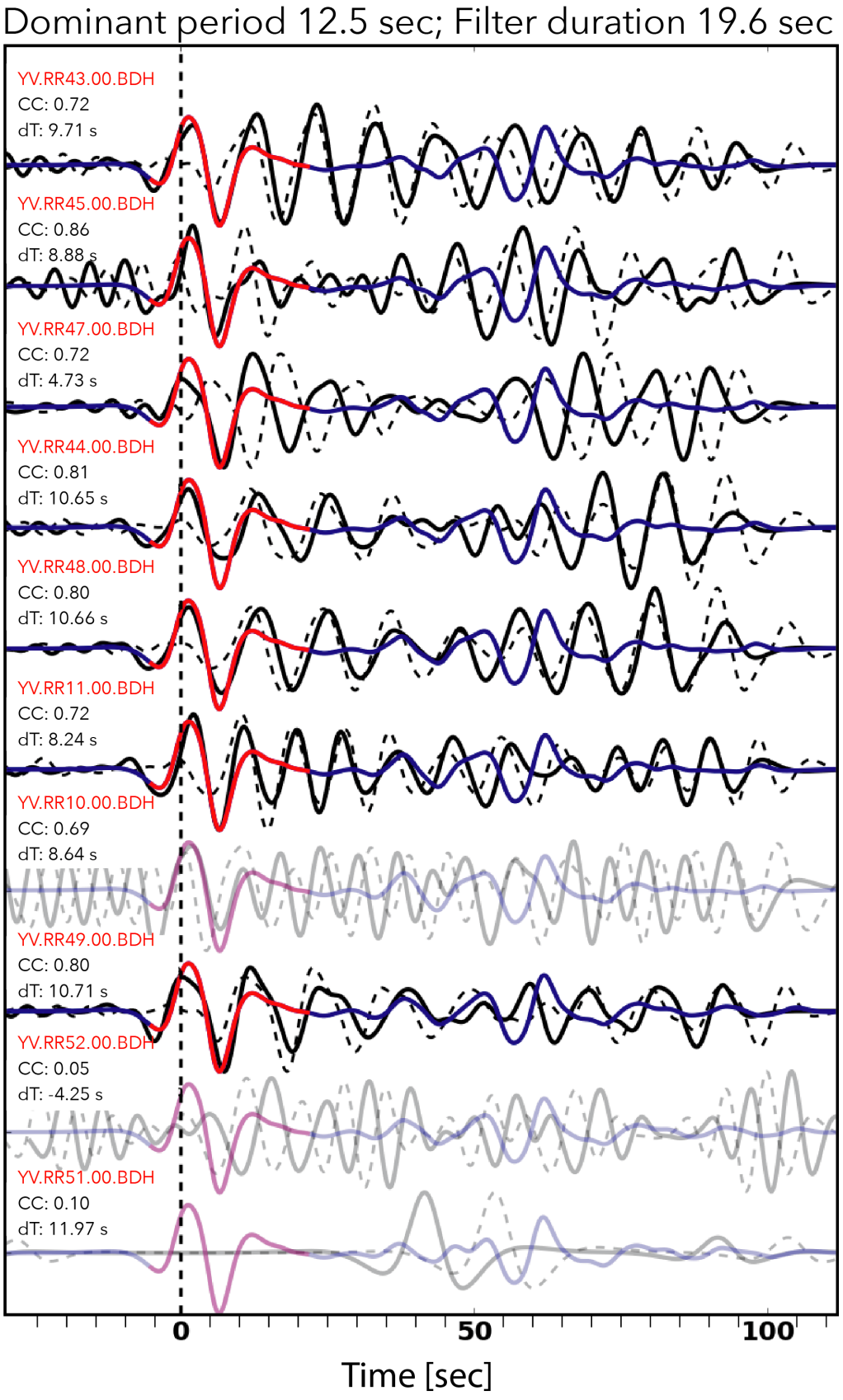

Figure 7.5: Cross-correlation of observed hydrophone data converted to velocity waveforms (black dashed lines) with synthetic velocity seismograms (blue and red lines). The red line highlights the cross-correlation time-window. The solid black line is the real data shifted according to the measured time residual by cross-correlation. Greyed out seismograms failed the first quality check and will not be used in the inversion. The average time shift is around 10 seconds for measurements with a cross correlation factors $> 70\%$. This Gabor filter worked very well and significantly increased the SNR. Reverberations are clearly visible after the onset of the first arrival (marked by a vertical dashed line in black).

example hydrophone recordings for a deep magnitude 7.1 earthquake in Banda Sea, Indonesia (11. Dec 2012, 160 km depth) are shown in Figure 7.4.

Figure 7.5 compares real and synthetic waveforms of ten RHUM-RUM hydrophones filtered by a Gabor filter with 12.5 s dominant period. Seven stations showed high cross-correlation factors, and three failed to pass the automatic quality check. The Gabor filters are tuned for hydrophone data by trial and error. The cross-correlation time windows had to be selected relatively short as the reverberations in the real data are not modelled in the synthetic waveforms. This shows one of the main difficulties in using hydrophone data. Large reverberations are recorded on observed hydrophone data, possibly due to reflections from the sea surface, and to correctly model them, a more sophisticated forward modelling tool is required.

To summarize, in order to use these valuable hydrophone recordings in waveform-based tomographic inversions, I need:

- more accurate forward modelling codes to correctly take into account the effects of crust and ocean. This should help to better model the strong reverberations in hydrophone recordings.
- better filtering strategies. Some of these reverberations are removable by using better filters. To this end, a more detailed analysis of the frequency content of hydrophone data needs to be conducted and (Gabor) filters should be chosen accordingly.
- accurate sensitivity kernel.

7.3.2 Future of deep Earth exploration

New possibilities to increase the data coverage in the oceans opened up in the last years. *MERMAIDS* (Simons et al., 2006, 2009; Hello et al., 2011; Nolet et al., 2016) can stay active up to five years, recording seismic activity in the SOFAR (or DSC) channel. The big advantage is that MERMAIDS are autonomous, easy and cheap to deploy. The downside is that the instruments are floating in the water and hence subject to strong

water currents (low SNR) and only P can be measured. Moreover, the instruments connect to the GPS only when surfacing, for example, after detecting an earthquake. Therefore, the location of the instrument needs to be corrected for the drift in the water column, for example, by using ocean circulation patterns (Nolet et al., 2016).

Another opportunity to investigate the mantle structure beneath the oceans is with *cables*. Nagumo and Walker (1989) suggested to reuse old telecommunication fiber-optic cables for geophysical measurements by deploying instruments next to the cables and connect them to each other. Recently and for the first time, Marra et al. (2018) showed seismic waveforms detected by fibre-optic cables. This method can result in vast amount of data recorded by large number of already-deployed cables, and the data can be used to explore the oceans and seismicity of Earth. Can we use such data for seismic tomography?

In addition to a better instrumentation in oceans and lands, we need to exploit all usable seismic phases in one waveform. This can be done in our current inversion scheme where we cross-correlate traveltimes and amplitudes for large seismological datasets of most seismic phases (e.g., except surface waves). In the future "real" sensitivity kernels, as opposed to Dahlen kernel, will enable us to generate sensitivity kernels for any arbitrary seismic phase.

Moreover, different data-types can be jointly used in one tomographic inversion. Body-wave tomography has its strength in the mid and lower mantle, but towards the surface and due to the nearly vertical incidence angle, vertical smearing occurs beneath stations. To overcome this, a joint surface and body-wave inversion could be beneficial, and ideally, this can result in a whole-mantle data coverage: core mantle boundary (using Pdiff), the mid-mantle (P, PP, etc.), and surface (using surface waves). Several studies have already demonstrated successful joint inversions of body and surface waves using ray-theory to model the body-wave measurements (e.g., Golos et al., 2018). The natural next step is a joint mulitfrequency body-wave and surface wave inversion using wavefield-based sensitivity kernels.

Appendices

—

A
Inversion results

Here, I present a series of inversions conducted to investigate the stability and quality of the tomographic models using the following datasets:

- **page 108** ISC-EHB (P phase)
- **page 109** ISC-EHB and multifrequency Pdiff
- **page 110** RHUM-RUM+ dataset (P phase)
- **page 111** ISC-EHB, multifrequency Pdiff and RHUM-RUM+ with $\frac{damping}{smoothing} = 0.3$
- **page 112** ISC-EHB, multifrequency Pdiff and RHUM-RUM+ with $\frac{damping}{smoothing} = 0.5$
- **page 113** ISC-EHB, multifrequency Pdiff and RHUM-RUM+ with $\frac{damping}{smoothing} = 0.7$
- **page 114** ISC-EHB, multifrequency Pdiff and RHUM-RUM+ with $\frac{damping}{smoothing} = 0.9$
- **page 115** ISC-EHB, multifrequency Pdiff and RHUM-RUM+ with $\frac{damping}{smoothing} = 1.2$
- **page 116** ISC-EHB, multifrequency Pdiff and RHUM-RUM+ with no traveltime corrections with $\frac{damping}{smoothing} = 0.7$
- **page 117** ISC-EHB (S phase)

- **page 118** S40RTS (S phase)
- **page 119** S40RTS and ISC-EHB (S phase)
- **page 120** RHUM-RUM (S phase)
- **page 121** S40RTS, ISC-EHB and RHUM-RUM (S phase)

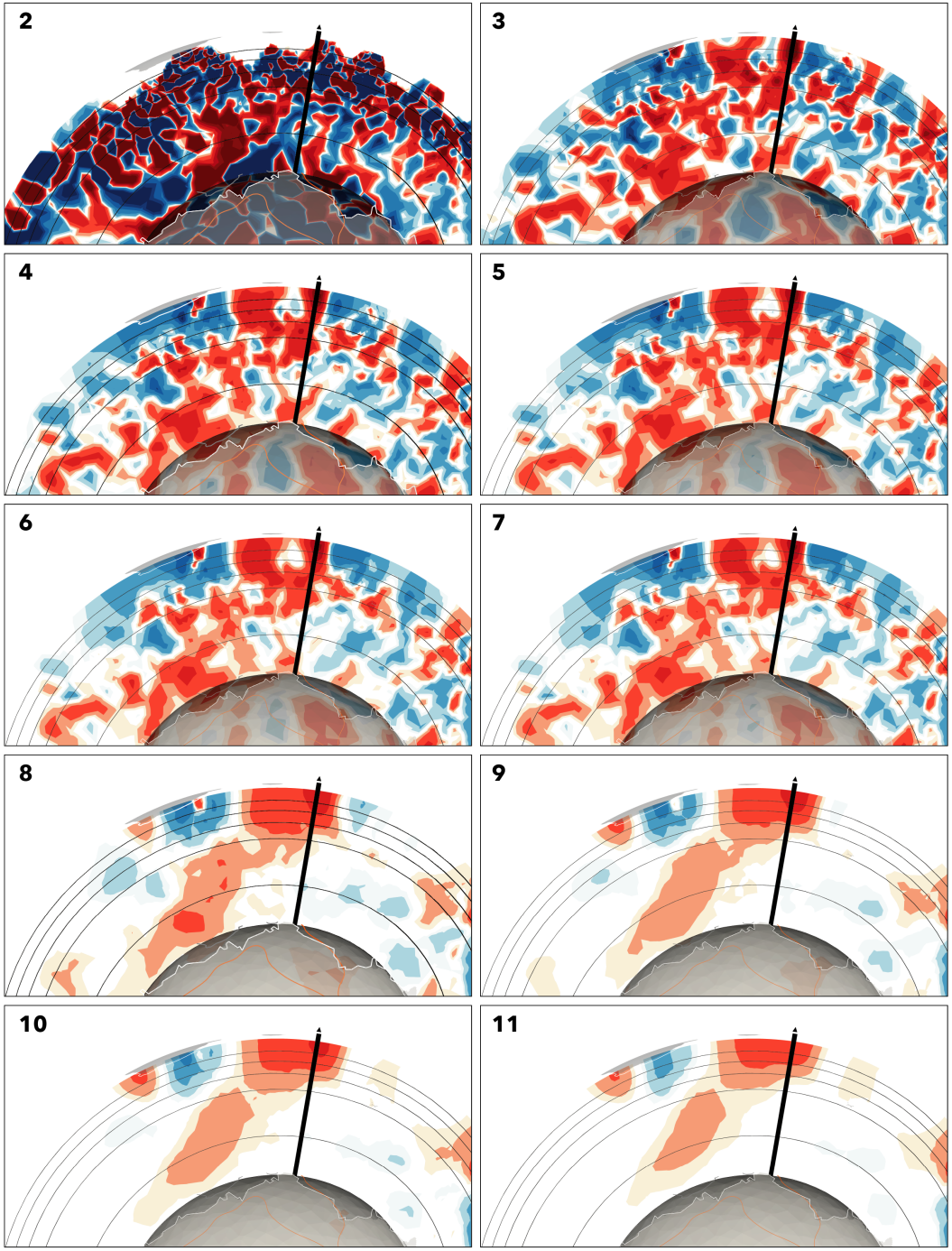

Details

Dataset	**ISC**	Phase(s)	**P**
apriory uncertainties	**0.99**	crustal model	**CRUST2.0**
apriory dlnVp[%]	**2**	$\frac{\text{damping}}{\text{smoothing}} =$	**0.3**
hypoctr corr (lat/lon; depth in km)	**20/20;5**	outliers	**132078 (5.6%)**
origin time correction (sec)	**10**	# row	**2342621**
		# col	**28429**

L - curve

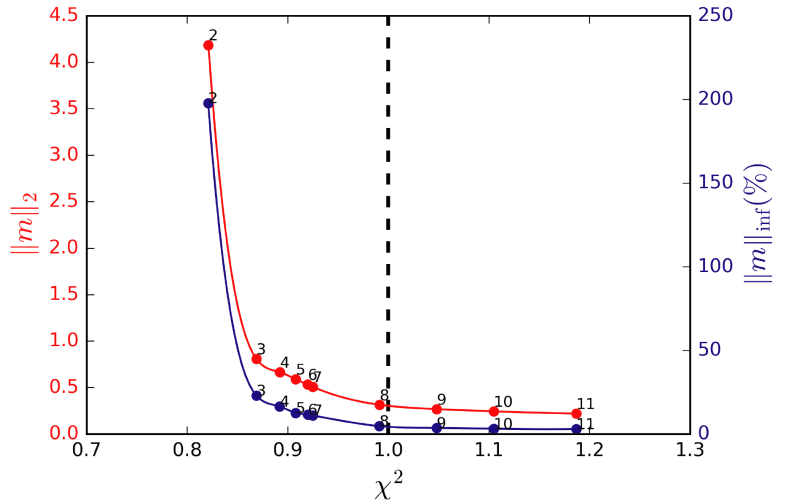

Best solution 3-D slice

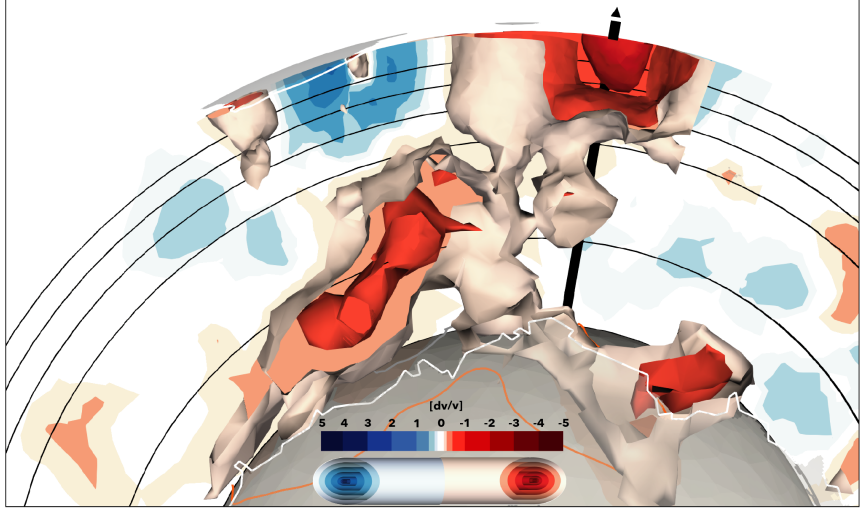

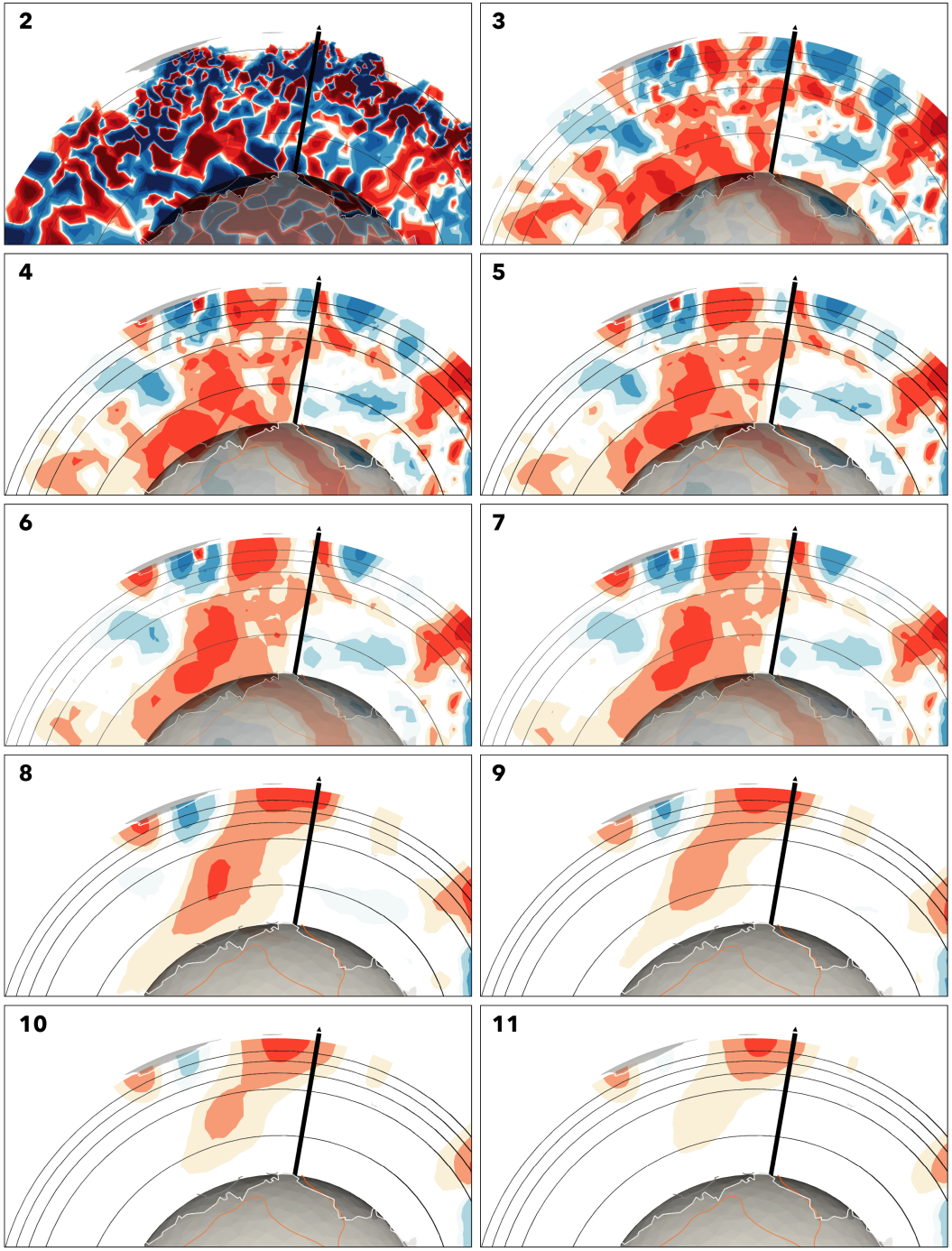

Details

Dataset	**ISC and P-diffracted**	Phase(s)	**P + Pdiff**
apriory uncertainties	**ISC 0.99; 80-85% 1.0; 85-90% 0.6; 90-95% 0.4; 95-100% 0.3**	crustal model	**CRUST2.0**
apriory dlnVp[%]	**2**	$\frac{\text{damping}}{\text{smoothing}} =$	**0.3**
hypoctr corr (lat/lon; depth in km)	**20/20; 5**	outliers	**147045 (5.8%)**
origin time correction (sec)	**10**	# row	**2532060**
		# col	**137839**

L - curve

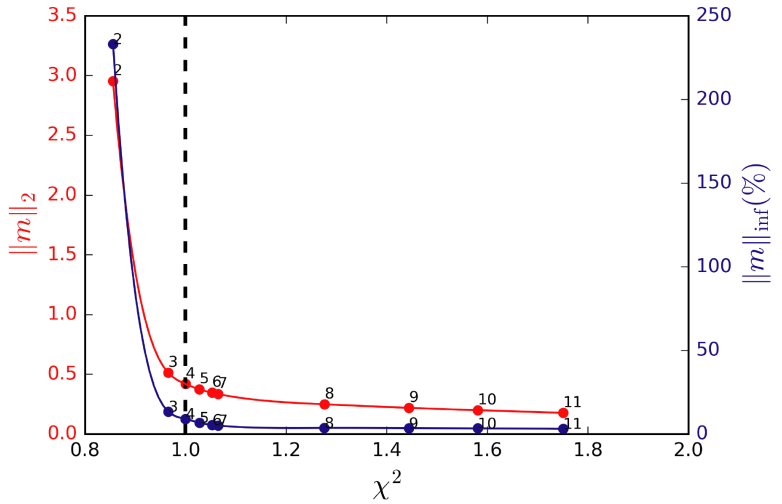

Best solution 3-D slice

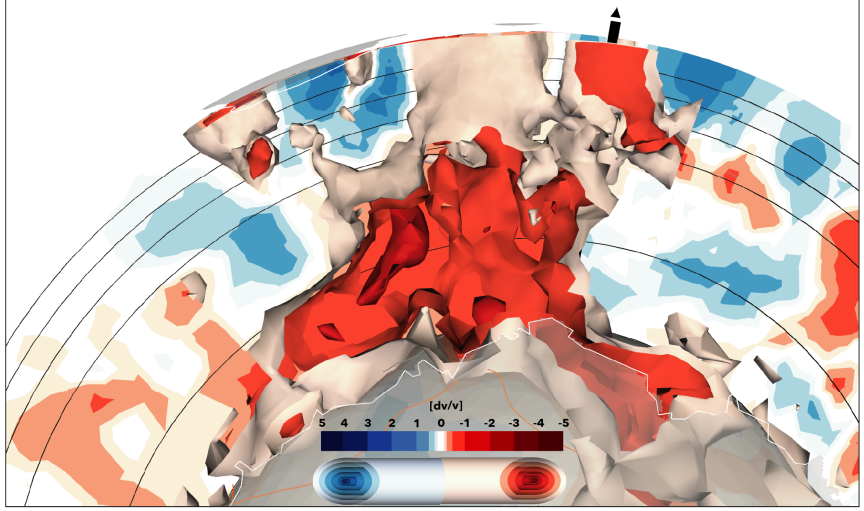

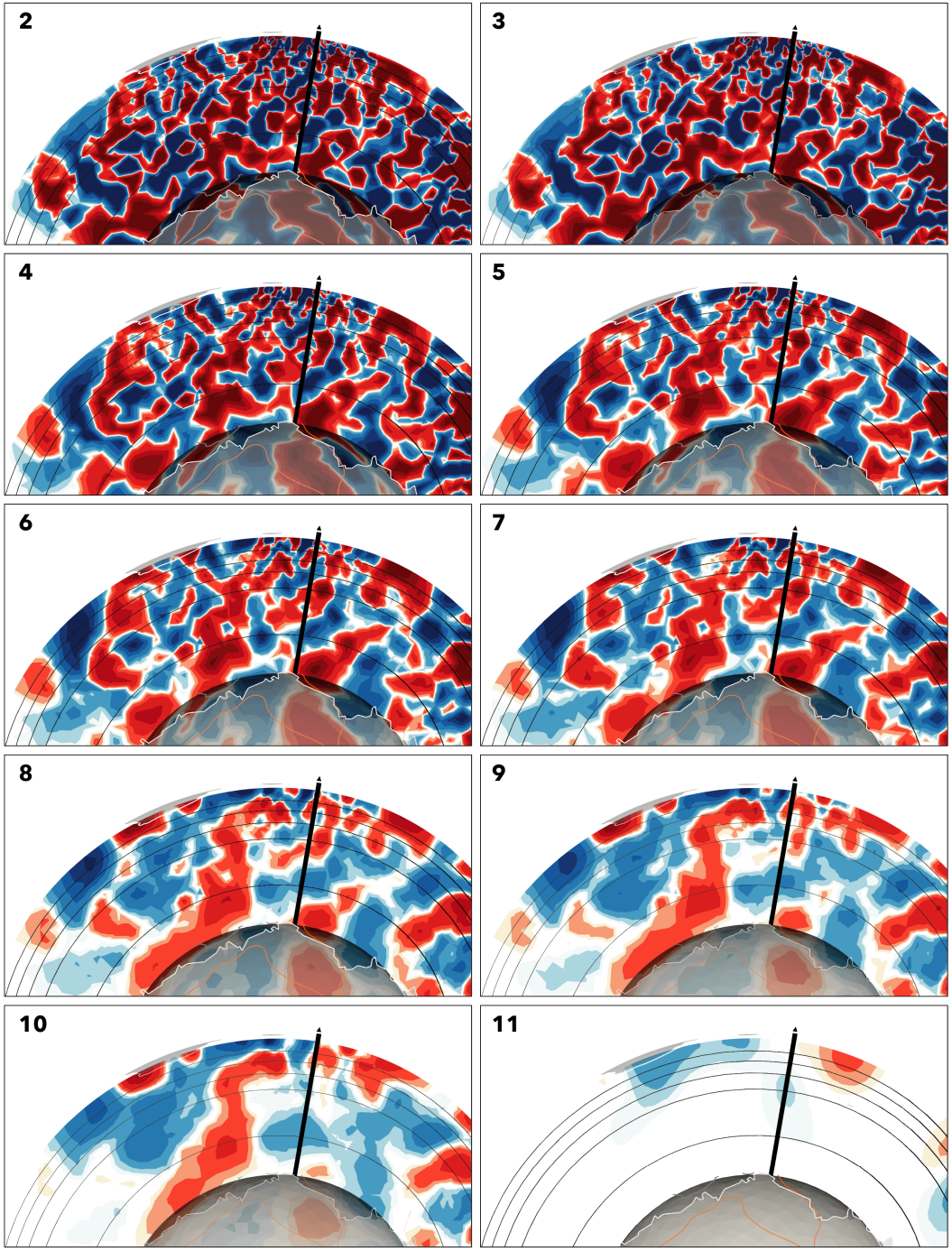

Details

Dataset	**RHUM-RUM (extended)**	Phase(s)	**P**
apriory uncertainties	**80-85% 1.0; 85-90% 0.6; 90-95% 0.4; 95-100% 0.3**	crustal model	**CRUST2.0**
apriory dlnVp[%]	**2**	$\frac{\text{damping}}{\text{smoothing}} =$	**0.3**
hypoctr corr (lat/lon; depth in km)	**20/20; 5**	outliers	**794 (1.4%)**
origin time correction (sec)	**10**	# row	**55657**
		# col	**62182**

L - curve

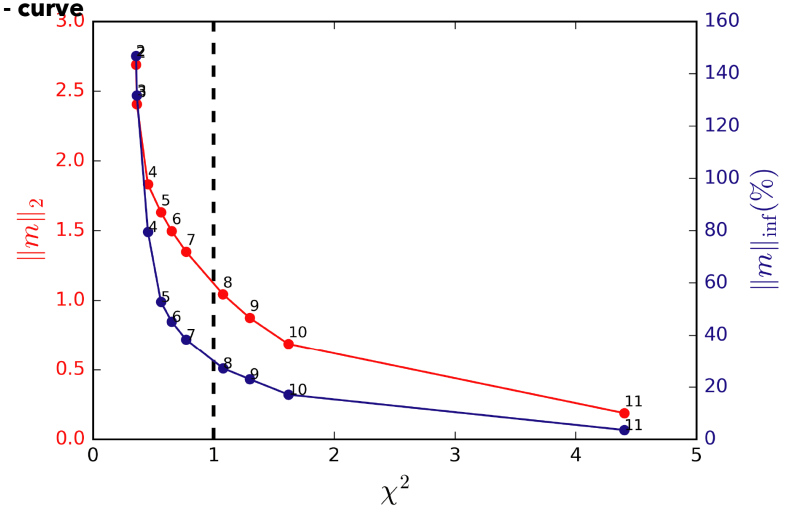

Best solution 3-D slice

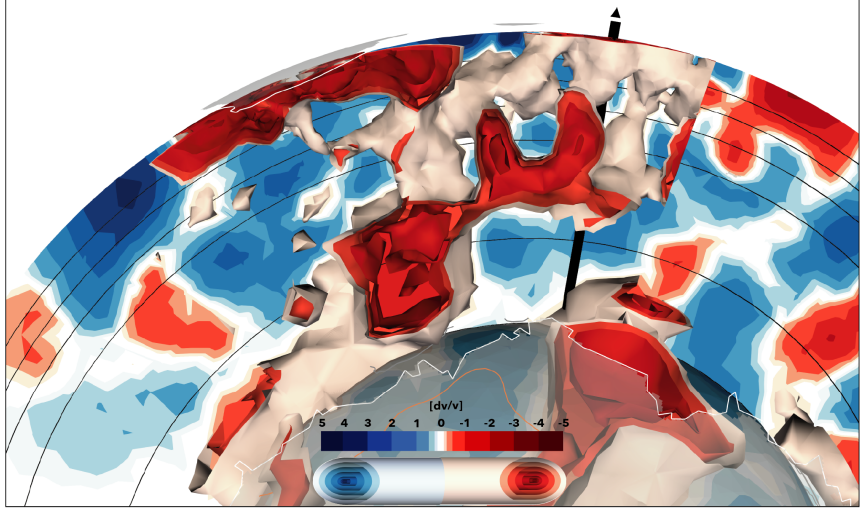

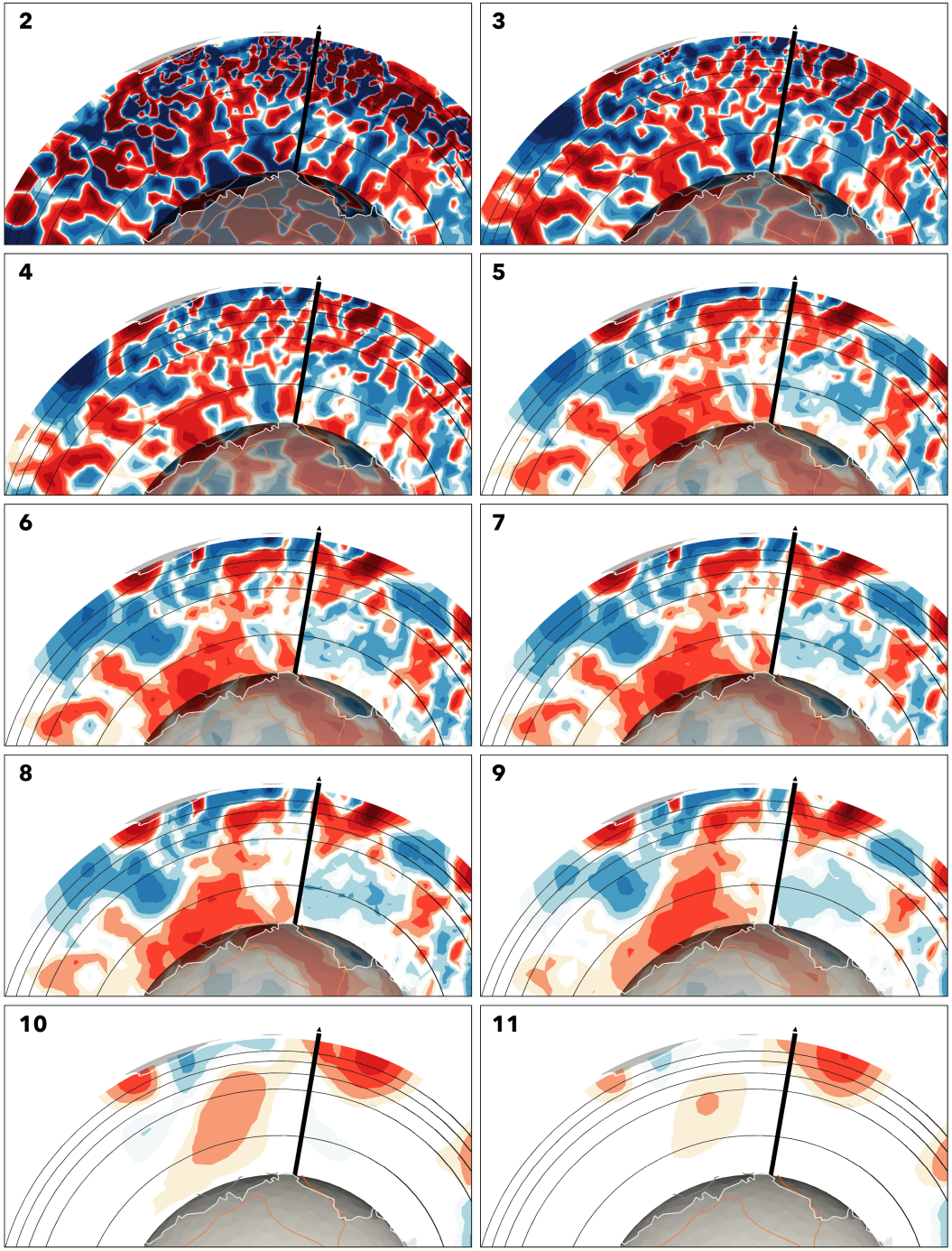

Details

Dataset	**RHUM-RUM, ISC and P-diffracted**	Phase(s)	**P + Pdiff**
apriory uncertainties	**ISC 0.99; 80-85% 1.0; 85-90% 0.6; 90-95% 0.4; 95-100% 0.3**	crustal model	**CRUST2.0**
apriory dlnVp[%]	**2**	$\frac{\text{damping}}{\text{smoothing}}$ =	**0.3**
hypoctr corr (lat/lon; depth in km)	**20/20; 5**	outliers	**150719 (5.8%)**
origin time correction (sec)	**10**	# row	**2587717**
		# col	**143937**

L - curve

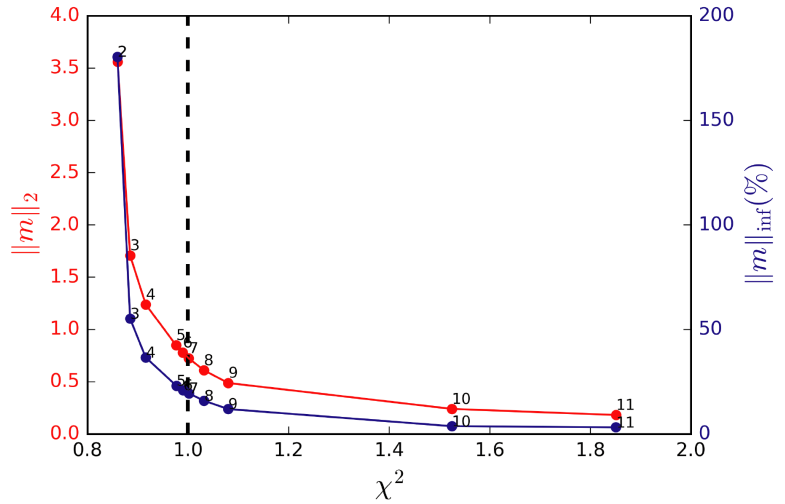

Best solution 3-D slice

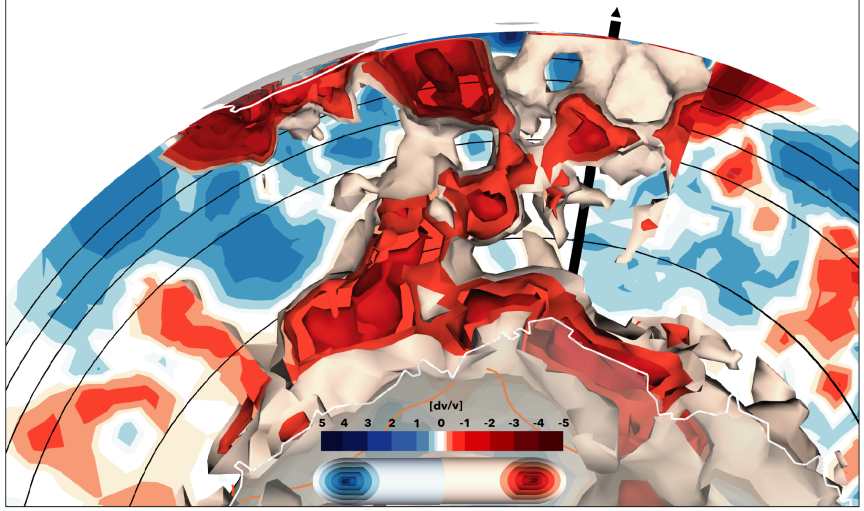

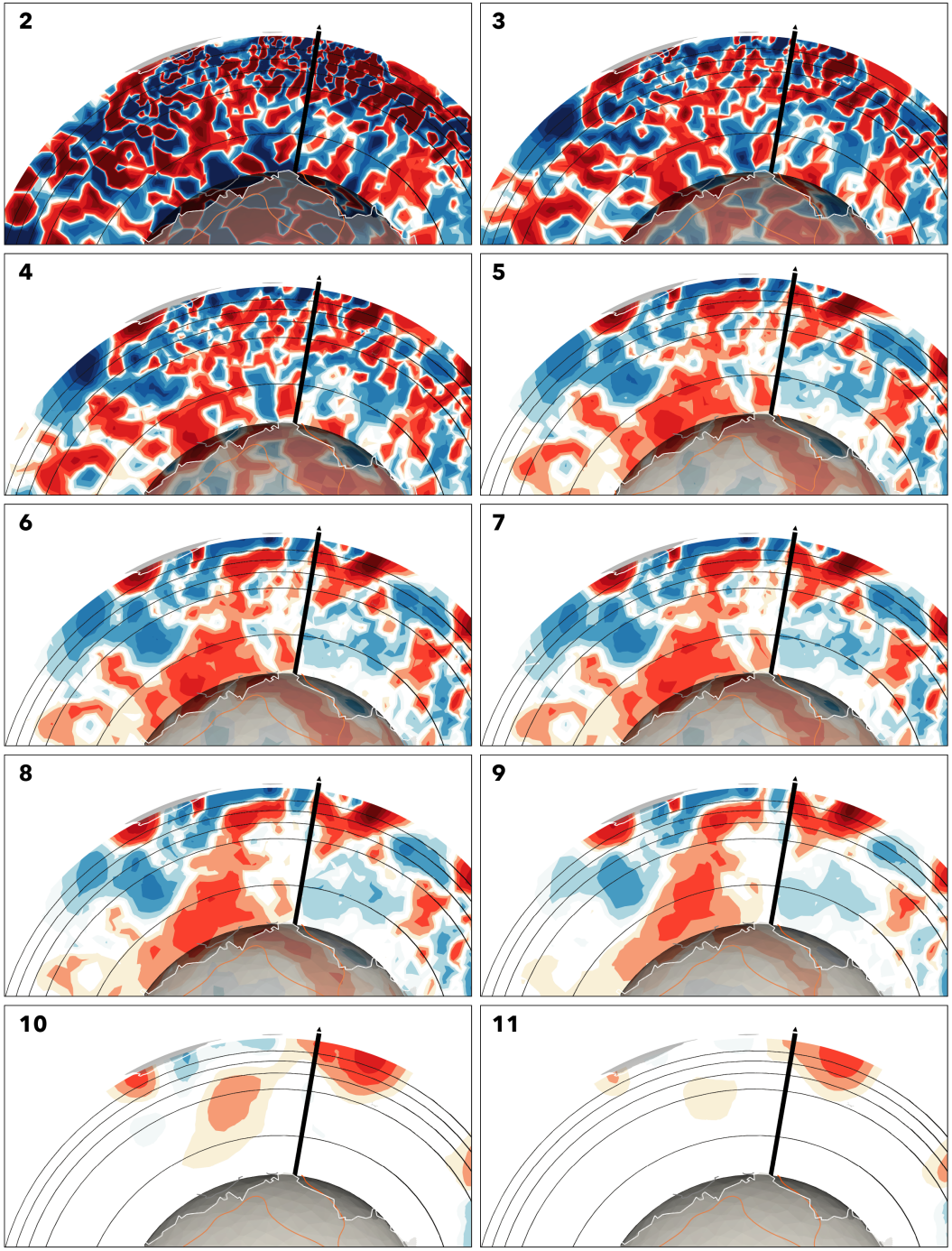

Details

Dataset	**RHUM-RUM, ISC and P-diffracted**	Phase(s)	**P + Pdiff**
apriory uncertainties	**ISC 0.99; 80-85% 1.0; 85-90% 0.6; 90-95% 0.4; 95-100% 0.3**	crustal model	**CRUST2.0**
apriory dlnVp[%]	**2**	$\frac{\text{damping}}{\text{smoothing}} =$	**0.5**
hypoctr corr (lat/lon; depth in km)	**20/20; 5**	outliers	**150719 (5.8%)**
origin time correction (sec)	**10**	# row	**2587717**
		# col	**143937**

L - curve

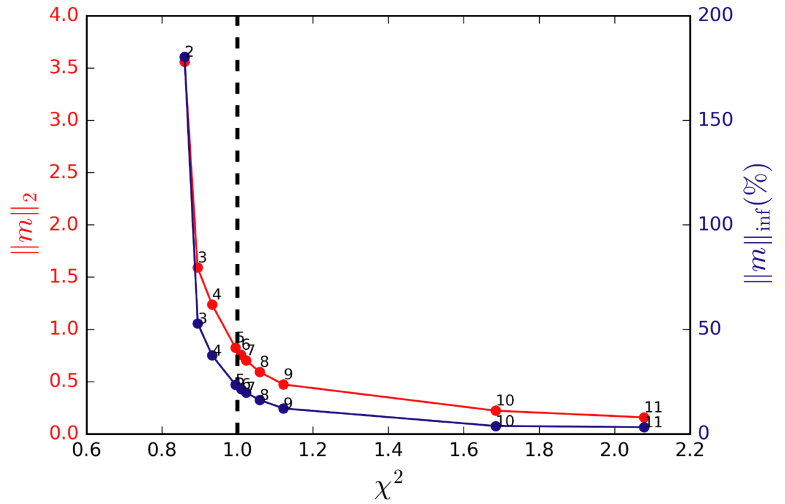

Best solution 3-D slice

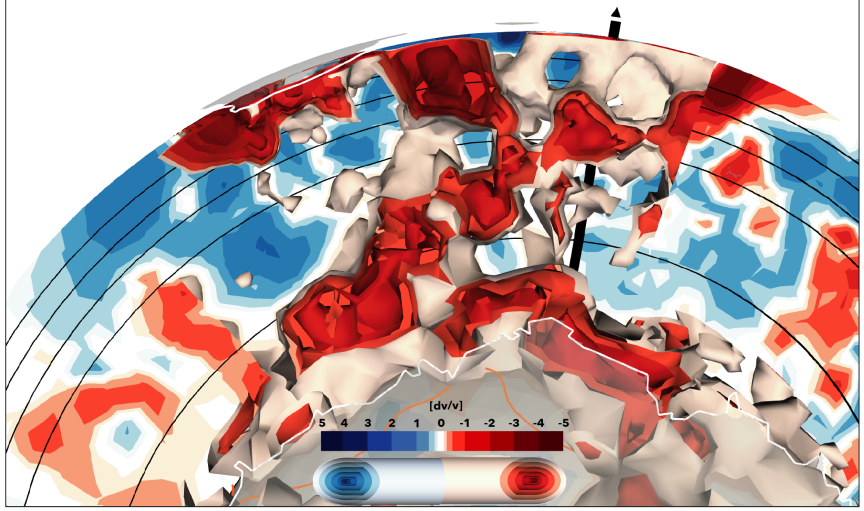

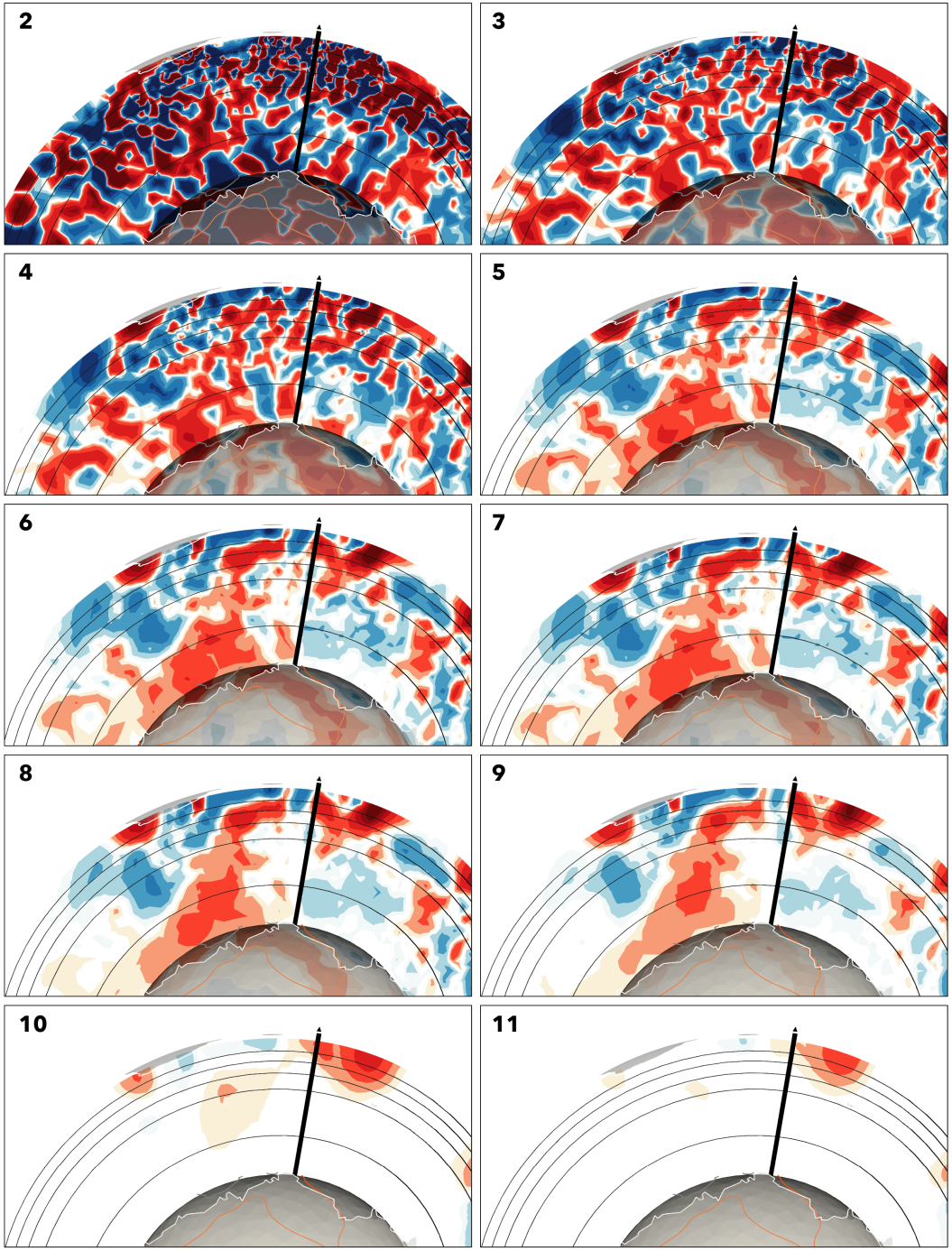

Details

Dataset	**RHUM-RUM, ISC and P-diffracted**	Phase(s)	**P + Pdiff**
apriory uncertainties	**ISC 0.99; 80-85% 1.0; 85-90% 0.6; 90-95% 0.4; 95-100% 0.3**	crustal model	**CRUST2.0**
apriory dlnVp[%]	**2**	$\frac{\text{damping}}{\text{smoothing}} =$	**0.7**
hypoctr corr (lat/lon; depth in km)	**20/20; 5**	outliers	**150719 (5.8%)**
origin time correction (sec)	**10**	# row	**2587717**
		# col	**143937**

L - curve

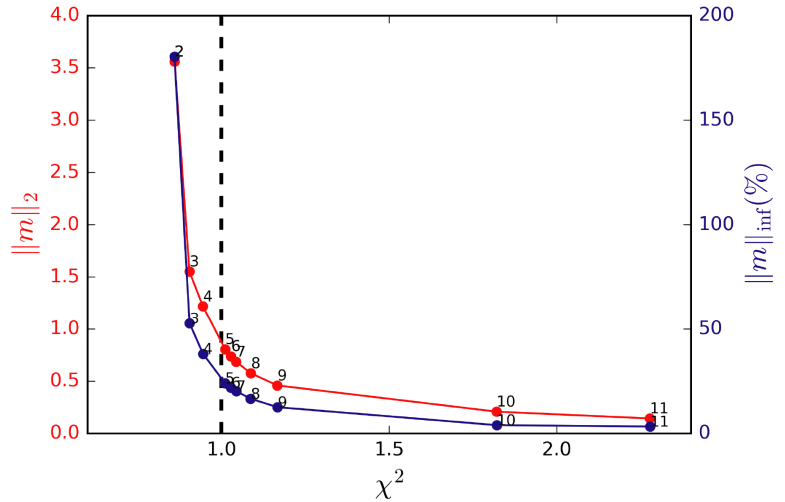

Best solution 3-D slice

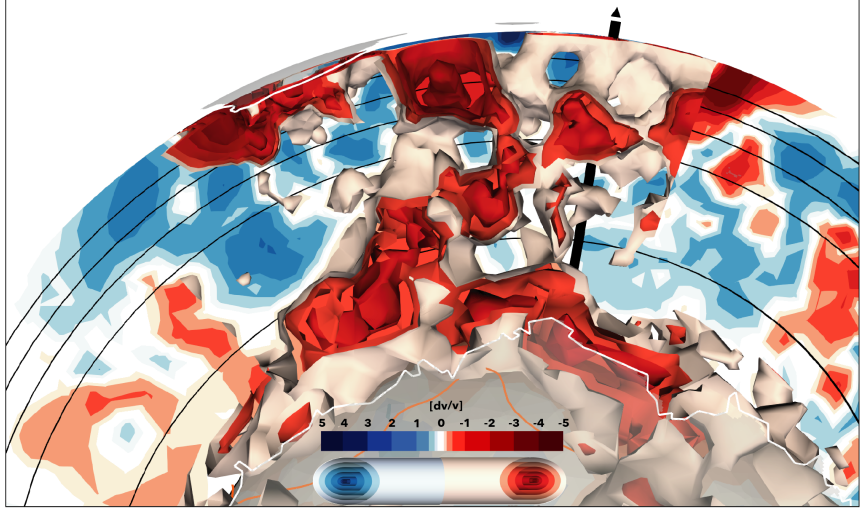

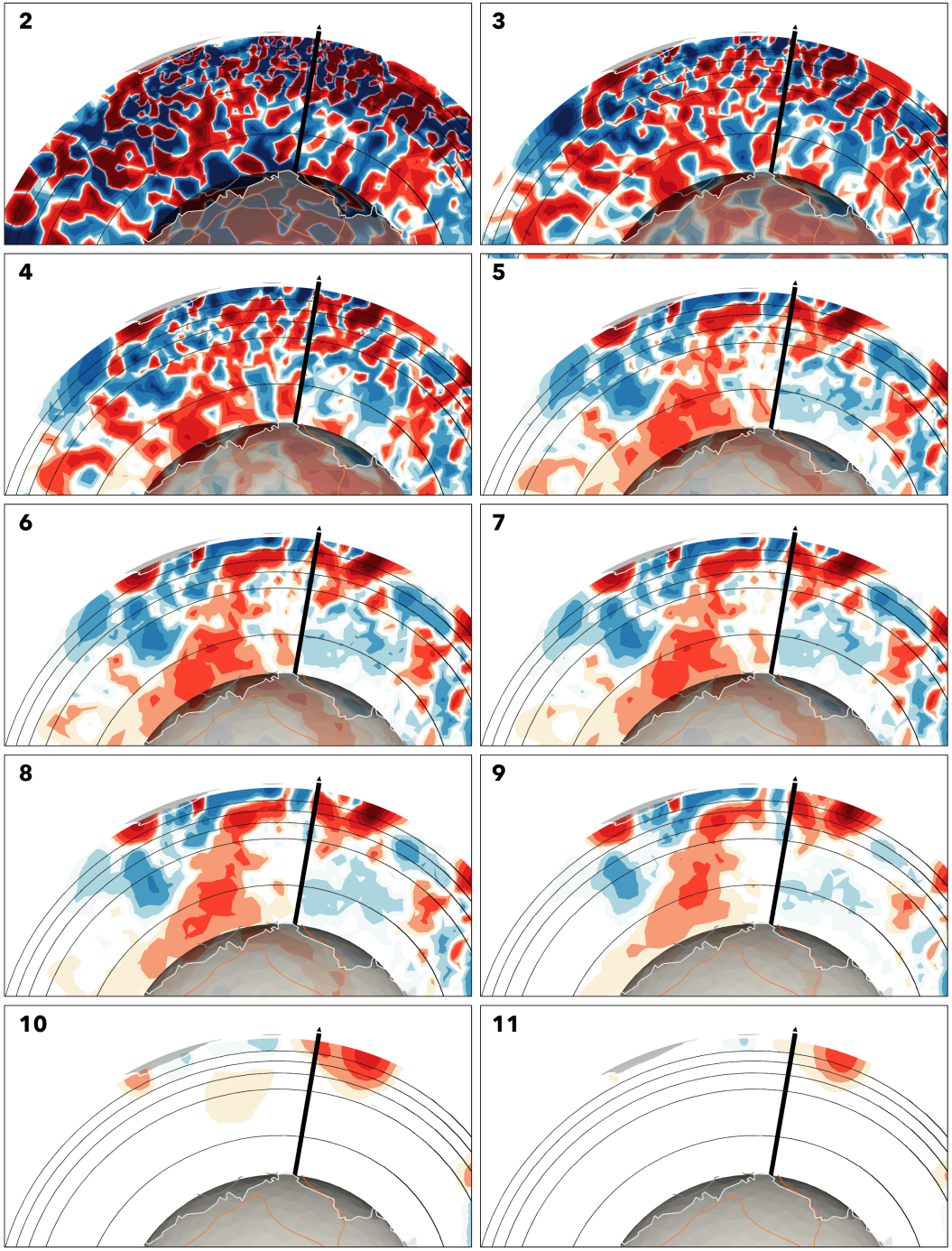

Details

Dataset	**RHUM-RUM, ISC and P-diffracted**	Phase(s)	**P + Pdiff**
apriory uncertainties	**ISC 0.99; 80-85% 1.0; 85-90% 0.6; 90-95% 0.4; 95-100% 0.3**	crustal model	**CRUST2.0**
apriory dlnVp[%]	**2**	$\frac{\text{damping}}{\text{smoothing}} =$	**0.9**
hypoctr corr (lat/lon; depth in km)	**20/20; 5**	outliers	**150719 (5.8%)**
origin time correction (sec)	**10**	# row	**2587717**
		# col	**143937**

L - curve

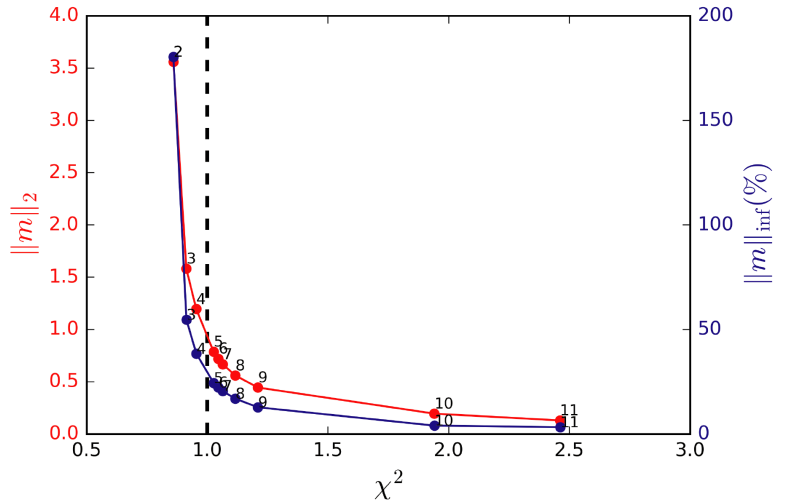

Best solution 3-D slice

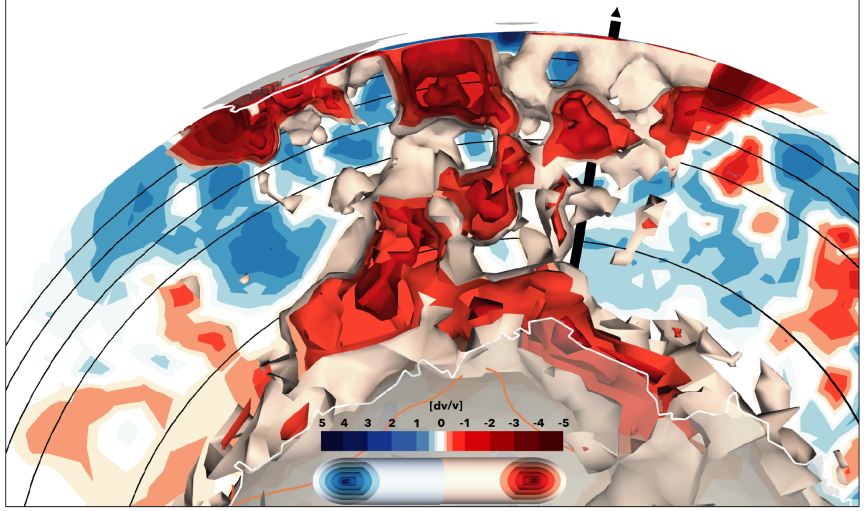

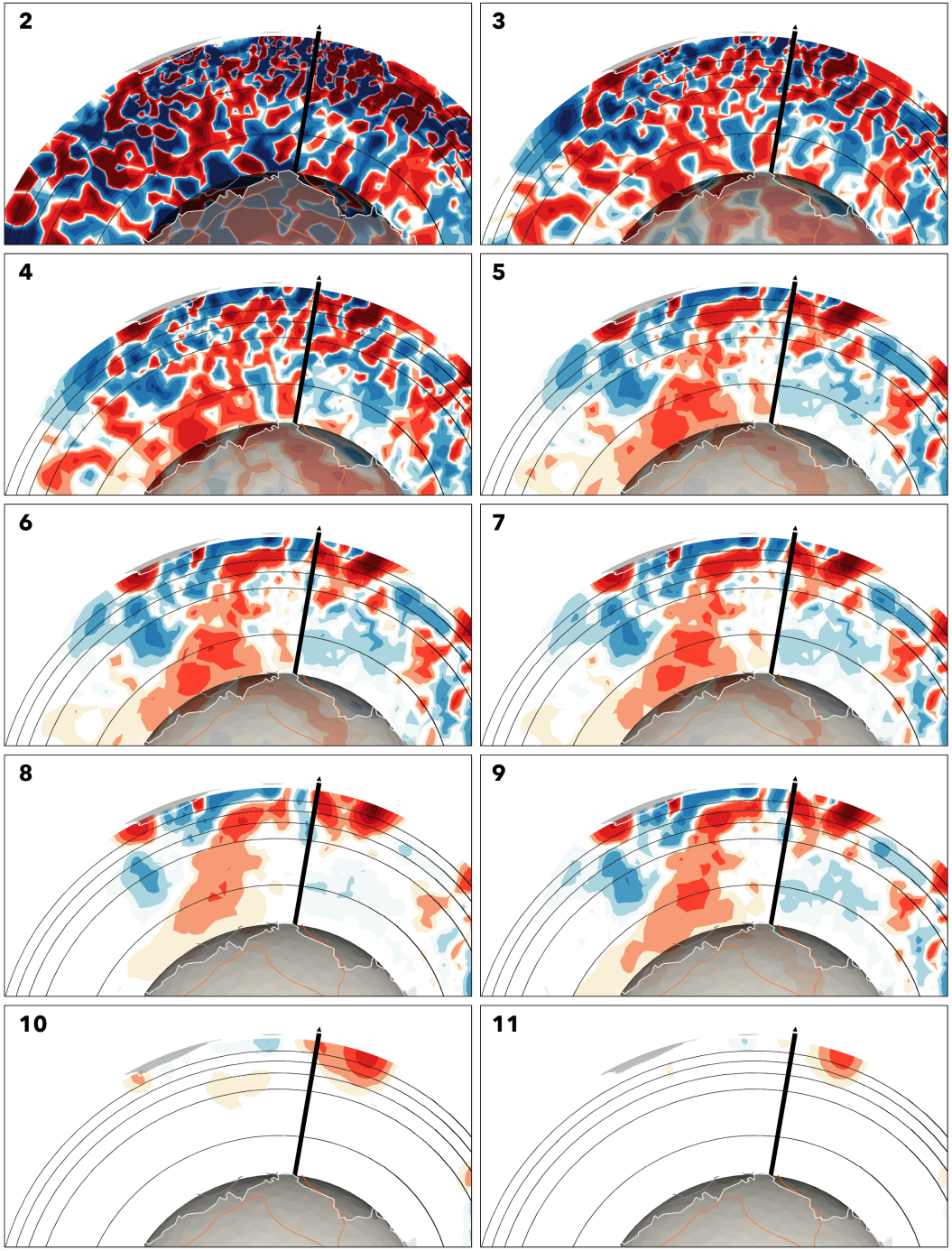

Details

Dataset	**RHUM-RUM, ISC and P-diffracted**	Phase(s)	**P + Pdiff**
apriory uncertainties	**ISC 0.99; 80-85% 1.0; 85-90% 0.6; 90-95% 0.4; 95-100% 0.3**	crustal model	**CRUST2.0**
apriory dlnVp[%]	**2**	$\frac{\text{damping}}{\text{smoothing}} =$	**1.2**
hypoctr corr (lat/lon; depth in km)	**20/20; 5**	outliers	**150719 (5.8%)**
origin time correction (sec)	**10**	# row	**2587717**
		# col	**143937**

L - curve

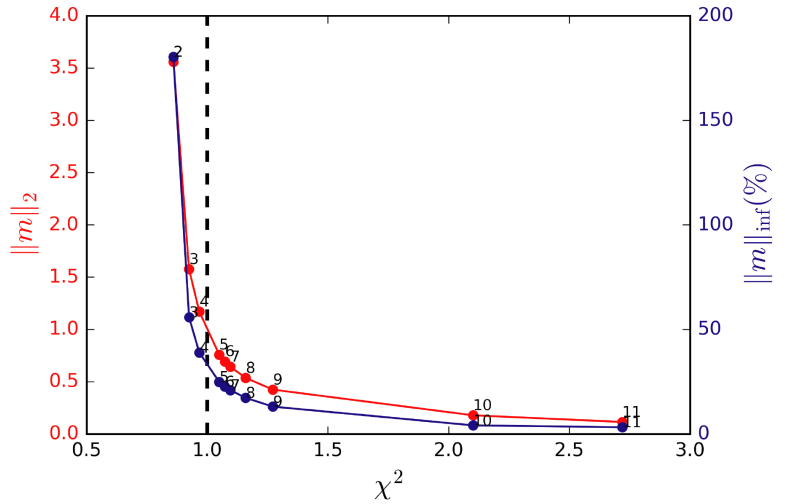

Best solution 3-D slice

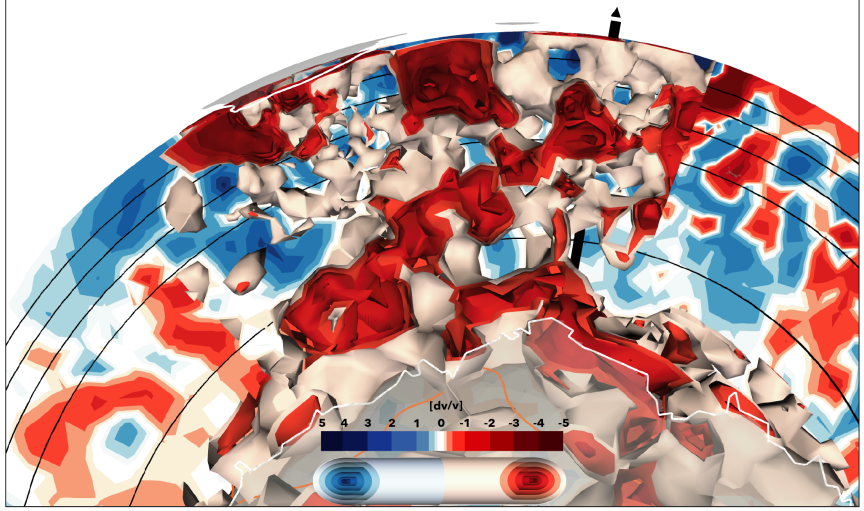

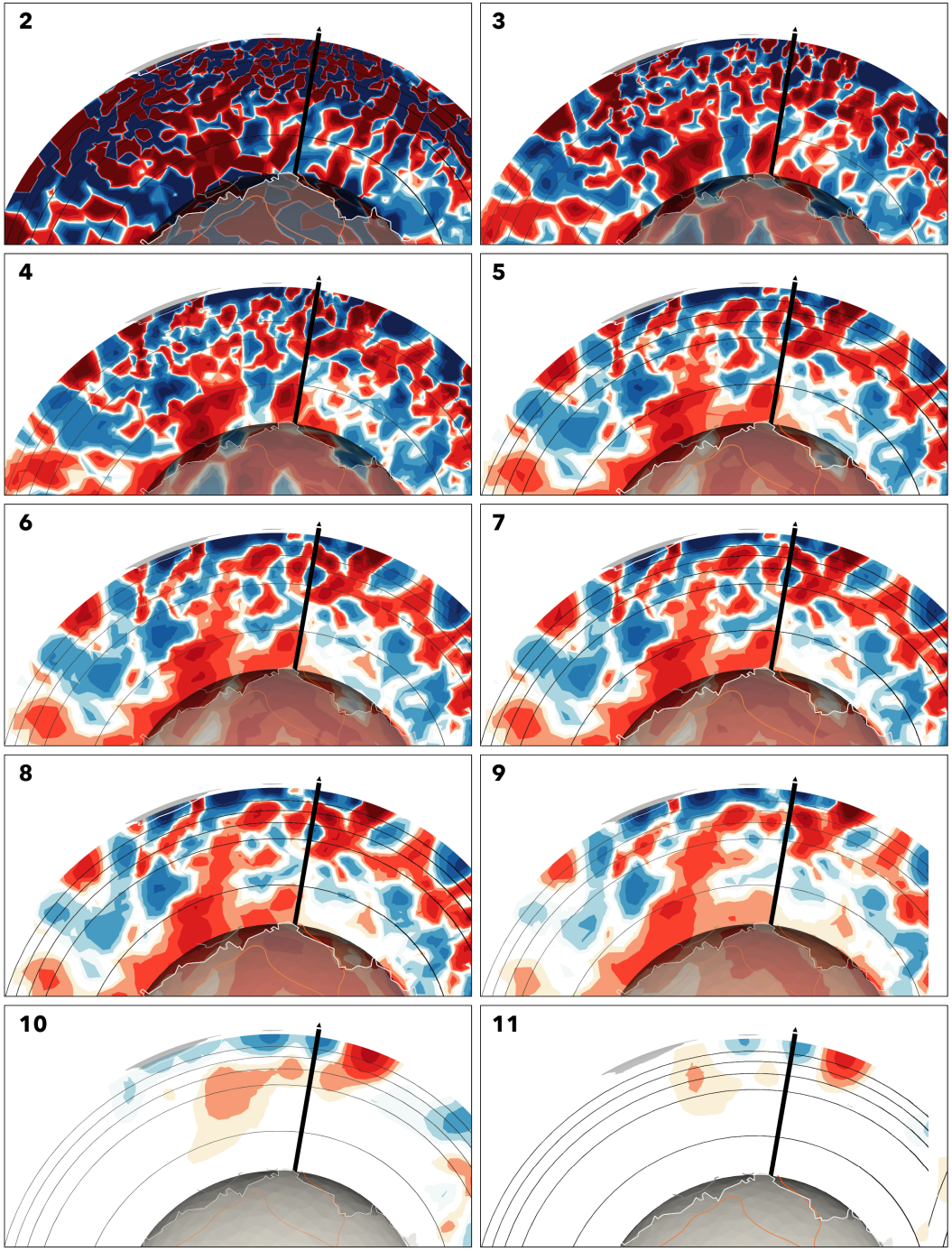

Details

Dataset	**RHUM-RUM, ISC and P-diffracted**	Phase(s)	**P + Pdiff**
apriory uncertainties	**ISC 0.99; 80-85% 1.0; 85-90% 0.6; 90-95% 0.4; 95-100% 0.3**	crustal model	**CRUST2.0**
apriory dlnVp[%]	**2**	$\frac{\text{damping}}{\text{smoothing}}$ =	**0.7**
hypoctr corr (lat/lon; depth in km)	**--**	outliers	**225898 (8.7%)**
origin time correction (sec)	**--**	# row	**2587717**
		# col	**56709**

L - curve

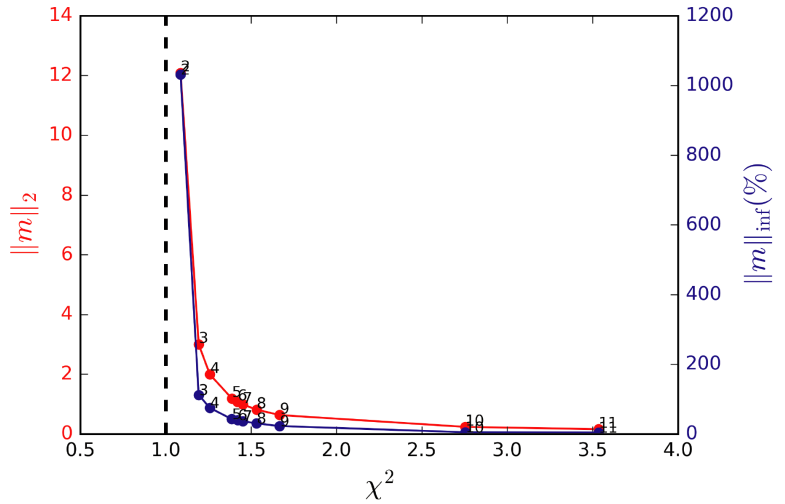

Best solution 3-D slice

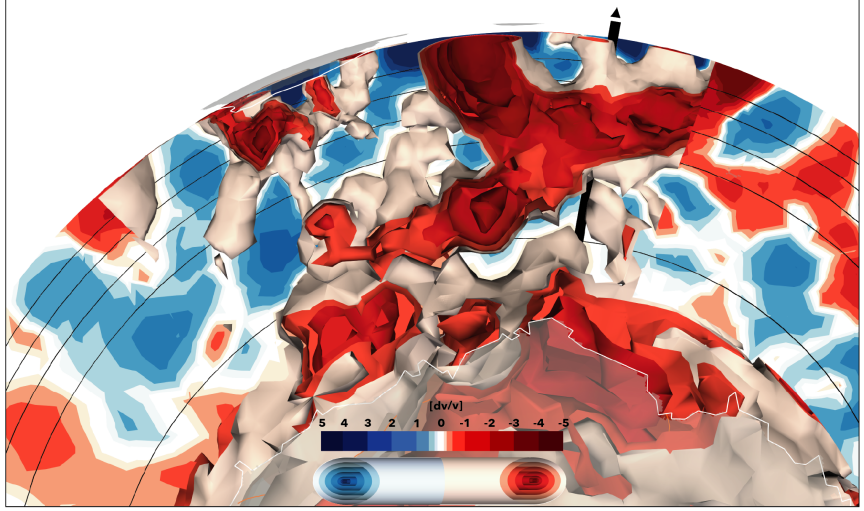

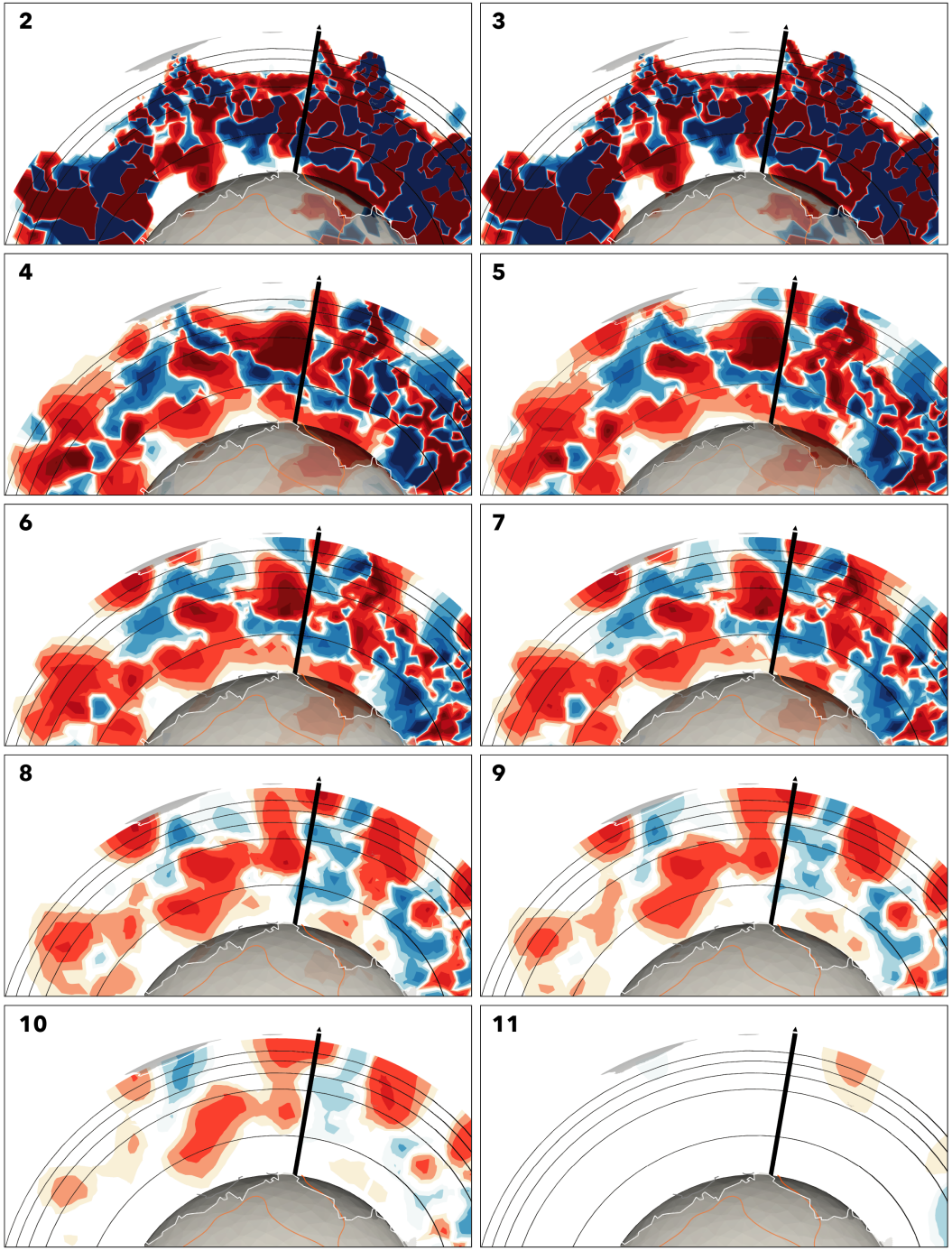

Details

Dataset	**ISC**	Phase(s)	**S**
apriory uncertainties	**0.99**	crustal model	**CRUST2.0**
apriory dlnVp[%]	**5**	$\frac{\text{damping}}{\text{smoothing}} =$	**0.3**
hypoctr corr (lat/lon; depth in km)	**20/20; 5**	outliers	**3384 (2.5%)**
origin time correction (sec)	**10**	# row	**133925**
		# col	**122593**

L - curve

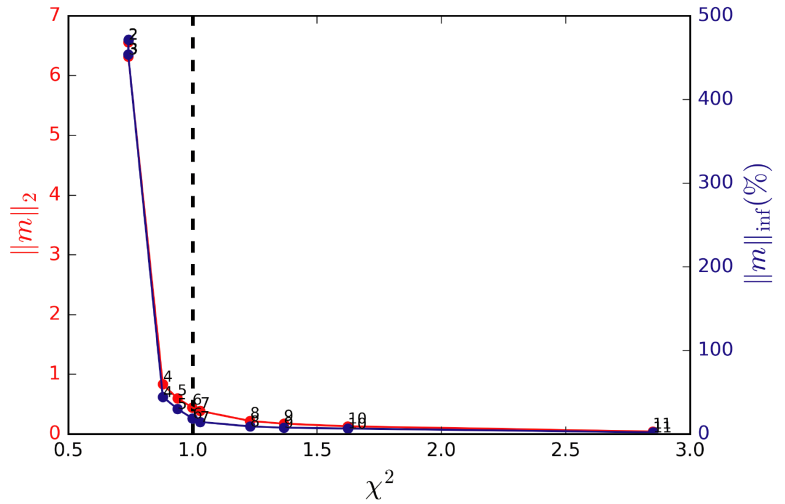

Best solution 3-D slice

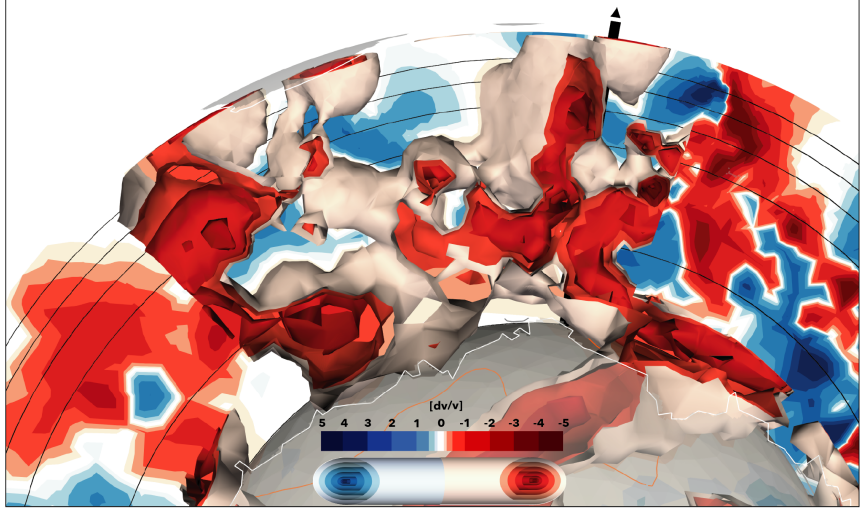

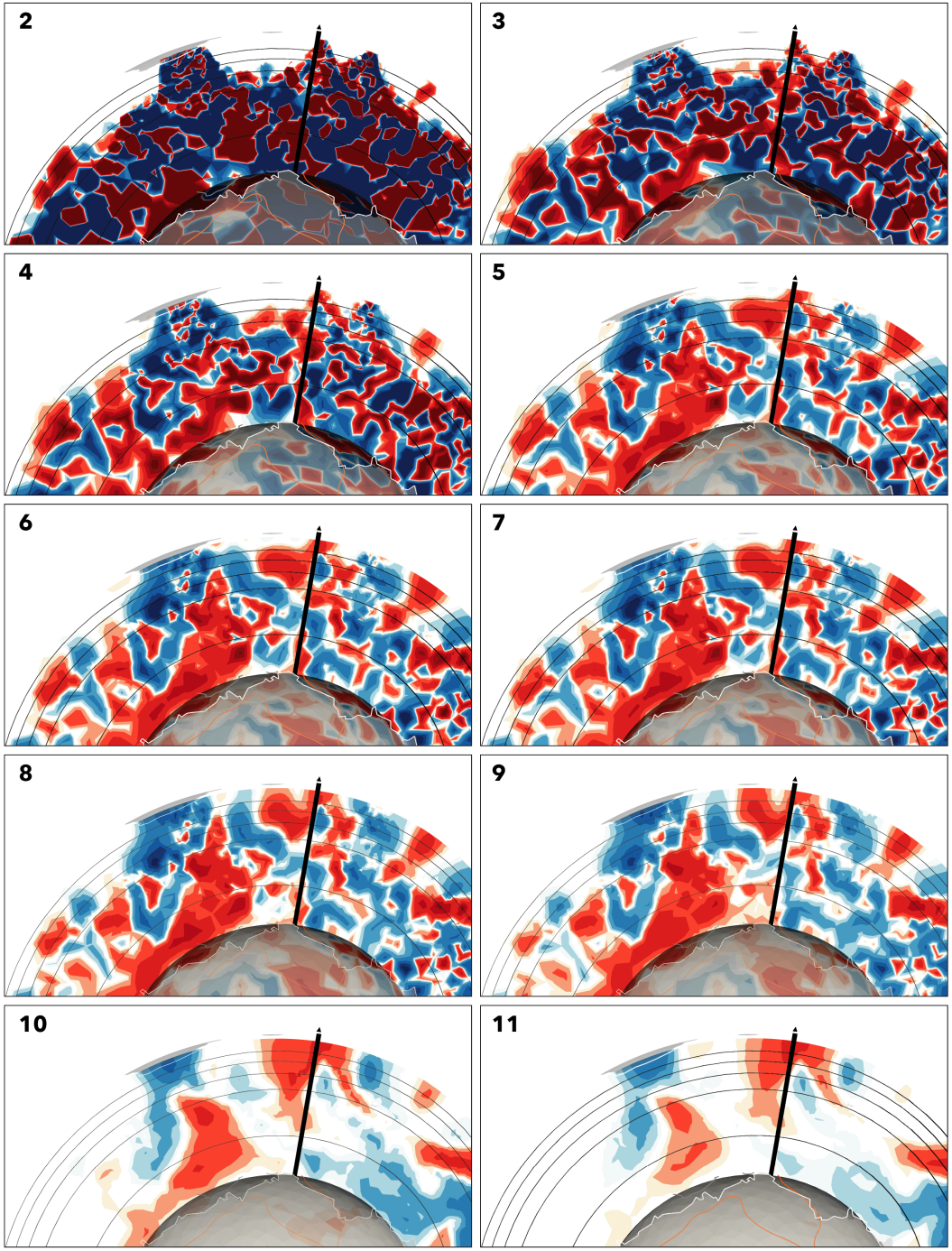

Details

Dataset	**S40RTS**	Phase(s)	**S**
apriory uncertainties	**0.99**	crustal model	**CRUST2.0**
apriory dlnVp[%]	**10**	$\frac{\text{damping}}{\text{smoothing}} =$	**0.7**
hypoctr corr (lat/lon; depth in km)	**20/20; 5**	outliers	**3543 (2.4%)**
origin time correction (sec)	**10**	# row	**145546**
		# col	**72537**

L - curve

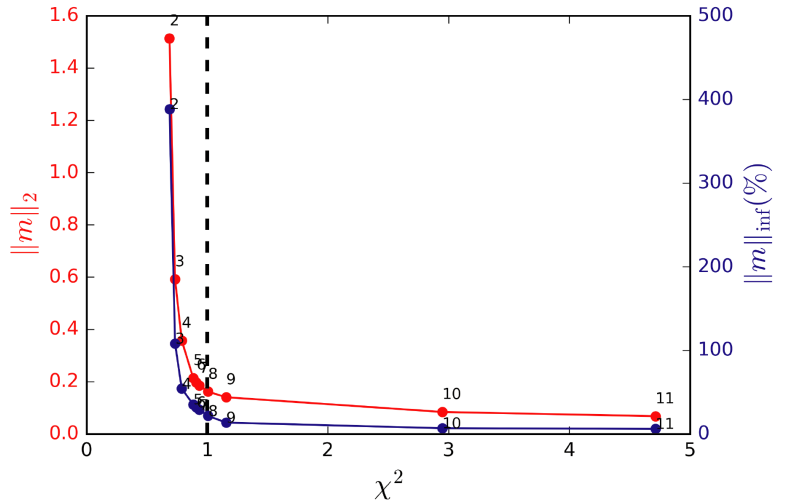

Best solution 3-D slice

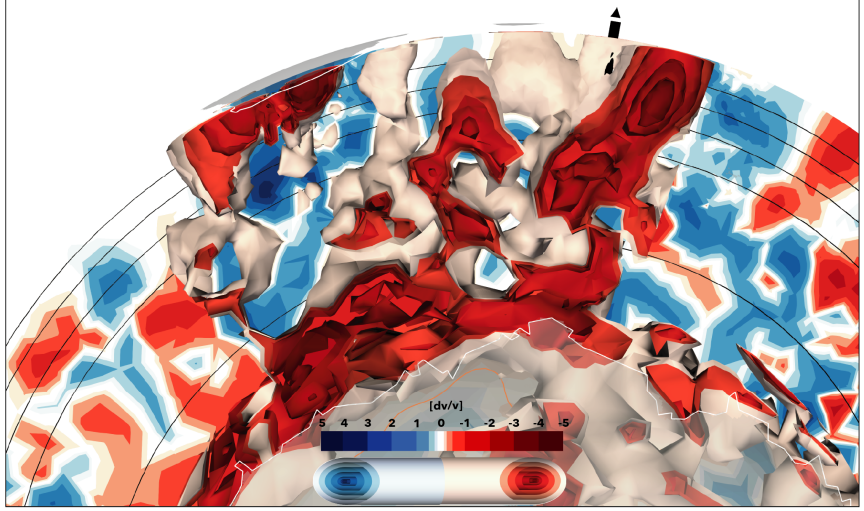

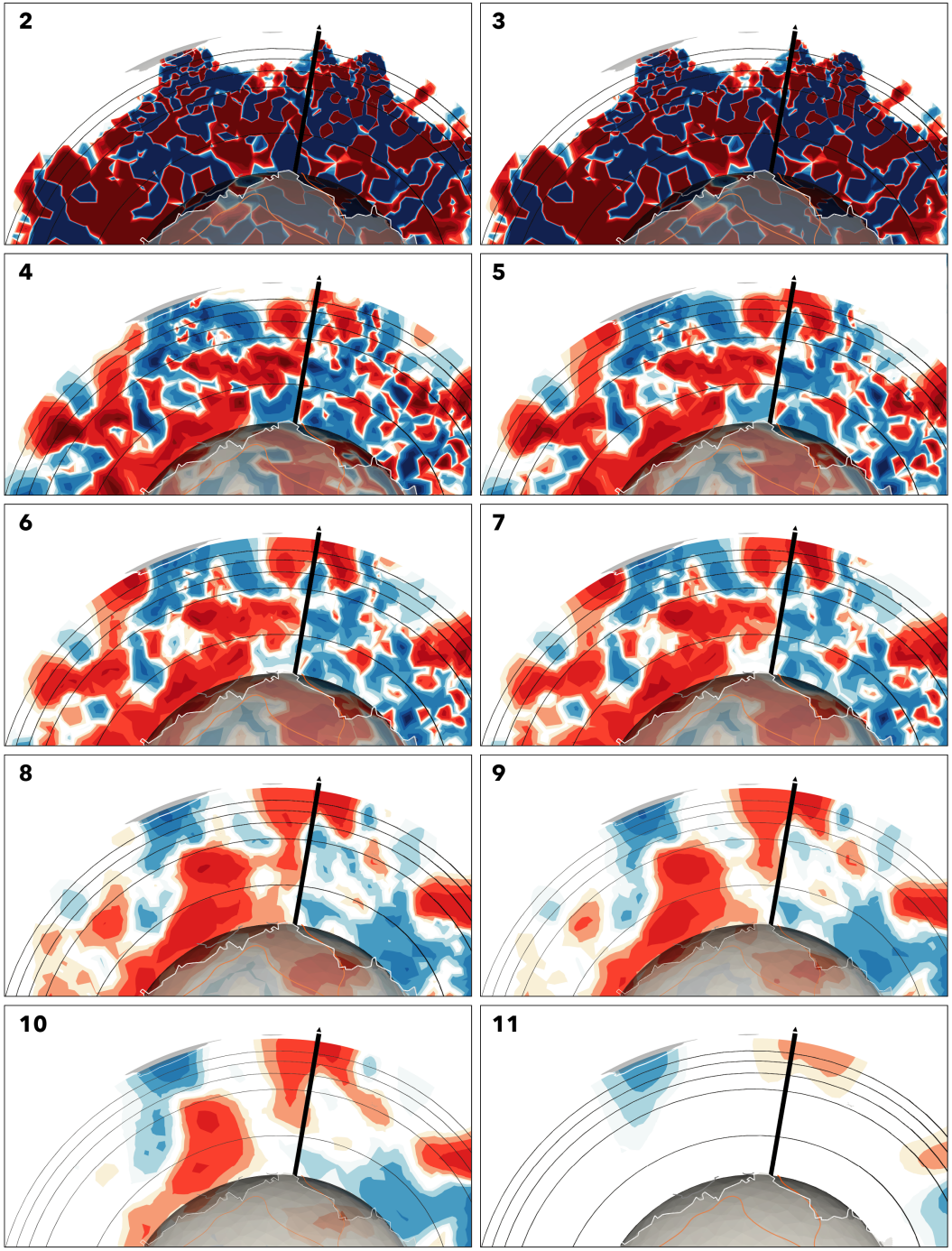

Details

Dataset	**ISC and S40RTS**	Phase(s)	**S**
apriory uncertainties	**0.99**	crustal model	**CRUST2.0**
apriory dlnVp[%]	**5**	$\frac{\text{damping}}{\text{smoothing}} =$	**0.3**
hypoctr corr (lat/lon; depth in km)	**20/20; 5**	outliers	**8835 (3.2%)**
origin time correction (sec)	**10**	# row	**279471**
		# col	**138421**

L - curve

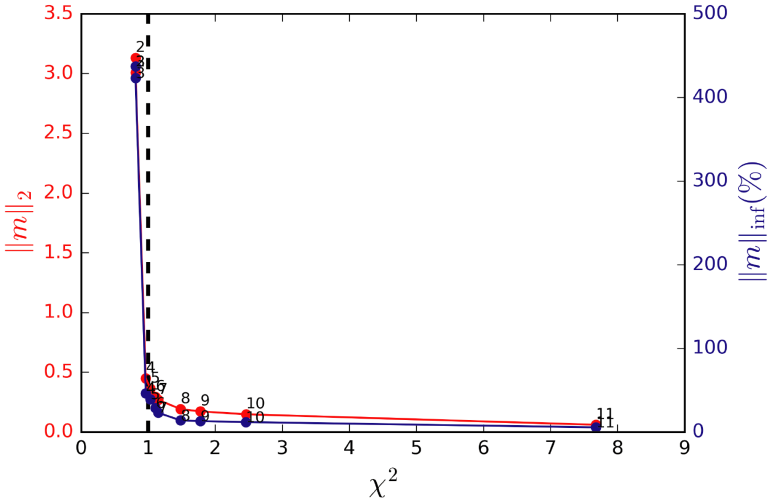

Best solution 3-D slice

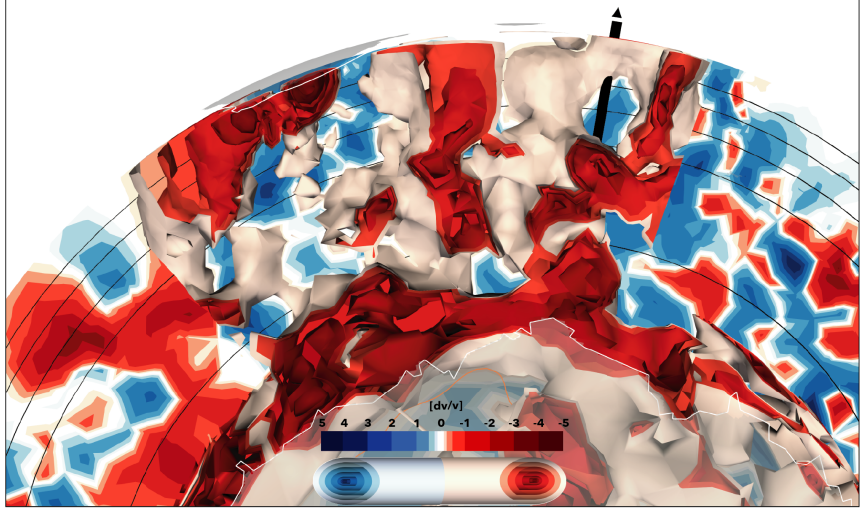

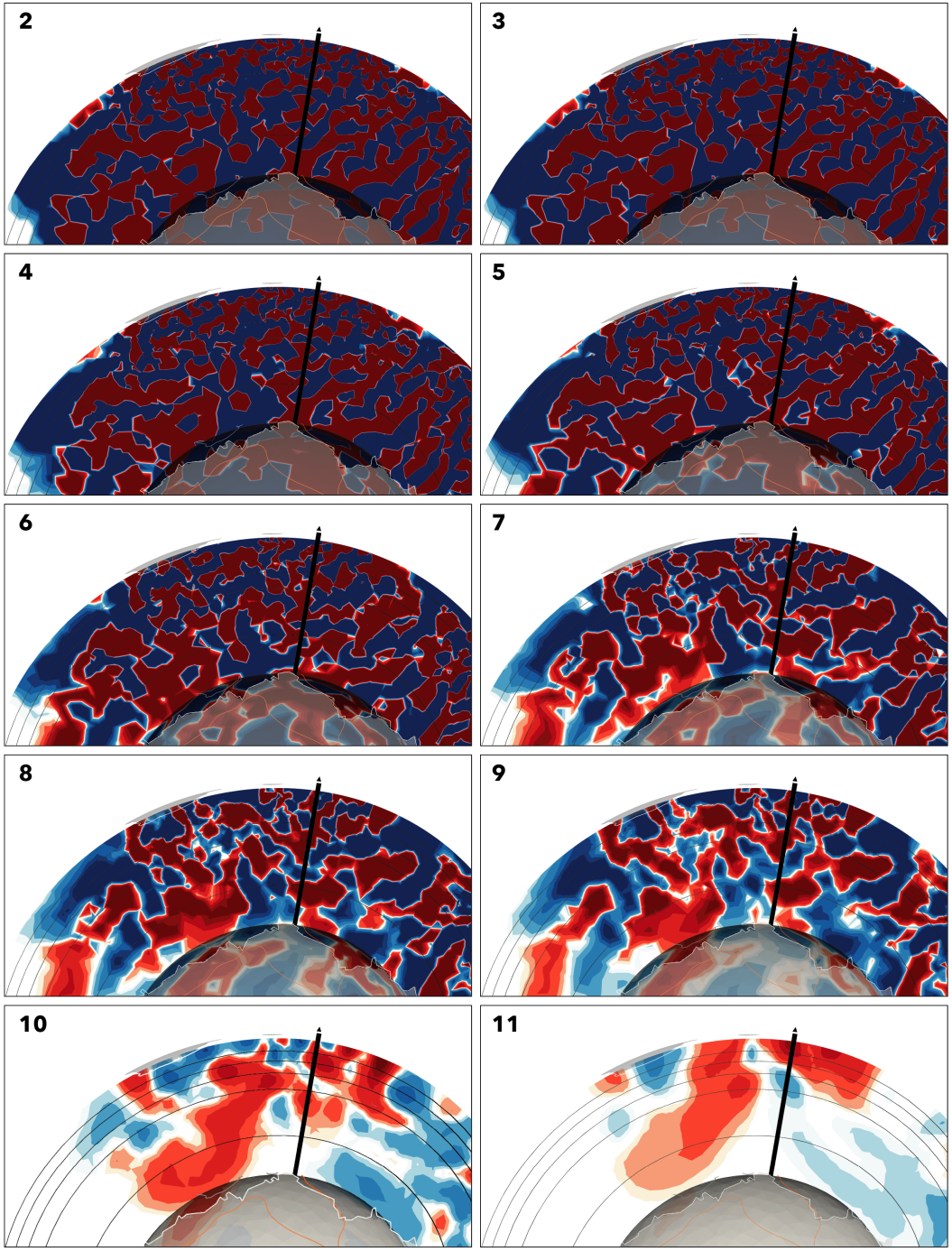

Details

Dataset	**RHUM-RUM (extended)**	Phase(s)	**S**
apriory uncertainties	**90-95% 0.8; 95-100% 0.6**	crustal model	**CRUST2.0**
apriory dlnVp[%]	**10**	$\frac{\text{damping}}{\text{smoothing}} =$	**0.7**
hypoctr corr (lat/lon; depth in km)	**20/20; 5**	outliers	**409 (0.9%)**
origin time correction (sec)	**10**	# row	**45539**
		# col	**62275**

L - curve

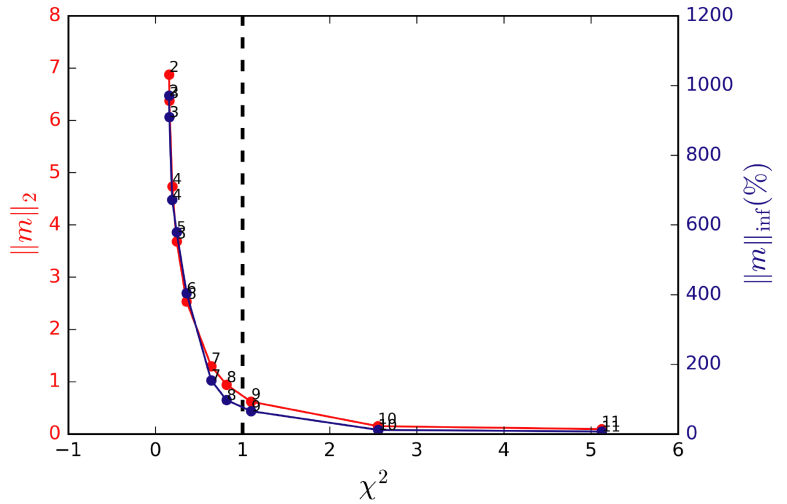

Best solution 3-D slice

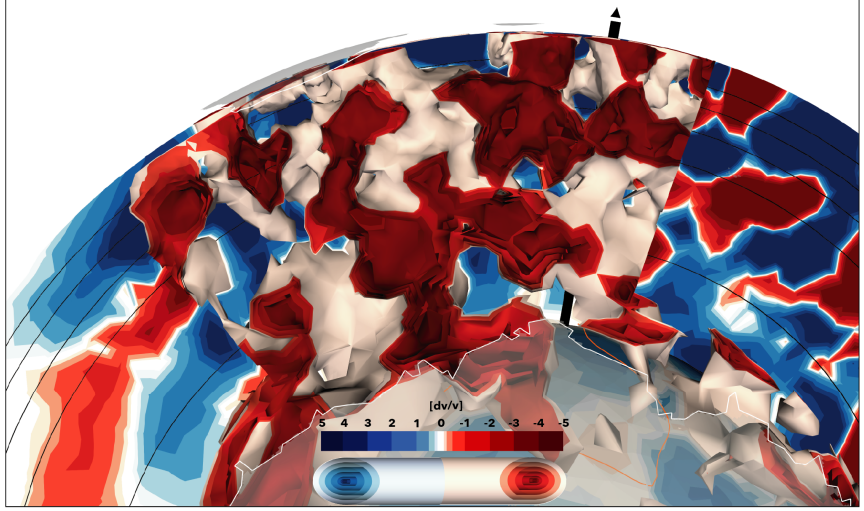

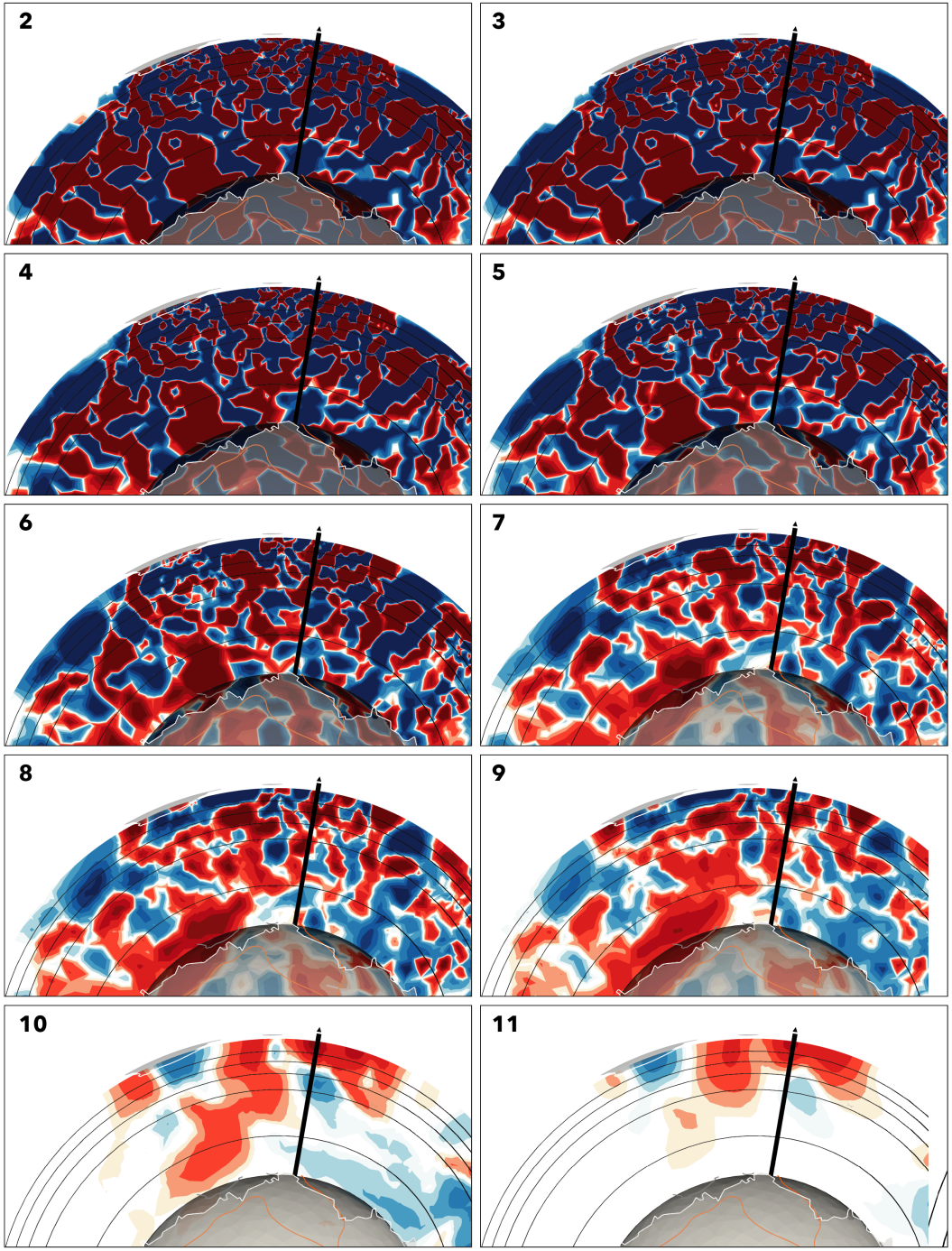

Details

Dataset	**ISC, S40RTS, RHUM-RUM**	Phase(s)	**S**
apriory uncertainties	**ISC 0.99; 90-95% 0.8; 95-100% 0.6**	crustal model	**CRUST2.0**
apriory dlnVp[%]	**10**	$\frac{\text{damping}}{\text{smoothing}} =$	**0.7**
hypoctr corr (lat/lon; depth in km)	**20/20; 5**	outliers	**10252 (3.2%)**
origin time correction (sec)	**10**	# row	**325010**
		# col	**143987**

L - curve

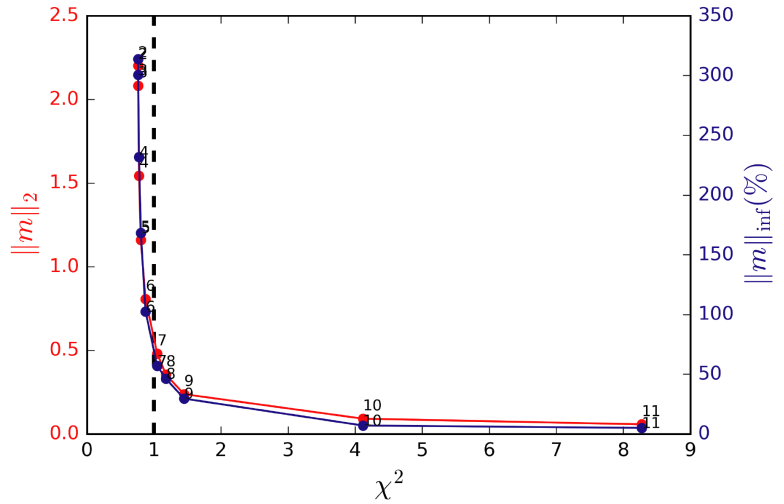

Best solution 3-D slice

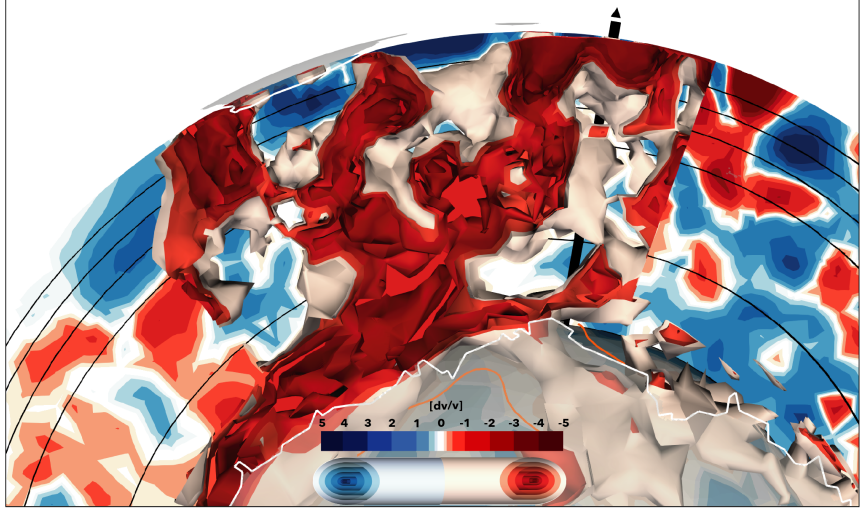

—

B
Resolution tests

Here, I present a series of resolution tests to investigate the quality of the tomographic models in the following order:

- **page 124** big chequerboards without noise
- **page 125** big chequerboards with noise
- **page 126** small chequerboards without noise
- **page 127** small chequerboards with noise
- **page 128** columns beneath hotspot locations without noise
- **page 129** columns beneath hotspot locations with noise
- **page 130** upper mantle columns beneath hotspot locations without noise
- **page 131** upper mantle columns beneath hotspot locations with noise
- **page 132** lower mantle columns beneath hotspot locations without noise
- **page 133** lower mantle columns beneath hotspot locations with noise

- **page 134** columns with alternating amplitude beneath hotspot locations without noise
- **page 135** columns with alternating amplitude hotspot locations with noise
- **page 136** geodynamic columns beneath three hotspot locations without noise
- **page 137** geodynamic columns beneath three hotspot locations with noise
- **page 138** thin columns beneath station locations without noise
- **page 139** thin upper mantle columns beneath station locations without noise
- **page 140** input resolution model is equal output inversion model (s/d=0.3) without noise
- **page 141** input resolution model equal output inversion model (s/d=0.3) minus sphere at mid-mantle without noise
- **page 142** input resolution model is equal output inversion model (s/d=0.3) minus sphere at mid-mantle with noise
- **page 143** input resolution model is equal output inversion model (s/d=0.3) minus upper 400 km without noise
- **page 144** input resolution model is equal output inversion model (s/d=0.3) minus high velocities without noise
- **page 145** input resolution model equal surface wave model without noise
- **page 146** input resolution model equal surface wave model with noise

Input

Output

400

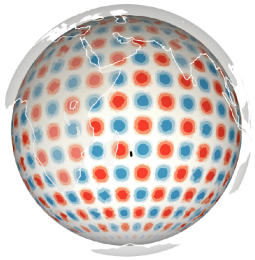

400

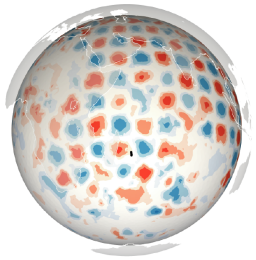

800

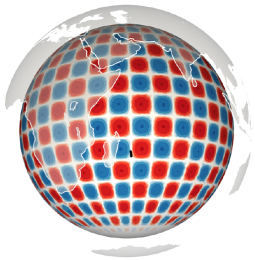

800

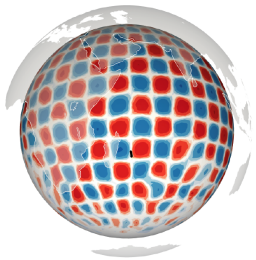

1500

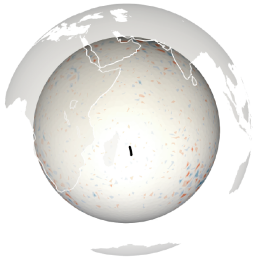

1500

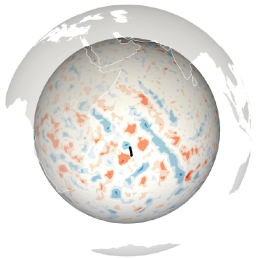

2000



2000

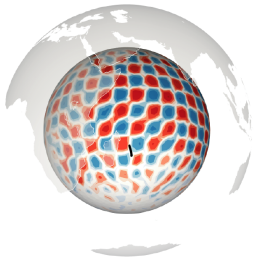

2800

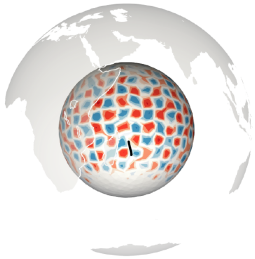

2800

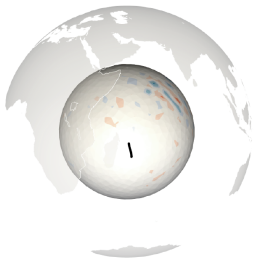

Description

Gaussian chequerboard test

10°×10° wide and 1000 km deep globally distributed boards at the surface;
the size of the boards is continuously decreasing down to 200 km radius at the CMB;
overall good resolution in area of interest, small anomalies at the CMB are not resolvable;

max. abs. amplitude: **3%** noise level: **no noise** $\frac{\text{damping}}{\text{smoothing}} =$ **0.7**

Input 3-D slice

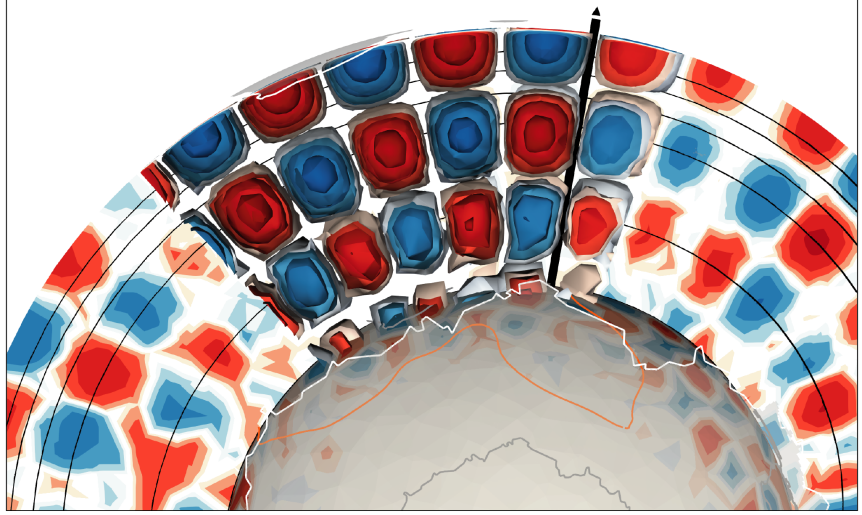

Output for best solution 3-D slice

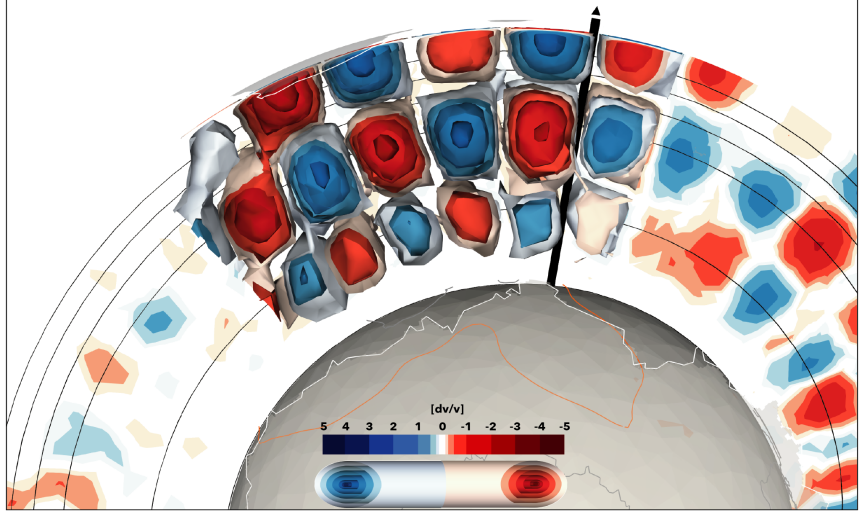

Input

Output

400

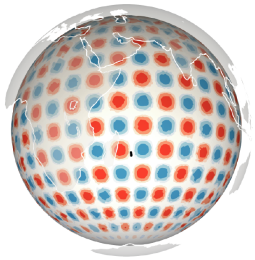

400

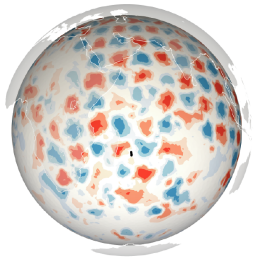

800

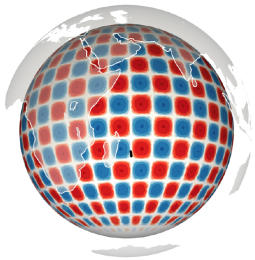

800

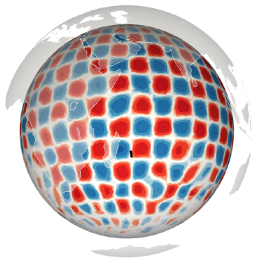

1500

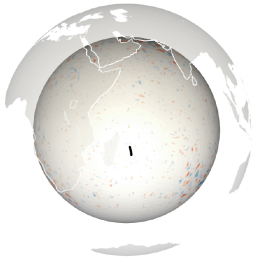

1500

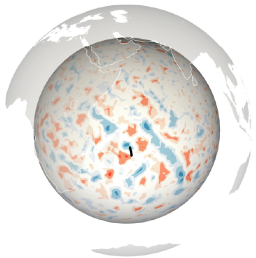

2000



2000

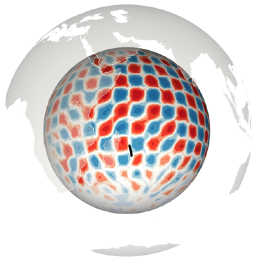

2800

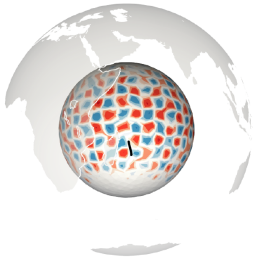

2800

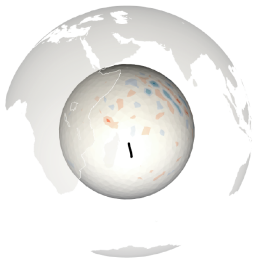

Description

Gaussian chequerboard test

10°×10° wide and 1000 km deep globally distributed boards at the surface;
the size of the boards is continuously decreasing down to 200 km radius at the CMB;
overall good resolution in area of interest, small anomalies at the CMB are not resolvable;

max. abs. amplitude: **3%** noise level: **uncertainties as standard-deviation** $\frac{\text{damping}}{\text{smoothing}} =$ **0.7**

Input 3-D slice

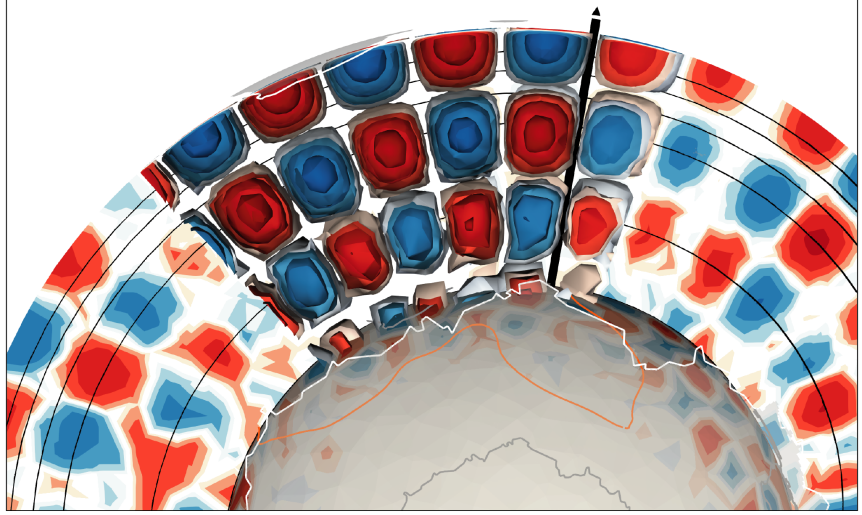

Output for best solution 3-D slice

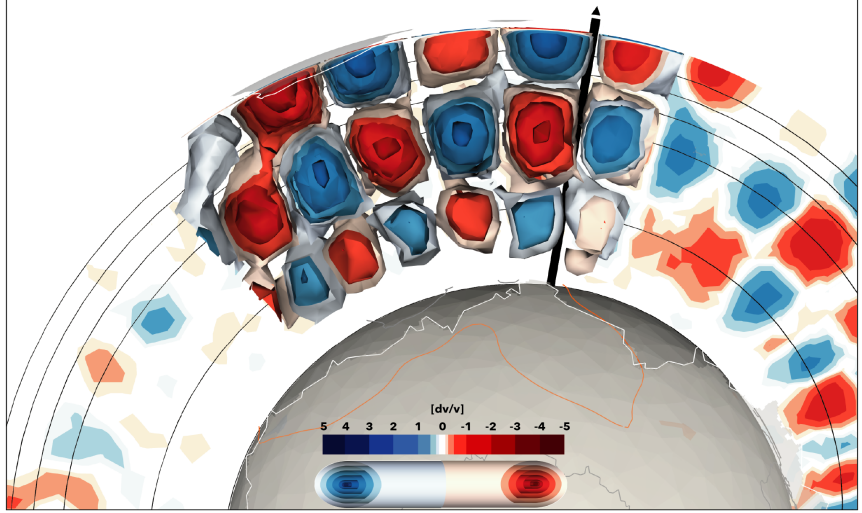

Input

Output

400

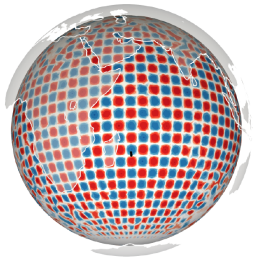

400

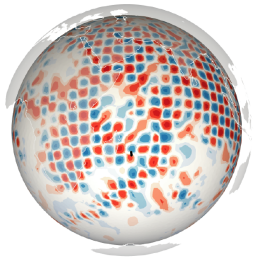

800

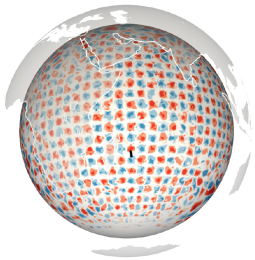

800

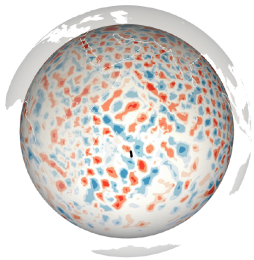

1500

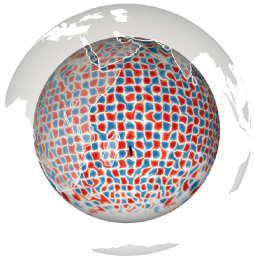

1500

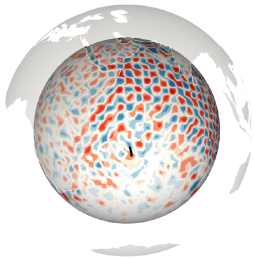

2000

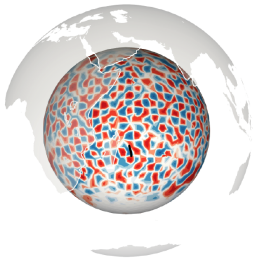

2000

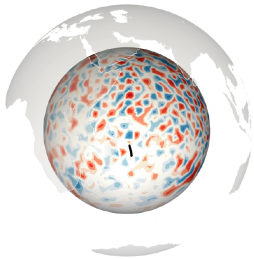

2800

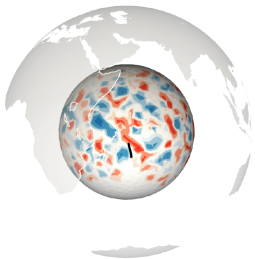

2800

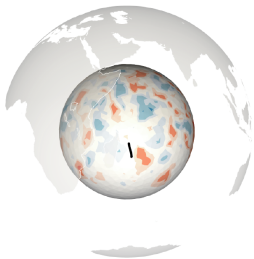

Description

Gaussian chequerboard test

5°×5° wide and 500 km deep globally distributed boards at the surface;
the size of the boards is continuously decreasing down to 100 km radius at the CMB;
good resolution in area of interest in upper and mid mantle; smearing occours for small anomalies; small anomalies at the CMB are not resolvable;

max. abs. amplitude: 3% noise level: no noise $\frac{\text{damping}}{\text{smoothing}} = 0.3$

Input 3-D slice

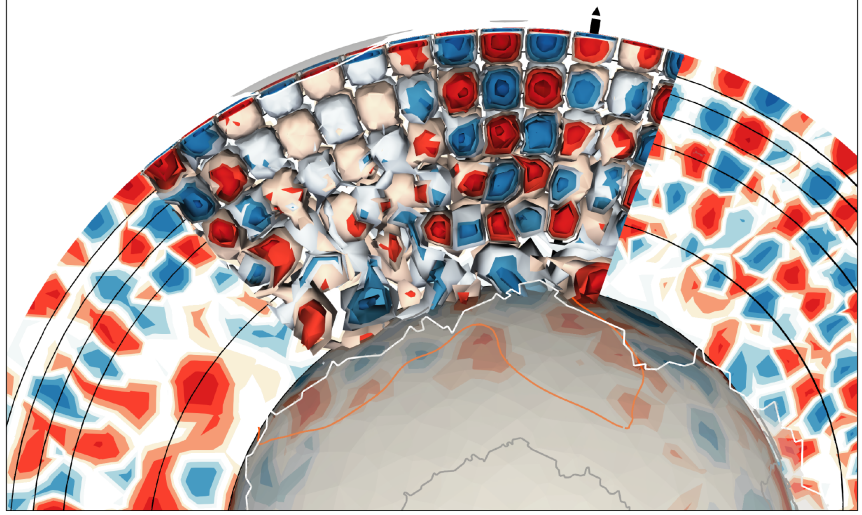

Output for best solution 3-D slice

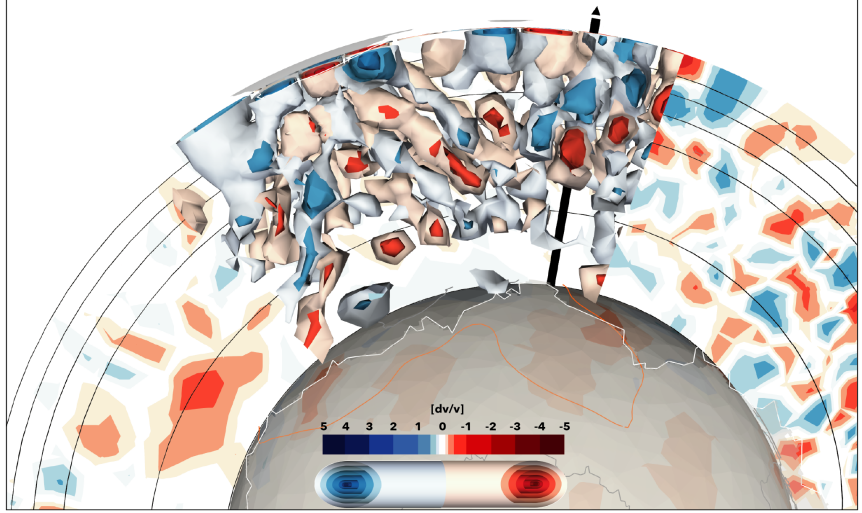

Input

Output

400

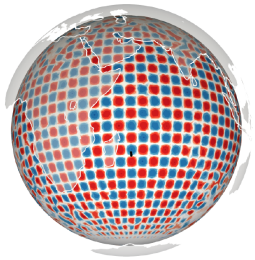

400

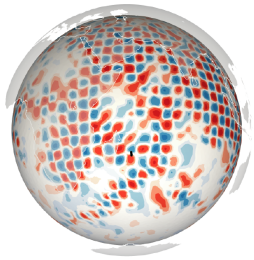

800

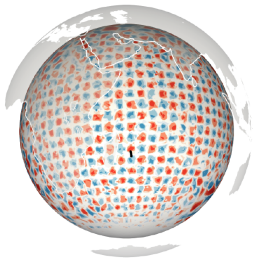

800

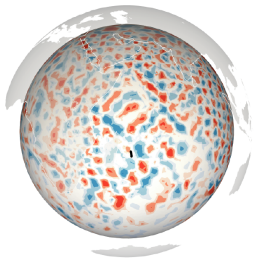

1500

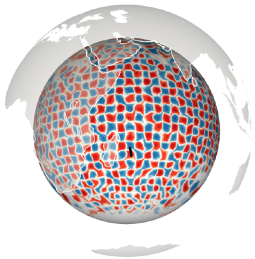

1500

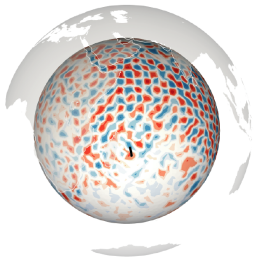

2000

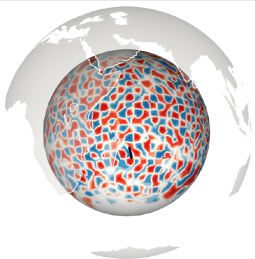

2000

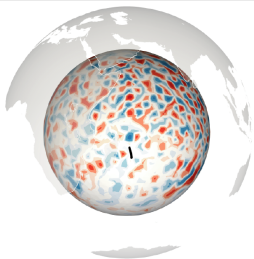

2800

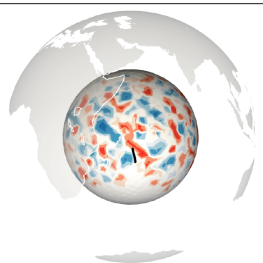

2800

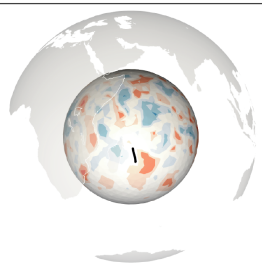

Description

Gaussian chequerboard test

5°×5° wide and 500 km deep globally distributed boards at the surface;
the size of the boards is continuously decreasing down to 100 km radius at the CMB;
good resolution in area of interest in upper and mid mantle; smearing occours for small anomalies; small anomalies at the CMB are not resolvable;

max. abs. amplitude: **3%** noise level: **uncertainties as standard-deviation** $\frac{\text{damping}}{\text{smoothing}} =$ **0.3**

Input 3-D slice

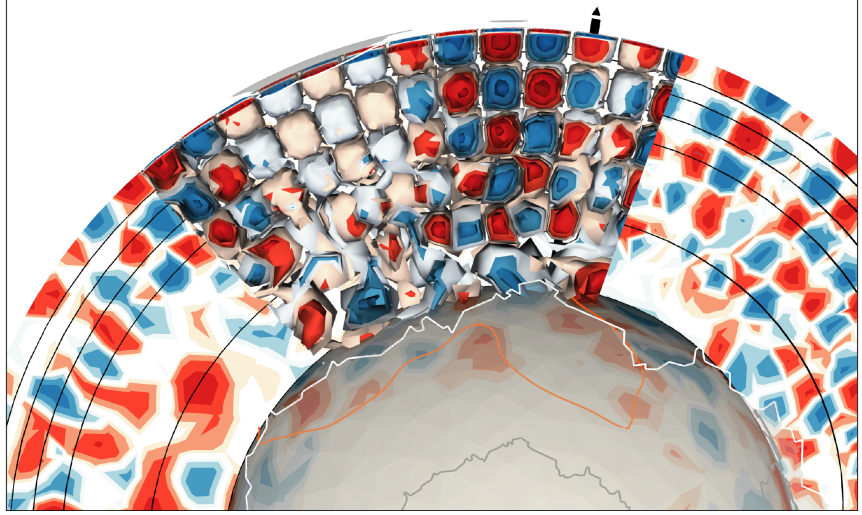

Output for best solution 3-D slice

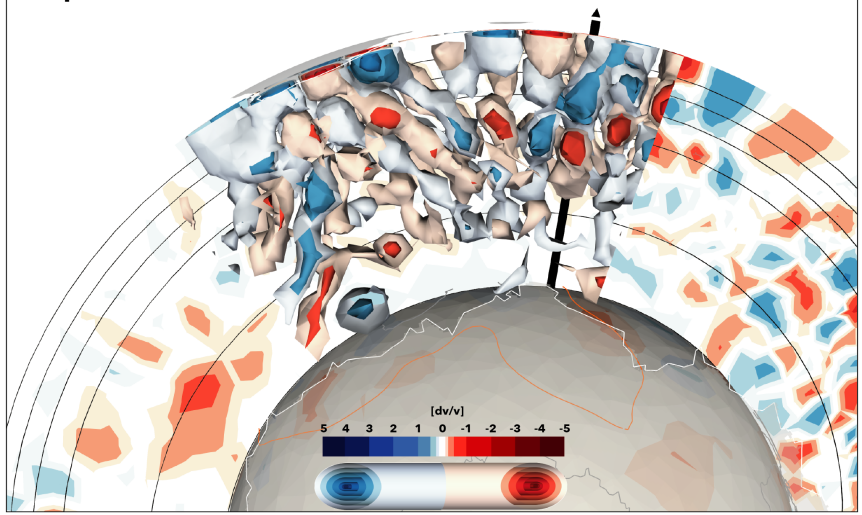

Input

Output

400

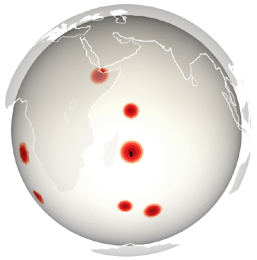

400

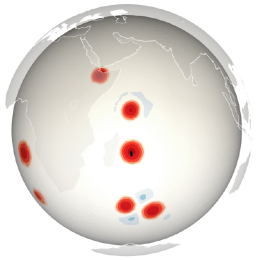

800

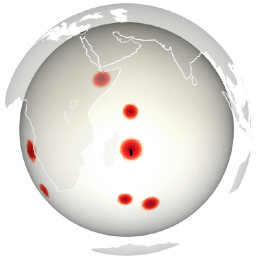

800

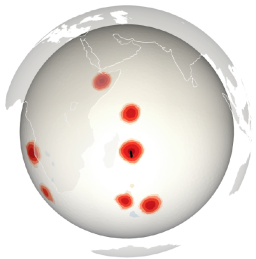

1500

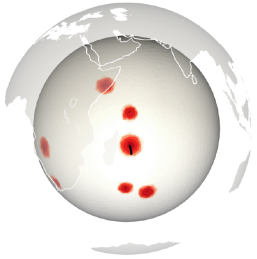

1500

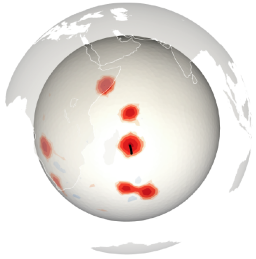

2000

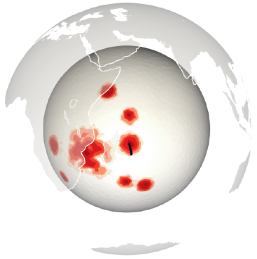

2000

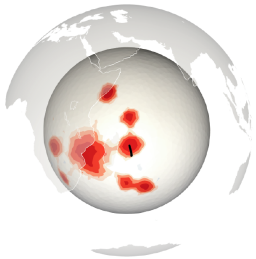

2800

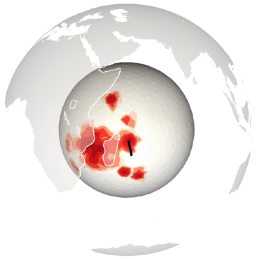

2800

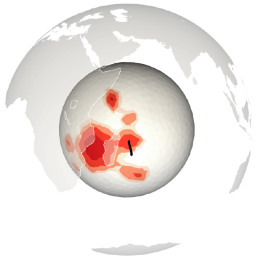

Description

Whole mantle columns at hotspot locations and LLVP

Variable sizes for columns (La Réunion: r=300km; Afar: r=250km; Seychelles: r=200km; Tristan da Cunha: r=200km; Kerguelen: r=250km; St Helena: r=300km; Marion: r=200km); overall good resolution with little smearing;

max. abs. amplitude: **3%** noise level: **no noise** $\frac{\text{damping}}{\text{smoothing}} =$ **0.3**

Input 3-D slice

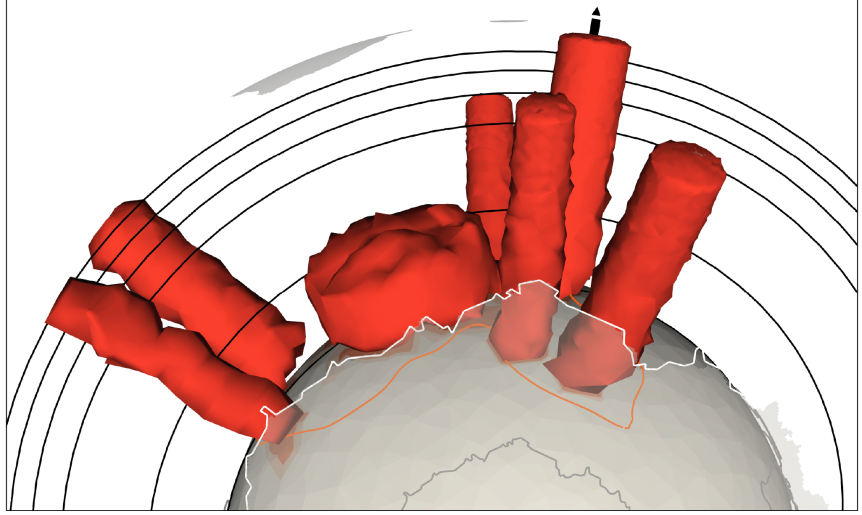

Output for best solution 3-D slice

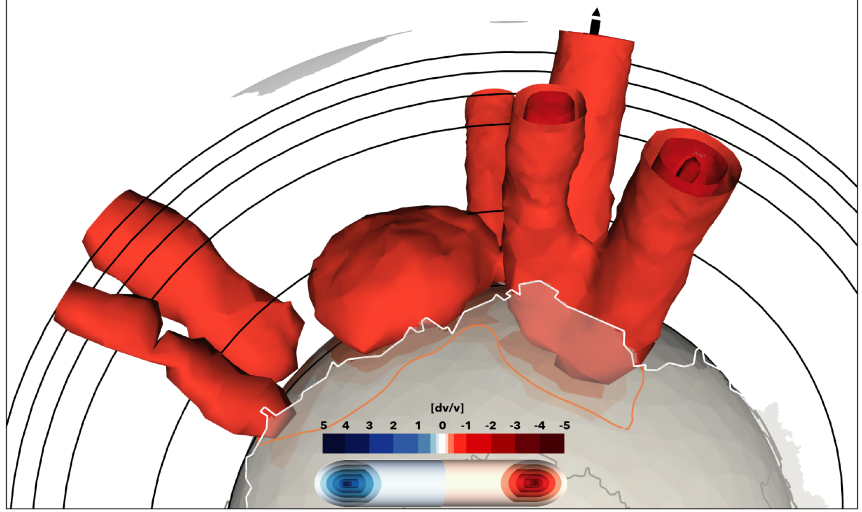

Input

Output

400

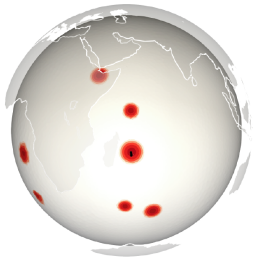

400

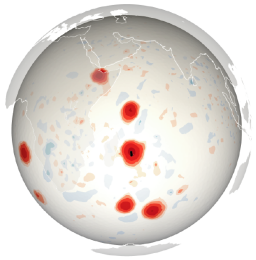

800

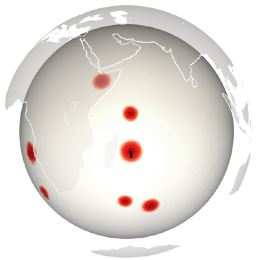

800

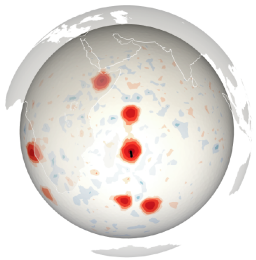

1500

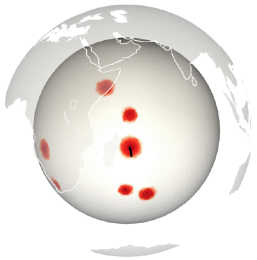

1500

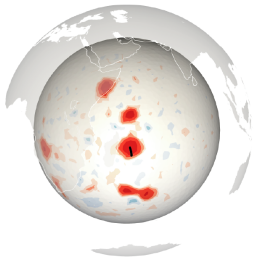

2000

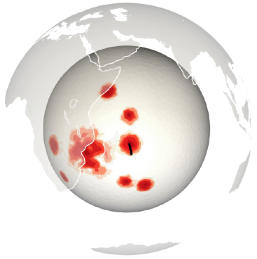

2000

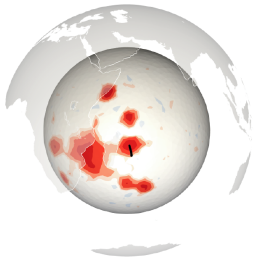

2800

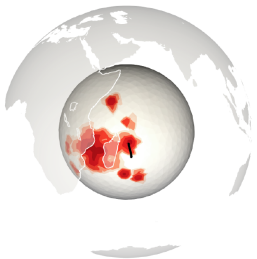

2800

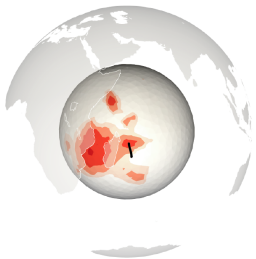

Description

Whole mantle columns at hotspot locations and LLVP

Variable sizes for columns (La Réunion: r=300km; Afar: r=250km; Seychelles: r=200km; Tristan da Cunha: r=200km; Kerguelen: r=250km; St Helena: r=300km; Marion: r=200km); still good resolution in area of interst with some more smearing; Tristan vanishes due to poor data coverage in the South Atlantic;

max. abs. amplitude: **3%** noise level: **uncertainties as standard-deviation** $\frac{\text{damping}}{\text{smoothing}} =$ **0.3**

Input 3-D slice

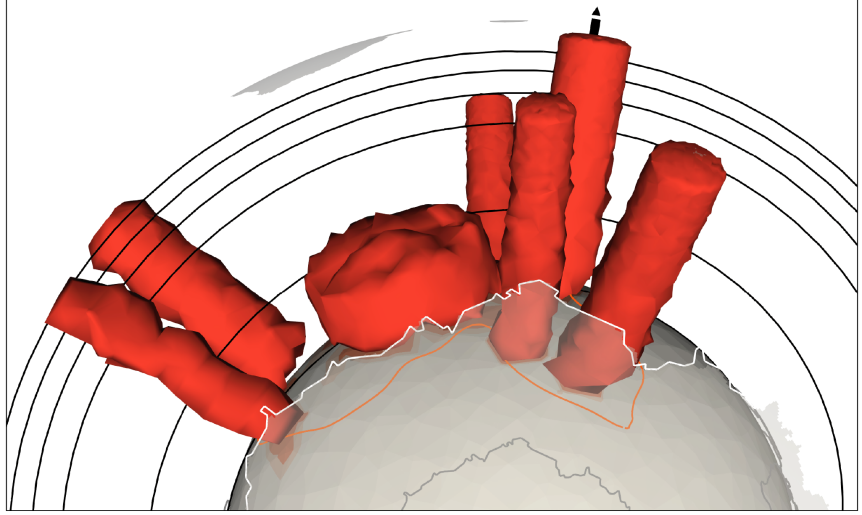

Output for best solution 3-D slice

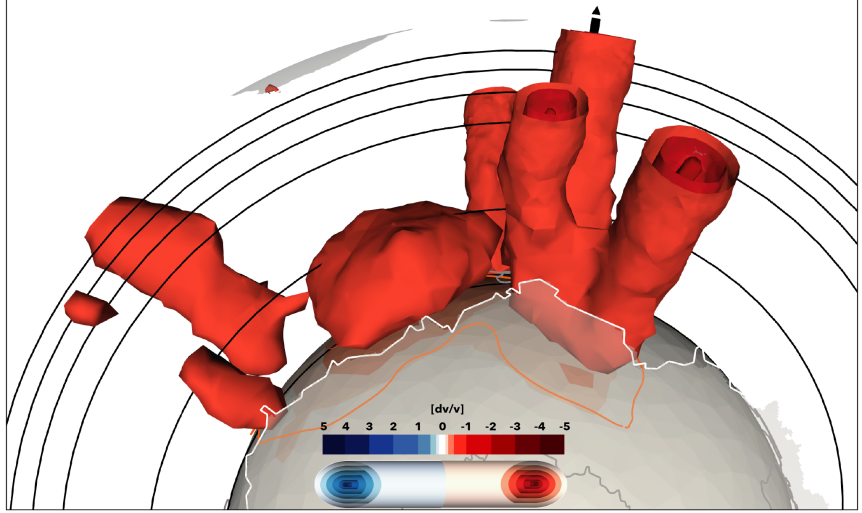

Input

Output

400

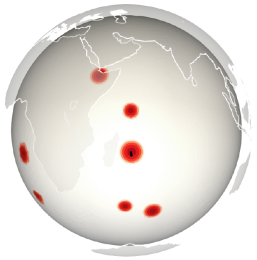

400

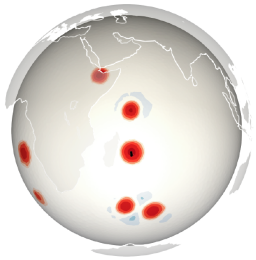

800

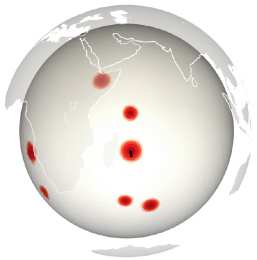

800

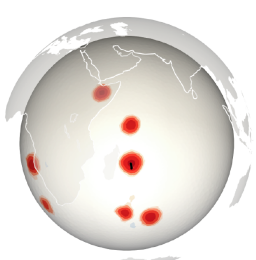

1500

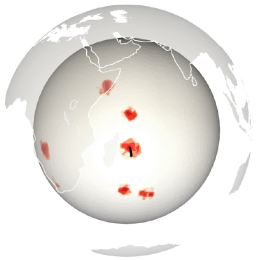

1500

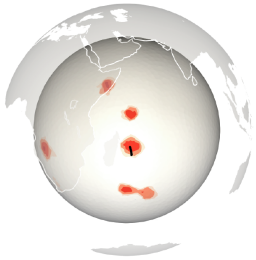

2000

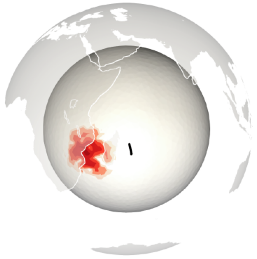

2000

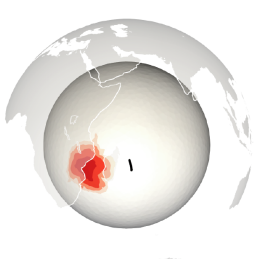

2800

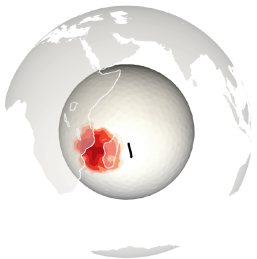

2800

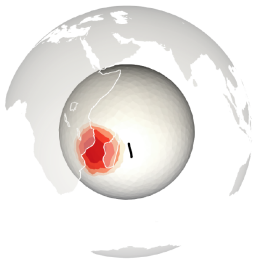

Description

Upper mantle columns at hotspot locations and LLVP

Variable sizes for columns (La Réunion: r=300km; Afar: r=250km; Seychelles: r=200km; Tristan da Cunha: r=200km; Kerguelen: r=250km; St Helena: r=300km; Marion: r=200km); overall good resolution with no smearing downwards;

max. abs. amplitude: **3%** noise level: **no noise** $\frac{\text{damping}}{\text{smoothing}} =$ **0.3**

Input 3-D slice

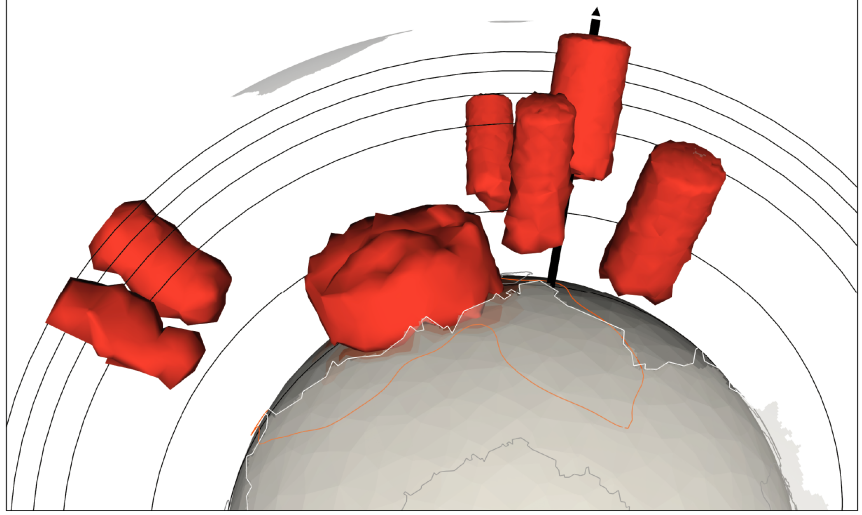

Output for best solution 3-D slice

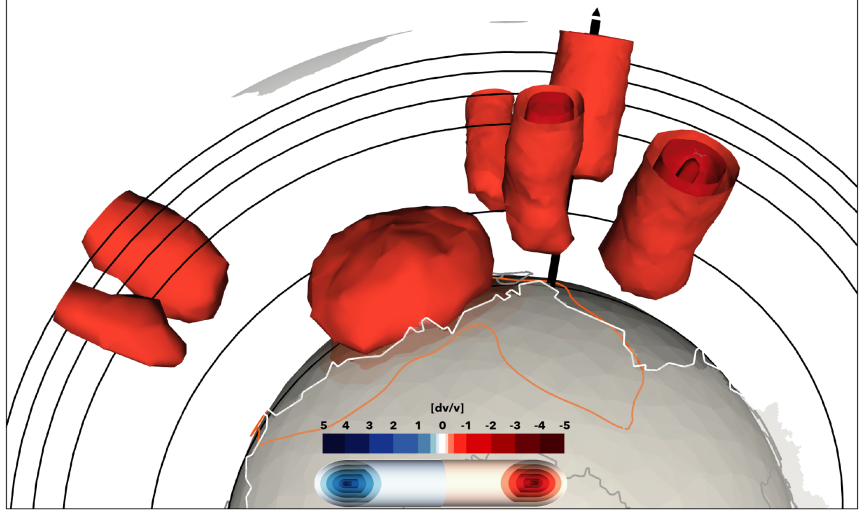

Input

Output

400

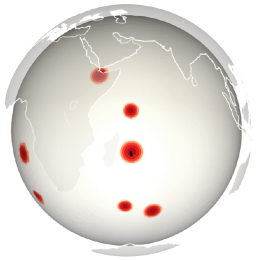

400

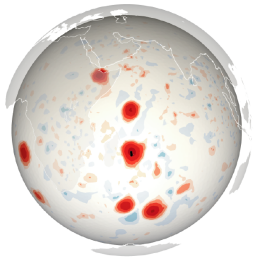

800

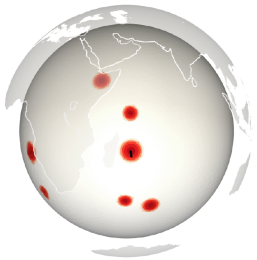

800

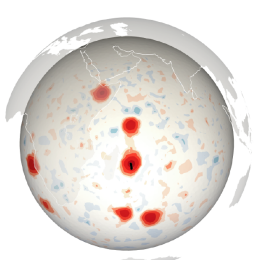

1500

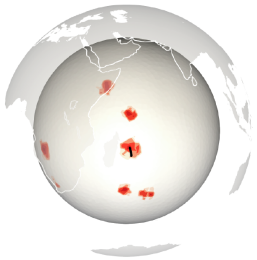

1500

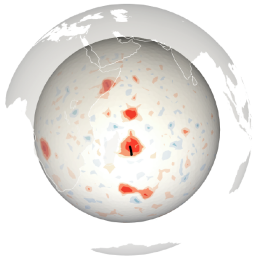

2000

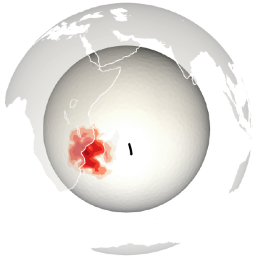

2000

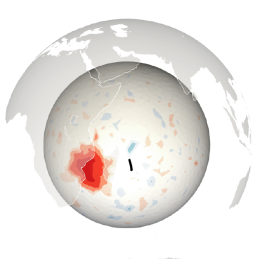

2800

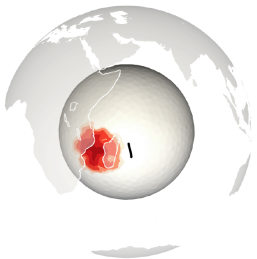

2800

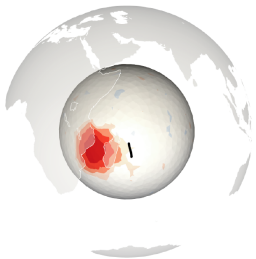

Description

Upper mantle columns at hotspot locations and LLVP

Variable sizes for columns (La Réunion: r=300km; Afar: r=250km; Seychelles: r=200km; Tristan da Cunha: r=200km; Kerguelen: r=250km; St Helena: r=300km; Marion: r=200km); still good resolution in area of interst with some lateral smearing; occurance of small-scale low amplitude anomalies;

max. abs. amplitude: **3%** noise level: **uncertainties as standard-deviation** $\frac{\text{damping}}{\text{smoothing}} =$ **0.3**

Input 3-D slice

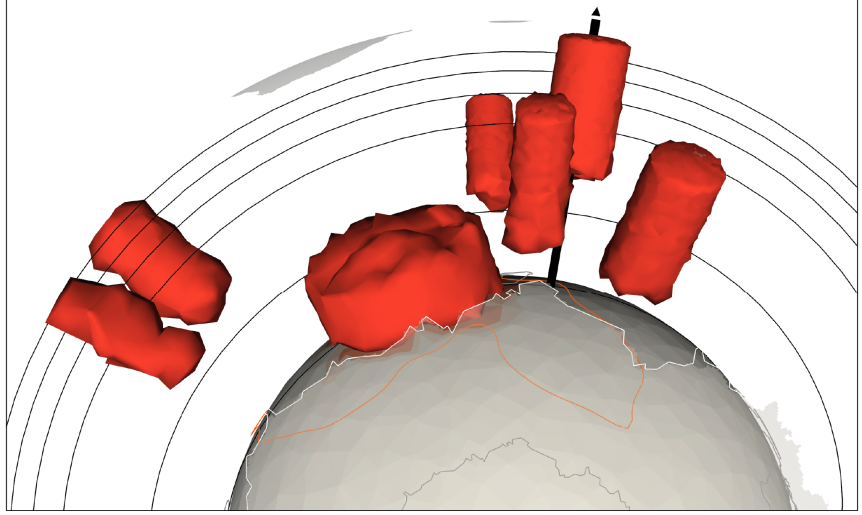

Output for best solution 3-D slice

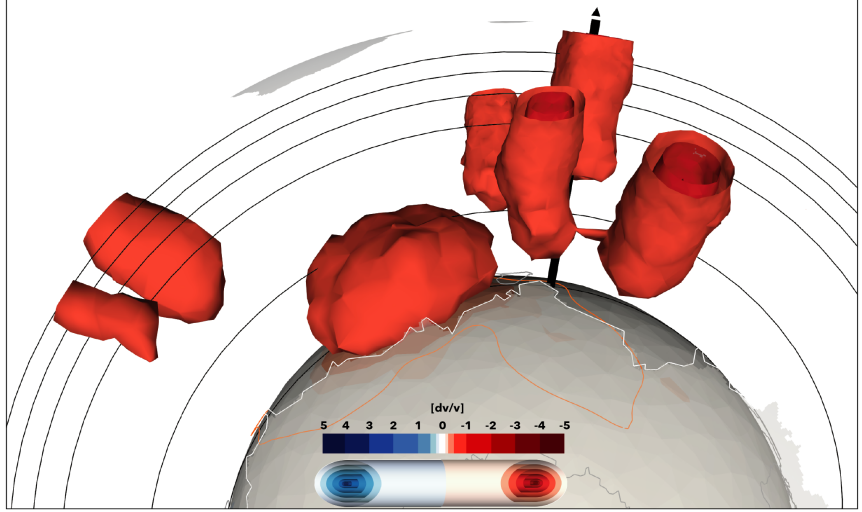

Input

Output

400



400

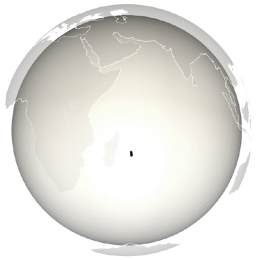

800

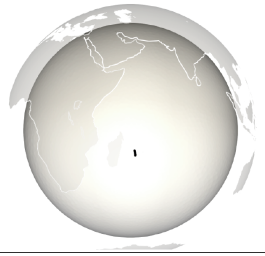

800

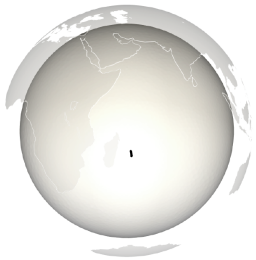

1500

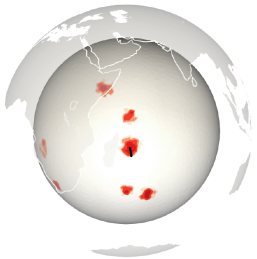

1500

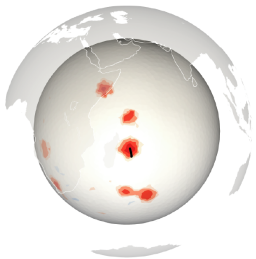

2000

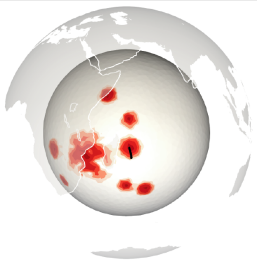

2000

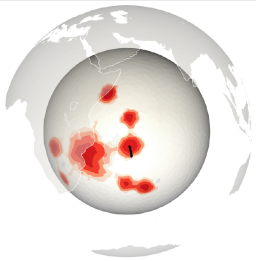

2800

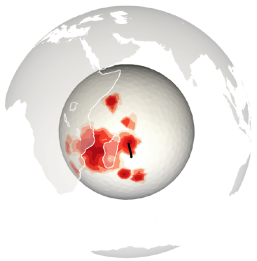

2800

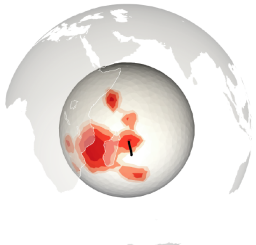

Description

Lower mantle columns at hotspot locations and LLVP

Variable sizes for columns (La Réunion: r=300km; Afar: r=250km; Seychelles: r=200km; Tristan da Cunha: r=200km; Kerguelen: r=250km; St Helena: r=300km; Marion: r=200km); overall good resolution with little lateral and upward smearing;

max. abs. amplitude: **3%** noise level: **no noise** $\frac{\text{damping}}{\text{smoothing}} =$ **0.3**

Input 3-D slice

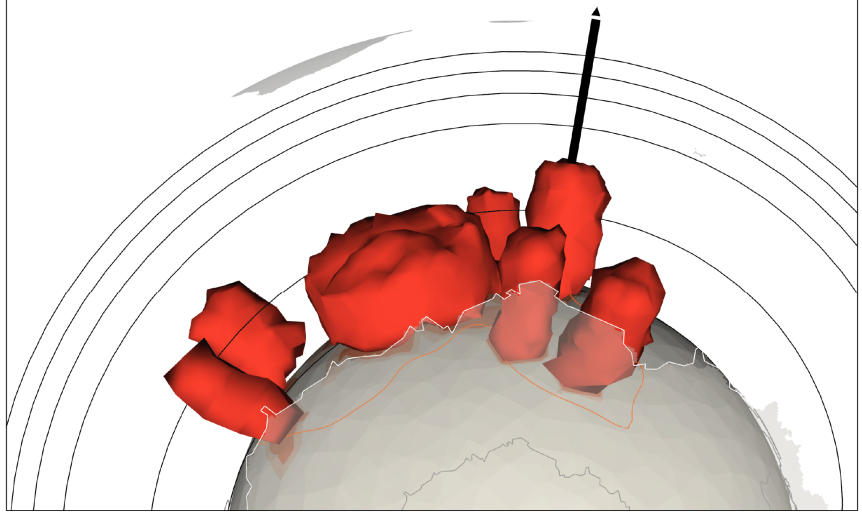

Output for best solution 3-D slice

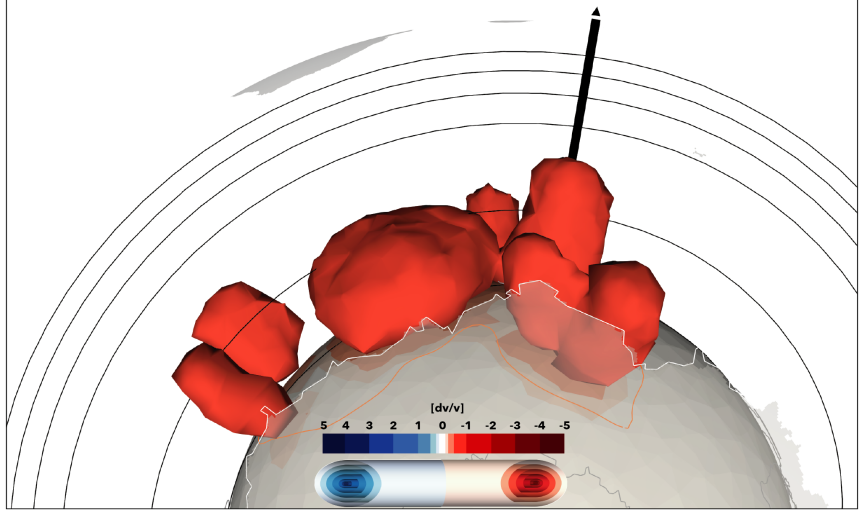

Input

Output

400



400

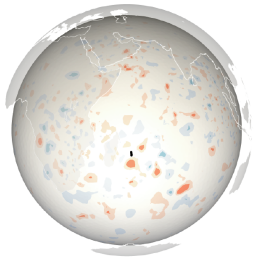

800

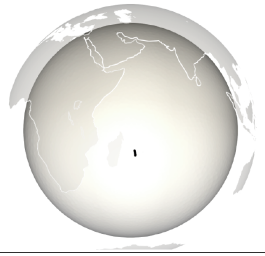

800

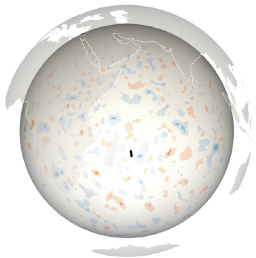

1500

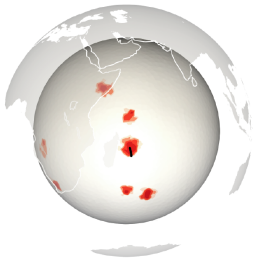

1500

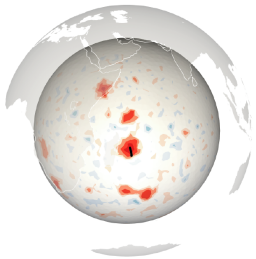

2000

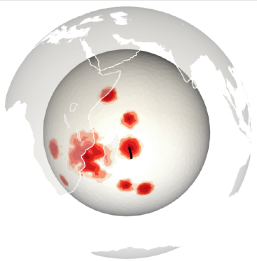

2000

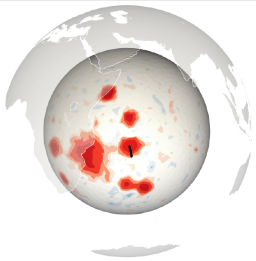

2800

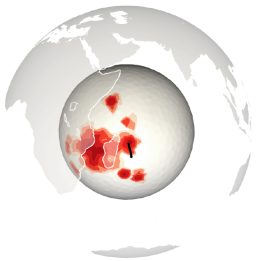

2800

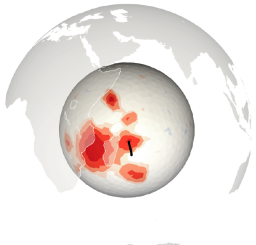

Description

Lower mantle columns at hotspot locations and LLVP

Variable sizes for columns (La Réunion: r=300km; Afar: r=250km; Seychelles: r=200km; Tristan da Cunha: r=200km; Kerguelen: r=250km; St Helena: r=300km; Marion: r=200km); still good resolution in area of interst with more lateral and upward smearing; upward smearing of small-scale low amplitude anomalies;

max. abs. amplitude: **3%** noise level: **uncertainties as standard-deviation** $\frac{\text{damping}}{\text{smoothing}} =$ **0.3**

Input 3-D slice

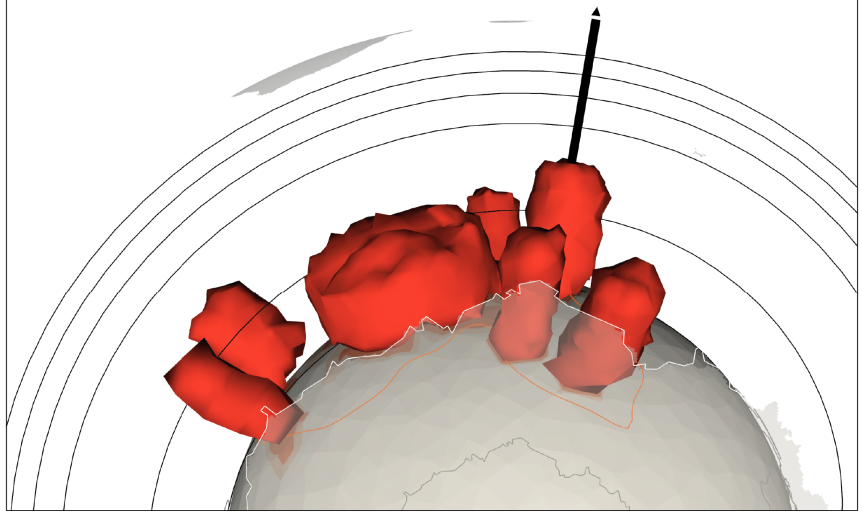

Output for best solution 3-D slice

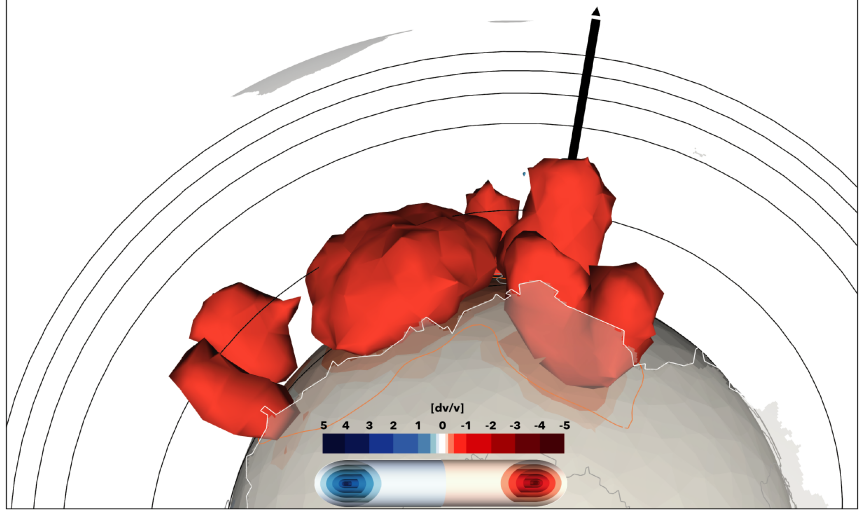

Input

Output

400

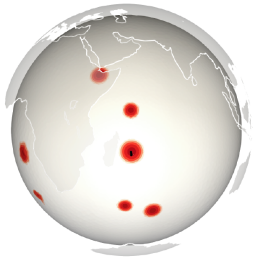

400

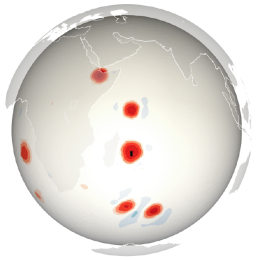

800

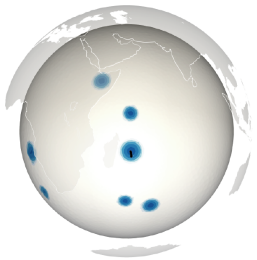

800

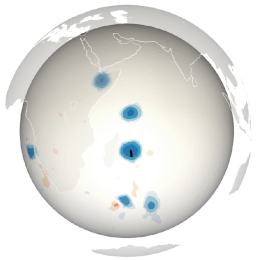

1500

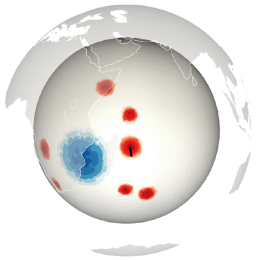

1500

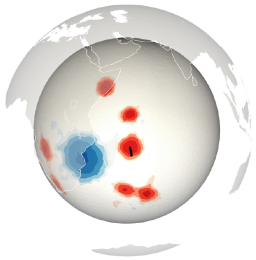

2000

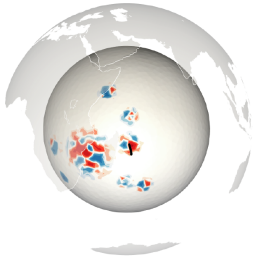

2000

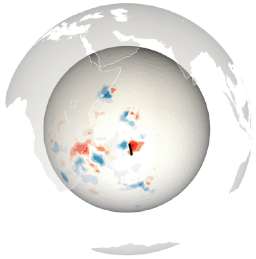

2800

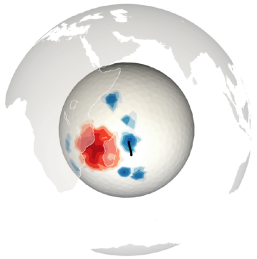

2800

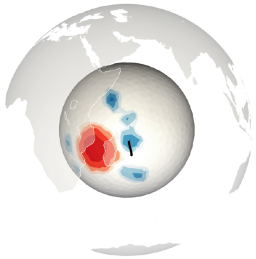

Description

Alternating mantle columns at hotspot locations and LLVP

Variable sizes for columns (La Réunion: r=300km; Afar: r=250km; Seychelles: r=200km; Tristan da Cunha: r=200km; Kerguelen: r=250km; St Helena: r=300km; Marion: r=200km); overall good resolution with little smearing in area of interst; Tristan is not well resolved;

max. abs. amplitude: **3%** noise level: **no noise** $\frac{\text{damping}}{\text{smoothing}} =$ **0.3**

Input 3-D slice

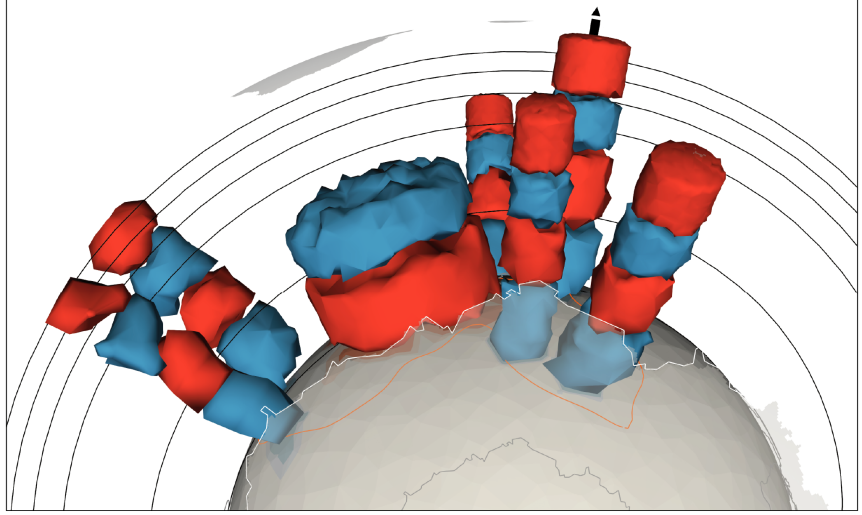

Output for best solution 3-D slice

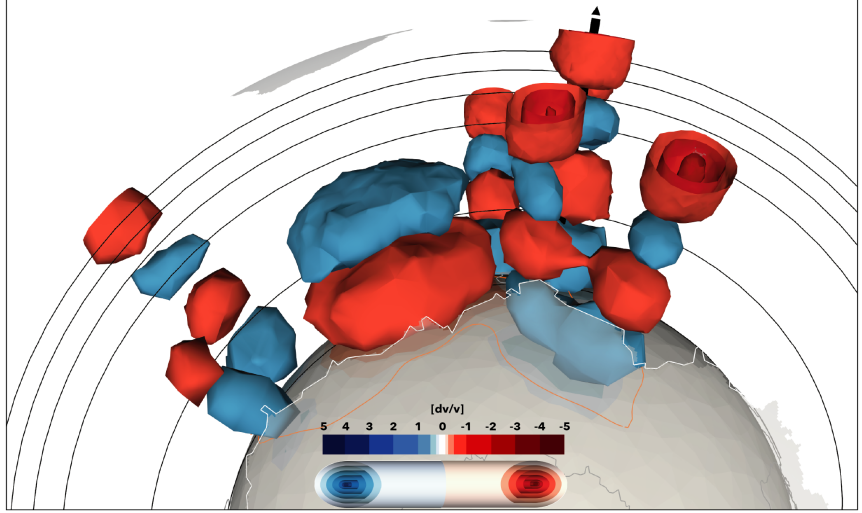

Input

Output

400

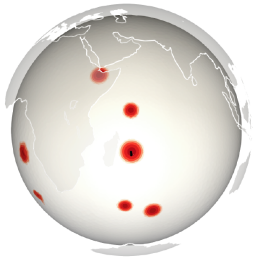

400

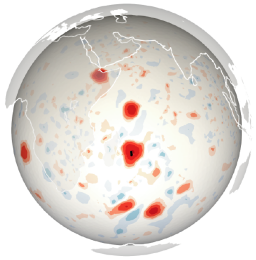

800

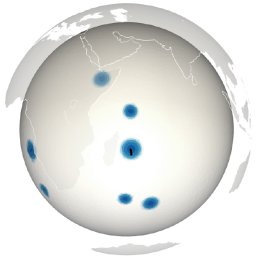

800

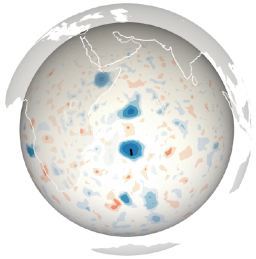

1500

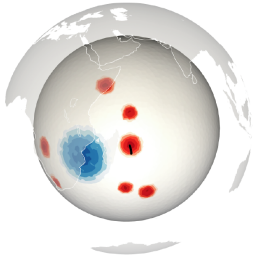

1500

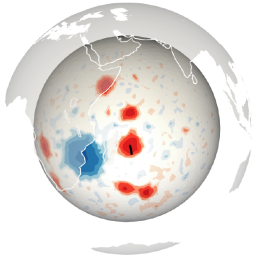

2000

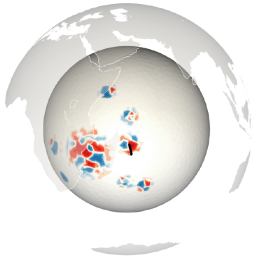

2000

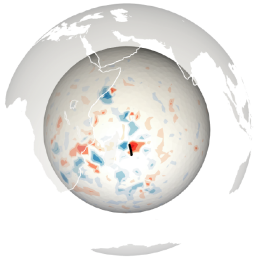

2800

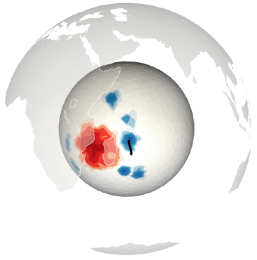

2800

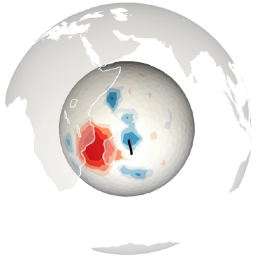

Description

Alternating mantle columns at hotspot locations and LLVP

Variable sizes for columns (La Réunion: r=300km; Afar: r=250km; Seychelles: r=200km; Tristan da Cunha: r=200km; Kerguelen: r=250km; St Helena: r=300km; Marion: r=200km); still good resolution in area of interst with some more smearing; Tristan vanishes due to poor data coverage in the South Atlantic; small-scale low amplitudes anomalies come up;

max. abs. amplitude: **3%** noise level: **uncertainties as standard-deviation** $\frac{\text{damping}}{\text{smoothing}} =$ **0.3**

Input 3-D slice

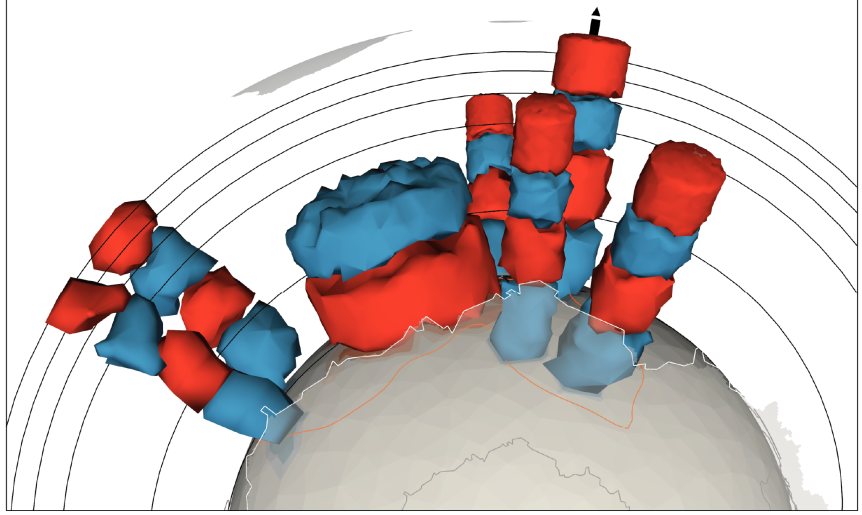

Output for best solution 3-D slice

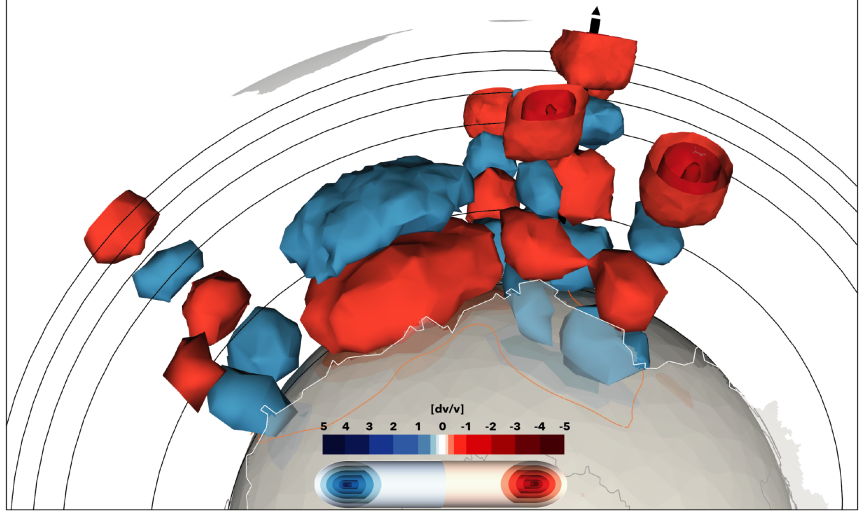

Input

Output

400

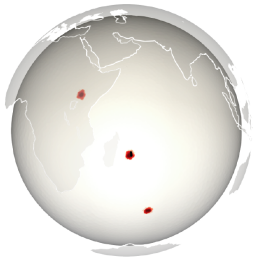

400

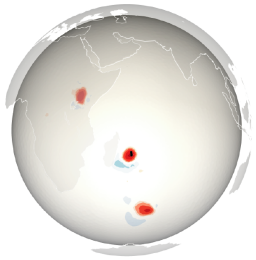

800

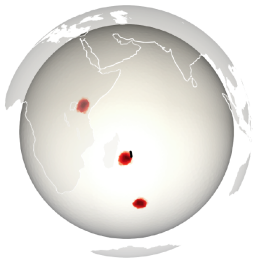

800

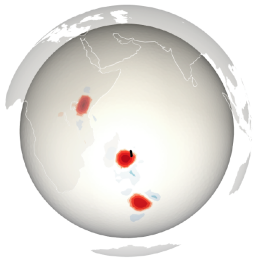

1500

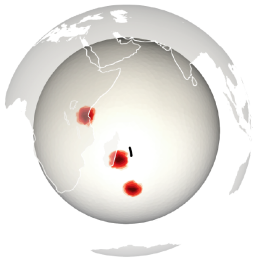

1500

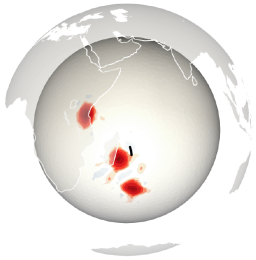

2000

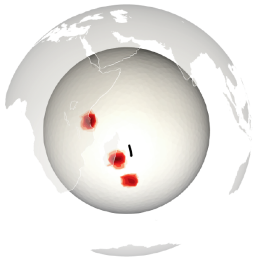

2000

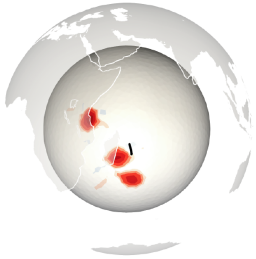

2800

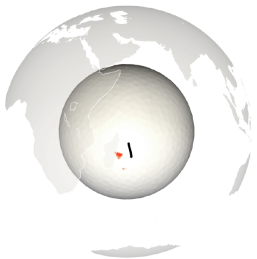

2800

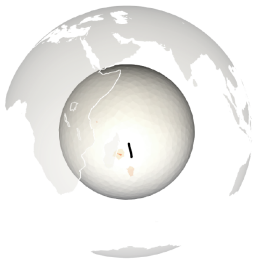

Description

Geodynamic mantle columns (from Steinberger et al., 2006) at hotspot locations

Tilted cone shaped columns beneath Afar, La Réunion and Kerguelen;
overall good resolution with little smearing for La Réunion; Kerguelen smears stronger; Afar well resolved;

max. abs. amplitude: **3%** noise level: **no noise** $\frac{\text{damping}}{\text{smoothing}} =$ **0.3**

Input 3-D slice

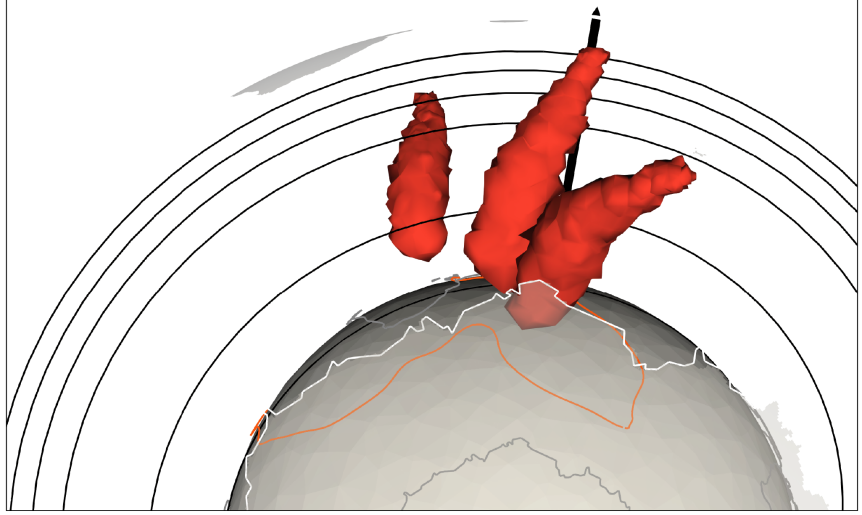

Output for best solution 3-D slice

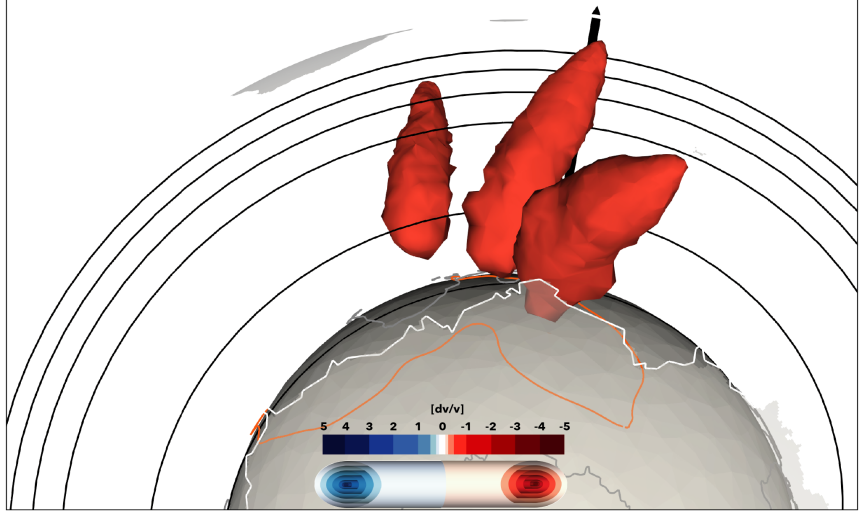

Input

Output

400

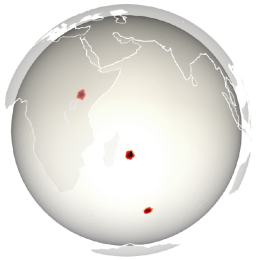

400

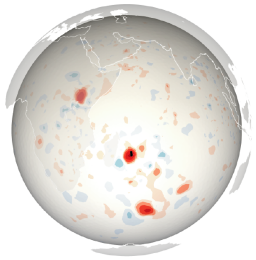

800

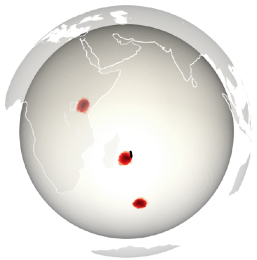

800

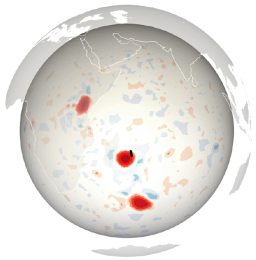

1500

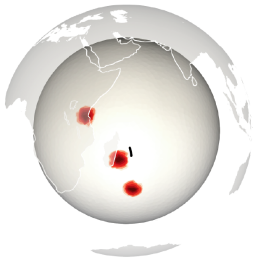

1500

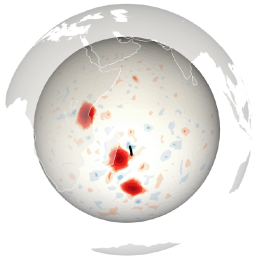

2000

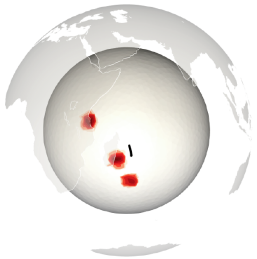

2000

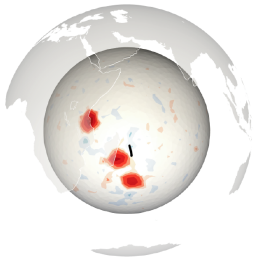

2800

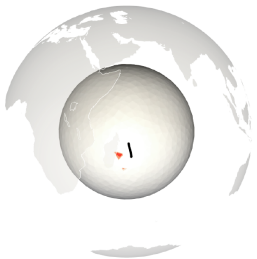

2800

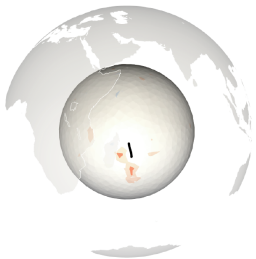

Description

Geodynamic mantle columns (from Steinberger et al., 2006) at hotspot locations

Tilted cone shaped columns beneath Afar, La Réunion and Kerguelen;
overall good resolution with little smearing for La Réunion; Kerguelen smears stronger; Afar well resolved; small-scale low amplitudes anomalies come up;

max. abs. amplitude: 3% noise level: uncertainties as standard-deviation $\frac{\text{damping}}{\text{smoothing}} = 0.3$

Input 3-D slice

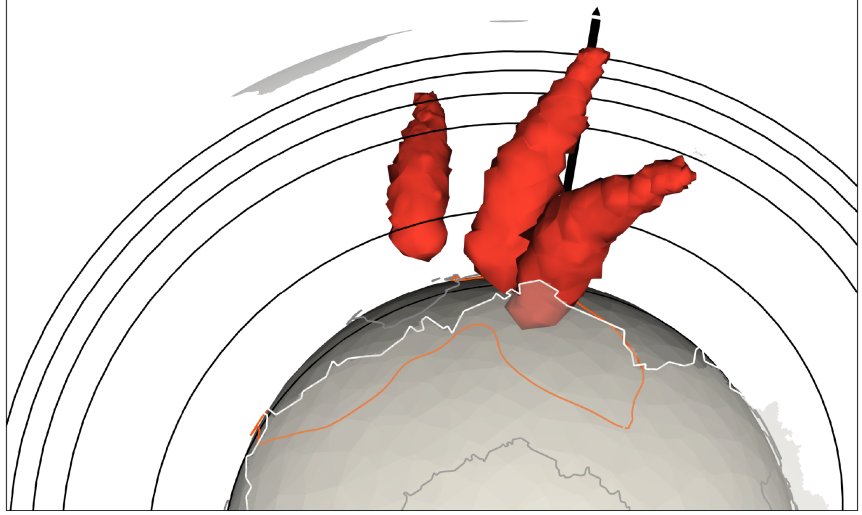

Output for best solution 3-D slice

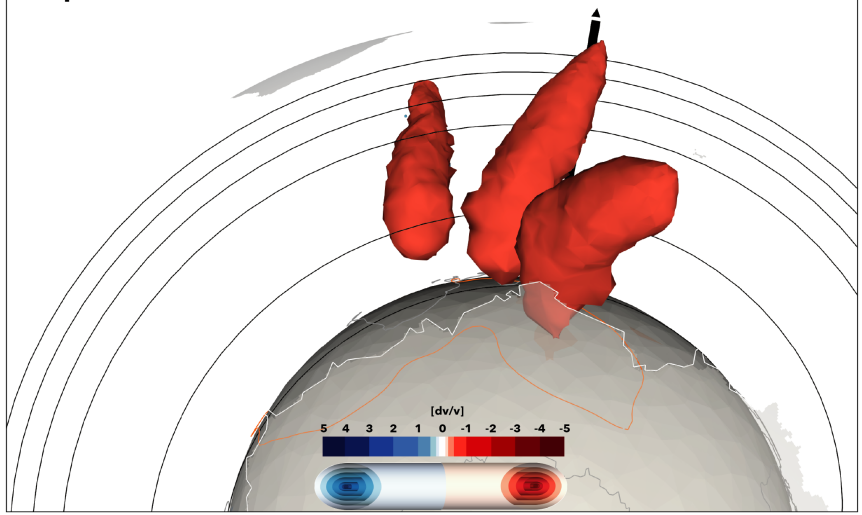

Input

Output

400

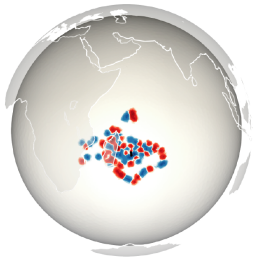

400

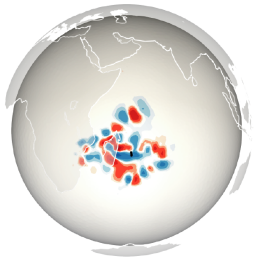

800

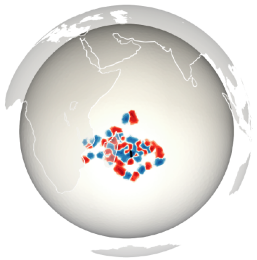

800

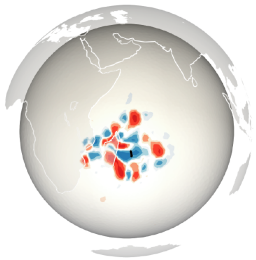

1500

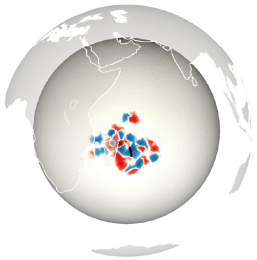

1500

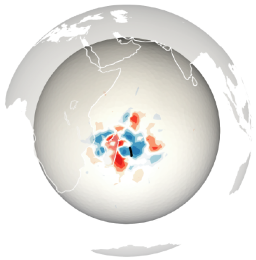

2000

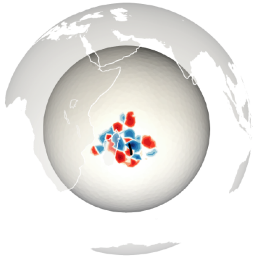

2000

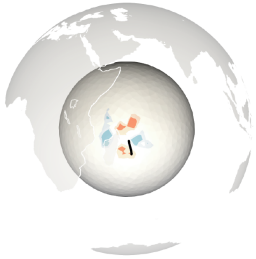

2800



2800

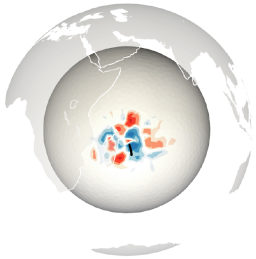

Description

Whole mantle columns at RHUM-RUM+ station locations

Uniform columns radius of 100 km; input model gets distorted for lower mantle due to the goemetry of the mesh; good resoltuion in the upper mantle with smearing; lower mantle is difficult to resolve since anomalies becoming very small;

max. abs. amplitude: **3%** noise level: **no noise** $\frac{\text{damping}}{\text{smoothing}} =$ **0.7**

Input 3-D slice

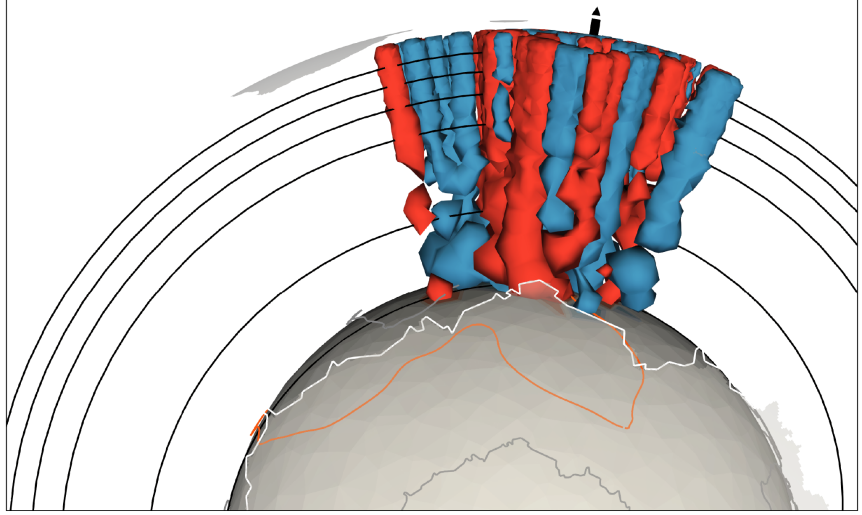

Output for best solution 3-D slice

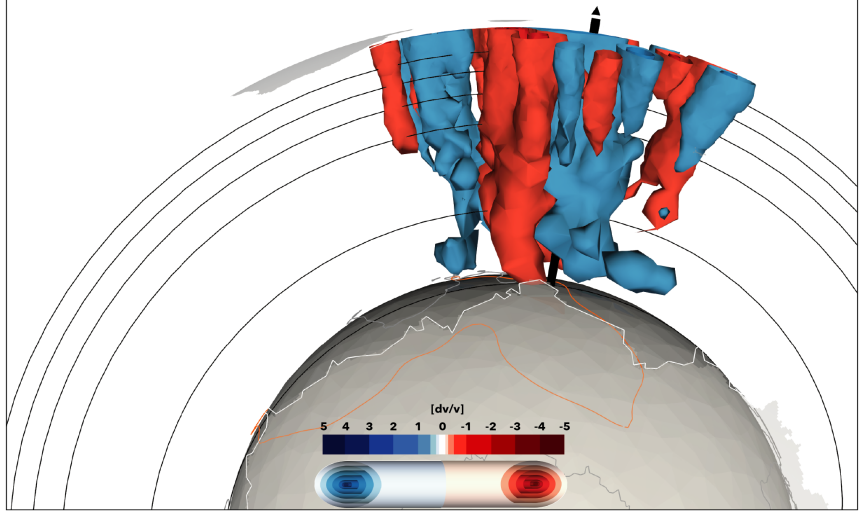

Input

Output

250



250

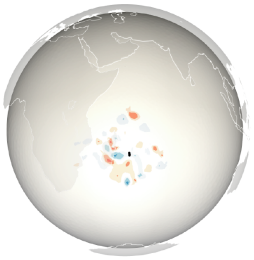

300

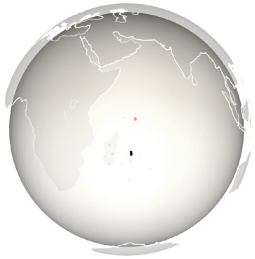

300

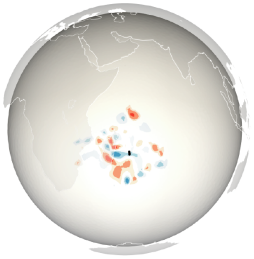

350

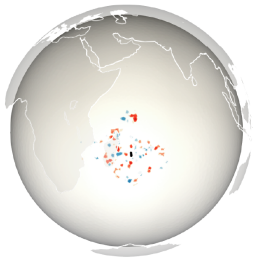

350

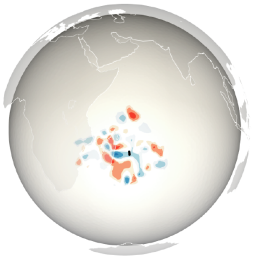

400

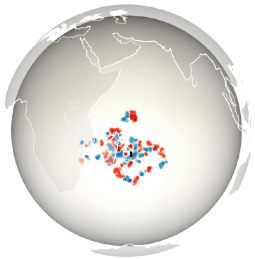

400

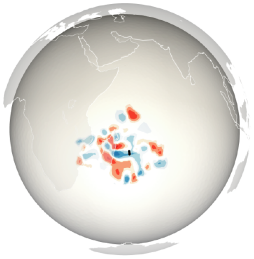

800

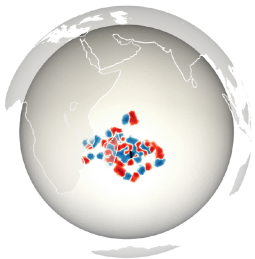

800

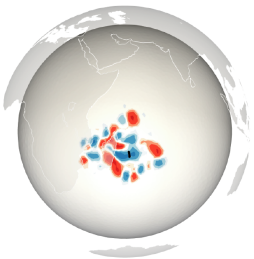

Description

Upper mantle columns at RHUM-RUM+ station locations

Uniform columns with radius of 100 km and between 400 and 1000km depth; Smearing occurs in all directions, since anomalies are very small, general features are still retrievable;

max. abs. amplitude: **3%** noise level: **no noise** $\frac{\text{damping}}{\text{smoothing}} =$ **0.7**

Input 3-D slice

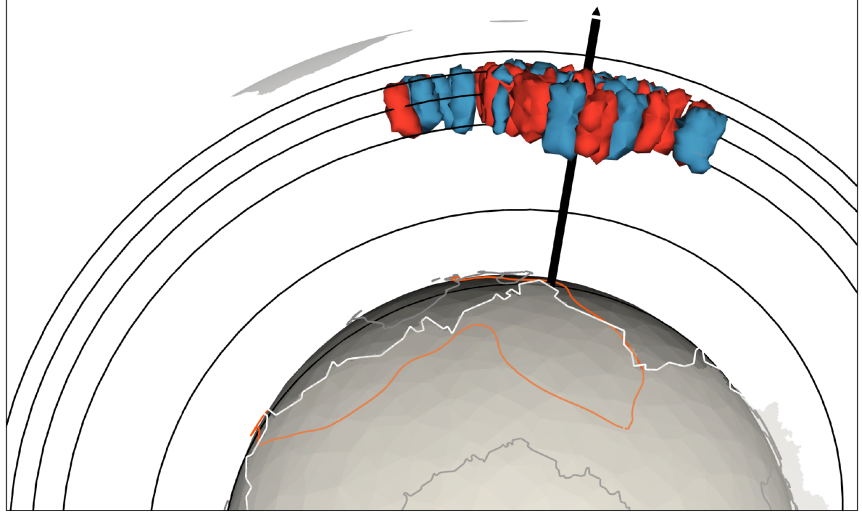

Output for best solution 3-D slice

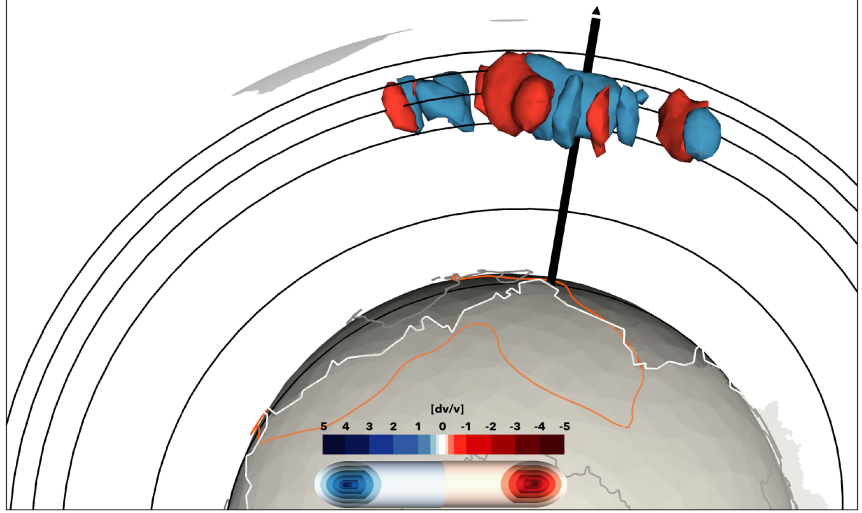

Input

Output

400

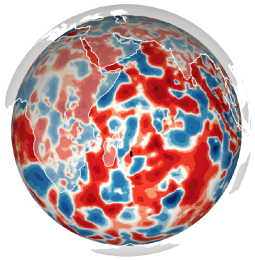

400

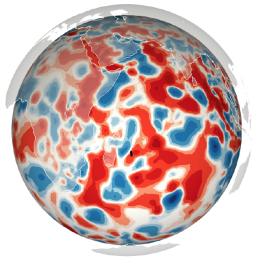

800

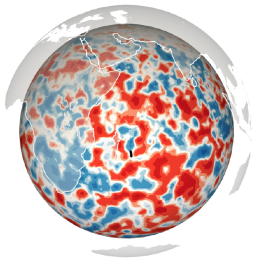

800

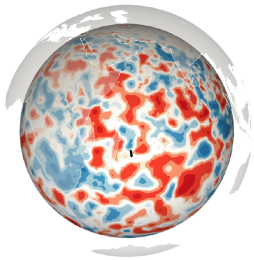

1500

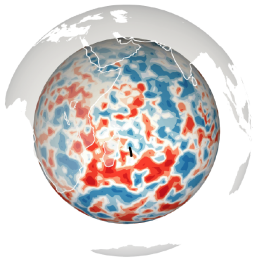

1500

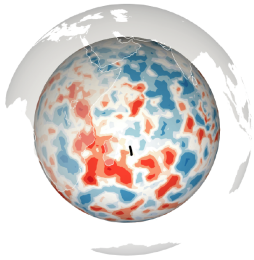

2000

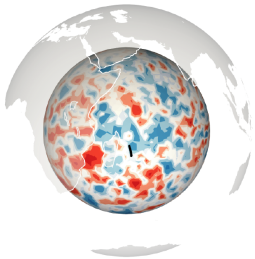

2000

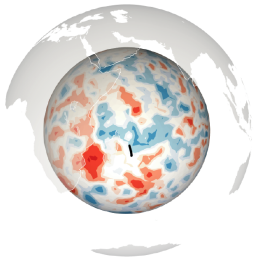

2800

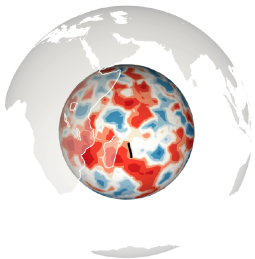

2800

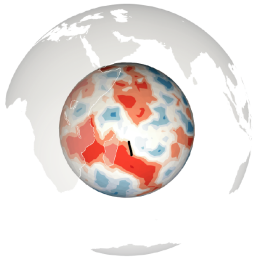

Description

Resolution input model = inverison output model

Main structures are recovered but output is smoother and more damped than input model;

max. abs. amplitude: **5%** noise level: **no noise** $\frac{\text{damping}}{\text{smoothing}} =$ **0.3**

Input 3-D slice

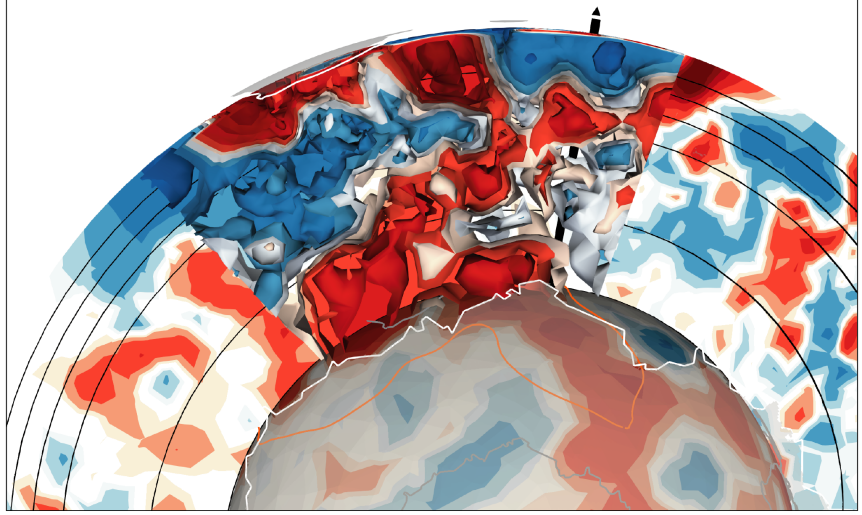

Output for best solution 3-D slice

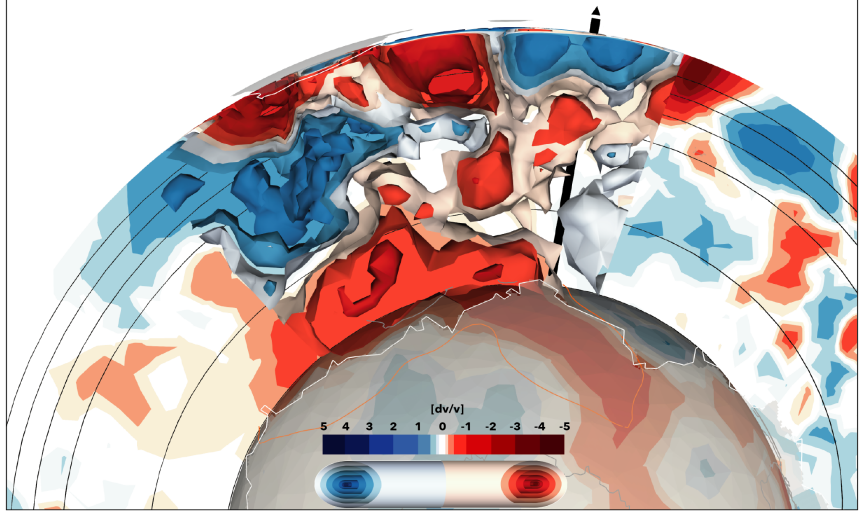

Input

Output

400

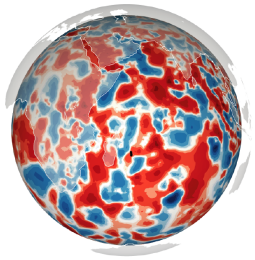

400

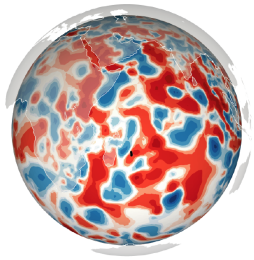

800

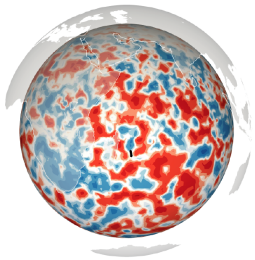

800

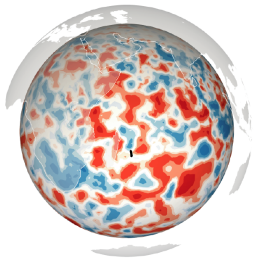

1500

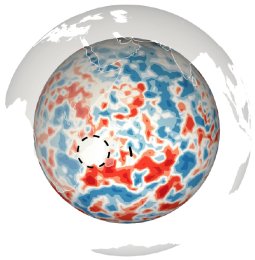

1500

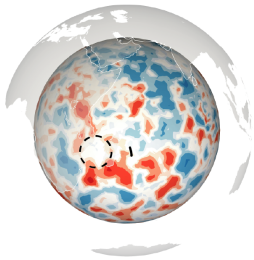

2000

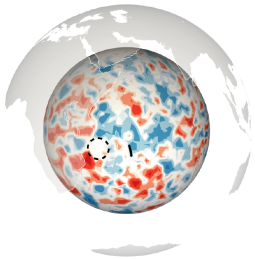

2000

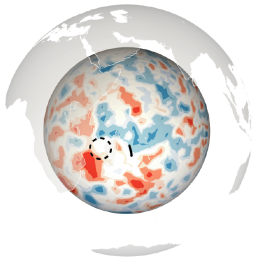

2800

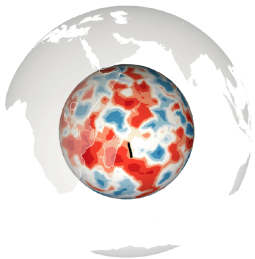

2800

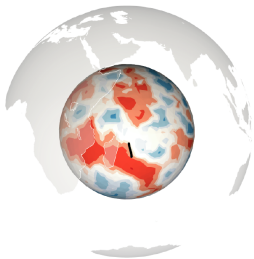

Description

Resolution input model = inversion output model - shpere in mid mantle

Sphere has a radius of 250 km and its centre is located in1500 km depth beneath South Mozambique (33°E/22°S). Location of cut out is marked in figures with dashed lines; good recovery with little smearing in mid mantle;

max. abs. amplitude: **5%** noise level: **no noise** $\frac{\text{damping}}{\text{smoothing}} =$ **0.3**

Input 3-D slice

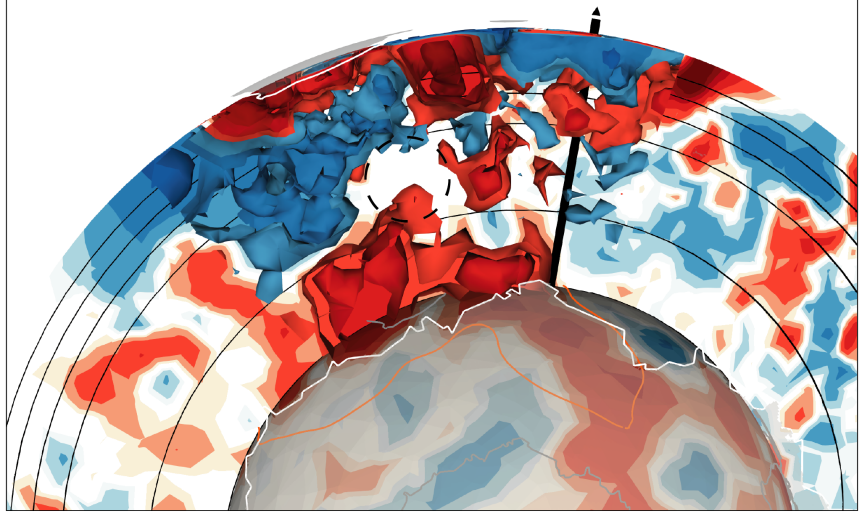

Output for best solution 3-D slice

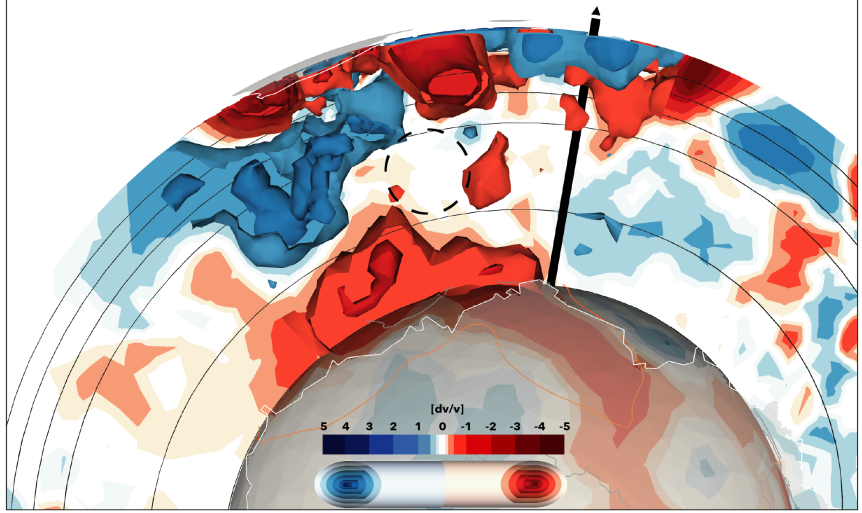

Input

Output

400

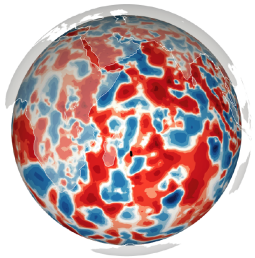

400

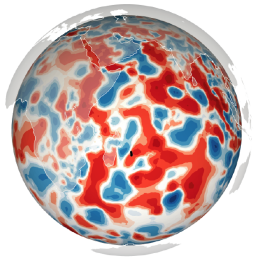

800

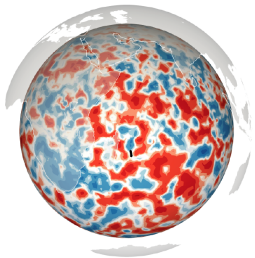

800

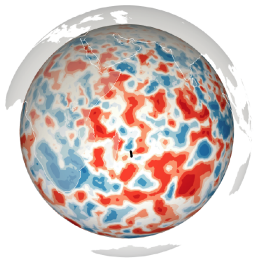

1500

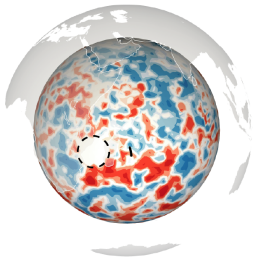

1500

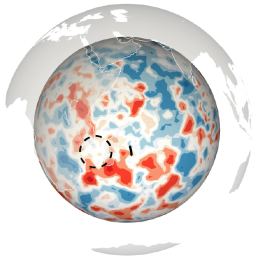

2000

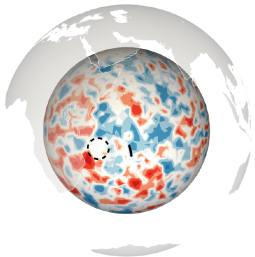

2000

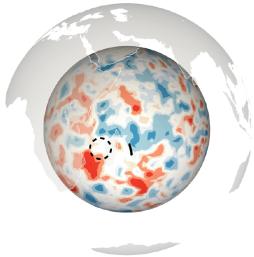

2800

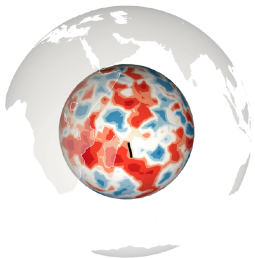

2800

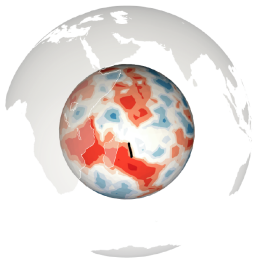

Description

Resolution input model = inversion output model - shpere in mid mantle

Sphere has a radius of 250 km and its centre is located in1500 km depth beneath South Mozambique (33°E/22°S). Location of cut out is marked in figures with dashed lines; good recovery with little smearing in mid mantle;

max. abs. amplitude: 5% noise level: uncertainties as standard-deviation $\frac{\text{damping}}{\text{smoothing}} = 0.3$

Input 3-D slice

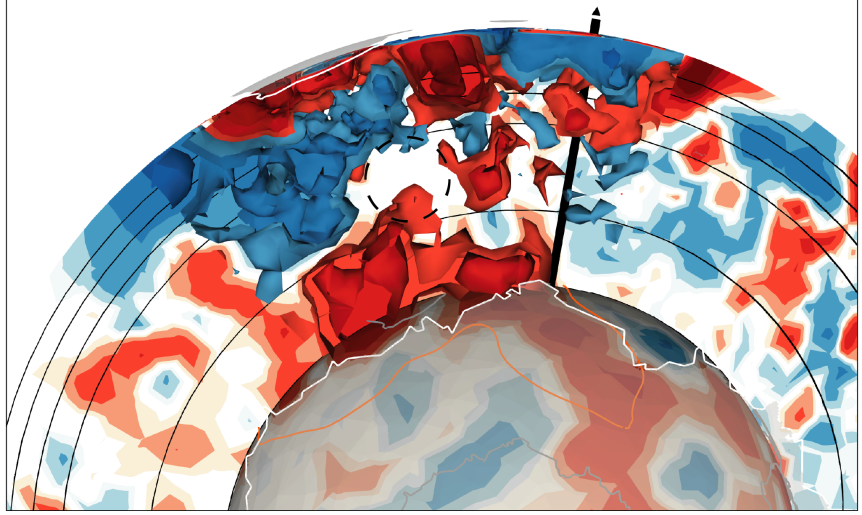

Output for best solution 3-D slice

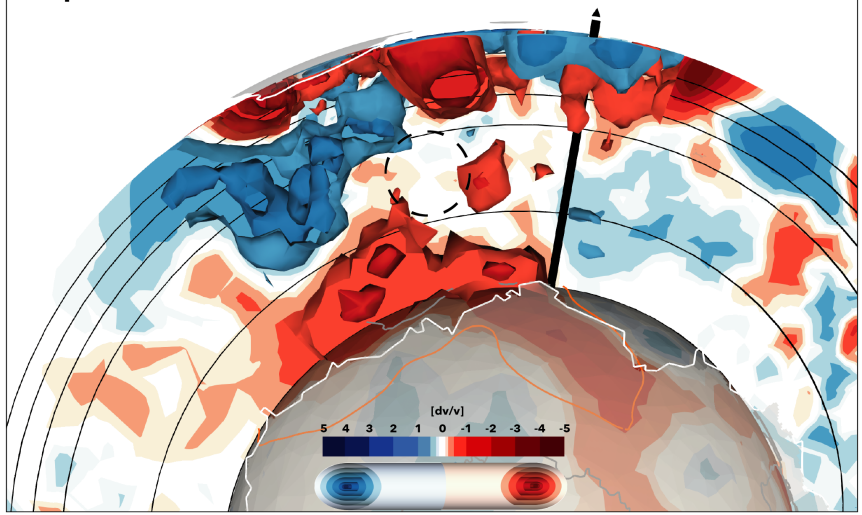

Input

Output

0

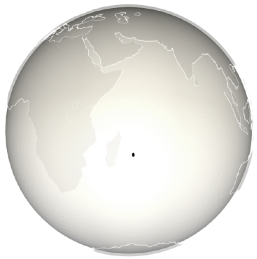

0

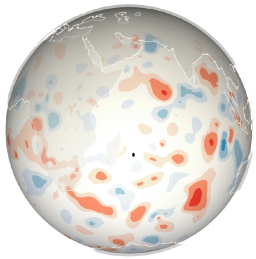

100



100

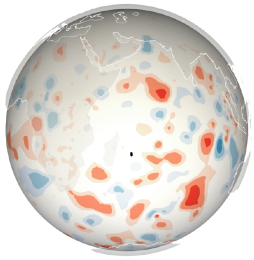

200



200

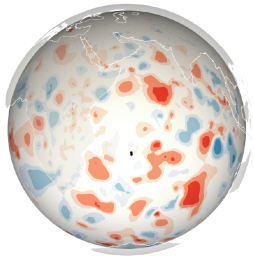

300

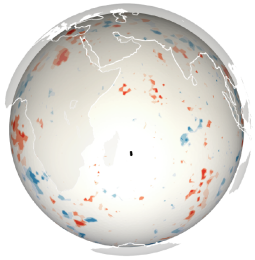

300

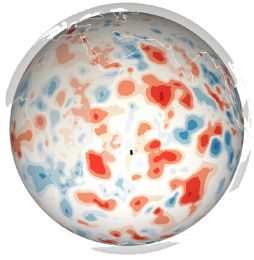

400

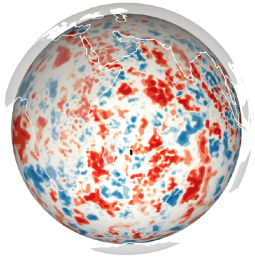

400

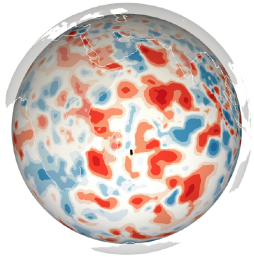

Description

Resolution input model = inverison output model - upper 400 km

Main structures are recovered but output is smoother and more damped than input model;
Upward smearing beneath Mozambique channeland South Atlantic;

max. abs. amplitude: 5% noise level: no noise $\frac{\text{damping}}{\text{smoothing}} = 0.3$

Input 3-D slice

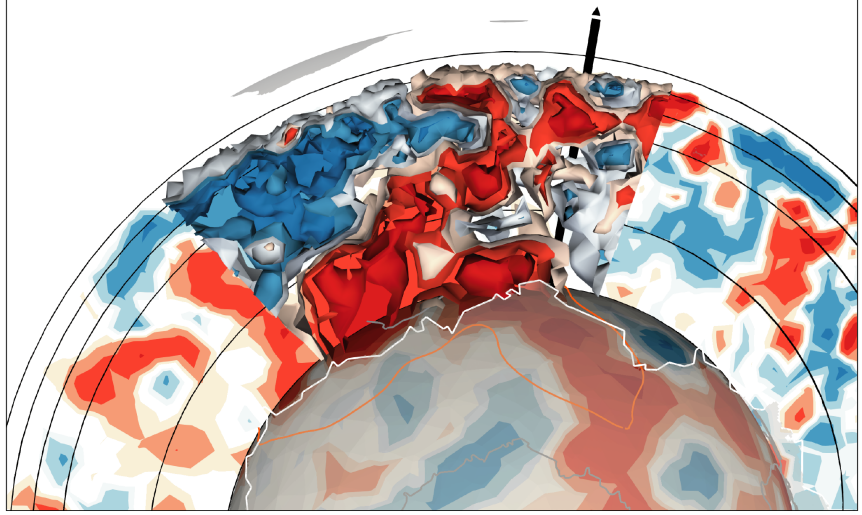

Output for best solution 3-D slice

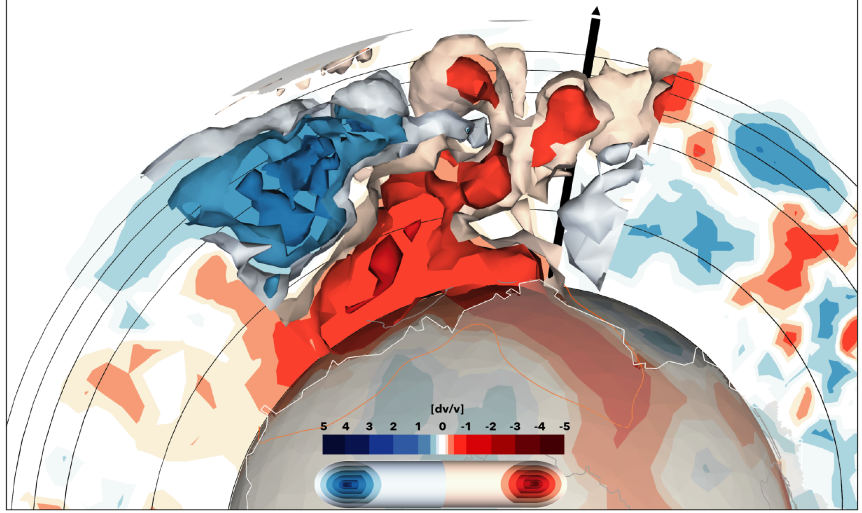

Input

Output

400

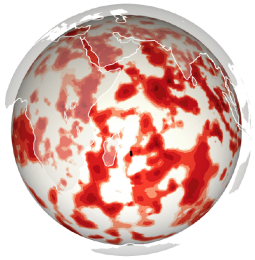

400

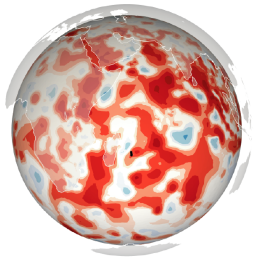

800

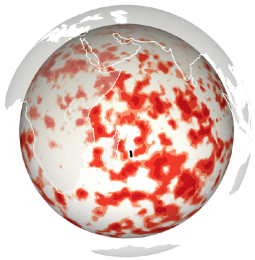

800

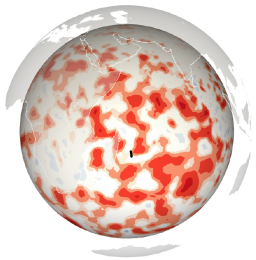

1500

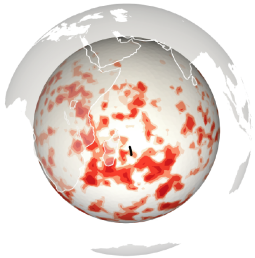

1500

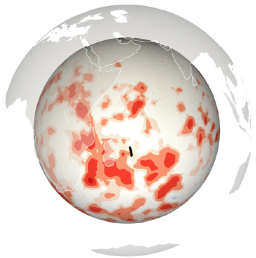

2000

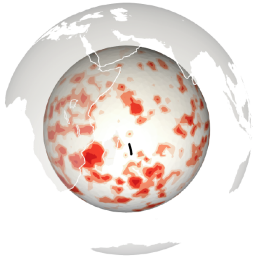

2000

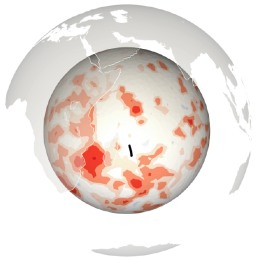

2800

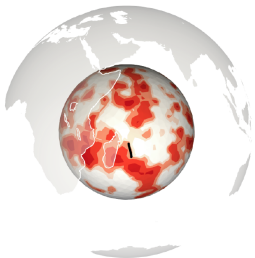

2800

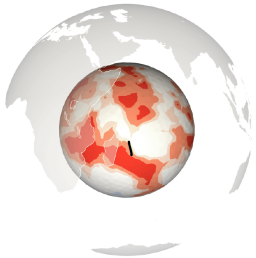

Description

Resolution input model = inversion output model - high velocities

Goee recovery of input model; lower amplitueds and smearing effects; high velocities show up in the upper mantle;

max. abs. amplitude: **5%** noise level: **no noise** $\frac{\text{damping}}{\text{smoothing}} =$ **0.3**

Input 3-D slice

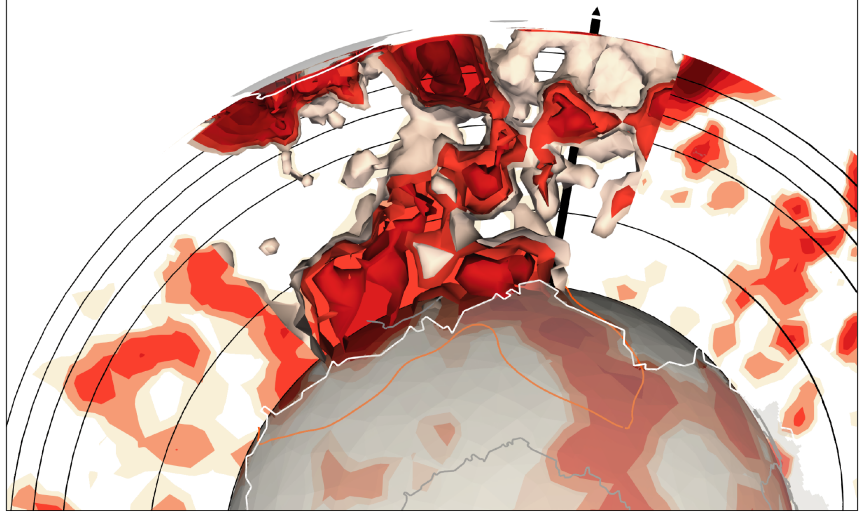

Output for best solution 3-D slice

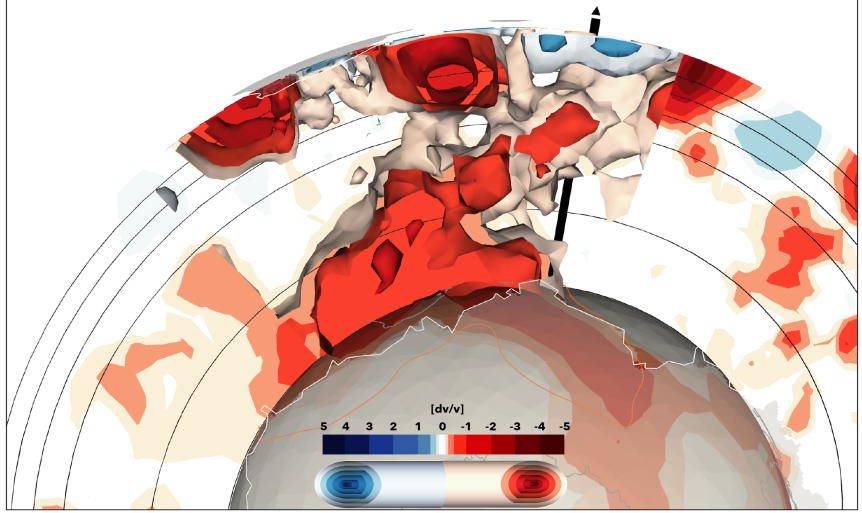

Input

Output

0

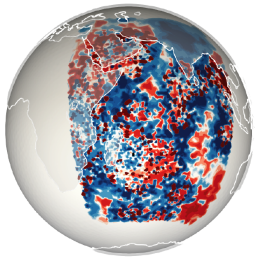

0

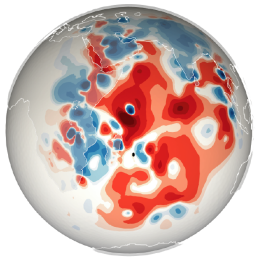

100

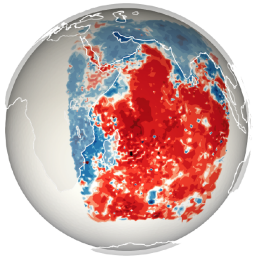

100

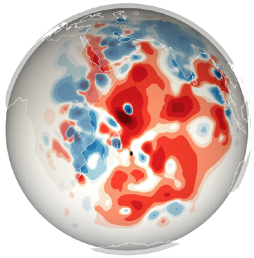

200

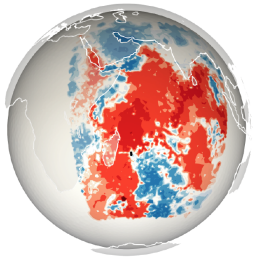

200

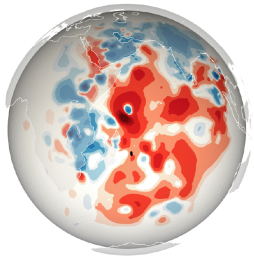

300

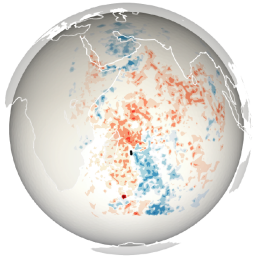

300

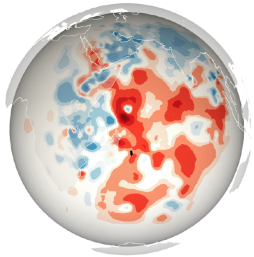

400



400

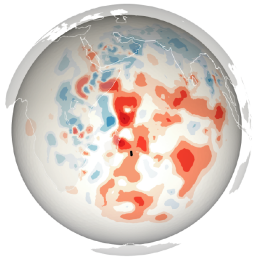

Description

Resolution input model = Surface tomography model from Mazzullo et al., 2017

Main features are recovered but output is smoother and more damped than input model; smearing downward; high velocities at 0 km are not well resolved, due to station coveage in the Western Indian Ocean;

max. abs. amplitude: **5%** noise level: **no noise** $\frac{\text{damping}}{\text{smoothing}} =$ **0.3**

Input 3-D slice

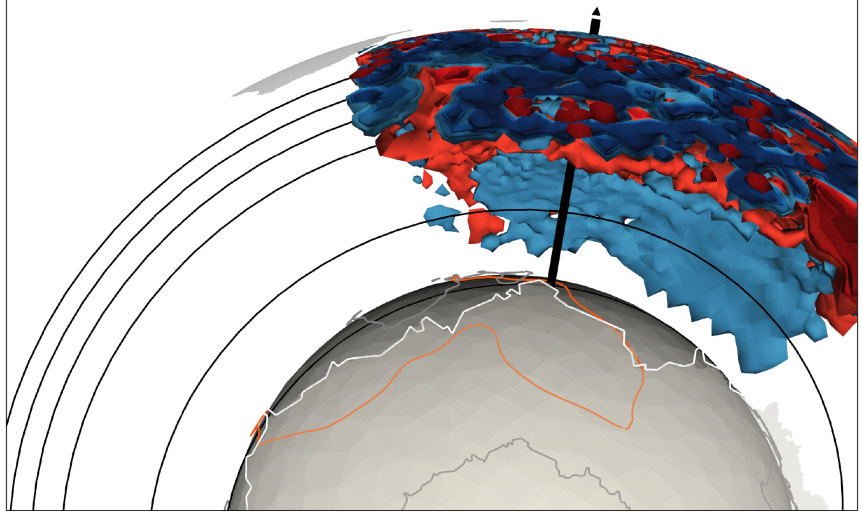

Output for best solution 3-D slice

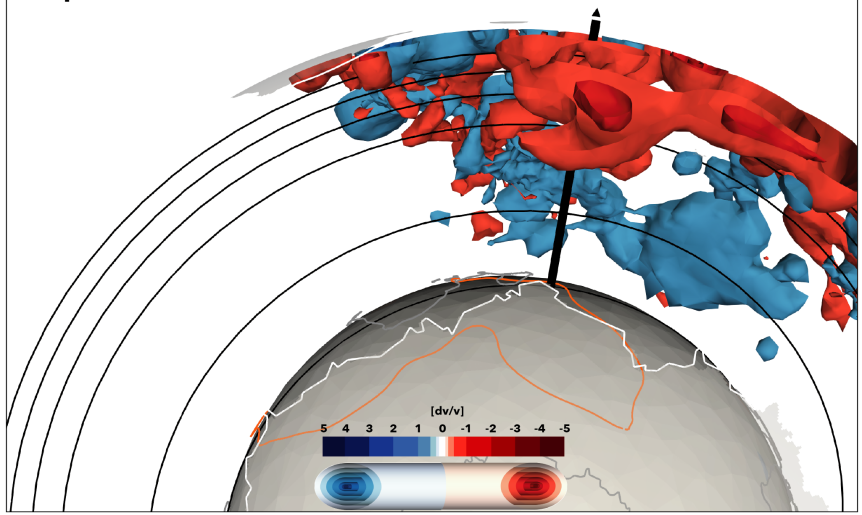

Input

Output

0

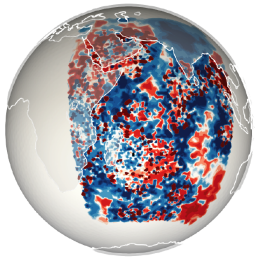

0

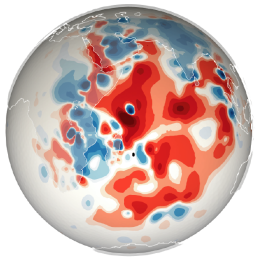

100

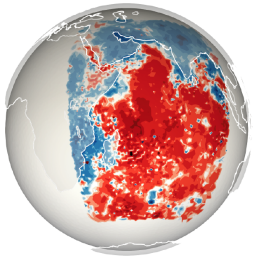

100

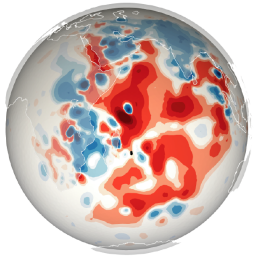

200

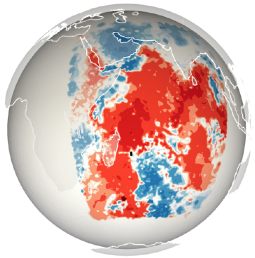

200

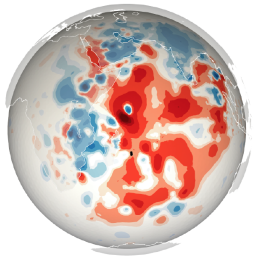

300

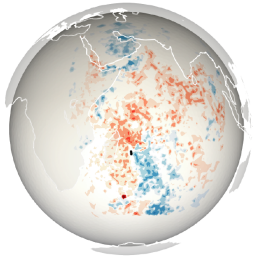

300

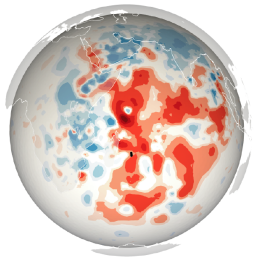

400



400

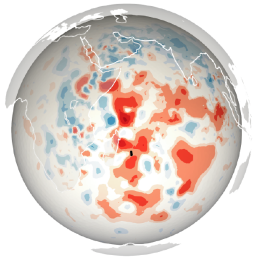

Description

Resolution input model = Surface tomography model from Mazzullo et al., 2017

Main features are recovered but output is smoother and more damped than input model; smearing downward; high velocities at 0 km are not well resolved, due to station coveage in the Western Indian Ocean;

max. abs. amplitude: **5%** noise level: **uncertainties as standard-deviation** $\frac{\text{damping}}{\text{smoothing}} =$ **0.3**

Input 3-D slice

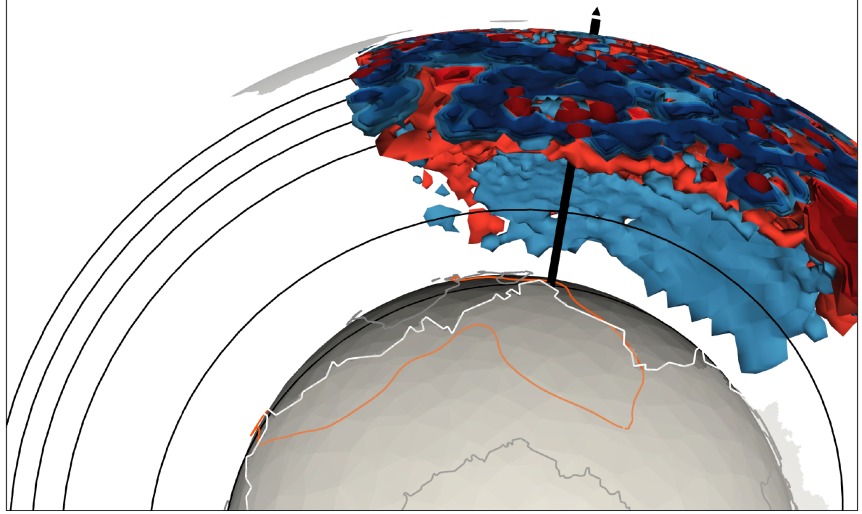

Output for best solution 3-D slice

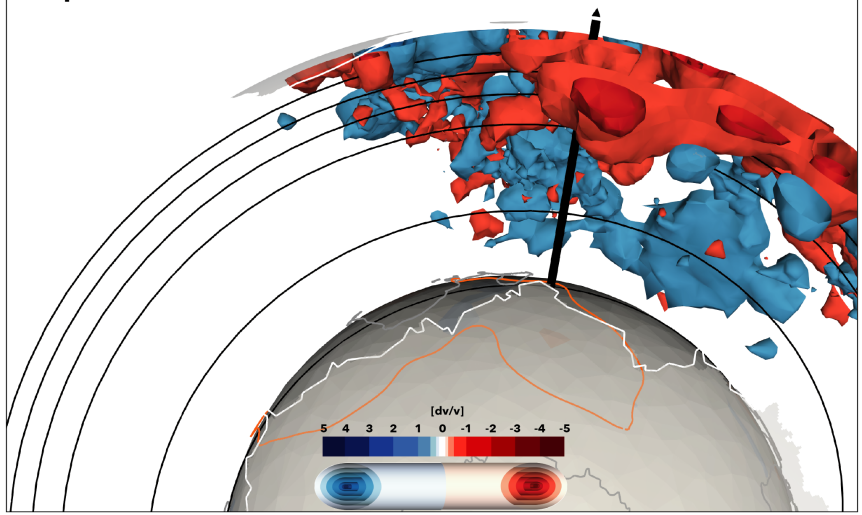

—

C
Model comparison

Here, I present a comparison between different tomographic models for following cross sections:

- La Réunion
- Afar
- Kerguelen

For more information regarding the different models and the vote map, please refer to Hosseini et al. (2019) and Shephard et al. (2017).

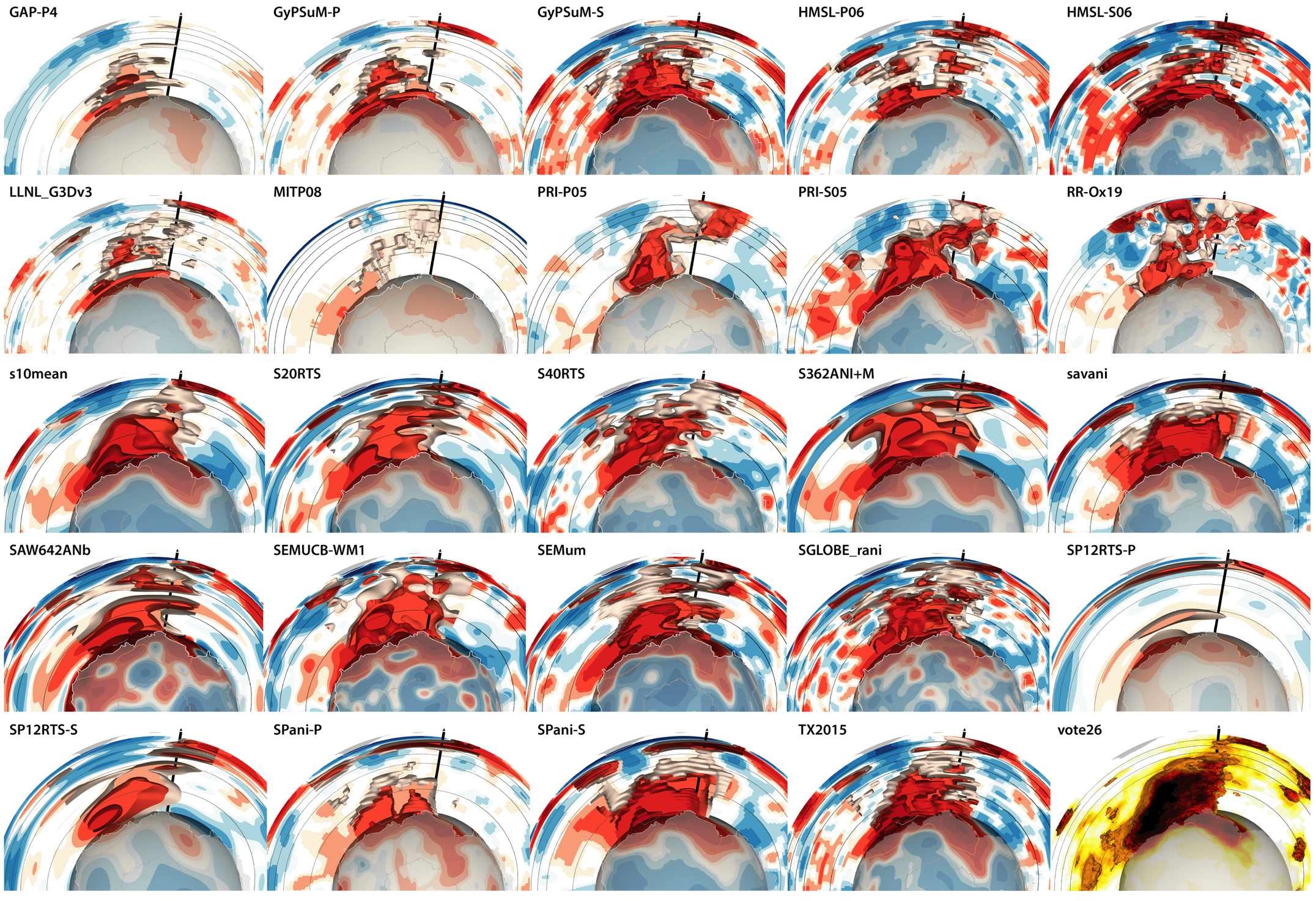
GAP-P4
GyPSuM-P
GyPSuM-S
HMSL-P06
HMSL-S06
LLNL_G3Dv3
MITP08
PRI-P05
PRI-S05
RR-Ox19
s10mean
S20RTS
S40RTS
S362ANI+M
savani
SAW642ANb
SEMUCB-WM1
SEMum
SGLOBE_rani
SP12RTS-P
SP12RTS-S
SPani-P
SPani-S
TX2015
vote26
5 4 3 2 1 0 -1 -2 -3 -4 -5
[dv/v]
26 24 22 20 18 16 14 12 10 8 6 4 2 0
Number of models of low velocity votes

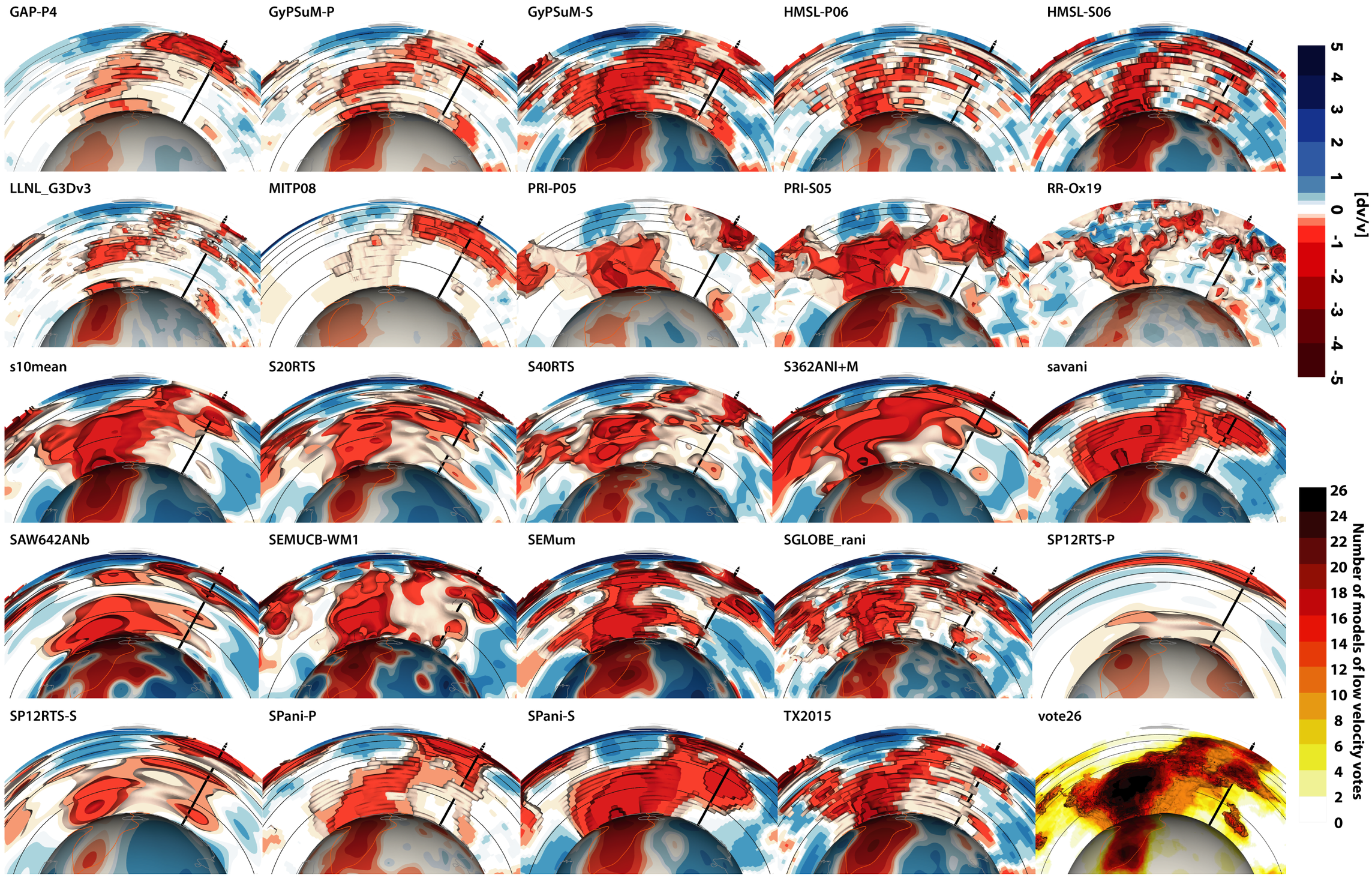
GAP-P4
GyPSuM-P
GyPSuM-S
HMSL-P06
HMSL-S06
LLNL_G3Dv3
MITP08
PRI-P05
PRI-S05
RR-Ox19
s10mean
S20RTS
S40RTS
S362ANI+M
savani
SAW642ANb
SEMUCB-WM1
SEMum
SGLOBE_rani
SP12RTS-P
SP12RTS-S
SPani-P
SPani-S
TX2015
vote26
5 4 3 2 1 0 -1 -2 -3 -4 -5
[dv/v]
26 24 22 20 18 16 14 12 10 8 6 4 2 0
Number of models of low velocity votes

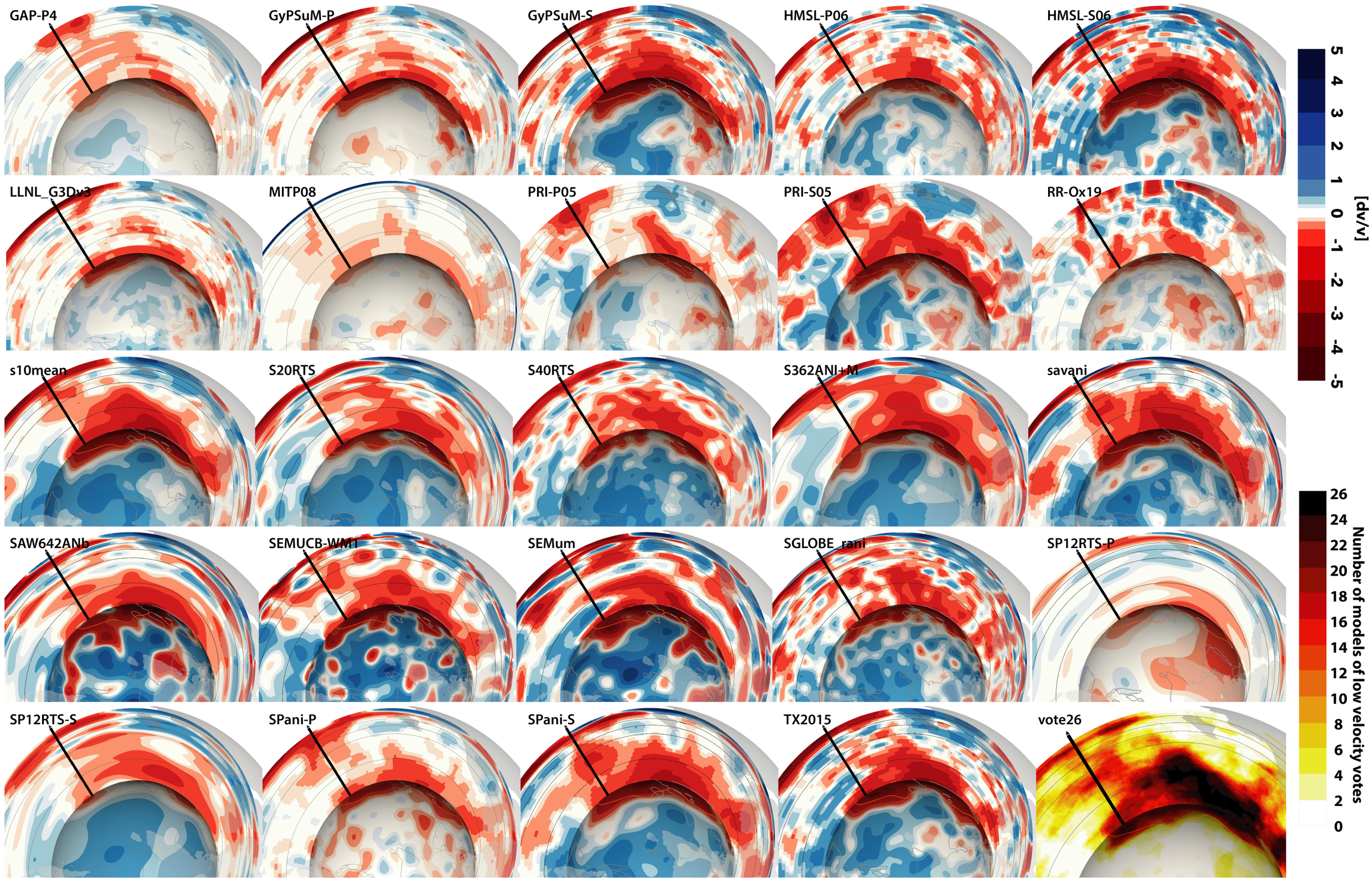
GAP-P4
GyPSuM-P
GyPSuM-S
HMSL-P06
HMSL-S06
LLNL_G3Dv3
MITP08
PRI-P05
PRI-S05
RR-Ox19
s10mean
S20RTS
S40RTS
S362ANI+M
savani
SAW642ANb
SEMUCB-WM1
SEMum
SGLOBE_rani
SP12RTS-P
SP12RTS-S
SPani-P
SPani-S
TX2015
vote26
5 4 3 2 1 0 -1 -2 -3 -4 -5
[dv/v]
26 24 22 20 18 16 14 12 10 8 6 4 2 0
Number of models of low velocity votes

D

Station performance, station quality and earthquake distribution

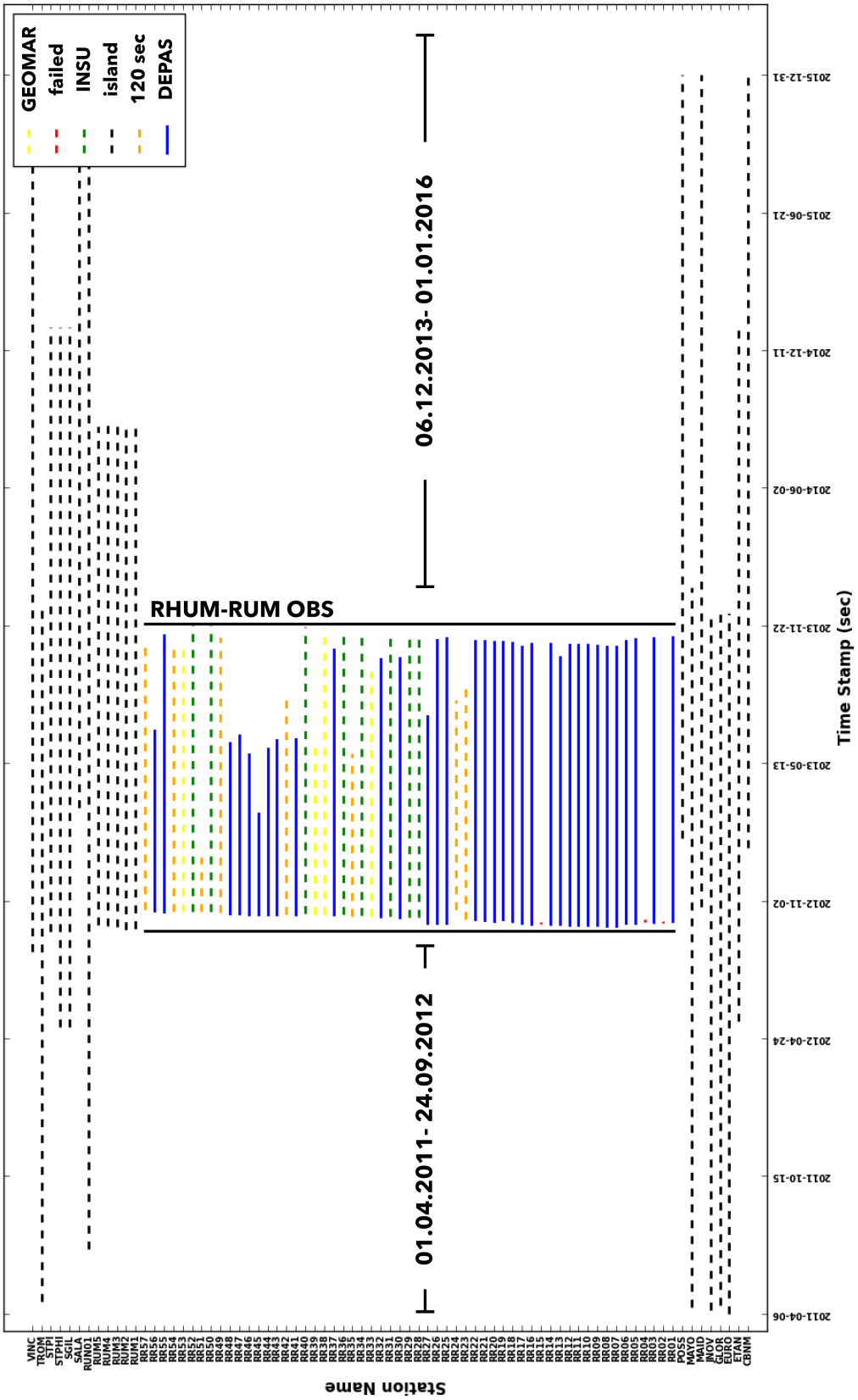

Figure D.1: Time-spans covered by for all deployed island and ocean stations. On the y-axis, station names are given, and the x-axis is time. Most island stations (black dashed lines) were installed before the deployments of the OBS and recorded more than a year after the recovery of the OBS. Three OBS did not record at all due to seismometer failure (short red lines). For an overview on the performance of RHUM-RUM stations, refer to Stähler et al. (2016a).

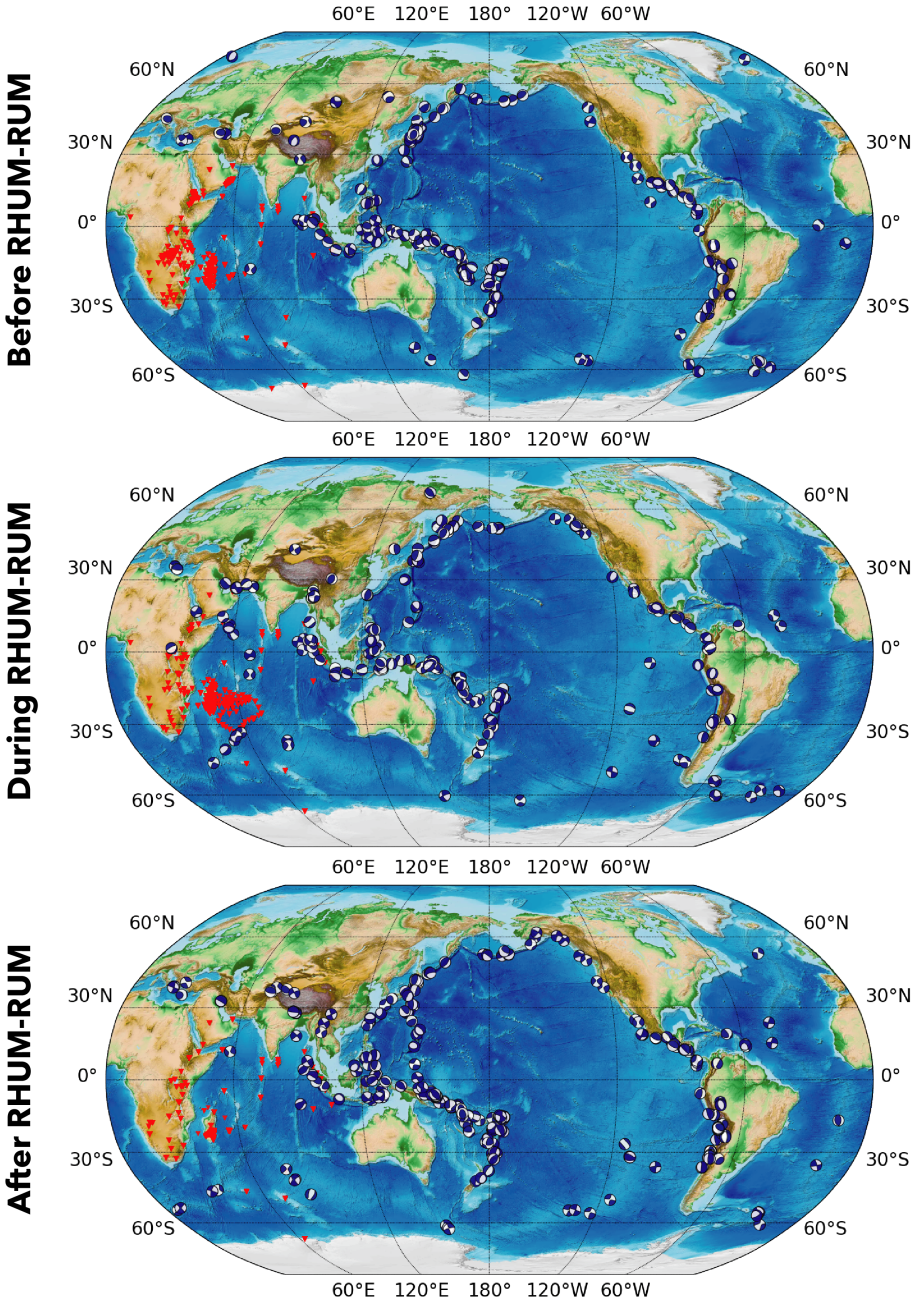

Figure D.2: Distribution of stations (red triangles) and earthquakes (blue beachballs) before (1. April 2011 - 24. September 2012), during (25. September 2012 - 5. December 2013) and after (6. December 2013 - 01. January 2016) RHUM-RUM experiment. Stations from the whole time (2011-2016) span are used for the multifrequency measurements. This dataset is referred as RHUM-RUM+ in the text.

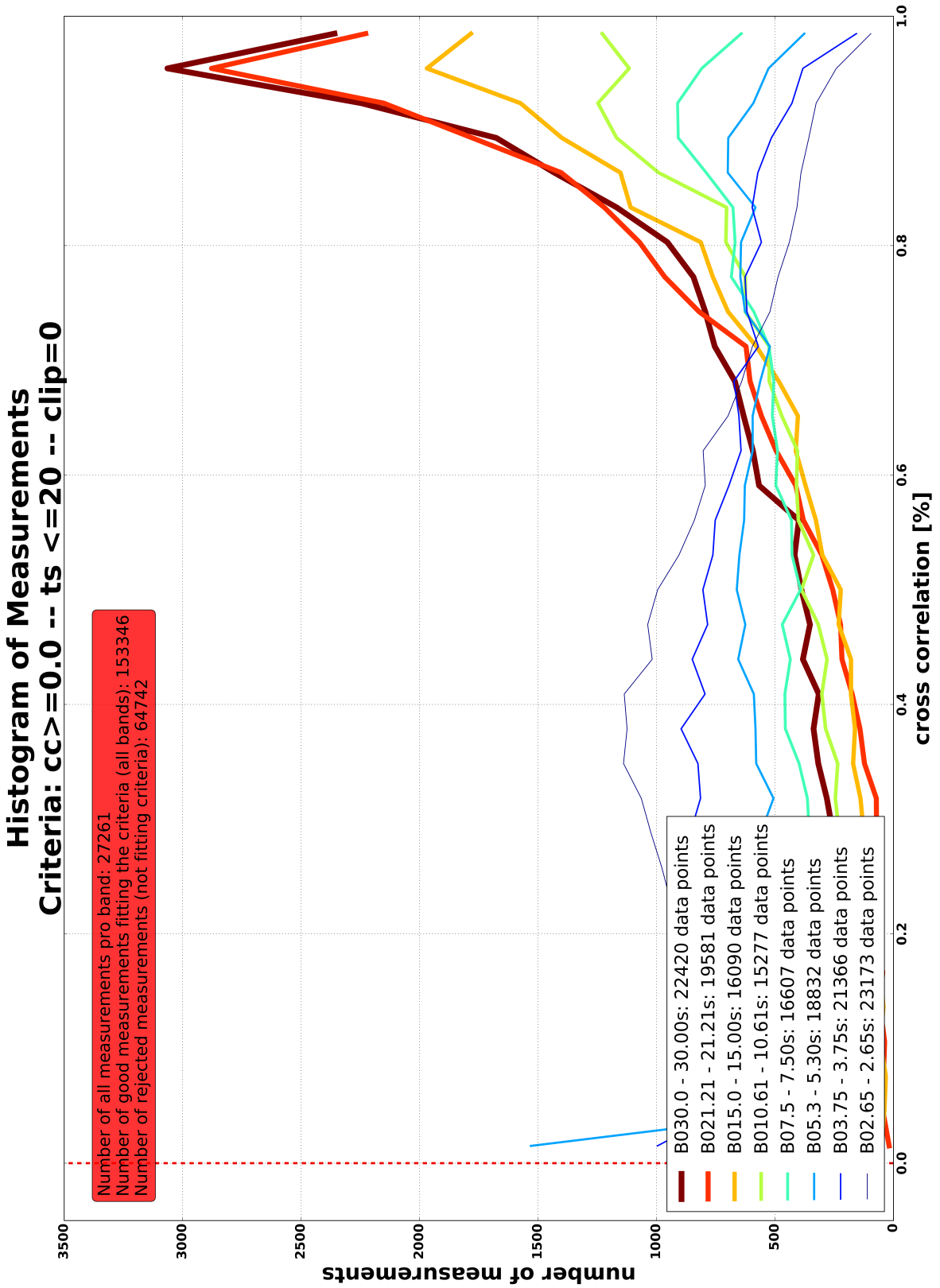

Figure D.3: Histogram of all measurements in the RHUM-RUM+ dataset. Band 1 and 2 show the highest number of good measurements. Thw low frequency bands have a characteristic peak around 50%, possibly due to noise effects (Hosseini, 2016).

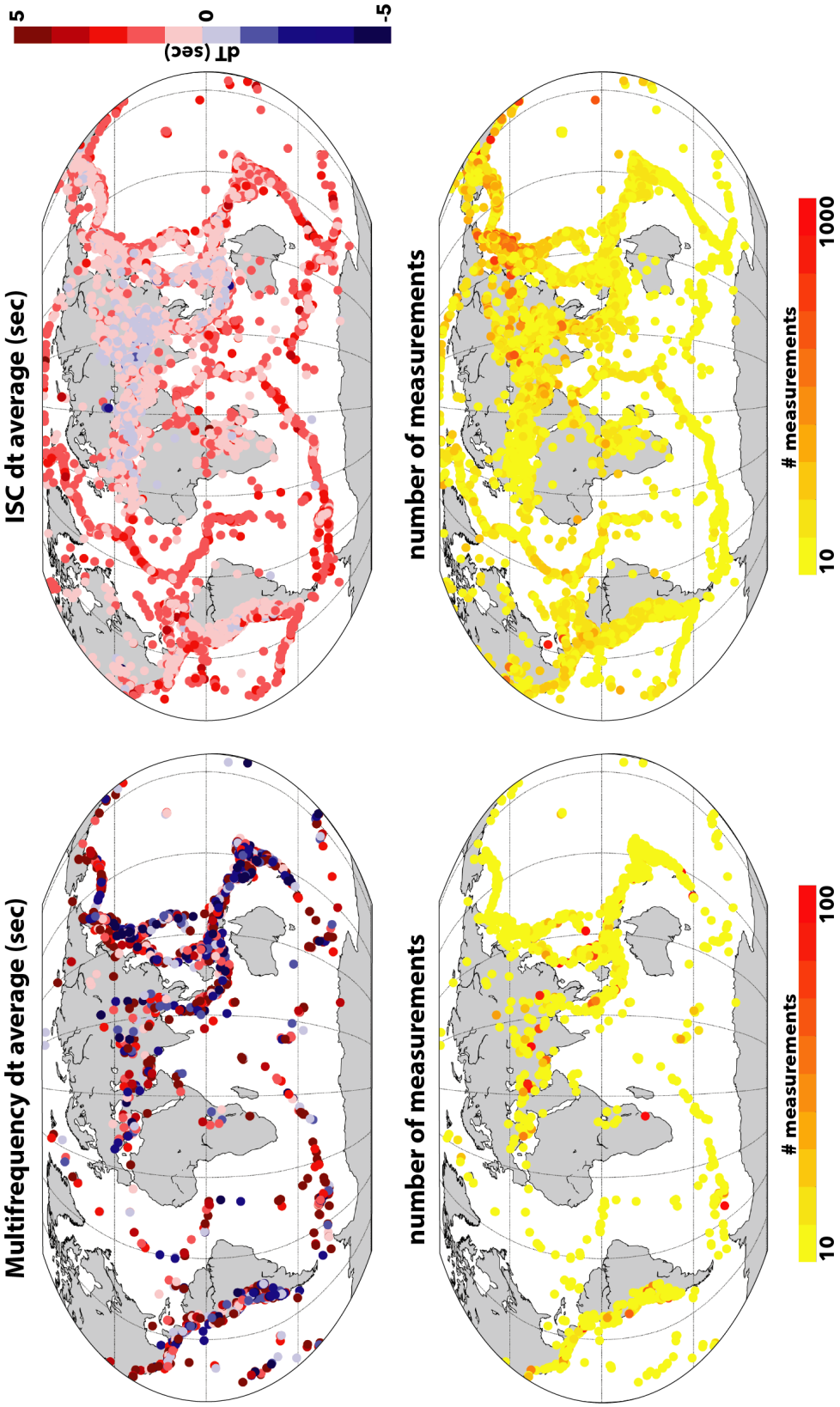

Figure D.4: 2,026 usable events for multifrequency measurements, including the events used in the P-diff dataset from (Hosseini, 2016). 17,929 events from the ISC-EHB catalogue for the years 1964-2008. Top row shows average traveltime measurements, and the second row shows the total number of measurements.

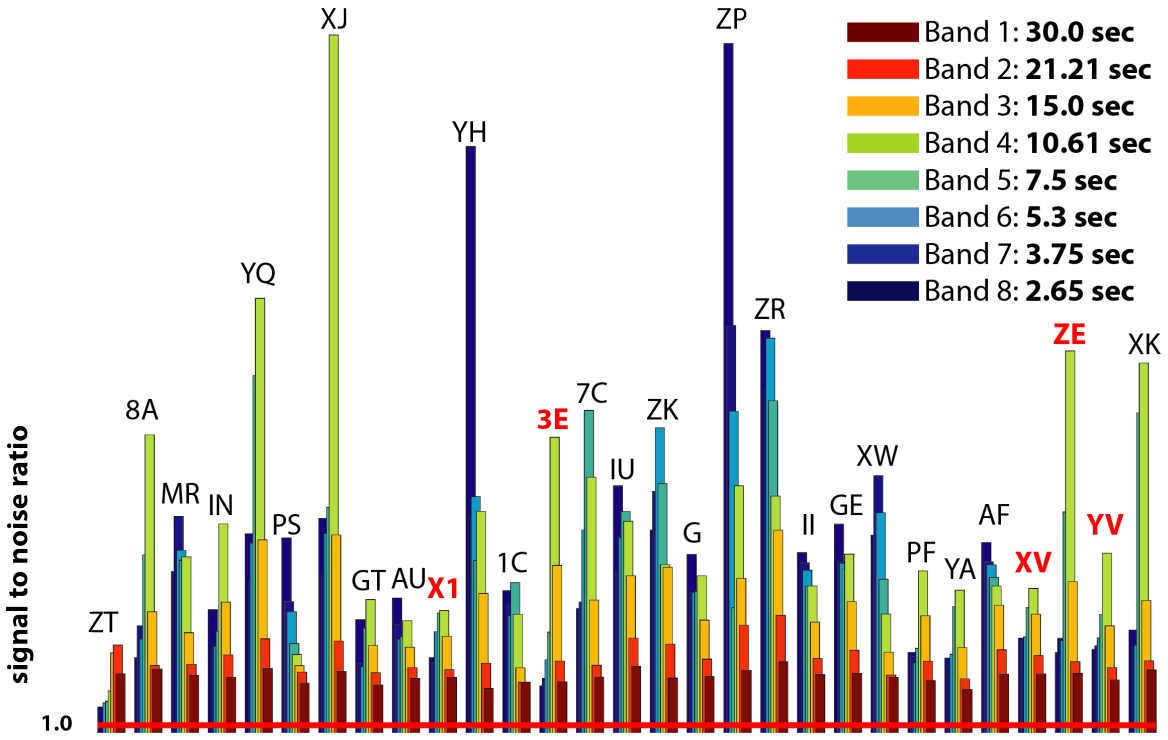

Figure D.5: Histograms of average SNR of selected networks in the RHUM-RUM+ dataset in different frequency bands. Listed networks belong either to RHUM-RUM (YV), partner projects (X1, 3E, XV, ZE) or other permanent and temporal experiments between 2011 and 2016 in the western Indian Ocean. Despite the fact the RHUM-RUM data shows considerable noise in the waveforms, the signal to noise ratio (SNR) has improved by using our multifrequency measurements technique.

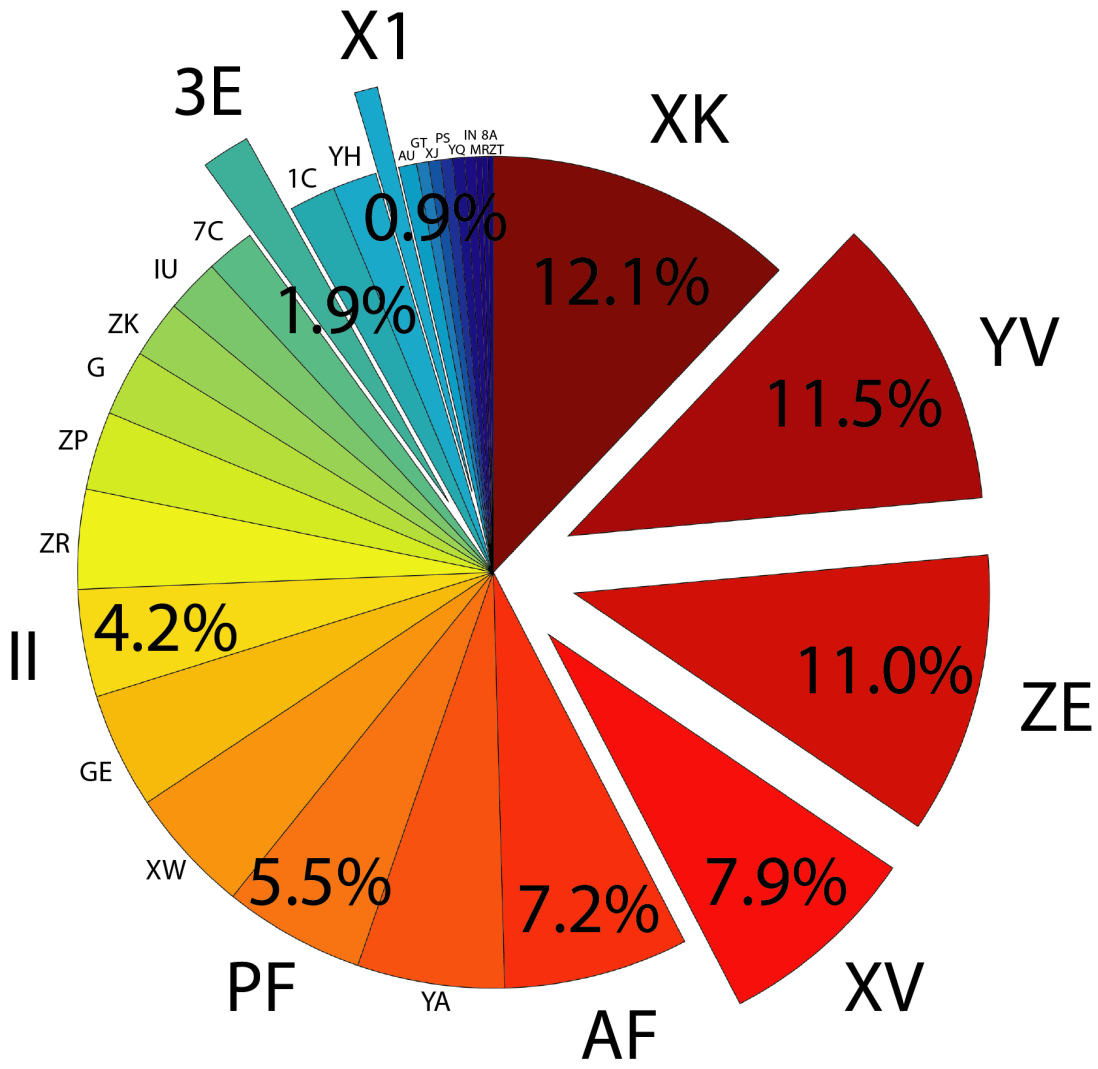

Figure D.6: Contribution of different networks to the high-quality measurements in the RHUM-RUM+ dataset. Listed networks belong either to RHUM-RUM (YV), partner projects (X1, 3E, XV, ZE) or other permanent and temporal experiments between 2011 and 2016 in the western the Indian Ocean.

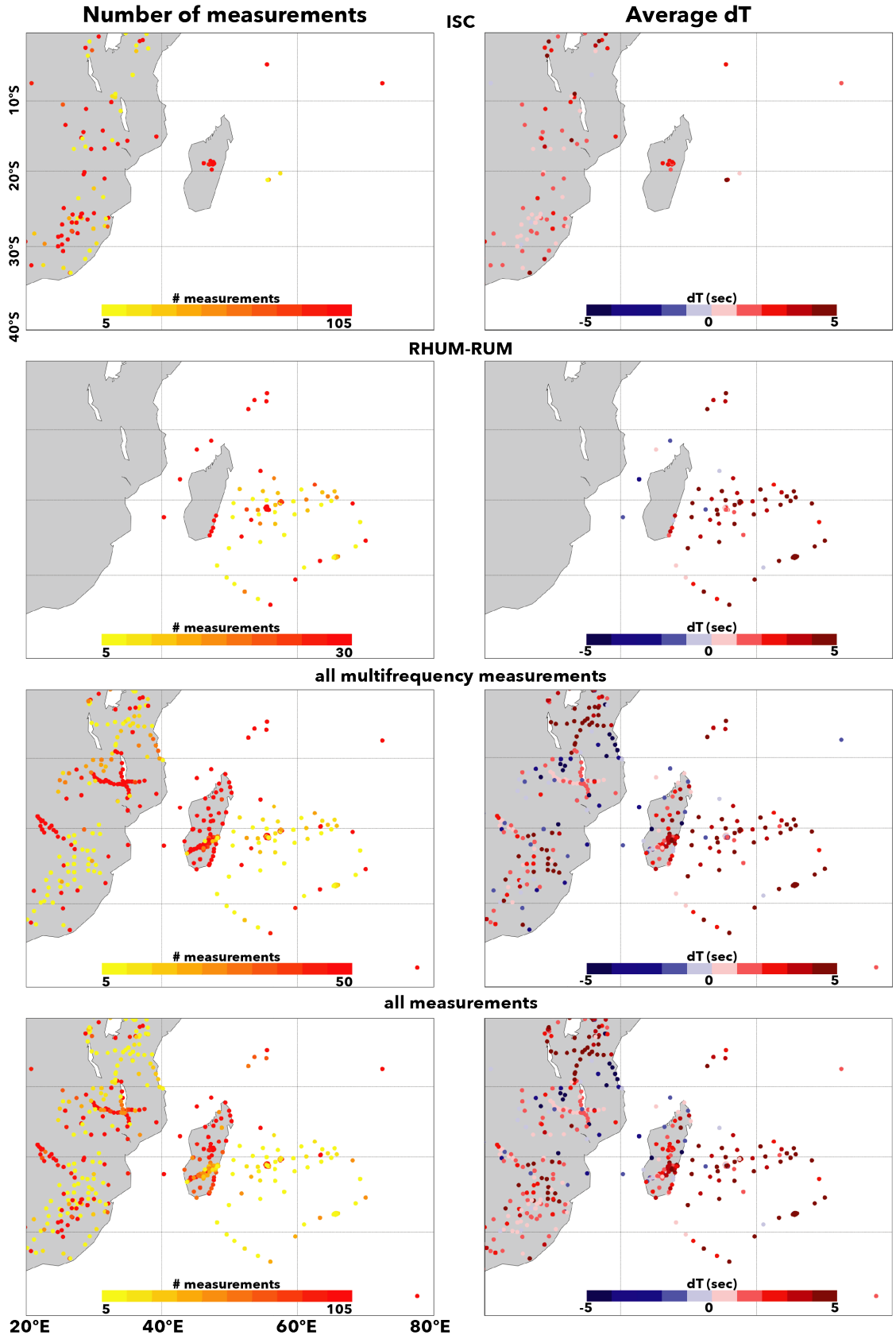

Figure D.7: Number of successful measurements (left) and average δT_s (right) plotted on the station locations. Each row belongs to one dataset: ISC, RHUM-RUM, all multifrequency measurements (including Pdiff) and all traveltimes together.

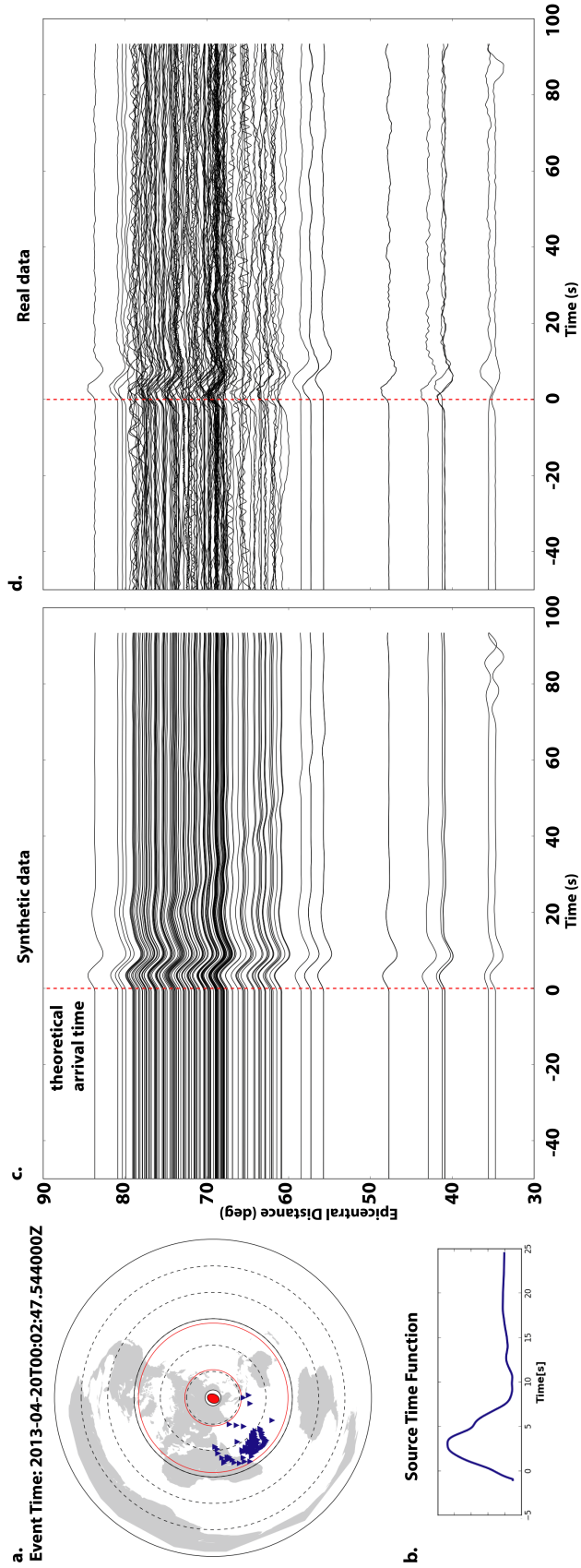

Figure D.8: Event information for FigureD.9. Event time 2013/04/20 (00:02:47.54) in Sichuan, China (lat: 30.308; lon: 102.888; Depth: 14.0 km) and a magnitude of 6.6 (mww). **(a)** Station and event location. **(b)** Estimated source time function. **(c)** Synthetic waveforms sorted by epicentral distance and aligned on their theoretical P arrival times. **(d)** Observed real data.

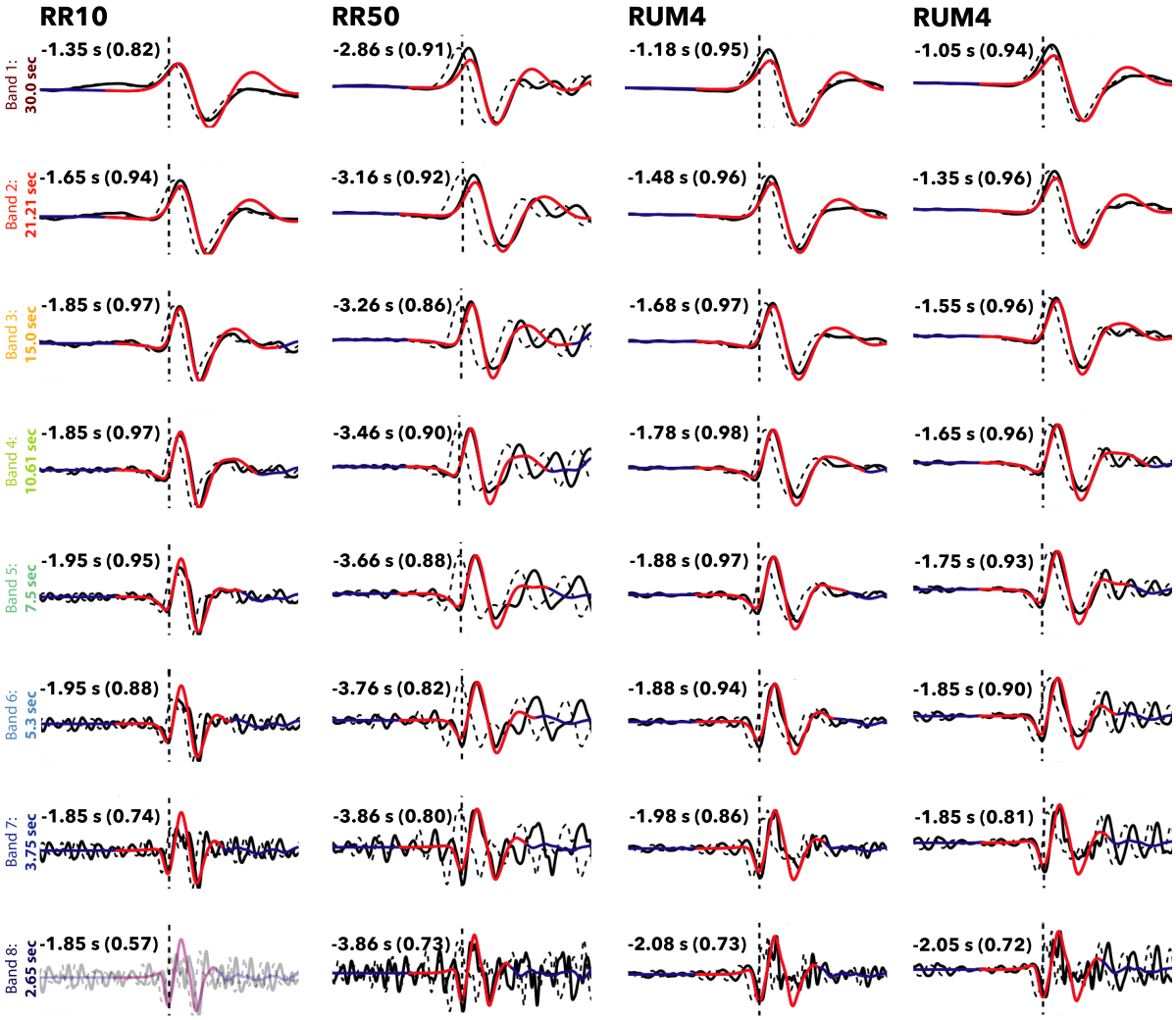

Figure D.9: Observed and predicted traveltime dispersions of P-waves for 2 OBS (RR10 and RR50) and two stations (RUM4 and RUM5) positioned on Madagascar for event in Figure D.8. The first number next to the waveforms is the traveltime shift and the number in brackets is the goodness of fit. The observed traveltime shift for all 4 examples is dispersive for similar paths: to higher frequencies (from top to bottom) the dashed waveform arrives increasingly early (for RR10 from -1.35 s to -1.85 s) w.r.t. IASP91.

To RHUM. Cheers!

— After the successful recovery of all OBSes in 2013.

References

Don L Anderson. Scoring hotspots: The plume and plate paradigms. *SPECIAL PAPERS-GEOLOGICAL SOCIETY OF AMERICA*, 388:31, 2005. ISSN 0072-1077.

L Auer, L Boschi, Tw Becker, Tarje Nissen-Meyer, and Domenico Giardini. Savani: A variable resultion whole-mantle model of anisotropic shear velocity variations based on multiple data sets. *Journal of Geophysical Research: Solid Earth*, pages 1–29, 2014. ISSN 21699313. doi: 10.1002/2013JB010773.Received. URL `http://onlinelibrary.wiley.com/doi/10.1002/2013JB010773/full`.

E Backus and J F Gilbert. Numerical Applications of a Formalism for Geophysical Inverse Problems. *Geophysical Journal of the Royal Astronomical Society*, pages 247–276, 1967.

George Backus and F Gilbert. Uniqueness in the inversion of inaccurate gross earth data. *JSTOR*, 266, 1970.

Maxim D. Ballmer, Lina Schumacher, Vedran Lekic, Christine Thomas, and Garrett Ito. Compositional layering within the large low shear-wave velocity provinces in the lower mantle. *Geochemistry Geophysics Geosystems*, pages 1000–1019, 2016. doi: 10.1002/2015GC006060.Received.

C. Bradford Barber, David P. Dobkin, and Hannu Huhdanpaa. The quickhull algorithm for convex hulls. *ACM Transactions on Mathematical Software*, 22(4):469–483, 1996. ISSN 00983500. doi: 10.1145/235815.235821. URL `http://portal.acm.org/citation.cfm?doid=235815.235821`.

Guilhem Barruol. PLUME investigates South Pacific Superswell. *Eos, Transactions American Geophysical Union*, 83(45):511, 2002. ISSN 0096-3941. doi: 10.1029/2002EO000354. URL `http://doi.wiley.com/10.1029/2002EO000354`.

Guilhem Barruol and Karin Sigloch. Investigating La Réunion hot spot from crust to core. *Eos*, 94(23):205–207, 2013. ISSN 23249250. doi: 10.1002/2013EO230002.

C Bassin, G Laske, and G Masters. The Current Limits of Resolution for Surface Wave Tomography in North America. *Eos*, 81, 2000.

Thorsten W Becker and Lapo Boschi. A comparison of tomographic and geodynamic mantle models. *Geochemistry Geophysics Geosystems*, 3:1003, 2002. ISSN 1525-2027. doi: Artn1003\rDoi10.1029/2001gc000168. URL `http://www.ncbi.nlm.nih.gov/entrez/query.fcgi?db=pubmed{&}cmd=Retrieve{&}dopt=AbstractPlus{&}list{_}uids=000173170800001{%}5Cnpapers2://publication/doi/10.1029/2001GC000168`.

Harmen Bijwaard and Wim Spakman. Tomographic evidence for a narrow whole mantle plume below Iceland. *Earth and Planetary Science Letters*, 166(3-4):121–126, 1999. ISSN 0012821X. doi: 10.1016/S0012-821X(99)00004-7.

Harmen Bijwaard, Wim Spakman, and E. Robert Engdahl. Closing the gap between regional and global travel time tomography. *Journal of Geophysical Research: Solid Earth*, 103(B12): 30055–30078, 1998. ISSN 01480227. doi: 10.1029/98JB02467. URL `http://doi.wiley.com/10.1029/98JB02467`.

C. Brown and R. W. Girdler. Interpretation of African gravity and its implications for the breakup of the continents. *Journal of Geophysical Research*, 85(B11):6443–6455, 1980. ISSN 01480227. doi: 10.1029/JB085iB11p06443.

A. L. Bull, A. K. McNamara, and J. Ritsema. Synthetic tomography of plume clusters and thermochemical piles. *Earth and Planetary Science Letters*, 278(3-4):152–162, 2009. ISSN 0012821X. doi: 10.1016/j.epsl.2008.11.018. URL `http://dx.doi.org/10.1016/j.epsl.2008.11.018`.

K E Bullen. Compressibility-pressure hypothesis and the Earth's interior. *Geophysical Journal International*, 5:335–368, 1949. ISSN 0956-540X.

Scott Burdick, Frank L. Vernon, Vladik Martynov, Jennifer Eakins, Trilby Cox, Jonathan Tytell, Taimi Mulder, Malcolm C. White, Luciana Astiz, Gary L. Pavlis, and Robert D. van der Hilst. Model Update May 2016: Upper-Mantle Heterogeneity beneath North America from Travel-Time Tomography with Global and USArray Data. *Seismological Research Letters*, 88(2A):319–325, 2017. ISSN 0895-0695. doi: 10.1785/0220160186. URL `http://srl.geoscienceworld.org/lookup/doi/10.1785/0220160186`.

Kevin Burke. The African plate. *South african journal of geology*, 99(4):341–409, 1996. ISSN 1012-0750.

Kevin Burke, Bernhard Steinberger, Trond H. Torsvik, and Mark A. Smethurst. Plume Generation Zones at the margins of Large Low Shear Velocity Provinces on the core-mantle boundary. *Earth and Planetary Science Letters*, 265(1-2):49–60, 2008. ISSN 0012821X. doi: 10.1016/j.epsl.2007.09.042.

Pat Castillo. The Dupal anomaly as a trace of the upwelling lower mantle. *Nature*, 336(6200): 667–670, 1988. ISSN 0028-0836. doi: 10.1038/336667a0. URL `http://www.nature.com/doifinder/10.1038/336667a0`.

Millard F Coffin, M S Pringle, R A Duncan, T P Gladczenko, M Storey, R D M Ller, and L A Gahagan. Kerguelen Hotspot Magma Output since 130 Ma. *JOURNAL OF PETROLOGY AUSTRALIA RECEIVED JUNE*, 43(14):1121–1139, 2002.

L. Colli, S. Ghelichkhan, and H. P. Bunge. On the ratio of dynamic topography and gravity anomalies in a dynamic Earth. *Geophysical Research Letters*, 43(6):2510–2516, 2016. ISSN 19448007. doi: 10.1002/2016GL067929.

Vincent Courtillot, Jean Besse, Didier Vandamme, Raymond Montigny, Jean-Jacques Jaeger, and Henri Cappetta. Deccan flood basalts at the Cretaceous/Tertiary boundary? *Earth and Planetary Science Letters*, 80(3-4):361–374, 1986. ISSN 0012-821X.

Vincent Courtillot, Anne Davaille, Jean Besse, and Joann Stock. Three distinct types of hotspots in the Earths mantle. *Earth and Planetary Science Letters*, 205(3-4):295–308, 2003. ISSN 0012821X. doi: 10.1016/S0012-821X(02)01048-8. URL `http://www.sciencedirect.com/science/article/pii/S0012821X02010488`.

F A Dahlen, S Hung, and Guust Nolet. Frechet kernels for finite-frequency traveltimes - I. Theory. *Geophys. J. Int.*, 141(July):157–174, 2000.

Juliane Dannberg and Rene Gassmöller. Chemical trends in ocean islands explained by plume–slab interaction. *Proceedings of the National Academy of Sciences*, page 201714125, 2018. ISSN 0027-8424. doi: 10.1073/pnas.1714125115. URL `http://www.pnas.org/lookup/doi/10.1073/pnas.1714125115`.

Anne Davaille. Simultaneous generation of hotspots and superwells by convetion in a heterogeneous planetary mantle. *Nature*, 402(6763):756–760, 1999. ISSN 00280836. doi: 10.1038/45461.

Anne Davaille, Fabien Girard, and Michael Le Bars. How to anchor hotspots in a convecting mantle? *Earth and Planetary Science Letters*, 203(2):621–634, 2002. ISSN 0012821X. doi: 10.1016/S0012-821X(02)00897-X.

Anne Davaille, Eléonore Stutzmann, Graça Silveira, Jean Besse, and Vincent Courtillot. Convective patterns under the Indo-Atlantic « box ». *Earth and Planetary Science Letters*, 239(3-4):233–252, 2005. ISSN 0012821X. doi: 10.1016/j.epsl.2005.07.024.

G F Davies. On the emergence of plate tectonics: Correction, 1992.

Geoffrey F Davies. Ocean bathymetry and mantle convection: 1. Large-scale flow and hotspots. *Journal of Geophysical Research: Solid Earth*, 93(B9):10467–10480, 1988. ISSN 2156-2202.

Geoffrey F Davies and Michael Gurnis. Interaction of mantle dregs with convection: Lateral heterogeneity at the core-mantle boundary. *Geophysical Research Letters*, 13(13):1517–1520, 1986. ISSN 0094-8276.

James Dewey and Perry Byerly. The early history of seismometry (to 1900). *Bulletin of the Seismological Society of America*, 59(November):183–227, 1969.

C. Moctar Doucouré and Maarten J. de Wit. Old inherited origin for the present near-bimodal topography of Africa. *Journal of African Earth Sciences*, 36(4):371–388, 2003. ISSN 08995362. doi: 10.1016/S0899-5362(03)00019-8.

Arthur Conan Doyle. *A Study in Scarlet*. Ward Lock & Co, 1 edition, 1887.

R A Duncan and D G Pyle. Rapid eruption of the Deccan flood basalts at the Cretaceous/Tertiary boundary. *Nature*, 333(6176):841, 1988. ISSN 1476-4687.

B. Dupre and C. J. Allegre. Pb-Sr isotope variation in Indian Ocean basalts and mixing phenomena. *Nature*, 303:142–145, 1983.

Adam M. Dziewonski and Don L. Anderson. Preliminary reference Earth model. *Physics of the Earth and Planetary Interiors*, 25(4):297–356, 1981. ISSN 00319201. doi: 10.1016/0031-9201(81)90046-7.

Adam M. Dziewonski and Don L Anderson. Seismic Tomography. *Scientific American*, 3(4): 3–6, 1984.

Adam M. Dziewonski, Bradford H. Hager, and Richard J. O'Connell. Large-scale heterogeneities in the lower mantle. *Journal of Geophysical Research*, 82(2):239–255, 1977. ISSN 01480227. doi: 10.1029/JB082i002p00239. URL `http://doi.wiley.com/10.1029/JB082i002p00239`.

E R Engdahl, R van der Hilst, and R Buland. Global Teleseismic Earthquake Relocation with Improved Travel Times and Procedures for Depth Determination. *Bssa*, 88(3):722–743, 1998.

John Ewing and Maurice Ewing. A Telemetering Ocean-Bottom Seismograph. *Journal of Geophysical Research*, 66(11):3863–3878, 1961.

Maurice Ewing and Allyn Vine. Deep sea measurements without wires or cables. *Eos Trans. AGU*, 19(1):248–251, 1938. ISSN 2324-9250. doi: 10.1029/TR019i001p00248. URL `https://doi.org/10.1029/TR019i001p00248`.

K A Farley and E Neroda. Noble gases in the earth's mantle. *Annual Review of Earth and Planetary Sciences*, 26(1):189–218, 1998. ISSN 0084-6597.

Cinzia G. Farnetani and Henri Samuel. Beyond the thermal plume paradigm. *Geophysical Research Letters*, 32(7):1–4, 2005. ISSN 00948276. doi: 10.1029/2005GL022360.

Dinzia G. Farnetani and Mark A. Richards. Thermal entrainment and melting in mantle plumes. *Earth and Planetary Science Letters*, 136(3-4):251–267, 1995. ISSN 0012821X. doi: 10.1016/0012-821X(95)00158-9.

Andreas Fichtner and Tristan Van Leeuwen. Journal of Geophysical Research : Solid Earth. *Journal ofGeophysical Research: Solid Earth*, 120:1–25, 2015. ISSN 21699313. doi: 10.1002/2015JB012106.Received.

Andreas Fichtner, Brian L N Kennett, Heiner Igel, and Hans Peter Bunge. Full seismic waveform tomography for upper-mantle structure in the Australasian region using adjoint methods. *Geophysical Journal International*, 179(3):1703–1725, 2009. ISSN 0956540X. doi: 10.1111/j.1365-246X.2009.04368.x.

Stewart Fishwick and Ian D. Bastow. Towards a better understanding of African topography: a review of passive-source seismic studies of the African crust and upper mantle. *Geological Society, London, Special Publications*, 357(1):343–371, 2011. ISSN 0305-8719. doi: 10.1144/sp357.19.

G. R. Foulger, M. J. Pritchard, B. R. Julian, J. R. Evans, R. M. Allen, G. Nolet, W. J. Morgan, B. H. Bergsson, P. Erlendsson, S. Jakobsdottir, S. Ragnarsson, R. Stefansson, and K. Vogfjord. The seismic anomaly beneath Iceland extends down to the mantle transition zone and no deeper. *Geophysical Journal International*, 142(3):1–5, 2000. ISSN 0956540X. doi: 10.1046/j.1365-246X.2000.00245.x.

Loïc Fourel, Angela Limare, Claude Jaupart, Emanoil Surducan, Cinzia G. Farnetani, Edouard C. Kaminski, Camelia Neamtu, and Vasile Surducan. The Earth's mantle in a microwave oven: thermal convection driven by a heterogeneous distribution of heat sources. *Experiments in Fluids*, 58(8):1–16, 2017. ISSN 07234864. doi: 10.1007/s00348-017-2381-3.

S. W. French and B. A. Romanowicz. Whole-mantle radially anisotropic shear velocity structure from spectral-element waveform tomography. *Geophysical Journal International*, 199(3):1303–1327, 2014. ISSN 1365246X. doi: 10.1093/gji/ggu334.

Scott W. French and Barbara Romanowicz. Broad plumes rooted at the base of the Earth's mantle beneath major hotspots. *Nature*, 525(7567):95–99, 2015. ISSN 0028-0836. doi: 10.1038/nature14876. URL `http://www.nature.com/doifinder/10.1038/nature14876`.

Edward J. Garnero and Allen K. McNamara. Structure and dynamics of earth's lower mantle. *Science*, 320(5876):626–628, 2008. ISSN 00368075. doi: 10.1126/science.1148028.

Edward J. Garnero, Allen K. McNamara, and Sang-Heon Shim. Continent-sized anomalous zones with low seismic velocity at the base of Earth's mantle. *Nature Geoscience*, 9(June): 481, 2016. ISSN 1752-0894. doi: 10.1038/ngeo2733. URL `http://www.nature.com/doifinder/10.1038/ngeo2733`.

Ana D Gibbons, Joanne M Whittaker, and R Dietmar Müller. The breakup of East Gondwana: Assimilating constraints from Cretaceous ocean basins around India into a best-fit tectonic model. *Journal of geophysical research: solid earth*, 118(3):808–822, 2013. ISSN 2169-9356.

E M Golos, H Fang, H Yao, H Zhang, S Burdick, F Vernon, A. Schaeffer, S Lebedev, and R. D. van der Hilst. Shear-wave tomography beneath the United States using a joint inversion of surface and body waves. *Journal of Geophysical Research: Solid Earth*, 2018. ISSN 21699313. doi: 10.1029/2017JB014894. URL `http://doi.wiley.com/10.1029/2017JB014894`.

Stephen P. Grand, Rob D. Van Der Hilst, and Sri Widiyantoro. Global seismic tomography: A snapshot of convection in the earth. *GSA Today*, 7(4):1–7, 1997. ISSN 10525173. doi: 10.1130/GSAT01707GW.1.

Griffiths and James. The adjustment of mantle plumes to change in plate motion. *Geophysical Research Letters*, 16(5):437–440, 1989.

Michael Gurnis, Jerry X. Mitrovica, Jeroen Ritsema, and Hendrik Jan Van Heijst. Constraining mantle density structure using geological evidence of surface uplift rates: The case of the African Superplume. *Geochemistry, Geophysics, Geosystems*, 1(7), 2000. ISSN 15252027. doi: 10.1029/1999GC000035.

Sarah Hable, Karin Sigloch, Guilhem Barruol, Simon C. Stähler, and Céline Hadziioannou. Clock errors in land and ocean bottom seismograms: high-accuracy estimates from multiple-component noise cross-correlations. *Geophysical Journal International*, 214(3): 2014–2034, 2018. ISSN 0956-540X. doi: 10.1093/gji/ggy236. URL `https://academic.oup.com/gji/article/214/3/2014/5038378`.

B. H. Hager, M. A. Richards, A. M. Dziewonski, R. P. Comer, and R. W. Clayton. Lower mantle heterogeneity, dynamic topography and the geoid. *Nature*, 314(6013):752–752, 1985. ISSN 0028-0836. doi: 10.1038/314752a0.

Samantha E. Hansen, Andrew A. Nyblade, and Margaret H. Benoit. Mantle structure beneath Africa and Arabia from adaptively parameterized P-wave tomography: Implications for the origin of Cenozoic Afro-Arabian tectonism. *Earth and Planetary Science Letters*, 319-320: 23–34, 2012. ISSN 0012821X. doi: 10.1016/j.epsl.2011.12.023. URL `http://dx.doi.org/10.1016/j.epsl.2011.12.023`.

J. R. Heirtzler. SEA-FLOOR SPREADING. *Scientific American*, 219(6):60–73, 1968.

Yann Hello, Anthony Ogé, Alexey Sukhovich, and Guust Nolet. Modern mermaids: New floats image the deep Earth. *Eos*, 92(40):337–338, 2011. ISSN 00963941. doi: 10.1029/2011EO400001.

Albrecht W. Hofmann and William M. White. Mantle plumes from ancient oceanic crust, 1982. ISSN 0012821X.

C Hofmann, V Courtillot, G Feraud, P Rochette, G Yirgu, E Ketefo, and R Pik. Timing of the Ethiopian flood basalt event and implications for plume birth and global change. *Nature*, 389(6653):838, 1997. ISSN 1476-4687.

Kasra Hosseini. *Global multiple-frequency seismic tomography using teleseismic and core-diffracted body waves*. PhD thesis, LMU, 2016.

Kasra Hosseini and Karin Sigloch. Multifrequency measurements of core-diffracted P waves (Pdiff) for global waveform tomography. *Geophysical Journal International*, 203(1):506–521, 2015. ISSN 1365246X. doi: 10.1093/gji/ggv298.

Kasra Hosseini and Karin Sigloch. ObspyDMT: A Python toolbox for retrieving and processing large seismological data sets. *Solid Earth*, 8(5):1047–1070, 2017. ISSN 18699529. doi: 10.5194/se-8-1047-2017.

Kasra Hosseini, Kara J. Matthews, Karin Sigloch, Grace E. Shephard, Mathew Domeier, and Maria Tsekhmistrenko. SubMachine: Web-Based Tools for Exploring Seismic Tomography and Other Models of Earth's Deep Interior. *Geochemistry, Geophysics, Geosystems*, pages 1–20, 2018. ISSN 15252027. doi: 10.1029/2018GC007431.

Kasra Hosseini, Karin Sigloch, Maria Tsekhmistrenko, Afsaneh Zaheri, Tarje Nissen-Meyer, and Heiner Igel. Global mantle structure from multifrequency tomography using P, PP and P-diffracted waves. *Geophys. J. Int.*, 220(1):96–141, 2019. doi: 10.1093/gji/ggz394.

A. Mark Jellinek and Michael Manga. Links Between Long-lived Hot Spots, Mantle Plumes, D", And Plate Tectonics. *Review of Geophysics*, 42(2003):1–35, 2003. doi: 10.1029/2003RG000144.1.INTRODUCTION. URL `http://www.seismo.berkeley.edu/{~}manga/paper72.pdf`.

Shun-ichiro Karato and Bijaya B. Karki. Origin of lateral variation of seismic wave velocities and density in the deep mantle. *Journal of Geophysical Research: Solid Earth*, 106(B10): 21771–21783, 2001. ISSN 01480227. doi: 10.1029/2001JB000214. URL `http://doi.wiley.com/10.1029/2001JB000214`.

P E Keken and C J Ballentine. Dynamical models of mantle volatile evolution and the role of phase transitions and temperature-dependent rheology. *Journal of Geophysical Research: Solid Earth*, 104(B4):7137–7151, 1999. ISSN 2156-2202.

Brian L. N. Kennett and E. R. Engdahl. Traveltimes for global earthquake location and phase identification. *Geophysical Journal International*, 105(2):429–465, 1991. ISSN 0956540X. doi: 10.1111/j.1365-246X.1991.tb06724.x. URL `http://dx.doi.org/10.1111/j.1365-246X.1991.tb06724.x{%}5Cnhttp://www3.interscience.wiley.com/journal/119359470/abstract{%}5Cnhttp://onlinelibrary.wiley.com/doi/10.1111/j.1365-246X.1991.tb06724.x/abstract`.

Scott D King and Jeroen Ritsema. African hot spot volcanism: small-scale convection in the upper mantle beneath cratons. *Science*, 290(5494):1137–1140, 2000. ISSN 0036-8075.

P. Koelemeijer, J. Ritsema, A. Deuss, and H. J. van Heijst. SP12RTS: A degree-12 model of shear- and compressional-wave velocity for Earth's mantle. *Geophysical Journal International*, 204(2):1024–1039, 2016. ISSN 1365246X. doi: 10.1093/gji/ggv481.

P. Koelemeijer, B. S.A. Schuberth, D. R. Davies, A. Deuss, and J. Ritsema. Constraints on the presence of post-perovskite in Earth's lowermost mantle from tomographic-geodynamic model comparisons. *Earth and Planetary Science Letters*, 494:226–238, 2018. ISSN 0012821X. doi: 10.1016/j.epsl.2018.04.056. URL `https://doi.org/10.1016/j.epsl.2018.04.056`.

Paula Koelemeijer, Arwen Deuss, and Jeroen Ritsema. Density structure of Earth's lowermost mantle from Stoneley mode splitting observations. *Nature Communications*, 8(May):15241, 2017. ISSN 2041-1723. doi: 10.1038/ncomms15241. URL `http://www.nature.com/doifinder/10.1038/ncomms15241`.

Ichiro Kumagai, Anne Davaille, Kei Kurita, and Eléonore Stutzmann. Mantle plumes: Thin, fat, successful, or failing? Constraints to explain hot spot volcanism through time and space. *Geophysical Research Letters*, 35(16), 2008. ISSN 00948276. doi: 10.1029/2008GL035079.

Carolina Lithgow-Bertelloni and Paul G. Silver. Dynamic topography, plate driving forces and the African superswell. *Nature*, 395(6699):269–272, 1998. ISSN 00280836. doi: 10.1038/26212.

Ross Maguire, Jeroen Ritsema, Mickaël Bonnin, Peter E. van Keken, and Saskia Goes. Evaluating the Resolution of Deep Mantle Plumes in Teleseismic Traveltime Tomography.

Journal of Geophysical Research: Solid Earth, pages 1–17, 2018. ISSN 21699356. doi: 10.1002/2017JB014730.

Giuseppe Marra, Cecilia Clivati, Richard Luckett, Anna Tampellini, Jochen Kronjäger, Louise Wright, Alberto Mura, Filippo Levi, Stephen Robinson, André Xuereb, Brian Baptie, and Davide Calonico. Ultrastable laser interferometry for earthquake detection with terrestrial and submarine cables. *Science*, 361(6401):486–490, 2018. ISSN 10959203. doi: 10.1126/science.aat4458.

Guy Masters, Thomas H. Jordan, Paul G. Silver, and Freeman Gilbert. Aspherical Earth structure from fundamental spheroidal-mode data. *Nature*, 298(5875):609–613, 1982. ISSN 00280836. doi: 10.1038/298609a0.

Guy Masters, Gabi Laske, Harold Bolton, and Adam Dziewonski. The Relative Behavior of Shear Velocity, Bulk Sound Speed, and Compressional Velocity in the Mantle: Implications for Chemical and Thermal Structure, jan 2000. URL `https://doi.org/10.1029/GM117p0063`.

William Menke. *Geophysical data analysis: Discrete inverse theory*. Academic press, 2018. ISBN 0128135565.

R. Montelli, G. Nolet, F. a. Dahlen, and G. Masters. A catalogue of deep mantle plumes: New results from finitefrequency tomography. *Geochemistry, Geophysics, Geosystems*, 7(11), 2006. ISSN 15252027. doi: 10.1029/2006GC001248.

Raffaella Montelli, Guust Nolet, F a Dahlen, Guy Masters, E Robert Engdahl, and Shu-Huei Hung. Finite-frequency tomography reveals a variety of plumes in the mantle. *Science (New York, N.Y.)*, 303(5656):338–343, 2004. ISSN 0036-8075. doi: 10.1126/science.1092485.

Caterina Montuori, Giovanni Battista Cimini, and Paolo Favali. Teleseismic tomography of the southern Tyrrhenian subduction zone: New results from seafloor and land recordings. *Journal of Geophysical Research: Solid Earth*, 112(3):1–15, 2007. ISSN 21699356. doi: 10.1029/2005JB004114.

Andy Moore, Tom Blenkinsop, and Fenton Cotterill. Southern African topography and erosion history: Plumes or plate tectonics? *Terra Nova*, 21(4):310–315, 2009. ISSN 13653121. doi: 10.1111/j.1365-3121.2009.00887.x.

Della S. Mora, L. Boschi, P. J. Tackley, T. Nakagawa, and D. Giardini. Low seismic resolution cannot explain S/P decorrelation in the lower mantle. *Geophysical Research Letters*, 38(12): 1–6, 2011. ISSN 00948276. doi: 10.1029/2011GL047559.

W. Jason Morgan. Convection Plumes in the lower mantle. *Nature*, 230:42–43, 1971.

W. Jason Morgan. Deep Mantle Convection Plumes and Plate Motions, 1972. ISSN 0149-1423. URL `http://aapgbull.geoscienceworld.org/content/56/2/203.abstract`.

P. Moulik and G. Ekström. The relationships between large-scale variations in shear velocity, density, and compressional velocity in the Earth's mantle. *Journal of Geophysical Research: Solid Earth*, 121(4):2737–2771, 2016. ISSN 21699356. doi: 10.1002/2015JB012679.

R. Dietmar Müller, Maria Seton, Sabin Zahirovic, Simon E. Williams, Kara J. Matthews, Nicky M. Wright, Grace E. Shephard, Kayla T. Maloney, Nicholas Barnett-Moore, Maral Hosseinpour, Dan J. Bower, and John Cannon. Ocean Basin Evolution and Global-Scale Plate Reorganization Events Since Pangea Breakup. *Annual Review of Earth and Planetary Sciences*, 44(1):107–138, 2016. ISSN 0084-6597. doi: 10.1146/annurev-earth-060115-012211. URL `http://www.annualreviews.org/doi/10.1146/annurev-earth-060115-012211`.

Motohiko Murakami, Kei Hirose, Katsuyuki Kawamura, Nagayoshi Sata, and Yasuo Ohishi. Post-perovskite phase transition in MgSiO3. *Science*, 304(5672):855–858, 2004. ISSN 0036-8075.

Shozaburo Nagumo and Daniel A Walker. Ocean Bottom Geoscience Observatories. *Eos Trans. AGU*, 70(26):673,677, 1989.

Takashi Nakagawa, Paul J Tackley, Frederic Deschamps, and James A D Connolly. Incorporating self-consistently calculated mineral physics into thermochemical mantle convection simulations in a 3-D spherical shell and its influence on seismic anomalies in Earth's mantle. *Geochemistry, Geophysics, Geosystems*, 10(3), 2009. ISSN 1525-2027.

Peter L. Nelson and Stephen P. Grand. Lower-mantle plume beneath the Yellowstone hotspot revealed by core waves. *Nature Geoscience*, 11(4):280–284, 2018. ISSN 17520908. doi: 10.1038/s41561-018-0075-y.

Sidao Ni, Eh Tan, Michael Gurnis, and Don Helmberger. Sharp sides to the African superplume. *Science*, 296(June):1850–1852, 2002.

T. Nissen-Meyer, M. Van Driel, S. C. Stähler, K. Hosseini, S. Hempel, L. Auer, A. Colombi, and A. Fournier. AxiSEM: Broadband 3-D seismic wavefields in axisymmetric media. *Solid Earth*, 2014. ISSN 18699529. doi: 10.5194/se-5-425-2014.

G. Nolet, Y. Hello, S. Bonnieux, J. Chen, A. Pazmino, A. Deschamps, M. M. Regnier, Y. Font, S. Van der Lee, and F. Simons. Seismometry in the Oceans: First Observations from an Array of Mermaids near Galapagos. *American Geophysical Union, Fall Meeting 2016, abstract #DI23C-02*, 2016. URL `http://adsabs.harvard.edu/abs/2016AGUFMDI23C..02N`.

Guust Nolet. Solving or resolving inadequate and noisy tomographic systems. *Journal of Computational Physics*, 61(3):463–482, 1985. ISSN 10902716. doi: 10.1016/0021-9991(85)90075-0.

Guust Nolet. *A Breviary of Seismic Tomography*. Cambridge University Press, Cambridge, 2008. ISBN 9780511984709. doi: 10.1017/CBO9780511984709. URL `http://ebooks.cambridge.org/ref/id/CBO9780511984709`.

Guust Nolet. Analyzing Mermaid Seismograms - A Tutorial. Technical report, Geoazur, 2016.

Guust Nolet and F A Dahlen. Wave front healing and the evolution of seismic delay times. *Journal of Geophysical Research: Solid Earth*, 105(B8):19043–19054, 2000. ISSN 2156-2202.

Guust Nolet, Shun Ichiro Karato, and Raffaella Montelli. Plume fluxes from seismic tomography. *Earth and Planetary Science Letters*, 248(3-4):685–699, 2006. ISSN 0012821X. doi: 10.1016/j.epsl.2006.06.011.

Guust Nolet, Richard Allen, and Dapeng Zhao. Mantle plume tomography. *Chemical Geology*, 241(3-4):248–263, 2007. ISSN 00092541. doi: 10.1016/j.chemgeo.2007.01.022.

Andrew A Nyblade and Scott W Robinson. The African Superswell. *Geophysical Research Letters*, 21(9):765–768, 1994.

M. Obayashi, J. Yoshimitsu, H. Sugioka, A. Ito, T. Isse, H. Shiobara, D. Reymond, and Daisuke Suetsugu. Mantle plumes beneath the South Pacific superswell revealed by finite frequency P-tomography using regional seafloor and island data. *Geophysical Research Letters*, 2016. ISSN 00948276. doi: 10.1002/2016GL070793. URL `http://doi.wiley.com/10.1002/2016GL070793`.

Richard Oldham. The Constitution of the Interior of the Earth, as Revealed by Earthquakes. *Geological Society of London*, xli(1895):13–21, 1906.

Peter Olson and In Seung Nam. Formation of seafloor swells by mantle plumes. *Journal of Geophysical Research: Solid Earth*, 91(B7):7181–7191, 1986. ISSN 01480227. doi: 10.1029/JB091iB07p07181. URL `http://doi.wiley.com/10.1029/JB091iB07p07181`.

Peter Olson and Harvey Singer. Creeping plumes. *Journal of Fluid Mechanics*, 158:511–531, 1985. ISSN 14697645. doi: 10.1017/S0022112085002749.

Christopher C. Paige and Michael A. Saunders. LSQR: An Algorithm for Sparse Linear Equations and Sparse Least Squares. *ACM Transactions on Mathematical Software*, 8(1): 43–71, 1982. ISSN 00983500. doi: 10.1145/355984.355989. URL `http://portal.acm.org/citation.cfm?doid=355984.355989`.

Per-olof Persson and Gilbert Strang. A Simple Mesh Generator in MATLAB. *SIAM Review*, 46(2):329–345, 2004.

M A Richards, R A Duncan, and V E Courtillot. Flood Basalts and Hot Spot Tracks: Plumes Heads and Tails. *Science*, 246(10):103–107, 1989.

Uwe Ring. The east African rift system. *Austrian Journal of Earth Sciences*, 107(1):132–146, 2014. ISSN 0251-7493.

J. Ritsema, H. J. Van Heijst, and J. H. Woodhouse. Complex Shear Wave Velocity Structure Imaged Beneath Africa and Iceland. *Science*, 286(5446):1925–1928, 1999. ISSN 00368075. doi: 10.1126/science.286.5446.1925.

J. Ritsema, H. J. van Heijst, J. H. Woodhouse, and a. Deuss. Long-period body wave traveltimes through the crust: Implication for crustal corrections and seismic tomography. *Geophysical Journal International*, 179(2):1255–1261, 2009. ISSN 0956540X. doi: 10.1111/j.1365-246X.2009.04365.x.

J. Ritsema, A. Deuss, H. J. Van Heijst, and J. H. Woodhouse. S40RTS: A degree-40 shear-velocity model for the mantle from new Rayleigh wave dispersion, teleseismic traveltime and normal-mode splitting function measurements. *Geophysical Journal International*, 184(3):1223–1236, 2011. ISSN 0956540X. doi: 10.1111/j.1365-246X.2010.04884.x.

Barbara Romanowicz. Seismic tomography of the Earth's mantle. *Annu*, pages 77–99, 1991.

Barbara Romanowicz. Global Mantle Tomography : Progress Status in the Past 10 Years. *Annual Review of Earth and Planetary Sciences*, 31(1):303–328, 2003. ISSN 0084-6597. doi: 10.1146/annurev.earth.31.091602.113555. URL `http://www.annualreviews.org/doi/abs/10.1146/annurev.earth.31.091602.113555`.

Henri Samuel and Cinzia G Farnetani. Thermochemical convection and helium concentrations in mantle plumes. *Earth and Planetary Science Letters*, 207(1-4):39–56, 2003. ISSN 0012-821X.

A. J. Schaeffer and S. Lebedev. Global shear speed structure of the upper mantle and transition zone. *Geophysical Journal International*, 194(1):417–449, 2013. ISSN 0956540X. doi: 10.1093/gji/ggt095.

Antje Schlömer, Wolfram H. Geissler, Wilfried Jokat, and Marion Jegen. Seismicity in the Vicinity of the Tristan Da Cunha Hot Spot: Particular Plate Tectonics and Mantle Plume Presence. *Journal of Geophysical Research: Solid Earth*, 122(12):10,427–10,439, 2017a. ISSN 21699356. doi: 10.1002/2017JB015017.

Antje Schlömer, Wolfram H. Geissler, Wilfried Jokat, and Marion Jegen. Hunting for the Tristan mantle plume – An upper mantle tomography around the volcanic island of Tristan da Cunha. *Earth and Planetary Science Letters*, 462:122–131, 2017b. ISSN 0012821X. doi: 10.1016/j.epsl.2016.12.028. URL `http://dx.doi.org/10.1016/j.epsl.2016.12.028`.

John Robert Scholz, Guilhem Barruol, Fabrice R Fontaine, Karin Sigloch, Wayne Crawford, and Martha Deen. Orienting Ocean-Bottom Seismometers from P-wave and Rayleigh wave polarisations. *Geophysical Journal International*, 208(3):1277–1289, 2016. ISSN 0956-540X. doi: 10.1093/gji/ggw426.

G. Schubert, G. Masters, P. Olson, and P. Tackley. Superplumes or plume clusters? *Physics of the Earth and Planetary Interiors*, 146(1-2):147–162, 2004. ISSN 00319201. doi: 10.1016/j.pepi.2003.09.025.

Peter M Shearer. *Introduction to seismology*. Cambridge University Press, 2009. ISBN 0521708427.

G. E. Shephard, K. J. Matthews, K. Hosseini, and M. Domeier. On the consistency of seismically imaged lower mantle slabs. *Scientific Reports*, 7(1):10976, 2017. ISSN 2045-2322. doi: 10.1038/s41598-017-11039-w. URL `http://www.nature.com/articles/s41598-017-11039-w`.

Hetu C. Sheth. Large Igneous Provinces (LIPs): Definition, recommended terminology, and a hierarchical classification. *Earth-Science Reviews*, 85(3-4):117–124, 2007. ISSN 00128252. doi: 10.1016/j.earscirev.2007.07.005.

Karin Sigloch. *Multiple-frequency body-wave tomography.* PhD thesis, Princeton University, 2008. URL `http://adsabs.harvard.edu/abs/2008PhDT.....77S`.

Karin Sigloch and Guust Nolet. Measuring finite-frequency body-wave amplitudes and traveltimes. *Geophysical Journal International*, 167(1):271–287, 2006. ISSN 0956540X. doi: 10.1111/j.1365-246X.2006.03116.x.

Karin Sigloch, Nadine McQuarrie, and Guust Nolet. Two-stage subduction history under North America inferred from multiple-frequency tomography. *Nature Geoscience*, 1(7): 458–462, 2008. ISSN 1752-0894. doi: 10.1038/ngeo231.

N. A. Simmons, S. C. Myers, G. Johannesson, and E. Matzel. LLNL-G3Dv3: Global P wave tomography model for improved regional and teleseismic travel time prediction. *Journal of Geophysical Research: Solid Earth*, 117(B10):n/a–n/a, 2012. ISSN 01480227. doi: 10.1029/2012JB009525. URL `http://doi.wiley.com/10.1029/2012JB009525`.

N a Simmons, S C Myers, G Johannesson, E Matzel, and S. P. Grand. Evidence for long-lived subduction of an ancient tectonic plate beneath the southern Indian Ocean. *Geophysical Research Letters*, pages 9270–9278, 2015. doi: 10.1002/2015GL066237.Received.

Nathan a. Simmons, Alessandro M. Forte, Lapo Boschi, and Stephen P. Grand. GyPSuM: A joint tomographic model of mantle density and seismic wave speeds. *Journal of Geophysical Research: Solid Earth*, 115(12):1–24, 2010. ISSN 21699356. doi: 10.1029/2010JB007631.

Fj Simons, G Nolet, Jm Babcock, Re Davis, and Ja Orcutt. A future for drifting seismic networks. *Eos*, 87(31):305–307, 2006. ISSN 0096-3941. doi: 10.1029/2006EO310002. URL `http://discovery.ucl.ac.uk/2433/`.

Frederik J. Simons, Guust Nolet, Paul Georgief, Jeff M. Babcock, Lloyd a. Regier, and Russ E. Davis. On the potential of recording earthquakes for global seismic tomography by low-cost autonomous instruments in the oceans. *Journal of Geophysical Research*, 114(B5):1–16, 2009. ISSN 0148-0227. doi: 10.1029/2008JB006088.

Norman H Sleep. Hotspots and Mantle Plumes: Some Phenomenology. *Journal of Geophysical Research*, 95:6715–6736, 1990. ISSN 0148-0227. doi: 10.1029/JB095iB05p06715.

Frank D Stacey and David E Loper. The thermal boundary-layer interpretation of D" and its role as a plume source. *Physics of the Earth and Planetary Interiors*, 33(1):45–55, 1983. ISSN 0031-9201.

S. C. Stähler and K Sigloch. Fully probabilistic seismic source inversion – Part 1: Efficient parameterisation. *Solid Earth*, 5:1055–1069, 2014. doi: 10.5194/se-5-1055-2014. URL `www.solid-earth.net/5/1055/2014/`.

S. C. Stähler, K. Sigloch, K. Hosseini, W. C. Crawford, G. Barruol, M. C. Schmidt-Aursch, M. Tsekhmistrenko, J. R. Scholz, A. Mazzullo, and M. Deen. Performance report of the RHUM-RUM ocean bottom seismometer network around la Réunion, western Indian Ocean. *Advances in Geosciences*, 41:43–63, 2016a. ISSN 16807359. doi: 10.5194/adgeo-41-43-2016.

Simon C. Stähler, Martin van Driel, Ludwig Auer, Kasra Hosseini, Karin Sigloch, and Tarje Nissen-Meyer. MC Kernel: Broadband Waveform Sensitivity Kernels for Seismic Tomography. *EGU General Assembly 2016, held 17-22 April, 2016 in Vienna Austria, id. EPSC2016-7020*, 18, 2016b. URL `http://adsabs.harvard.edu/abs/2016EGUGA..18.7020S`.

B. Steinberger and M. Antretter. Conduit diameter and buoyant rising speed of mantle plumes: Implications for the motion of hot spots and shape of plume conduits. *Geochemistry, Geophysics, Geosystems*, 7(11), 2006. ISSN 15252027. doi: 10.1029/2006GC001409.

Bernhard Steinberger and Richard J O'Connell. Advection of plumes in mantle flow: implications for hotspot motion, mantle viscosity and plume distribution. *Geophysical Journal International*, 132(2):412–434, 1998. ISSN 0956540X. doi: 10.1046/j.1365-246x.1998.00447.x. URL `http://doi.wiley.com/10.1046/j.1365-246x.1998.00447.x`.

Bernhard Steinberger and Trond H. Torsvik. A geodynamic model of plumes from the margins of Large Low Shear Velocity Provinces. *Geochemistry, Geophysics, Geosystems*, 13(1), 2012. ISSN 15252027. doi: 10.1029/2011GC003808.

Daisuke Suetsugu, H. Sihiobara, H. Sugioka, G. Barrruol, F. Schindele, D. Reymond, A. Bonneville, E. Debayle, T. Isse, T. Kanazawa, and Y. Fukao. Probing south pacific mantle plumes with ocean bottom seismographs. *Eos*, 86(44), 2005. ISSN 00963941. doi: 10.1029/2005EO440001.

Daisuke Suetsugu, T. Isse, S. Tanaka, M. Obayashi, H. Shiobara, H. Sugioka, T. Kanazawa, Y. Fukao, G. Barruol, and D. Reymond. South Pacific mantle plumes imaged by seismic observation on islands and seafloor. *Geochemistry, Geophysics, Geosystems*, 10(11), 2009. ISSN 15252027. doi: 10.1029/2009GC002533.

Eh Tan and Michael Gurnis. Metastable superplumes and mantle compressibility. *Geophysical Research Letters*, 32(20), 2005. ISSN 0094-8276.

Eh Tan and Michael Gurnis. Compressible thermochemical convection and application to lower mantle structures. *Journal of Geophysical Research: Solid Earth*, 112(B6), 2007. ISSN 2156-2202.

Carl Tape, Qinya Liu, and Jeroen Tromp. Finite-frequency tomography using adjoint methods - Methodology and examples using membrane surface waves. *Geophysical Journal International*, 168(3):1105–1129, 2007. ISSN 0956540X. doi: 10.1111/j.1365-246X.2006.03191.x.

Andrea Tesoniero, Fabio Cammarano, and Lapo Boschi. Geochemistry, Geophysics, Geosystems. *Geochemistry Geophysics Geosystems*, 17:2825–2834, 2016. ISSN 0012821X. doi: 10.1002/2014GC005684.Key.

Yue Tian, S. H. Hung, Guust Nolet, Raffaella Montelli, and F. a. Dahlen. Dynamic ray tracing and traveltime corrections for global seismic tomography. *Journal of Computational Physics*, 226(1):672–687, 2007a. ISSN 00219991. doi: 10.1016/j.jcp.2007.04.025.

Yue Tian, Raffaella Montelli, Guust Nolet, and F. a. Dahlen. Computing traveltime and amplitude sensitivity kernels in finite-frequency tomography. *Journal of Computational Physics*, 226(2):2271–2288, 2007b. ISSN 00219991. doi: 10.1016/j.jcp.2007.07.004.

Yue Tian, Karin Sigloch, and Guust Nolet. Multiple-frequency SH-wave tomography of the western US upper mantle. *Geophysical Journal International*, 178(3):1384–1402, 2009. ISSN 0956540X. doi: 10.1111/j.1365-246X.2009.04225.x.

Frederik Tilmann, Xiaohui Yuan, Georg Rümpker, and Elisa Rindraharisaona. SELASOMA Project, Madagascar 2012-2014, 2012.

T. H. Torsvik, R. van der Voo, P. V. Doubrovine, K. Burke, B. Steinberger, L. D. Ashwal, R. G. Tronnes, S. J. Webb, and A. L. Bull. Deep mantle structure as a reference frame for movements in and on the Earth. *Proceedings of the National Academy of Sciences*, 111(24): 8735–8740, 2014. ISSN 0027-8424. doi: 10.1073/pnas.1318135111. URL `http://www.pnas.org/cgi/doi/10.1073/pnas.1318135111`.

Trond H. Torsvik and L. Robin M. Cocks. Gondwana from top to base in space and time. *Gondwana Research*, 24(3-4):999–1030, 2013. ISSN 1342937X. doi: 10.1016/j.gr.2013.06.012. URL `http://dx.doi.org/10.1016/j.gr.2013.06.012`.

Trond H. Torsvik, Mark A. Smethurst, Kevin Burke, and Bernhard Steinberger. Large igneous provinces generated from the margins of the large low-velocity provinces in the deep mantle. *Geophysical Journal International*, 167(3):1447–1460, 2006. ISSN 0956540X. doi: 10.1111/j.1365-246X.2006.03158.x.

Trond H Torsvik, Mark A Smethurst, Kevin Burke, and Bernhard Steinberger. Long term stability in deep mantle structure : Evidence from the ˜ 300 Ma Skagerrak-Centered Large Igneous Province (the SCLIP). *Earth and Planetary Science Letters*, 267:444–452, 2008a. doi: 10.1016/j.epsl.2007.12.004.

Trond H. Torsvik, Bernhard Steinberger, L. Robin M. Cocks, and Kevin Burke. Longitude: Linking Earth's ancient surface to its deep interior. *Earth and Planetary Science Letters*, 276(3-4):273–282, 2008b. ISSN 0012821X. doi: 10.1016/j.epsl.2008.09.026. URL `http://dx.doi.org/10.1016/j.epsl.2008.09.026`.

Trond H Torsvik, Kevin Burke, Bernhard Steinberger, Susan J Webb, and Lewis D Ashwal. Diamonds sampled by plumes from the core-mantle boundary. *Nature*, 466(7304):352–355, 2010. ISSN 0028-0836. doi: 10.1038/nature09216. URL `http://dx.doi.org/10.1038/nature09216`.

R. D. van der Hilst, S. Widiyantoro, and E. R. Engdahl. Evidence for deep mantle circulation from global tomography, 1997. ISSN 0028-0836.

Martin van Driel, L. Krischer, S. C. Stähler, K. Hosseini, and T. Nissen-Meyer. Instaseis: instant global seismograms based on a broadband waveform database. *Solid Earth*, 6(2): 701–717, 2015. ISSN 1869-9529. doi: 10.5194/se-6-701-2015. URL `http://www.solid-earth.net/6/701/2015/`.

Peter E. van Keken. Evolution of starting mantle plumes: a comparison between numerical and laboratory models. *Earth and Planetary Science Letters*, 148:1–11, 1997. ISSN 0012821X. doi: 10.1016/S0012-821X(97)00042-3.

John C VanDecar, David E James, and Marcelo Assumpção. Seismic evidence for a fossil mantle plume beneath South America and implications for plate driving forces. *Nature*, 378 (6552):25, 1995. ISSN 1476-4687.

Alfred Wegener. *Die Enstehung der Kontinente und Ozeane*. Friedr. Vieweg & Sohn Akt.-Ges., 1920.

J. Weston, E. R. Engdahl, J. Harris, D. Di Giacomo, and D. A. Storchak. ISC-EHB: Reconstruction of a robust earthquake data set. *Geophysical Journal International*, 214(1): 474–484, 2018. ISSN 1365246X. doi: 10.1093/gji/ggy155.

J. M. Whittaker, S. Williams, S. M. Masterton, J. C. Afonso, M. Seton, T. C. Landgrebe, M. F. Coffin, and D. Müller. Interactions among plumes, mantle circulation and mid-ocean ridges. *American Geophysical Union, Fall Meeting 2013, abstract id. DI13A-04*, 2013. URL `http://adsabs.harvard.edu/abs/2013AGUFMDI13A..04W`.

J. M. Whittaker, J. C. Afonso, S. Masterton, R. D. Müller, P. Wessel, S. E. Williams, and M. Seton. Long-term interaction between mid-ocean ridges and mantle plumes. *Nature Geoscience*, 8(May):479–484, 2015. ISSN 1752-0894. doi: 10.1038/ngeo2437. URL `http://www.nature.com/doifinder/10.1038/ngeo2437`.

J. Tuzo Wilson. Continental Drift. *Science Advances*, 208(4):86–103, 1963.

C. J. Wolfe, S. C. Solomon, G. Laske, J. A. Collins, R. S. Detrick, J. A. Orcutt, D. Bercovici, and E. H. Hauri. Mantle Shear-Wave Velocity Structure Beneath the Hawaiian Hot Spot. *Science*, 326(5958):1388–1390, 2009. ISSN 0036-8075. doi: 10.1126/science.1180165. URL `http://www.sciencemag.org/cgi/doi/10.1126/science.1180165`.

Cecily J. Wolfe, Ingi Th Bjarnason, John C. VanDecar, and Sean C. Solomon. Seismic structure of the iceland mantle plume, 1997. ISSN 00280836.

J. H. Woodhouse and A. Deuss. Theory and Observations – Earth ' s Free Oscillations. In *Time*, pages 31–66. Elsevier B.V., 2007.

Z. Wu and R. M. Wentzcovitch. Spin crossover in ferropericlase and velocity heterogeneities in the lower mantle. *Proceedings of the National Academy of Sciences*, 111(29):10468–10472, 2014. ISSN 0027-8424. doi: 10.1073/pnas.1322427111. URL `http://www.pnas.org/cgi/doi/10.1073/pnas.1322427111`.

Michael Wysession, Douglas Wiens, and Andy Nyblade. Investigation of sources of intraplate volcanism using passcal broadband instruments in Madagascar, the Comores, and Mozambique, 2011.

Christophe Zaroli, Sophie Lambotte, and Jean Jacques Lévêque. Joint inversion of normal-mode and finite-frequency S-wave data using an irregular tomographic grid. *Geophysical Journal International*, 203(3):1665–1681, 2015. ISSN 1365246X. doi: 10.1093/gji/ggv388.

D Zhao, D A Wiens, L Dorman, J Hildebrand, S Webb, and M McDonald. High resolution seismic tomography of the Tonga slab and Lau back-arc basin. *Eos Trans. AGU*, 76(46): F392, 1995.

Dapeng Zhao, Yingbiao Xu, Douglas A. Wiens, Le Roy Dorman, John Hildebrand, and Spahr Webb. Depth extent of the Lau back-arc spreading center and its relation to subduction processes. *Science*, 278(5336):254–257, 1997. ISSN 00368075. doi: 10.1126/science.278.5336.254.

Hejun Zhu, Ebru Bozdağ, Daniel Peter, and Jeroen Tromp. Structure of the European upper mantle revealed by adjoint tomography. *Nature Geoscience*, 5(7):493–498, 2012. ISSN 1752-0894. doi: 10.1038/ngeo1501.

I fell in love with this project, hard and early on. Like with all things you rush into a bit too fast, with a bit too little thought you end up wondering : *"What have I gotten myself into? I cannot do this and I have no idea how this works!"*. And like with every crush that turns into a long-term relationship, there were happy times, times we were fighting, we were determined to work through our problems, had a good laugh from time to time and were close to breaking up at some point. Now, after 4 years, I can say we both came out stronger than we were at the beginning.

But now it's time to say goodbye.